Prediction of macrosegregation in steel ingot

A thesis submitted to the University of Leoben

for the degree of Doctor of Montanistic Sciences (Dr. mont.)

presented by

Jun Li

Leoben, July 2013

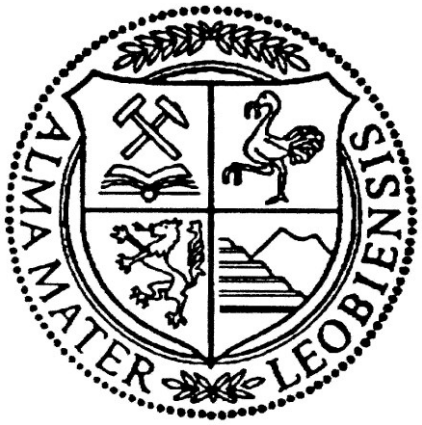

Examiner: assoz. Prof. Dr.-Ing. Menghuai Wu
Chair for Simulation and Modelling of Metallurgical Processes
Department of Metallurgy

Co-Examiner: Univ.-Prof. Dipl.-Ing. Dr.phil. Peter Schumacher
Chair of Casting Research
Department of Metallurgy

Eidesstattliche Erklärung

Ich erkläre an Eides statt, dass ich diese Arbeit selbstständig verfasst, andere als die angegebenen Quellen und Hilfsmittel nicht benützt und mich auch sonst keiner unerlaubten Hilfsmittel bedient habe.

Leoben, 04.07.2013

M. Sc. Jun Li

Affidavit

I declare in lieu of oath, that I wrote this thesis and performed the associated research myself, using only literature cited in this volume.

Leoben, 04.07.2013

M. Sc. Jun Li

Acknowledgement

I would like to express my sincere gratitude to my major PhD supervisor Prof. Menghuai Wu for his support and guidance during the three years of my thesis. His constant guidance and invaluable suggestions have made my graduate research a great learning experience. This work would not have been possible without his supervision. I am also very grateful to Prof. Andreas Ludwig for giving me the opportunity to study at University of Leoben and work at the chair of Simulation and Modelling of Metallurgical Processes (SMMP). In addition I am grateful to Dr. Abdellah Kharicha for his help with some of my lectures. It is an honor and pleasure working with them. I sincerely thank Prof. Peter Schumacher for reviewing this thesis.

I sincerely thank the China Scholarship Council and Christian-Doppler Laboratory for "Advanced Process Simulation of Solidification and Melting" for their generous financial support for my thesis for these three years.

I would like to thank my colleagues, Dr. Alexander Vakhrushev, Dr. Mahmoud Ahmadein, Dr. Jan Bohacek, Dr. Samiullah Baig, Dr. Johann Mogeritsch, DI. Josef Domitner, DI. Andreas Kemminger, DI. Ebrahim Karimi-Sibaki, Mag. Konrad Schrempf, DI. Michaela Stefan-Kharicha, DI. Günter Unterreiter, Georg Nunner, Sabine Rosenblattl, Jenny Dorner for their help in the course of this work. I would especially like to thanks Otto Klaus-Jürgen for his support with the installation of ANSYS-Fluent software and application of computer clusters.

I express a lot of thanks to Prof. Tongmin Wang and Prof. Tingju Li at Dalian University of Technology. Without their help, encouragement and unfailing support it would not have been possible for me to reach University of Leoben and complete my research here.

Many thanks to my parents for their love, support, and encouragement not only throughout the course of my Ph.D study, but also throughout my entire life. I would like also thank my parents in law for their support and encouragement.

Finally, I would like to thank my wife, Ying Zhou, and my daughter Angela Li. My wife's love and support is unfailing. Without her support I could not concentrate to finish this thesis. My daughter has been an inspiration. This work is dedicated to them.

Kurzfassung

Das Ziel dieser Arbeit ist die Verwendung eines Multiphasenmodells zur Untersuchung von Makroseigerungsphänomenen beim Blockguss von Stahl, um die Entstehung von Makroseigerungen in großen Stahlblöcken quantitativ vorherzusagen.

Zunächst wurde ein zweiphasiges Erstarrungsmodell verwendet, um die Entstehung von Kanalseigerungen im Labormaßstab an einer Legierung aus Sn-10 wt% Pb zu untersuchen. Dabei wurden erstmals dreidimensionale, lamellen- sowie stabförmige Kanalseigerungen numerisch vorhergesagt. Dieses Resultat wurde später von H. Combeau und seinen Mitarbeitern bestätigt. Ein zweistufiger Entstehungsmechanismus, der aus der Initiierung und dem Wachstum der Kanäle besteht, wird vorgeschlagen. Die Initiierung eines Kanals wird durch Strömungsinstabilitäten nahe der Erstarrungsfront (in der sogenannten Mushy Zone) verursacht. Dies kann durch die Rayleigh-Zahl der Mushy Zone charakterisiert werden. Beim Überschreiten einer kritischen Rayleigh-Zahl (0.12 – 0.24) beginnt die Kanalbildung. Das Wachstum des Kanals resultiert dann aus einer Interaktion zwischen der Strömung und dem Festkörper. In Abhängigkeit von der Strömungsrichtung kann der ursprünglich entstandene Kanal weiter zu einem stabilen Kanal heranwachsen, oder aber aufgrund der fortschreitenden Erstarrung wieder verschwinden.

Im zweiten Teil der Arbeit wurde ein dreiphasiges Erstarrungsmodell verwendet, um die Entstehung von Makroseigerungen in einem 2.45 Tonnen schweren Stahlblock zu untersuchen. Die grundlegende Seigerungsverteilung im Block wurde vorhergesagt: kegelförmige negative Seigerungen im Fußbereich, positive Seigerungen im Kopfbereich sowie einige A-förmige Seigerungsbänder im Wandbereich des Blocks. Es wurde gezeigt, dass die Sedimentation globulitischer Erstarrungskristalle eine wichtige Rolle bei der Seigerungsentstehung in einem derartigen Gussblock spielt. Die Entstehungsmechanismen der A-Seigerungen wurden analysiert: Strömungsinstabilitäten bewirken die Entstehung

quasi A-förmiger Seigerungen, welche durch globulitische Erstarrungskristalle und deren Interaktion mit stängelförmigen Dendriten verstärkt werden. Die globulitische Phase allein ist nicht notwendigerweise für die Entstehung der quasi A-förmigen Seigerungen verantwortlich. Die numerisch vorhergesagte Makrostruktur sowie die Makroseigerungen stimmten qualitativ mit experimentellen Untersuchungen überein. Signifikante quantitative Abweichungen waren jedoch feststellbar. Der Grund für diese Abweichungen liegt in der Vernachlässigung der Dendritenmorphologie im ursprünglich verwendeten dreiphasigen Simulationsmodell. Aus diesem Grund wurde das Modell im Rahmen dieser Arbeit weiterentwickelt, indem eine vereinfachte dendritische Morphologie berücksichtigt wurde. Dadurch kann die quantitative Aussagekraft der numerischen Simulation signifikant verbessert werden.

Zusätzlich wurde auch die Seigerungsentstehung in einem 25 Tonnen schweren Stahlblock untersucht. Die Seigerungsverteilung konnte gut vorhergesagt werden und eine annehmbare Übereinstimmung mit experimentellen Resultaten wurde erzielt. Da ein relativ grobes Netz für die Simulation dieses 25-Tonnen-Blocks verwendet wurde, konnten jedoch die A-Seigerungen nicht in der erforderlichen Auflösung vorhergesagt werden.

Schließlich wurde noch ein vierphasiges Erstarrungsmodell eingeführt, um die Entstehung von Makroseigerungen und von Schrumpfungslunkern miteinander zu verbinden. Dabei wurde eine zusätzliche Phase, nämlich die Gasphase, berücksichtigt. Die Lunkerentstehung im heißen Hot-Top Bereich des Blocks wurde vorhergesagt. Die Form des numerisch vorhergesagten Lunkers ist mit experimentell ermittelten Lunkerformen vergleichbar. Die Makroseigerung unter dem Lunker entspricht jedoch nicht der experimentell ermittelten Verteilung. Daher sind noch weitere Anstrengungen erforderlich, um die Anwendbarkeit des numerischen Vierphasenmodells zu verbessern.

Abstract

The main goal of this thesis is to use a multiphase approach to study and predict the macrosegregation in steel ingots.

Firstly, a two-phase columnar solidification model was employed to study the formation of channel segregation in a laboratory benchmark of Sn-10 wt.% Pb. For the first time 3D lamellar- and rod-structured channel segregates were numerically predicted. This result was later confirmed by H. Combeau and co-workers. A two-step mechanism of the channel formation was proposed, i.e. the initiation and the growth of the channel. The initiation of a channel is caused by flow perturbations near the solidification front in the mushy zone, which can be characterized by a mushy zone Rayleigh (R_a) number. When the maximum R_a number reaches a critical value (0.12 - 0.24), a channel may start to form. After the initial formation, a channel may either further develop (grow) into a stable channel, or disappear depending on the flow-solidification interaction in the two-phase mushy zone.

In the second part of this thesis, a three-phase mixed columnar-equiaxed model was employed to study the macrosegregation in a 2.45 ton steel ingot. The general segregation pattern was predicted: cone shape negative segregation in the bottom region, positive segregation in the top region, and some A-segregation bands near the wall. The equiaxed sedimentation was found playing an important role in the formation of global segregation in such big ingot. The formation mechanism of A-segregation was analyzed: flow instability causes the formation of quasi A-segregates, but both the appearance of equiaxed crystals and their interaction with the growing columnar dendrites strengthen the segregated severity significantly. The equiaxed phase was found not a necessary condition for the formation of quasi A-segregates. The predicted macrostructure and macrosegregation results agreed qualitatively with the experimentally reported segregation pattern, although the quantitative discrepancy between the calculations and the experimental results was still significant. The

reason for this discrepancy is due to the ignorance of the dendritic morphology by the original three-phase model. Therefore, in this thesis a further model-development step was made by implementing a simplified dendritic morphology. This consideration has been verified to improve the quantitative accuracy of the numerical prediction significantly.

Additionally, a 25-ton steel ingot was also calculated. The global segregation pattern was well predicted, and a reasonable agreement with the experimental result was obtained. As a relative coarse grid was used in this calculation, A-segregation bands cannot be predicted with sufficient resolution.

Finally, a four-phase solidification model was established to combine the formation of macrosegregation and shrinkage cavity. An additional phase, i.e. gas phase, was considered. It has predicted the shrinkage cavity in the hot top region, and the predicted shape of the cavity is quite similar to the experiment one. However, the predicted macrosegregation below the shrinkage cavity did not agree with the experimental one. Therefore, further effort is still required to improve the model capability.

Contents

Nomenclature

c_0	initial concentration of the alloy	-
c_ℓ , c_s , c_e , c_c	species concentration	-
c_ℓ^* , c_s^*	interface equilibrium species concentration	-
c_mix	mixture concentration	-
$c_\mathrm{p}^\ell, c_\mathrm{p}^\mathrm{s}$	specific heat	$\mathrm{J{\cdot}kg^{-1}{\cdot}K^{-1}}$
D_ℓ , D_s	diffusion coefficient	$\mathrm{m^2{\cdot}s^{-1}}$
$d_\mathrm{c}, d_\mathrm{e}$	diameter	m
f_ℓ , $f_\mathrm{s}, f_\mathrm{e}, f_\mathrm{c}, f_\mathrm{a}, f_\mathrm{p}$	volume fraction	-
f_s^c	packing limit	-
$\vec{g}$	gravity	$\mathrm{m{\cdot}s^{-2}}$
G	temperature gradient	$\mathrm{K{\cdot}m^{-1}}$
$H^*, H_{\ell\mathrm{a}}$	volume heat exchange rate	$\mathrm{W{\cdot}m^{-3}{\cdot}K^{-1}}$
h	heat transfer coefficient	$\mathrm{W{\cdot}m^{-2}{\cdot}K^{-1}}$
$h_\ell, h_\mathrm{s}, h_\mathrm{a}$	enthalpy	$\mathrm{J{\cdot}kg^{-1}}$
K	permeability	$\mathrm{m^2}$
k	solute partition coefficient	-
$k_\ell, k_\mathrm{s}, k_\mathrm{a}$	thermal conductivity	$\mathrm{W{\cdot}m^{-1}{\cdot}K^{-1}}$
$M_{\ell\mathrm{s}}$	solidification mass transfer rate	$\mathrm{kg{\cdot}s^{-1}{\cdot}m^{-3}}$
m	liquidus slope of the binary phase diagram	$\mathrm{K\ (wt.\%)^{-1}}$
N_0	Initial equiaxed grain number density	$\mathrm{m^{-3}}$
p	pressure	Pa
$Q_{\mathrm{ca}}, Q_{\ell\mathrm{a}}, Q_{\mathrm{ea}}$	energy exchange term	$\mathrm{J{\cdot}m^{-3}{\cdot}s^{-1}}$

R	isotherm velocity	$m \cdot s^{-1}$
R_c	radius of columnar trunk	m
R_f	far field radius of columnar trunk	m
S_e, S_s	surface concentration	m^{-1}
T, T_ℓ, T_s	temperature	K
$\dot{T}$	cooling rate	$K \cdot s^{-1}$
T_{ref}	reference temperature for enthalpy definition	K
T_{EXT}	external temperature	K
t	time	s
$\vec{U}_{ca}, \vec{U}_{\ell a}, \vec{U}_{ea}$	momentum exchange	$kg \cdot m^{-2} \cdot s^{-2}$
$\vec{u}_\ell, \vec{u}_e, \vec{u}_a$	velocity vector	$m \cdot s^{-1}$
v_{R_c}	columnar trunk growth velocity	$m \cdot s^{-1}$
v_{tip}	columnar tip growth velocity	$m \cdot s^{-1}$
v_ℓ	liquid velocity	$m \cdot s^{-1}$
v_s	solid velocity	$m \cdot s^{-1}$
v^*	moving interface velocity	$m \cdot s^{-1}$
β	expansion coefficient	-
χ, χ_d, χ_ℓ	dimensionless diameter, eq (3.4)-(3.6)	-
$\varepsilon_\ell, \varepsilon_c, \varepsilon_d^e, \varepsilon_s^e, \varepsilon_{si}\ \varepsilon_f$	volume fraction in dendritic model	-
λ_1	primary dendrite arm spacing of columnar	m
λ_2	second dendrite arm spacing of columnar	m
$\rho_\ell,\ \rho_s$	density	$kg \cdot m^{-3}$
μ_ℓ	viscosity	$kg \cdot m^{-1} \cdot s^{-1}$
$\bar{\bar{\tau}}_{\ell s}$	stress-strain tensors	$Kg \cdot m^{-1} \cdot s^{-2}$

Subscripts ℓ, s, a, e, c indicate liquid, solid, air, equiaxed, columnar phases, respectively.

1 Introduction

1.1 Background

The essential feature in the solidification of a metallic alloy is the liquid-solid phase transition associated with the release of latent heat and the solute redistribution. The solutes are often redistributed non-uniformly in the fully solidified casting, giving birth to the segregation. Segregation occurring at the microscopic scale (i.e., between and within dendritic arms) is known as microsegregation. While segregation occurring at the macroscopic scale (i.e., in a range from several millimeters to centimeters or even meters) is called macrosegregation. Microsegregation can be removed by homogenization heat treatments, but it is practically impossible to remove macrosegregation due to the distances over which species are required to diffuse. Almost all macrosegregation is undesirable for casting manufacturers as the chemical variations can lead to non-uniform microstructural and mechanical properties. Thus there has been, and still remains, a great interest in predicting and eliminating macrosegregation in cast products.

Large steel ingots are the fundamental components in heavy industries such as power plants, petrochemical engineering, marine and metallurgical equipment. Today, the demand on large steel ingots seems increasing both in amount and size. However, macrosegregation defect in the large steel ingot becomes a difficult issue to control for the foundryman. Although research has been ongoing for more than hundred years, this problem has become even more crucial with the increase of ingot size. Macrosegregation seems to occur in steel ingots of different size, as shown in Figure 1.1 [1]. The macrosegregation problem in the big steel ingot is especially serious.

An excessive number of macrosegregation defects can require a large amount of cropping at a considerable cost of material and energy [2]. Therefore it is very important to understand the formation mechanism of macrosegregation in the steel ingot from the industrial point of view. Since the experimental investigation for large steel ingot is very expensive, in order to save the research cost many mathematical models were established to study the macrosegregation in steel ingots instead of by means of real casting trials [3-6]. However, it is still difficult to predict them quantitatively due to the complex nature of the involved multiphase flow phenomena.

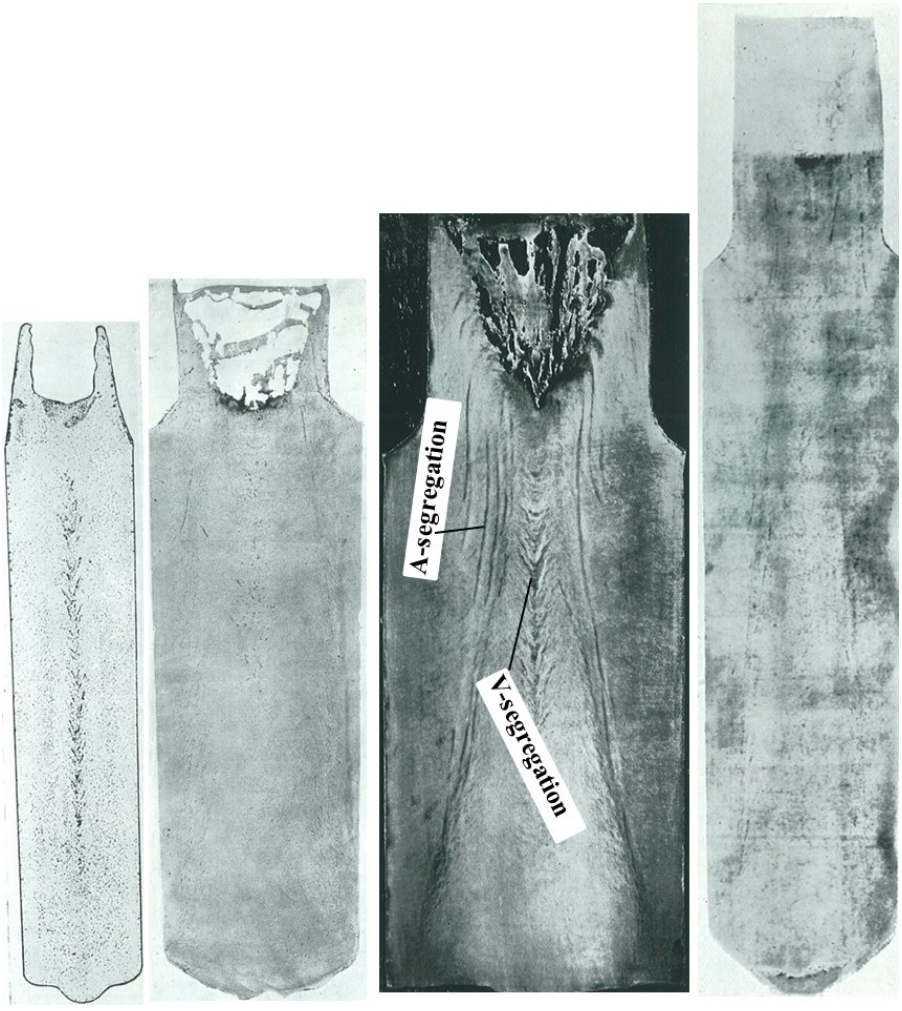

(a) 1.25 ton (b) 3 ton (c) 10.5 ton (d) 20 ton

Figure 1.1: Sulfur print result for different size of steel ingots [1]: (a) Ingot with twelve-side section, 0.35 m in diameter at the top, 0.33 m in diameter at the bottom, and 1.65 m in length; (b)Ingot with rectangular section, 0.60 X 0.45 m^2 at the top, 0.55 m X 0.40 m at the bottom, and 1.57 m in length; (c) Ingot with octagon section, 0.91 m in diameter in the top, 1.52 m in length; (d) Ingot with octagon section, 0.94 m in diameter at the top, 0.89 m in diameter at the bottom, and 3.05 m in length.

From the scientific point of view, the solidification processing of steel ingots involves the following phenomena: heat transfer with phase change; thermal-solutal convection in liquid and mushy zones and fluid flow driven by solidification shrinkage; redistribution of solutes both in liquid and solid phases and transport of solute by the melt flow; the growth of columnar and equiaxed crystals and their interaction with each other; the sedimentation of the equiaxed crystals or solid fragments; deformation of the solid network due to thermal and shrinkage stresses. These complicated phenomena in steel ingot result in defects such as shrinkage pipe, cone-shape negative segregation, hot-top segregation, A-segregation, V-segregation and so on [7]. Hence, the numerical simulation on the formation of defects is a very challenging field.

1.2 Objective

The target of this doctoral dissertation is to simulate the macrosegregation phenomena in large steel ingot. For this purpose, a three-phase mixed columnar-equiaxed solidification model [8-11] is employed to simulate different size of steel ingots. This numerical model can take into account the following phenomena: the growth of the columnar dendrite trunks from the ingot surface; the nucleation and growth of the equiaxed crystals; the sedimentation of the equiaxed crystals; the thermal and solutal buoyancy flow and its interactions with the growing crystals; the solute partitioning at the solid-liquid interface during solidification; the solute transport due to melt convection and equiaxed sedimentation. Additionally, in order to make the model be applicable to big steel ingots, some model modification should be made eventually:

1) The model is extended to consider the influence of the dendritic structure on the solidification processes;

2) The model is extended to combine the formation of macrosegregation and shrinkage cavity.

In this thesis different sizes of castings, from the laboratory benchmark to the 25-ton steel ingot, are simulated.

1) Firstly, the formation of channel segregation (i.e. A-type segregation in steel ingot) in the laboratory benchmark of Sn-10 wt.% Pb [12] alloy case is simulated. The 3D channel segregation is predicted and analyzed in this benchmark. The formation mechanism of channel segregation is analyzed.

2) Secondly, the macrosegregation in a 2.45-ton (Square section, 0.48 m in the top and 0.43 m in the bottom in square, 1.42 m in length) steel ingot is simulated with both the non-dendritic and simplified dendritic models. In addition, a simplified four-phase shrinkage model is established and applied to simulate the combination of macrosegregation and shrinkage cavity.

3) Finally, another big steel ingot weighted 25 ton (Octagon section, 1.09 m in the top and 1.02 m in the bottom in diameter, 4.5 m in length) is simulated. With the increase of ingot size, the requirement of computation time increases dramatically. So far, the maximum steel ingot presented in this thesis is 25 ton. Though it is possible to apply the simulation to larger steel ingot, the time consumption is unacceptable to retain the reasonable precision.

2 State of the art

2.1 Macrosegregation

It is known that fluid flow plays a major role in the development of macrosegregation [13-15]. Therefore, any factor that induces fluid flow during the solidification process contributes to the formation of macrosegregation. The four main causes of macrosegregation are illustrated in Figure 2.1 are [16]:

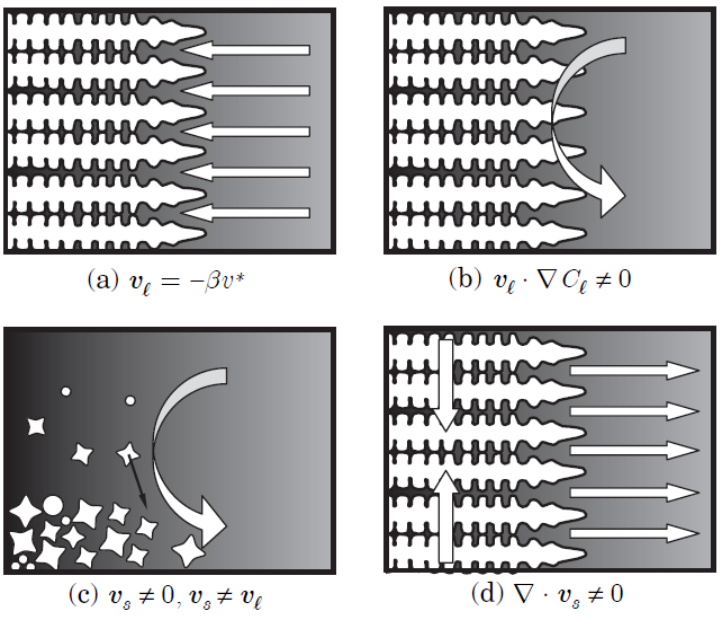

Figure 2.1: Various types of macrosegregation induced by (a) solidification shrinkage, (b) interdendritic flow, (c) grain movement and (d) deformation of the solid [16].

(a) Macrosegregation is associated with solidification shrinkage. In this case, the suction of the liquid induced by the moving interface is opposite to the speed of the isotherms and leads to what is known as inverse segregation.

(b) Macrosegregation is associated with natural or forced convection (e.g. electromagnetic force). If velocity of the liquid is parallel to the composition isopleths, i.e., perpendicular to the solute gradient, there is no macrosegregation. However, when the flow enters or exits the mushy zone macrosegregation will be induced.

(c) Macrosegregation is associated with grain movement. As long as the grains move with the same velocity as the liquid, there is no macrosegregation. However, equiaxed grains have a tendency to settle, or in a few cases to float, leading to macrosegregation.

(d) Macrosegregation is associated with deformation of the mushy solid. In this case, the overall velocity of the solid (v_s) is small but $\nabla \cdot v_s \neq 0$. In other words, the mushy solid behaves like a sponge expelling or sucking in the liquid.

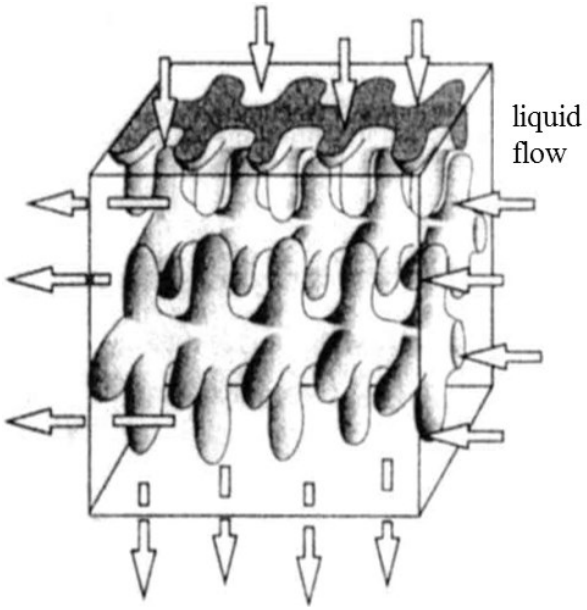

Figure 2.2: Schematic of liquid flow through fixed dendritic solid network [30].

In the last decades numerous experimental investigations have been carried out to study the macrosegregation in alloy casting [17-22]. Tewari and Shah [19-20] experimentally studied the macrosegregation resulting from the thermosolutal convection in the interdendritic melt

during steady-state columnar growth of lead dendrites in Pb-Sn alloys. They found that primary dendrite spacing show a systematic decrease with increasing convection. However, the convection in the interdendritic mushy zone has significantly more influence on the spacing than that in the overlying melt, immediately ahead of the dendrite tips. Spinelli et al. [21] experimentally studied the influence of thermosolutal convection on the dendritic arm spacing in the downward vertical unsteady-state directional solidification of Sn-Pb hypoeutectic alloys. The primary dendritic arm spacings were found affected by the direction of growth: decreasing in conditions of downward vertical solidification when compared with those grown vertically upwards.

Mathematical modeling of macrosegregation during solidification has experienced extensive growth [23-26] since the pioneering studies of Flemings and co-workers in the mid-1960s [27-30]. They considered the flow of interdendritic liquid through a fixed dendritic solid network, as shown in Figure 2.2, while accounting for the different densities of the solid and liquid. A so-called 'local solute redistribution equation' (LSRE) was derived to analyze the interdendritic flow induced macrosegregation:

$$\frac{df_\ell}{dc_\ell} = -\frac{(1-\beta)}{(1-k)}\left[1+\frac{v\cdot\nabla T}{\dot{T}}\right]\frac{f_\ell}{c_\ell} \tag{2.1}$$

where $\beta = \frac{\rho_s - \rho_\ell}{\rho_s}$ is the solidification shrinkage rate; v is the liquid velocity vector; ∇T is the temperature gradient; $\dot{T} = \frac{\partial T}{\partial t}$ is the local cooling rate.

The physical significance of LSRE can be understood as follows (for k < 1):

1) LSRE reduces to the Scheil equation, implying no macrosegregation, when β and v both vanish.

2) At an impenetrable chill face the shrinkage β is finite (>0), positive macrosegregation will result; this is the so called inverse segregation often observed in casting of aluminum alloys.

3) Flow in the same direction as the shrinkage flow (i.e. in the direction of decreasing temperature), but with a speed greater than the shrinkage velocity results in negative macrosegregation.

4) If the flow velocity in the direction of ∇T is so large that the term in the square brackets in equation (2.1) becomes negative, local melting occurs, leading to the formation of channel segregation.

The first numerical model that accounted for the coupling of the flow between the mushy and bulk liquid zones was reported by Rideer et al. [31]. They solved the coupled set of equations given by Darcy's law, the energy equation, LSRE in the mushy zone, and the momentum and energy equations in the liquid region. Solutal convection in the bulk liquid was neglected. They predicated macrosegregation patterns compared favorably with experimental measurements. Beckermann [32] did a comprehensive review of the macrosegregation models and their application to relevant casting industries. Recently, Keiji Nakajima et al. [33] summarized the works on modeling of macrosegregation in the macro-scale simulation.

2.1.1 Channel segregation

Channel segregation is one of the most frequently observed segregation patterns in large steel ingots, vacuum-arc remelting or electro-slag remelting ingots [34-35], and as cast super alloys [36-37]. These segregation defects are often referred to as 'A' segregate [38-39] or lamellar-structured segregate [40-41] in large steel ingots and 'freckles' or chimney [42-43, 19] in vertically solidified castings such as in the process of directionally solidification of superalloy castings.

The freckles are observed as long and narrow trails, aligned parallel to the direction of gravity in directionally solidified castings, and are enriched in the normally segregating elements and depleted of the inversely segregating elements. An example of freckles in directionally solidified Ni-based superalloy ingot was illustrated in Figure 2.3 [42]. A-segregation is lamellar or rod-like type of segregation that appears as one or more series of discontinuous lines outside of the V-segregates in a zone parallel to the end of the branched columnar zone (but generally it appears slightly before the end of these dendrites) [40], as schematically shown in Figure 1.1. A-segregates typically have a width of a few centimeters and a length of 10-500 mm, depending on the thermal conditions prevailing during solidification.

Figure 2.3: Freckles at the surface of a 0.1 m diameter cylinder of a MAR-M200 superalloy [42].

It is widely recognized that the channel segregation is formed by a convective flow of a liquid into a mushy zone, resulting from the liquid density changes due to solutal and thermal gradient. Pioneering works of the channel segregation were done by Flemings et al. [27-29, 44] and Hunt [45-46]. Later on, numerous studies, with both experiment and simulation, in the area of solidification have contributed to the understanding of channel segregation formation, but they did not clarify the channel formation mechanism [47-55].

Several experimental studies with wide variety of alloy systems provided evidence of the formation of freckles during solidification processes [42, 48, 56]. Giamei and Kear [42] studied the development of freckles in directionally solidified nickel base superalloy castings. They observed that the freckles form along the vertical lines mostly on the exterior surfaces of the Ni base castings, and the number of freckle lines decrease gradually farther away from the chill. They also found experimentally that the tendency of freckling varies with the composition of the alloy. Sarazin and Hellawell [48] studied channel segregation in three alloy systems (binary Pb-Sn and Pb-Sb, and ternary Pb-Sn-Sb) during unidirectional solidification in base-chilled ingots and found that the channels originate from flow perturbations, which can be characterized with the Rayleigh number. They found that increase of temperature gradient and growth rate will require a large driving force for channel formation. Mori et al. [56] systematically investigated the formation condition of channel segregation using unidirectionally solidified Al-Mg and Al-Mg-Cu alloys. They

concluded that channel segregation formed when the solidification rate is below a critical value which depends on the alloy composition and the inclination angle of specimen to the horizontal plane. Recently, Fautrelle and co-worker [57-58] experimental investigated the solidification of Sn-3wt.%t Pb and Sn-10 wt.% Bi alloys in a rectangle cell. The heat flux was extracted from vertical side of the ingot. By means of the X-ray analysis their results reveal the development of channel segregates near the cold wall.

The opacity of metals prevents direct observation of the origin and growth of channels during solidification. Observations are usually done by decanting the ingot at different stages of solidification and analyzing the solidified macrostructure. In order to understand the dynamics of the channel formation, several studies [45-46, 59-62] have been conducted with transparent alloys which solidify similarly to metallic systems. McDonald and Hunt [45-46] built an ammonium chloride water system to study the effect of growth conditions and convection on 'A' segregate, and were the first to observe that the formation of 'A' segregate which was directly caused by the extensive fluid motion in the interdendritic region. They also suggested that density differences between the bulk liquid and interdendritic liquid due to variations in temperature and solute concentration led to the fluid flow. The dimensions of segregation channels occurring in those systems were shown to be comparable to those found by metallographic examinations in fully solidified metallic castings [49].

Although these similarities give point to extrapolate the findings from the transparent materials to metal alloys to a certain extent, corresponding measurements in real metallic materials would attract wide interest. Eckert et al. [63-66] carried out a series of experiments to investigate the unidirectional solidification process of Ga-In alloy system. The solidification process was visualized using a microfocus X-ray tube. They were able to visualize the formation of freckles in real metallic material, as shown in Figure 2.4 [66]. These figures shown a sequence of image frames recorded from the solidification process. According to their experiments results, the development of the chimneys is significantly affected by the melt flow. The best conditions for chimney formation were found at positions behind strong and stable plumes. Fluctuations arising for both the local and global flow pattern and the dendrite growth process may disturb or even suppress the chimney development. In many cases already existing channels become blocked or overgrown. The generation of a dominating forced flow almost perpendicular to the main growth direction leads to an enrichment of solute in the mushy zone and creates new segregation freckles.

The development of the chimneys and the probability of their surviving depend sensitively on the spatial and temporal evolution of the flow field.

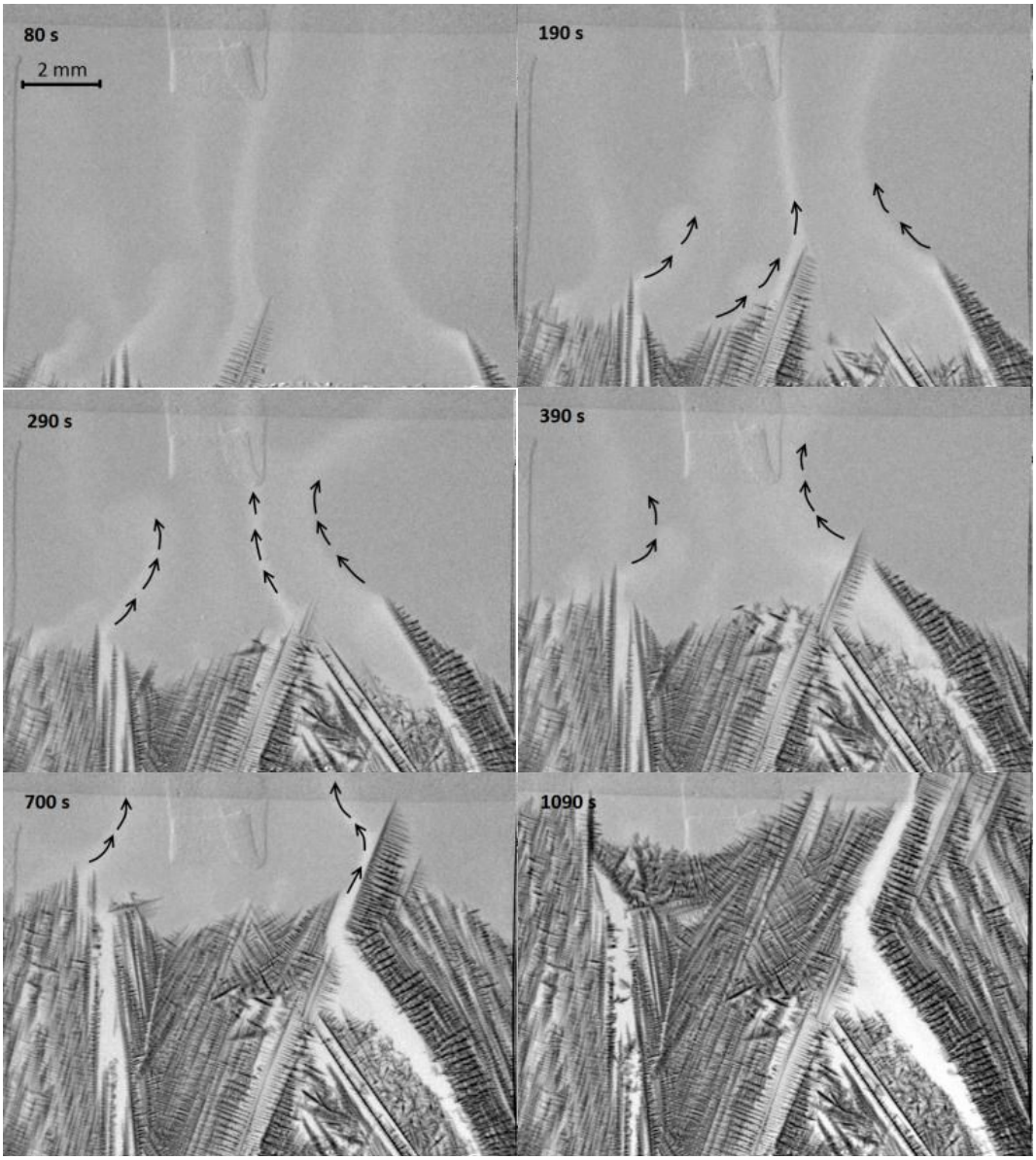

Figure 2.4: Image sequence showing the dendrite growth and the formation of segregation freckles at different time steps [66].

On the other hand, a number of computational models have been developed to simulate the heat and mass transport phenomena during alloy solidification using the full set of conservation equations to study channel segregation. These numerical models have successfully predicated channel-like macrosegregation, in most case, used the finite volume

method or finite difference method [67-71], or, more occasionally, used the finite element method [72-74]. Most of the simulations were carried out on 2D case [58, 75-76], only a few trials were made on 3D case [77-81]. In addition, some others simulated the formation of channel segregation under the influence of magnetic force [82-84].

Predicting the conditions leading to the possible occurrence of channel segregates can help improving the yield rates and lead to successful manufacturing of defect free castings at lower cost. A criterion for channel segregates is desired to understand the fluid-flow dynamics in the mushy zone and to find measures to control channel segregates. Many different versions of criterion exist. Generally, all the criteria proposed can be classified into three categories:

1) The first one is the cooling rate criterion. It is also termed as *G-R* criterion [85]. The first example was proposed by Copley et al. [54] based on industry experience. They suggested a criterion for channel formation that is based on a critical cooling rate, $\dot{T}$, which is equal to $G \times R$,where G is the temperature gradient, R is isotherm velocity. Below a critical number of $G \times R$ channels are likely to form. Suzuki and Miyamoto [34, 39] deduced that A-segregation in the 0.7 wt.% C steel occurred when $G \times R^{2.1} \leq 8.75$. They suggested that this critical thermal condition is also likely to change with change in the steel composition. Their criterion, later on, was verified by Yamada et al [86]. They examined the dependence of the critical thermal condition on the composition of the steel, and found that the critical value, $G \times R^{2.1} \leq 8.75$, for A-segregation was reduced when alloying with elements in the order C, Cr, Ni, with the lowest value for low-Si steel.

2) The second one is derived from the micro-flow continuity principle, which was proposed by Flemings and his co-workers [23, 44, 87]. Mehrabian and Flemings [44] considered that the channel-type segregates result from a flow instability which occurs at a critical condition of flow. This condition of flow is $v \cdot \nabla T / \dot{T} < -1$, where v is the interdendritic flow velocity; ∇T is the temperature gradient; and $\dot{T}$ is the cooling rate at a given position in the ingot. The physical meaning of the criterion is that if the interdendritic fluid-flow velocity in the direction of crystal growth is greater than the growth rate, there will be freckle formation. This critical condition later on was summarized and optimized by Moore and Shah [40].

3) The third one is based on the convective flow-instability theory, as is termed the Rayleigh number [44, 53, 88]. The criterion is based on a maximum value of the dimensionless parameter, Rayleigh number, R_a, which indicates that the magnitude of buoyancy forces with respect to the retarding frictional forces. The most complete work in this field is published by Worster [89]. Beckermann et al. [90] obtained a critical value for the Rayleigh number based on the experimental data from literature and then used numerical simulations to confirm their finding. They found that the critical Rayleigh number decreases with increasing inclination of the the solidification direction from the vertical. After that, they [91] found that the use of the ratio of thermal diffusivity to the casting speed, instead of the distance from the liquid mush interface, as the characteristic length scale for the calculation of Rayleigh number provided more reasonable prediction of the formation of freckles. They also mentioned that exceeding the critical number does not imply formation of freckles, but rather that the conditions for such phenomena are favorable. Compared to the *G*-*R* relation, R_a reflects the chemical, elemental-segregation, processing-effect, and physical status of the system. Therefore, it is a more comprehensive expression that considers all aspects of channel segregation phenomenon.

More recently, Yuan and Lee [92] predicted the formation of freckle in unidirectionally solidified Pb-Sn alloy by a 3D model at the microstructure scale. They proposed a new mechanism for freckle initiation: dendrite overgrowth, local remelting and dendrite deflection, due to high solute concentrations and continuous upward convection of segregated liquid, result in the formation of an open solute channel that can cause the initiation of freckles. The interdendritic flow introduces warmer liquid from the bulk and segregated solute from the surrounding dendrites into the channel which not only retains the high solute content in the channel but would also assist the detachment of secondary arms. Both effects enable self-sustaining channels to exist and freckles to form.

2.1.2 Macrosegregation in steel ingot

The first examinations of macrosegregation phenomena in steel ingots were carried out many decades ago and although our understanding of the processes leading to segregation has improved considerably, the same patterns can still be observed in ingots made today [93-94]. These, shown in Figure 2.5 (a), include: centerline positive segregation near the centerline, particularly in the top part; a cone-shape negative segregation in the bottom part;

V-segregates along the centerline; and A-segregates in the middle radius region. Fundamental knowledge about them is as follows: 1) the positive segregation in the top region arises from the thermal and solutal convection and shrinkage-driven interdendritic fluid flow during the final stages of solidification; 2) core-shape negative segregation results from the sedimentation of equiaxed grain which finally piled up in the bottom of ingot. The equiaxed grains with poor solute content, which have been solidified in the early stage, settle down to the bottom resulting in the negative segregation cone; 3) the A-segregations are channels formed in mushy zone during solidification. The channels are filled with highly-segregated melt, which solidifies at the end stage; 4) the V-segregation in the center of the ingot arises from the equiaxed grains settling, the deformation of connected solid skeleton and the solidification shrinkage. Figure 2.5(b) is the sulfur print result of a 10.5 ton steel ingot. The A segregation, V-segregation and cone of negative segregation are clearly shown [1].

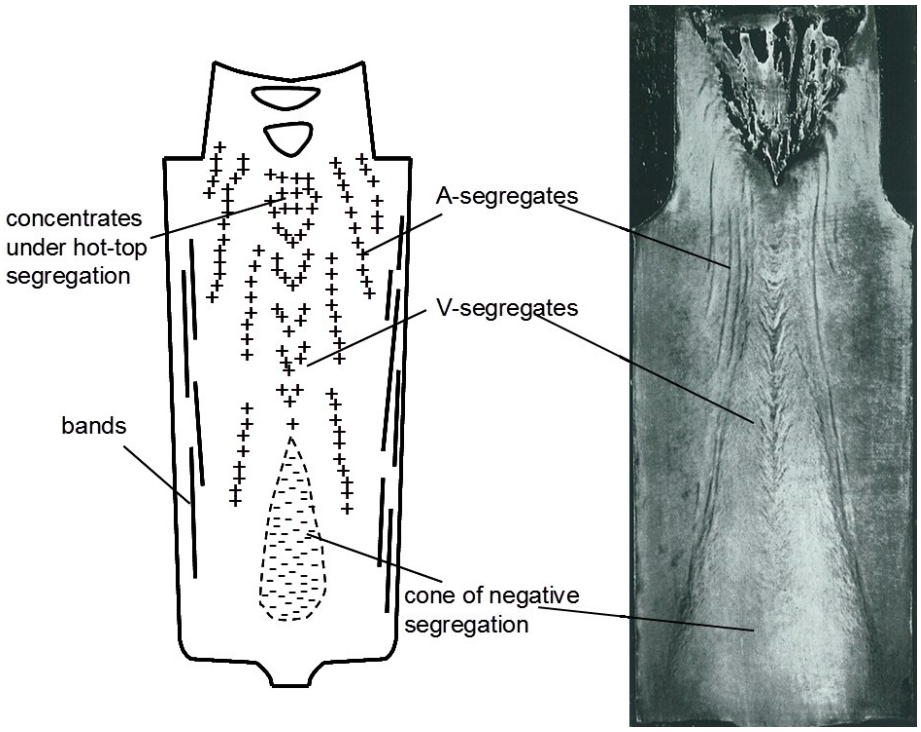

(a) (b)

Figure 2.5: Schematic of the macrosegregation pattern in steel ingot (a) [94]; and sulfur print result of a 10.5 ton steel ingot (b) [1].

People have experimentally investigated the steel ingot for more than 100 years [1, 41, 95-103]. Among them, one of the most important works is the report on the heterogeneity of

steel ingots, presented by a sub-committee of the British Iron and Steel Institute [1]. 16 carbon steel ingots ranging from 0.635 ton to 172 ton in weight were presented. Figure 2.6 shows the macro-etched axial section result of two typical ingots. In both ingots the lamellar type of V-segregation and A-segregation were observed. V-segregation was observed around the ingot axial starting from the top part of the ingot extended to the bottom just near by the cone shape negative segregation zone. They proposed that the formation mechanism of V-segregation was that in the final stages of solidification the contraction of the ingot causes segregates to be drawn downwards from the sink head. A-segregation was observed as series of discontinuous lines outside the V-segregation. The lines incline slightly toward the vertical axial in an upward direction.

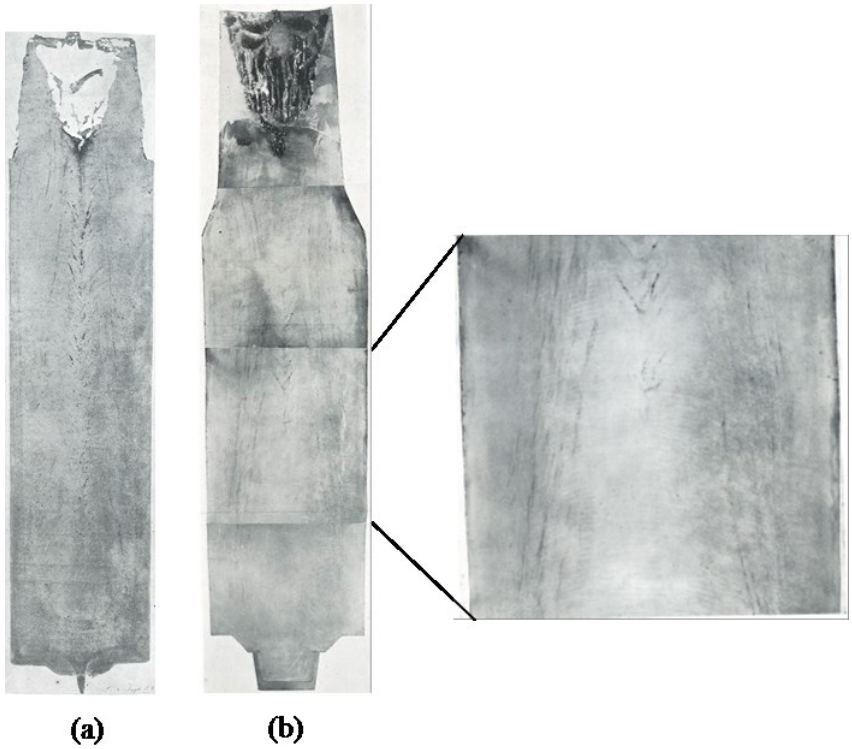

Figure 2.6: Macro-etched axial section results. (a) 3 ton in weight, twelve-side with top 0.52 m and 0.495 m wide, 1.7 m long; (b) 24.5 ton in weight, octagon with top 1.09 m and bottom 1.02 m across, 4.5 m long [1].

With decanting experiments result from Nelson [99], Marburg [41] derived the effect of the width/height (w/h) ratio upon the solidification pattern. They found that a cone of vertical solidification above the base cone is developed. The vertical cone surmounts a zone of

accelerated vertical solidification and is surrounded by zone of accelerated transverse solidification. In ingot with low *w*/*h* ratio, the vertical cone does not reach the top. Above the vertical core, solidification is completed transversely and V porosity may be developed axially. They found that ingots of intermediate sizes (38 to 64 cm width) are more subject to the formation of V-segregation than either smaller or larger ingots are. The V-segregation is also less pronounced in big-end-up ingots than in big-end-down ingots. In addition, they deemed that the negative segregation zone in the lower middle portions of ingots develops as a result of selective solidification vertically of the purest metal available from the relatively pure metal in the lower portion of the contained liquid metal. However, most people [6-7, 100-101] considered that the main factor for these negative segregation zones is the sedimentation of equiaxed grain.

Flemings [94] presented a largely qualitative discussion of ingot solidification and ingot design based on actual experiments and analytical studies. He highlighted the importance of a thermally insulating hot-top design. He showed that such a design will reduce the number of equiaxed grains, and by reducing the thermal gradient, the intensity of the segregation in the top part. He proposed that the ingots be rotated at a modest rate during solidification so as to produce a radial acceleration that is comparable to acceleration due to gravity, thereby partially counteracting the gravitational effects that lead to macrosegregation.

Olsson et al. [97] examined the segregation pattern in two 1.7 ton steel ingots with the same solidification condition but with different steel grades. The interdendritic liquid of the first steel ingot, which contained 0.07 wt.% carbon and 3.36 wt.% silicon, had a density lighter than the bulk liquid in the whole liquid-solid two phase region due to the effect of silicon on the density distribution. The interdendritic liquid of the second steel ingot, which contained 0.47 wt.% carbon and 0.96 wt.% molybdenum, had a density closer to the bulk density but increased near the end of solidification which due to the molybdenum content. Sulfur print results were shown in Figure 2.7. Both A and V-segregation were observed in ingot 1, while only V-segregation was observed in ingot 2. The positive segregation in ingot 1 was more severe than ingot 2. The temperature, in the central of ingot, for each ingot during solidification was monitored by four thermal-couples. The distributions of alloying element for both ingots were also determined by drill probes with a diameter of 1-1.3 mm, which were chemically analyzed. Moreover, the carbon content versus time at one point was also measured which provided very useful information for the successors to verify their simulation model.

In addition, some others studied the non-metallic inclusion segregates in large ingots [102]. Blank and Pickering [102] examined the distribution of the oxide inclusions in the heavily segregated regions towards the bottom of several 15-ton ingots of 1.5% wt. Mn steel. They found that the distribution pattern of the major inclusions was similar in each of the ingots examined. The oxide (silicate) inclusions segregated mainly in the bottom third of the ingot. The form of the segregated regions was a hollow pyramid which followed the shape of the ingot within the confines imposed by the columnar dendrites. They also found that the segregation index for manganese, and also for chromium, increases with increasing carbon content. The effect of ingot size does not seem to be very pronounced on the segregation index for manganese.

Yamada and co-workers [103] investigated solidification in 8-ton sand mould ingots of high purity CrMoV steel grades. Experimental data were supplemented by theoretical analyses as well as laboratory experiments with small unidirectionally solidified melts. There were large carbon segregates because of small partition coefficient of carbon due to high δ solidification ratio and because of heavy density due to high Mo content. The remarkable macrosegregation with opposite inclining angle compared with that seen in conventional ingots was also observed, which was caused by the sinking of heavy segregated liquid.

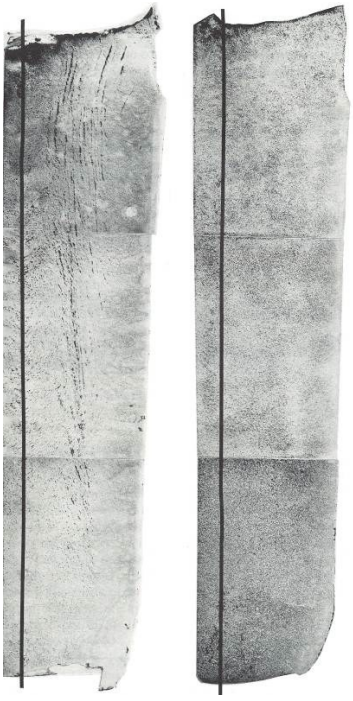

Figure 2.7: Sulfur print result of 1.7 ton ingot. (a) ingot 1 (left), 0.07 wt.% carbon and 3.36 wt.% silicon; (b) ingot 2 (right), 0.47 wt.% carbon and 0.96 wt.% molybdenum [97].

Because the experimental costs are usually extremely high for most of the steel ingots, there are few literatures since the 90s about the experimental study of steel ingots. Among these, Wang and co-workers [104] investigated a 100-ton 30Cr2Ni4MoV heavy steel ingot with vacuum carbon deoxidation refining technique. The heavy 30Cr2Ni4MoV forging ingots have been extensively used to fabricate the low-pressure rotors, which play a crucial role in the large nuclear power plant. They cut the ingot and its axial plane was analyzed to observe the distribution and size of the shrinkage porosity in the sectioned surface.

On the other hand, more and more people pay attention to the modeling study of steel ingot instead of experimental study. The application of solidification model is a challenging issue due to the size of the ingots and the variety of the phenomena to be accounted for. Some of those phenomena to be accounted for are thermosolutal convection of the liquid, equiaxed grain motion, evolution of grain morphology by suitably considering a coupled grain growth model in the macroscopic solidification model, the columnar to equiaxed transition, and shrinkage, etc. Each of these phenomena is very important to the solidification pattern. The first generation of models, however, appeared with the aim of estimating the effect of one or two of these phenomena [44, 94, 97]. Olsson and co-workers [97] developed a simple equation that predicted the negative macrosegregation due to sedimentation of equiaxed as a function of the relative height of the sediment zone and the fraction of solid in that zone. These equations was applied to study the 1.7 ton steel ingot, the results were compared with their experimental ones. They also noted that the LSRE (equation (2.1)) might not be valid for large steel ingot because the distance between the free crystals is so large that the assumption of a well-mixed liquid in equilibrium with the solid does not apply. Mehrabian and co-workers [44] studied the combined effect of the shrinkage and the natural convection of the liquid phase, for a case in which the gravity is perpendicular to the direction of solidification. In this case, they showed that the macrosegregation pattern strongly depended on the sense of variation in the density of the interdendritic liquid versus the solid fraction.

These models were limited in application because of their drawbacks. It is necessary to track both the liquid- and solid-mushy boundaries in order to apply specific conservation equations. Later on, significant progress was made with the development of macroscopic conservation equations which are identical for the liquid, mushy, and solid zones. These macroscopic conservation equations have been derived using a mixture theory or a volume averaging procedure. It is not necessary to track the different boundaries owing to that these

approaches have only one conservation equation which valid for the whole domain to be solved for each conserved quantity.

Based on the Schneider and Beckermann's [105] multicomponent macrosegregation model, Gu and Beckermann [6] simulated the solidification of a 43-ton steel ingot. Their model was a single domain and fully coupled. The model considers eleven alloying elements in steel, including their different segregation behaviors and effects on the liquid density. The highly coupled advection-diffusion equations in the model were discretized on a two-dimensional (2D) rectangular grid using the finite volume method. The solid phase was assumed to be fixed. The shrinkage flow was taken into account including the computation of the hot pipe which employed a special scheme. A grid of 38x54 control volume was used for their simulation; the calculation time step was 0.15 s and 5 s depending on the convection inside the ingot; total CPU time was reported on the order of several weeks on an HP J200 single processor workstation. The predicted result of the vertical centerline segregation was in good agreement with the measured experimental values in the bottom and top regions. However, the neglect of the sedimentation of equiaxed crystals in the model leaded to the underestimation of the measured negative macrosegregation over the middle half of the ingot. Moreover, this model fails to predict A-segregation.

Based on the same theory Liu and co-workers [106] developed a continuous two phase model to numerically simulate the steel ingot. The model has taken into account the heat transfer, melt convection, composition distribution, nucleation, and grain evolution at the system scale. A weak-coupling numerical procedure was designed to solve conservation equations. Their model was gradually applied to a laboratory Fe-0.8 wt. % C alloy ingot [106], a 3.3-ton and 5-ton steel ingot [107-108], and a 360-ton multiconcentration poured steel ingot [109].

Vannier and co-workers [4] presented a two phase model to study the macrosegregation of a 6.2 ton large steel ingot. The model was able to consider the heat, mass and momentum coupled transports during solidification of multicomponent alloys in a mold. However, the evolution of grain morphology and the grain motion during solidification was not taken into account, which significantly limited the application of the model. Some improvement was implemented based on this model by Combeau and co-workers. Combeau et al. extended this model by considering the motion of equiaxed grains [100-101, 110-111] and also the evolution of grain morphology during solidification [100-101, 110].

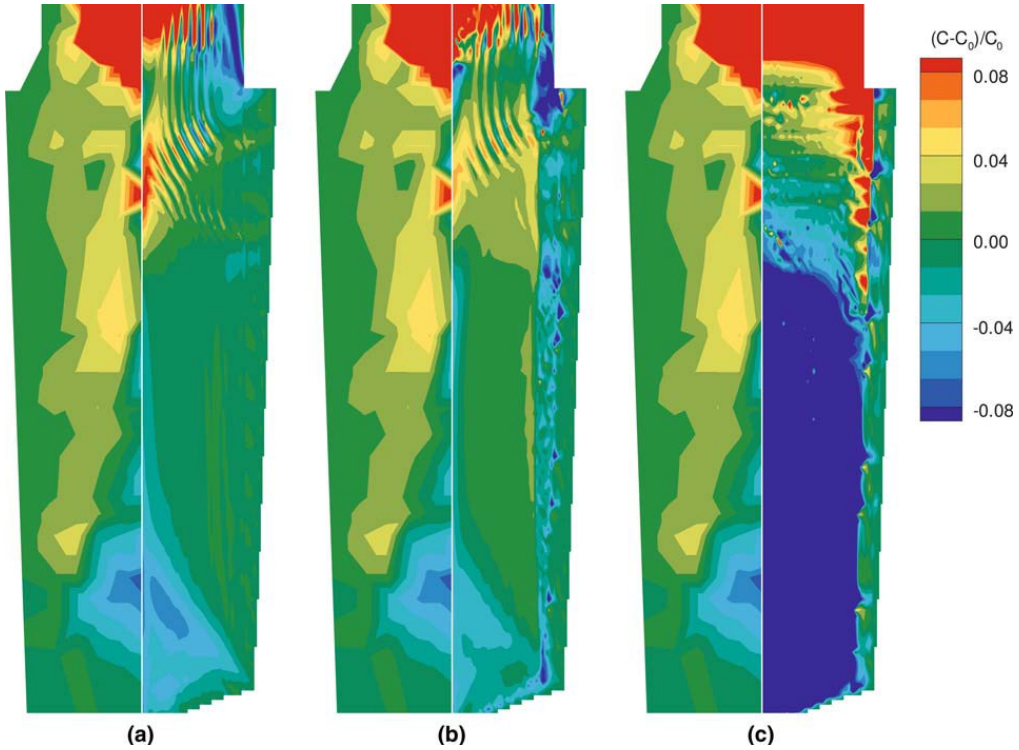

Figure 2.8: Numerical study of macrosegregation in a 3.3-ton ingot [101]. Left: experimental results. Right: numerical simulation. (a) Case 1: fixed solid phase. (b) Case 2: dendritic free-floating grains, $N_0 = 10^9$ m^{-3}. (c) Case 3: globular free-floating grains, $N_0 = 10^9$ m^{-3}.

Combeau et al. [101] presented a two phases and multiscale model to study the macrosegregation in a 3.3-ton steel ingot. The model tackled the morphology evolution of the equiaxed grain and their motion, and also accounted for the flow of the interdendritic liquid in the region in which the grains were packed and motion of the grain was blocked. The ingot was an octagonal ingot 2 m in height and 0.6 m in mean width. The total real solidification time was in the order of 90 minutes. For their computation, a rectilinear axisymmetric mesh composed of 11,057 cells was used which including 6408 cells contained in the steel ingot and the rest in the mold. Three cases were simulated to study the effect of grain motion and morphology on the macrosegregation in the ingot. Three cases were considered: the solid phase is fixed everywhere; dendritic free-floating grain; globular free-floating grains. The results for different cases were compared with each other and as well as the experiment one, shown in Figure 2.8. The same segregation tendencies were found between fixed solid phase case and dendritic free-floating grains case. However, the discrepancy between these two cases with the globular free-floating grains case was apparent. The centerline macrosegregation distributions were also compared with

experiment result. The reasonable comparison results were obtained for both the fixed solid phase case and dendritic free-floating grains case. Some other steel ingots, including the 3.3-ton [100], 6.2-ton [110], and 65-ton [111] steel ingot, were also studied by them.

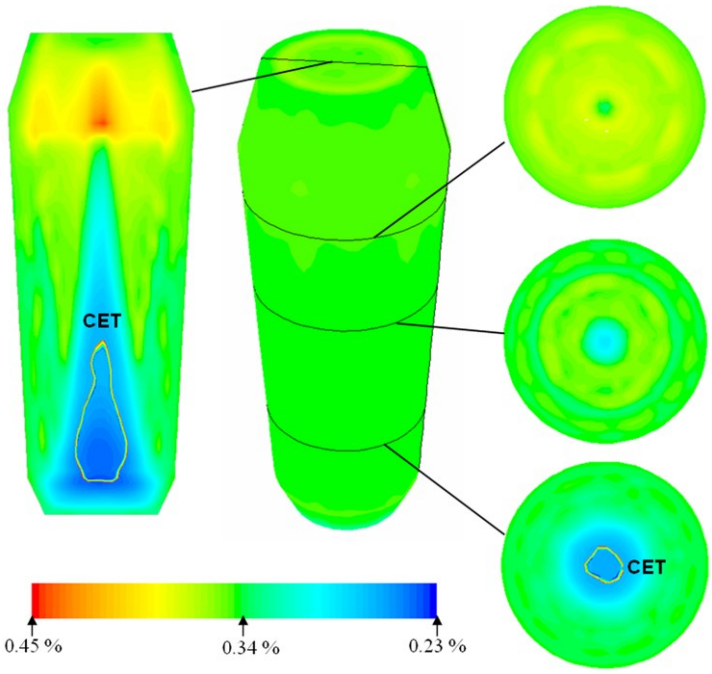

Figure 2.9: Predicted mix concentration c_{mix} in the steel ingot (Fe-0.34. % C), scaled from 0.23 wt.% C to 0.45 wt.% C. The area of 100% equiaxed macrostructure is enveloped by the CET line [10-11].

However, these models did not take into account a realistic growth of the columnar phase, they just simply presumed a preinstalled columnar phase layer or even ignored the columnar phase, neither the evolution of the columnar tip track. This drawback limited the application of this model. Wu and Ludwig [10-11] presented a three-phase mixed columnar-equiaxed model on the predication of macrosegregation in steel ingot. Their model consists of three individual phases: liquid, columnar, and equiaxed. This model accounts for not only the individual growth of each phases, but also the interactions between phases, e.g., the columnar to equiaxed transition (CET). Both 2D and 3D case were simulated. Figure 2.9 [10-11] shows the final macrosegregation distribution of the 3D benchmark steel ingot. The positive segregation in the upper region, cone shape negative segregation in the bottom region, and the CET region were successfully predicted, which is similar to the classic macrosegregation pattern. Ishmurzin et al. [112] presented a model which coupled the multicomponent/multiphase thermodynamic and kinetics with

multiphase/multicomponent flow. Their model was applied to the highly alloyed steel ingots both in a 32 Kg benchmark ingot and a 2-ton industrial ingot. The results obtained qualitatively agreed with experimental data.

2.2 Shrinkage

Shrinkage cavities or porosities are defects accompanying macrosegregation. They interact with each other. Shrinkage defects occur when liquid for feeding is not available to compensate the solidification shrinkage. Shrinkage defects can be split into two different types: open shrinkage defects and closed shrinkage defects. Open shrinkage defects are open to the atmosphere as the shrinkage cavity forms air compensates. There are two types of open air defects: pipes and caved surfaces. Pipes form at the surface of the casting and burrow into the casting, while caved surfaces are shallow cavities that form across the surface of the casting. Closed shrinkage defects, also known as shrinkage porosity, are defects that form within the casting. Isolated pools of liquid form inside solidified metal are called hot spots. The shrinkage defect usually forms at the top of the hot spots. They require a nucleation point, so impurities and dissolved gas can induce closed shrinkage defects. The defects are broken up into macroporosity and microporosity (or microshrinkage), where macroporosity can be seen by the naked eye while microporosity cannot.

For ingot casting, as the molten steel has been poured into the mold, it solidifies first at the bottom and walls of the mold. Solidification progresses gradually upward and inward. The solidified metal occupies a somewhat smaller volume than the liquid, so that there is a progressive shrinkage of volume as solidification goes on. The last metal to solidify is at the top of the mold, but due to shrinkage there is not enough metal to fill the mold completely, and a depression or cavity is formed. This may extend quite deeply into the ingot as shown in Figure 2.10 [1]. After early breakdown of the ingot into a bloom, this shrinking cavity is cut away or cropped. If this is not done completely before final rolling or forging into shape, the unsound metal will show up as voids called "pipe" in the finished product. Such internal discontinuities, or pipe, are obviously undesirable for most uses and constitute a true defect. In addition, the shrinkage flow was also found to be very important to the formation of final macrosegregation pattern, such as the positive segregation zone under the shrinkage pipe which was reported result from the formation of shrinkage pipe [94].

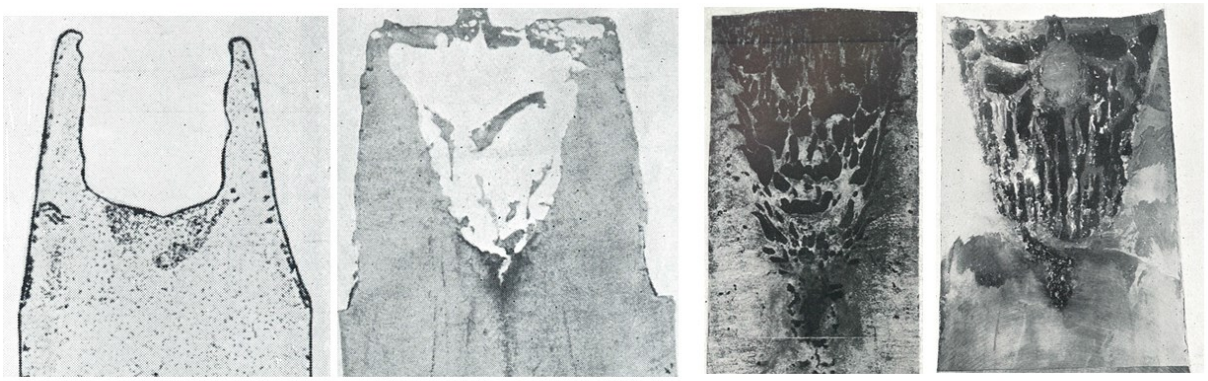

Figure 2.10: Selected examples of shrinkage cavities in hot top region of ingot. Sulfur print indicates severe segregation zone below the shrinkage cavities [1].

Many researchers have studied the shrinkage defects experimentally and numerically [114-133]. One of the approaches used to predict shrinkage defects are criterion functions [114-116]. Criterion functions are semi-empirical formulae which use local macroscopic information about the cooling and solidification process like the solidification front velocity or cooling rate and the local temperature gradient and combine them to form general relations which allow identifying areas with high potential for porosity formation. The most famous one of these criterion functions is the Niyama criterion [116] for the prediction of centerline porosities in steel casting. Though this approach for some cases is proved to provide acceptable agreement with experimental data, it has some disadvantages. The main disadvantage is connected with the fact that porosity in this approach is predicted not by solution of a physical problem but is based on some empirical correlations.

Detailed modeling of shrinkage defects based on direct numerical simulation has been developed. Some of them are 1D geometry [117-119], some others in 2D [120-122] and occasionally also in 3D [123-126]. Pioneering work in porosity prediction for casting has been carried out by Flemings and co-workers who developed a 1-D microporosity model [117]. An extensive review of the research in this area is provided by Lee and co-workers [127].

Bounds and co-workers [123] proposed a model for shrinkage prediction based on the coupling of the free-surface flow, heat transfer, and solidification. Numerical schemes for solving the Navier-Stokes equation are complex and convergence is difficult to obtain in

their model. Furthermore, some of the assumptions underlying the physics of microporosity formation are unclear.

Kuzenetsov and Vafai [128] developed a three-phase (liquid, solid and gas) model of the mushy zone to study the porosity formation in Al-Cu casting. Their model has taken into account the release of the dissolved gas from the alloy as well as heat transfer and interdendritic fluid flow in the mushy zone. The influence of porosity formation on pressure and residual porosity distributions in the mushy zone was investigated. An analytical criterion, identifying conditions under which there will be no porosity formation was also established. However, their model was based on the assumption of uniform solidification which limited the validity of the model.

Sabau et al. [129] provided a 3-D model for microporosity of aluminum alloy castings. Their model is able to take into account solidification, shrinkage-driven interdendritic fluid flow, hydrogen precipitation, and porosity evolution. Their model computes flow and pressure both in the liquid region and in the mushy zone. When feeding flow to a region is cut off, they no longer solve for pressure or velocity in the region, but rather compute porosity such that it compensates for all the shrinkage occurring in that region. Their numerical results reproduced the characteristic microporosity profiles observed in the experimental results and also agreed quantitatively with the experimentally measured porosity levels.

Rappaz and co-workers [130] presented a microporosity model, which coupled for the first time with macroporosity and pipe-shrinkage prediction, and applied to Al-Cu and Al-Si alloy castings. They incorporated their model into casting solidification simulation by superimposing a fine finite volume grid onto the coarser finite element mesh used for heat flow computations. The governing equations of microporosity formation are only solved within the mushy zone and imposed appropriate boundary conditions. To determine the boundary conditions, they must decide if each liquid region of the casting is connected to a free surface (open regions), surrounded by a mushy zone (partially closed regions) or surrounded by solid (closed regions). The pipe shrinkage is obtained by integration of total shrinkage in respect to the overall mass balance. Pipe shrinkage and macroporosity were predicted as shown in Figure 2.11. Improvements of this model in order to predict the porosity formation of volatile solute elements, e.g. zinc, on porosity formation in aluminum- and copper-base alloys has been considered in [113]. Couturier and co-workers

[131] improved this model to multicomponent alloys and multi-gas systems. Subsequently, Counturier and Rappaz [132] extended this model to the multicomponent alloys and multi-gas system, this model has also considered volatile solute elements.

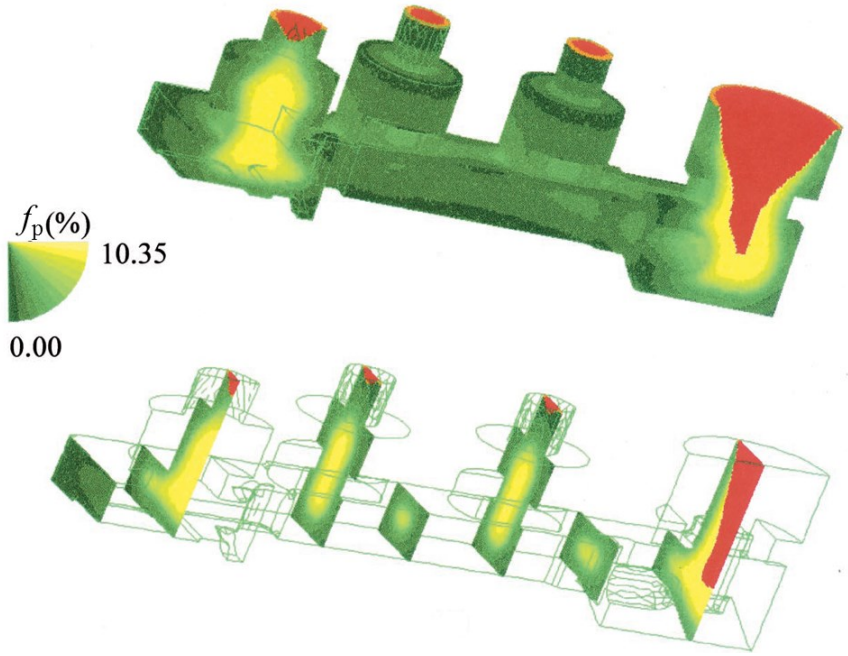

Figure 2.11: Numerical result of the microporosity and pipe shrinkage in a 3-D Al-4.5 wt% Cu casting. [130]

However, those models did not couple with the model of macrosegregation. Wang et al. [133] presented a three-phase volume averaging model to simulation the shrinkage flow and the formation of macrosegregation in the globular equiaxed solidification process. Three phases they considered are liquid, equiaxed grain and air. The thermosolutal convection, grain movement and shrinkage flow are all taken into account in this model. The moving free surface caused by solidification shrinkage is tracked by the volume averaging approach. The model was successfully applied to an Al-4 %wt. Cu alloy benchmark ingot casting. Both the shrinkage pipe and macrosegregation pattern were predicted reasonably.

2.3 Numerical model

Since last 30 years, many numerical models were established to investigate the solidification process and segregation phenomenon. Most of them have been discussed in previous sections [7, 105-111]. The key feature of those models is to consider the

multiphase flow. Beckermann and Viskanta developed the theoretical fundamentals of multiphase solidification models in the 1990's [4, 134]. On this base several two- or three-phase models with different assumptions have been applied and published [135-137]. These models separate volume-averaged equations for mass, momentum, energy, and species conservation which are derived for a solid and a liquid phase.

The group of Ludwig and Wu at University of Leoben has been studying solidification process with multiphase approach for many years. Several solidification models, starting from 2 phase to 5 phases, have been developed [8-11, 138-150]. Their first publication, about the modeling of macrosegregation with a two-phase globular equiaxed model, was presented in 2002 [8]. In that model, both liquid and solid are treated as separated but highly coupled interpenetrating continua. Nucleation of the equiaxed grains, diffusion-controlled growth of equiaxed phases, interphase exchanges, and interactions such as mass transfer during solidification, drag force, solute partitioning at the liquid/solid interface, and release of latent heat are taken into account.

In 2006 [10], a three-phase mixed columnar-equiaxed solidification model was proposed. The three phases are the melt, the solidifying columnar dendrities and globular equiaxed grains. The morphology of the solidifying crystals is simplified: sphere for equiaxed and step-wise cylinder for columnar. All the three phases are considered as spatially coupled and interpenetrating continua by mean of the Eulerian approach. The conservation equations of mass, momentum, species, and enthalpy are solved for all three phases. Nucleation of the equiaxed grains, diffusion-controlled growth of both columnar and equiaxed phases, interphase exchanges, and interactions such as mass transfer during solidification, drag force, solute partitioning at the liquid/solid interface, and release of latent heat are taken into account. The melt convection and grain sedimentation, macrosegregation, columnar-to-equiaxed-transition (CET), and macrostructure distribution are also taken into account.

The key advantages of this model are as follows:

1) The major involving phases are considered;

2) Although the calculation cost is still very high, it is most likely to be applicable for the calculation of large ingots (>100 tons) in the near future;

3) The most important macrosegregation mechanisms in steel ingots can be considered, e.g. crystal sedimentation induced bottom cone shaped negative segregation, thermal-solutal convection induced positive segregation in hot top region, interdendritic flow induced quasi-A segregation, etc.

Therefore, this thesis is mainly based on this three-phase mixed columnar-equiaxed model, although later on some dendritic models [141-144], which considered both the columnar and equiaxed dendritic structural, were proposed.

3 Simulation of macrosegregation

In this thesis macrosegregation in different ingot castings were numerically studied from a laboratory benchmark to a 25-ton heavy steel ingot. Firstly, a two-phase columnar model was used to study the formation of channel segregation in a laboratory benchmark; then, the three-phase mixed columnar-equiaxed model was employed to investigate the macrosegregaton in a 2.45-ton steel ingot; finally, the macrosegregation in a 25-ton steel ingot was simulated. Significant results were summarized here, details were described in the publications appending in the last part of this thesis.

3.1 General model description and assumptions

All the simulations in this study were based on the three-phase mixed columnar-equiaxed model. Details of the model description can be found in the literature [8,10-11,145, 151-152] and Publication IV. Here, only a brief outline of the model and assumptions is given.

In this model Eulerian volume-averaging multiphase approach is used. The different phases, as defined subsequently, are treated mathematically as interpenetrating continua. Volume fractions represent the space occupied by each phase and sum to one. Conservation equations for each phase are derived and solved for the relevant physical variables. Model closure is achieved by providing constitutive relations obtained from solidification dynamics and kinetics, empirical information, or the laws of fluid dynamics

1) Phase definitions: primary liquid (ℓ), equiaxed secondary phase (e), and columnar secondary phase (c). Their volume fractions, f_ℓ , f_e and f_c are obtained by solving the mass-transport equations with consideration of the mass transfer due to solidification/melting. As shown in Figure 3.1, in the volume element indexed with

$i_c = 0$, only equiaxed (e) and liquid (ℓ) phases coexist, i.e., $f_c \equiv 0$. In the element indexed with $i_c = 1$, which includes columnar tips, all three phases coexist. In the element indexed with $i_c = 2$, which has already been passed by the columnar front, again all three phases are allowed to coexist (not necessary).

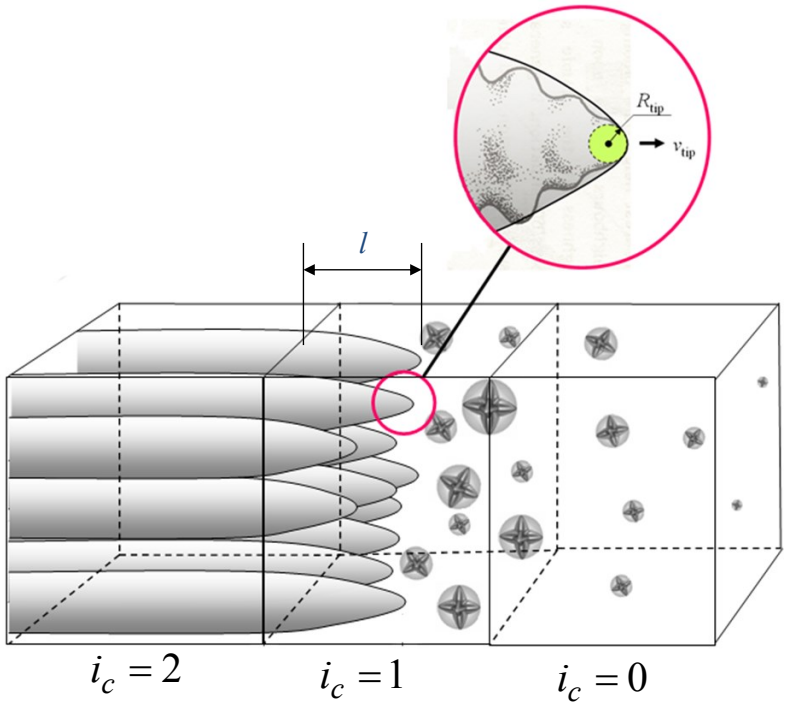

Figure 3.1: Schematic diagram of the control volumes in the vicinity of the columnar tip front.

2) Both primary and equiaxed phases are moving phases, for which the corresponding Navier–Stokes equations are solved for the velocity fields $\vec{u}_\ell$ and $\vec{u}_e$. The columnar phase is assumed to solidify from the wall toward the bulk melt and remain stationary; thus, no momentum equation for the columnar phase is considered.

3) Enthalpy equations for all three phases are solved. Due to the fact that thermal diffusion is much higher than solute diffusion, only one temperature that was assumed to represent each volume element. Therefore, a large volume heat-transfer coefficient between the phases is applied to balance the temperatures of the phases in each element.

4) Three volume-averaged concentrations, c_ℓ, c_e, and c_c, are solved. As shown in Figure 3.2, the thermodynamic equilibrium condition was assumed always applies at the liquid-solid interface. Therefore, an equilibrium concentration of liquid, c_ℓ^*, is calculated according to the local temperature, *T*, based on the phase diagram. The constitutional undercooling ($c_\ell^* - c_\ell$) serves as the driving force for solidification.

5) Ideal morphologies for both solid phases are assumed: spheres for equiaxed (globular) grains and cylinders for columnar (cellular) dendrite trunks. As shown in Figures 3.1 and 3.2, the grain growth is controlled by diffusion according to the analytically solved concentration profiles around the corresponding crystal.

6) The columnar grains are assumed to originate from the mold wall. Neither nucleation of columnar grains nor equiaxed-to-columnar transition is taken into account.

7) A continuous three-parameter (Gaussian) heterogeneous nucleation law is applied to model the equiaxed grain nucleation. [8-9] Transport of the grains is also considered. Grain fragments brought into the mold during filling, further fragmentation of dendrites during solidification, and the attachment of equiaxed grains into columnar tips (as a part of the columnar phase) are ignored.

8) The grain size, d_e, the grain number density, *n*, of equiaxed grains, and the diameter, d_c, of the columnar trunks are explicitly calculated, while a constant value for the primary arm spacing, λ_1, of columnar dendrites is used.

9) Shrinkage porosity is not considered. The Boussinesq approach is employed to model thermosolutal convection, grain sedimentation, and sedimentation-induced melt convection [8].

10) Resistance to interdendritic flow in the mushy zone is calculated using a permeability law based on the Blake-Kozeny approach [153].

11) The growth of the columnar primary tips stops when the volume fraction of the equiaxed phase reaches 0.49 (hard blocking criterion) in front of the primary columnar dendrite tips [154].

12) The packing limit for the equiaxed phase is set as $f_e + f_c \geq 0.637$ [138], and the equiaxed crystals are trapped by the columnar dendrite trunk when the local volume fraction of the columnar phase reaches a critical value of 0.2 [146].

13) The linearized, binary phase diagram is used with a constant solute redistribution coefficient, k, and a constant liquidus slope, m.

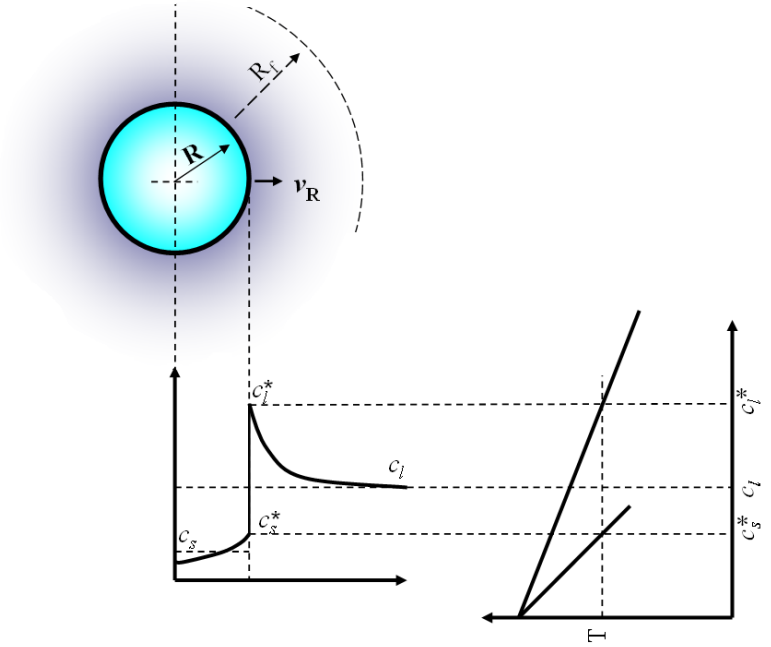

Figure 3.2: Schematic principle of diffusion-controlled crystal growth. For equiaxed grains, R denotes the radius of the grain (d_e/2). For the columnar grains, R denotes half of the diameter of the columnar trunk (d_c/2).

3.2 Channel segregates in laboratory benchmark

In this case, only liquid and columnar two phases were taken into account. The columnar tip was also not taken into account. Details about the two-phase columnar solidification model can be found in the publication [145,151].

The simulations were carried out for both 2D and 3D configurations. Here only the 3-D result is discussed. More detail results can be found in the Publications I and II. A sketch of

the 2-D benchmark described by Bellet et al. [12] is shown in Figure 3.3. Due to the geometric and heat extraction symmetry, only half of the ingot is modeled and a symmetry boundary condition is defined at the left boundary. The thickness of the 3-D geometry is 0.03 m. The casting alloy is Sn-10 wt.% Pb. For a 2D calculation heat is extracted from one vertical wall and a symmetry boundary condition is imposed at the symmetry plane. At time $t = 0$, the mold is filled with melt at uniform temperature and composition. The mold walls have a constant temperature, T_{EXT}. A constant heat transfer coefficient, h, is applied between the casting and the mold. The 3D simulation takes the same boundary conditions as the 2D case. Additionally, non-slip flow boundary condition for front and back walls is treated, and a convective cooling boundary condition was applied there: $h = 50$ W m^{-2} K^{-1} and $T_{EXT} = 298$ K.

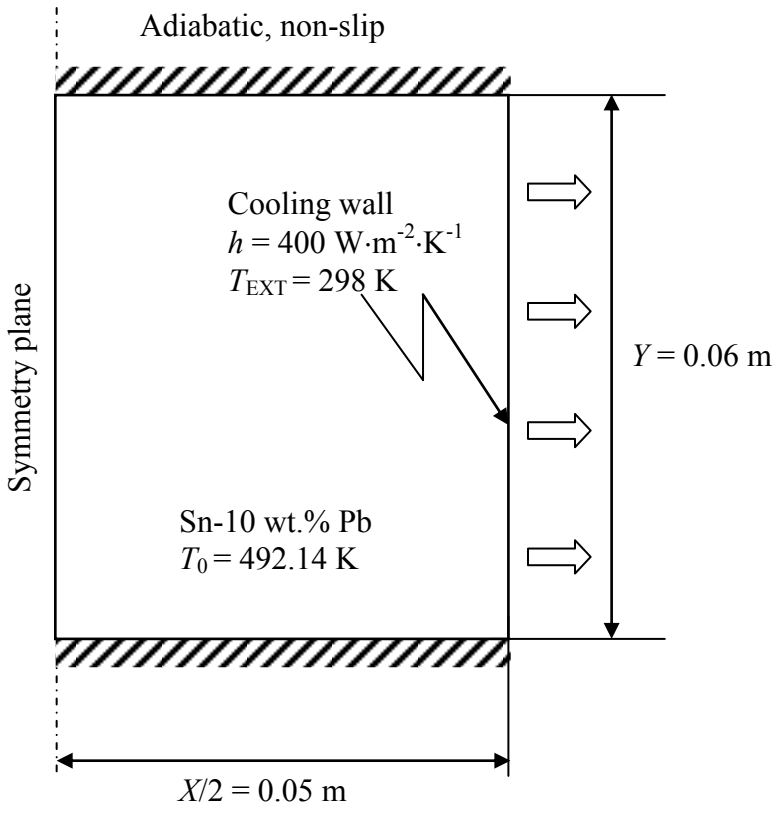

Figure 3.3: Benchmark geometry with boundary and initial conditions.

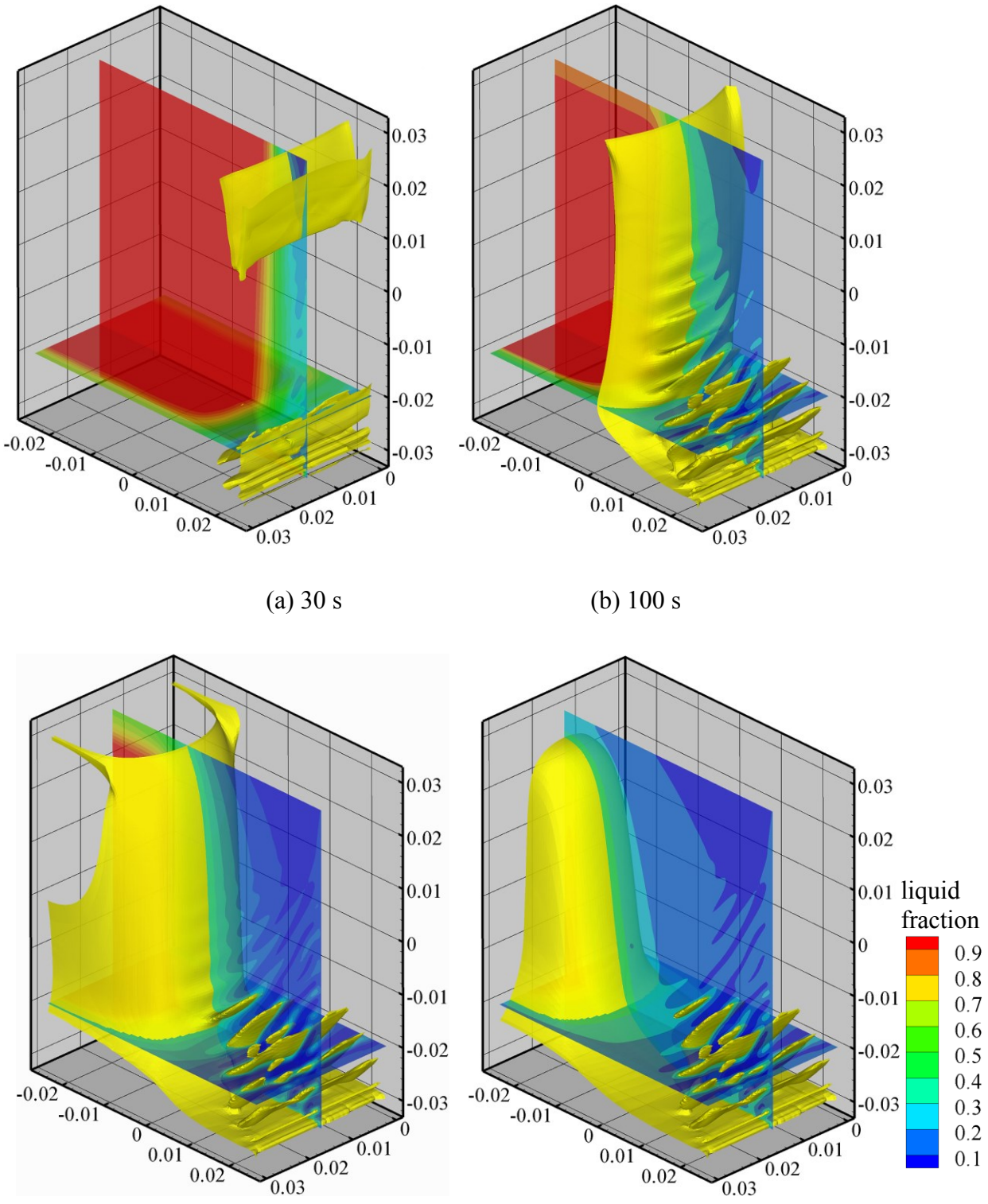

(a) 30 s (b) 100 s

(c) 150 s (d) 400 s

Figure 3.4: Evolution of solidification in the 3-D benchmark with 0.03 m thickness at (a) 30 s, (b) 100 s, (c) 150 s, and (d) 400 s. The liquid volume fraction in two planes (a vertical center plane and a horizontal plane with 0.01 m from bottom) is shown in color scale. The isosurfaces (yellow) of liquid volume fraction (f_ℓ = 0.35) are also shown to demonstrate the evolution of the flow channels.

Figures 3.4 (a)-(d) show snapshots of the evolution of solidification at t = 30, 100, 150 and 400 s. In each frame the liquid fraction distributions are shown in a vertical center plane and horizontal plane. Isosurfaces (yellow) of liquid volume fraction (f_ℓ = 0.35) are also shown to demonstrate the evolution of the flow channels. The regions bounded by the isosurfaces, where f_ℓ is larger than 0.35, represent the flow channels. At 30 s the channels have formed in the right bottom region adjacent to the chill wall, but they are not well pronounced. At 100 s, the number of channels near the chilled wall region has grown and a portion of these are already fully developed. The channels are generally 3-D in nature; most of them are lamellar-structured, discontinuous, while a few of them are rod-like. They occur only in the right bottom region, which is roughly a quarter of the whole calculation domain. The channel spacing (distance between neighboring channels) is nearly constant, varying slightly over time during solidification.

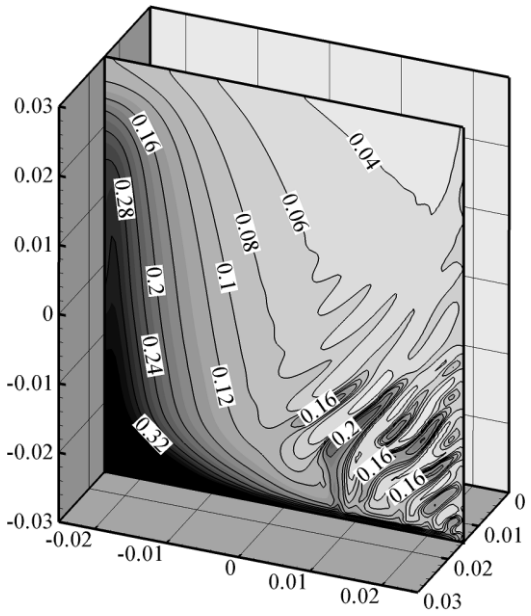

Figure 3.5: Distribution of the Pb mixture concentration, c_{mix}, at the end of solidification is shown in gray scale (dark for the highest and light for the lowest value) along with labeled c_{mix} isolines.

The macrosegregation profile of the solidified ingot in the vertical center plane is shown in Figure 3.5. Negative segregation, with mixture concentration (c_{mix}) as small as nominal composition 0.04, is predicted in the upper-right region and positive segregation, with c_{mix} as large as 0.32, is predicted in the lower-left region. The channel segregation pattern is

clearly shown in the lower right region. The pattern of the segregates (inclined angle, channel spacing, number of the channels) corresponds to the flow patterns that develop during solidification.

Figure 3.6 shows the final channel segregation pattern in 3-D from two angles. The isosurface of a segregation index, as defined by $(c_{mix} - c_0)/c_0 = 1.5$, is displayed. The channel segregates are predominately lamellar-structured with some rod-like morphology, which is in agreement with 3-D channel segregation previously described in the literature [40-41]. This kind of channel segregation pattern was numerically predicted for the first time by the current author. This result was later on verified by H. Combeau and co-workers [154]. The channel segregation pattern is observed only in the lower right region and shows an upward slanting pattern with an angle of 40-60 degree from the horizontal plane. The average thickness of the channels is 0.002 m, the channel spacing is 0.004 m and the length of the largest channel is approximately 0.019 m.

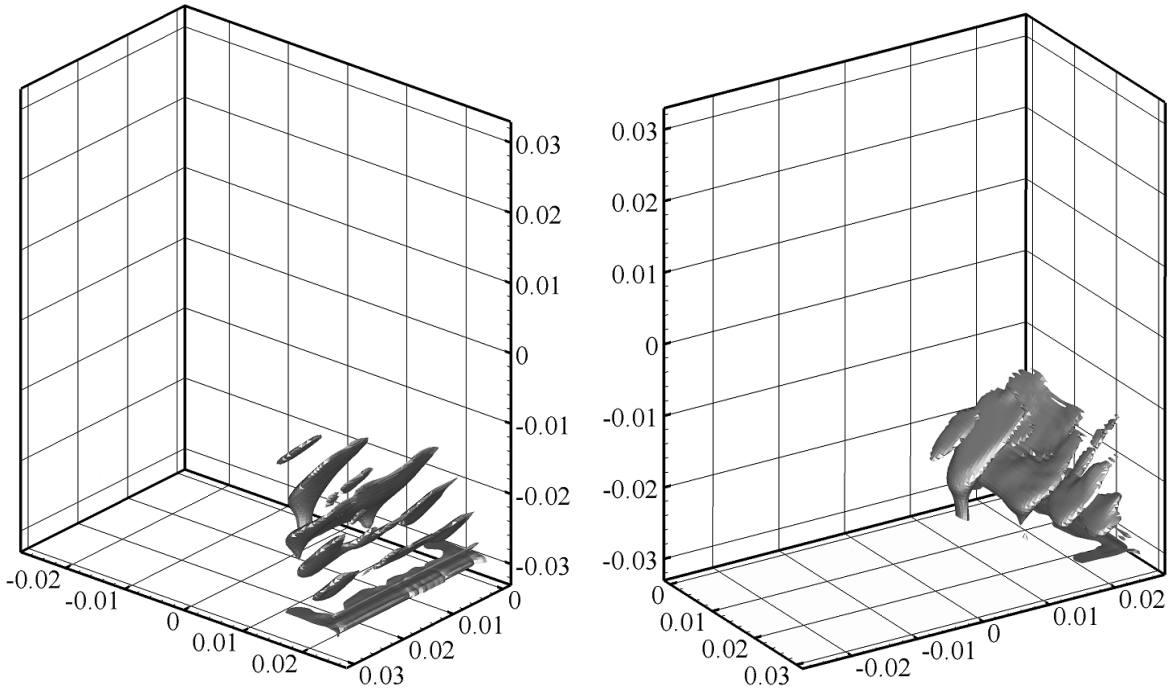

Figure 3.6: The isosurface of Pb segregation ratio, as defined by $(c_{mix} - c_0)/c_0 = 1.5$ from two viewing angles.

3.3 Segregates in 2.45-ton steel ingot

A large number of industry steel ingots have been poured and analyzed for macrosegregation during the last century [2, 41]. In this thesis, a 2.45-ton, big-end-up ingot (Fe-0.45 wt.% C) is simulated. The ingot had a square, cross-sectional area and was cast in a chilled mould; here a 2-D axis-symmetrical simulation was performed to approximate the solidification behavior in the square cross-section of the ingot. The configuration of this ingot, labeled with the necessary boundary and initial conditions, is described in Figure 3.7. Because the experiment was performed many decades ago and because of the lack of a precise process description, assumptions must be made for certain process parameters and boundary conditions. Here, the heat transfer coefficient is based on the final solidification time, which refers to the classical theory and experimental values [41]. This ingot was simulated with three numerical models: the non-dendritic and the simplified dendritic three-phase mixed columnar-equiaxed model, and the four-phase shrinkage model. All of them are based on the previous three-phase mixed columnar-equiaxed model [10-11].

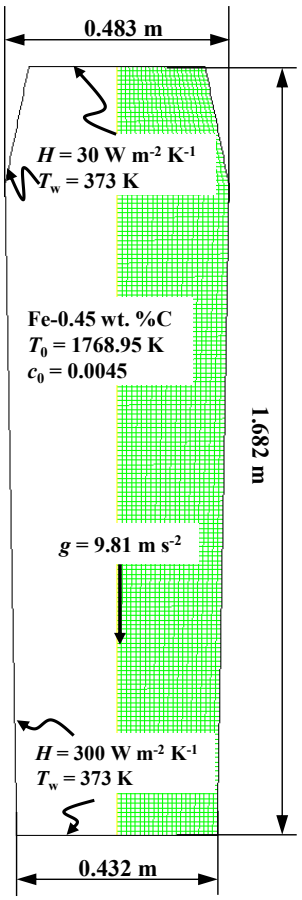

Figure 3.7: Configuration of the 2.45-ton industry steel ingot.

3.3.1 Non-dendritic three-phase mixed columnar-equiaxed model

Short description of the non-dendritic three-phase mixed globular equiaxed solidification model was given in section 3.1 more detail about this model can be found in the literature [8, 10-11, 151-152] and publication IV.

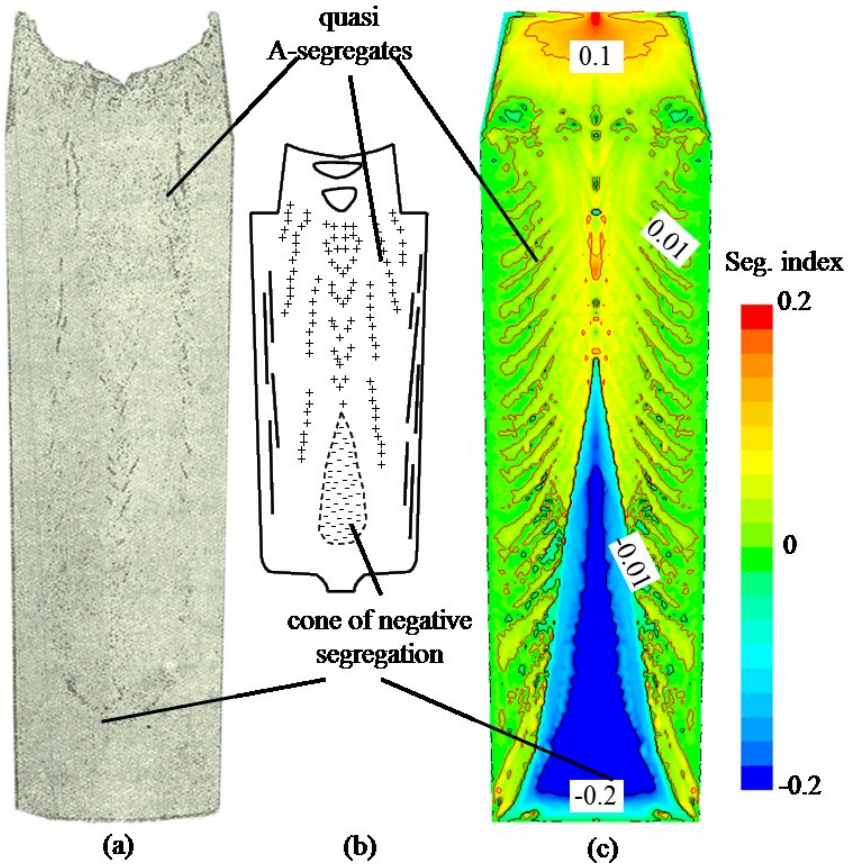

Figure 3.8: Macrosegregation pattern. (a) Sulphur print of the as-cast ingot [1], (b) schematic of the typical macrosegregation pattern in steel ingots [40], and (c) predicted macrosegregation pattern overlapped with isolines of segregation index. The segregation is quantified by a segregation index: $(c_{\mathrm{mix}} - c_0)/c_0$.

Figure 3.8 shows the predicted segregation pattern and the comparison with the sulphur print as well as the classic macrosegregation pattern. A positive segregation in the top and a conic negative segregation in the bottom were observed. Obviously, the lower conic negative segregation is caused by the equiaxed sedimentation. The settling grains are poor in solute elements, thus their accumulation results in negative segregation. The positive segregation at the top region of the ingot is caused by the flow of the enriched melt in the bulk region. A streak-like segregation pattern in the middle radius region between the outer

surface and the ingot centerline is predicted. One may notice that this streak-like segregation has a similar contour to the classical A-segregation (Figure 3.8(b)), the author cannot justify if the classical A-segregation is the same as streak-like segregation or originates from this type of streak-like segregation. According to the most widely accepted empirical explanation [40], A-segregation belongs to a type of channel segregation in large steel ingots, which originates and develops in the stationary dendritic mushy zone. Therefore, the author referred to the streak-like segregations as quasi A-segregates (or quasi A-segregation). Further discussion about the formation mechanism of the quasi A-segregates can be read in the Publication IV.

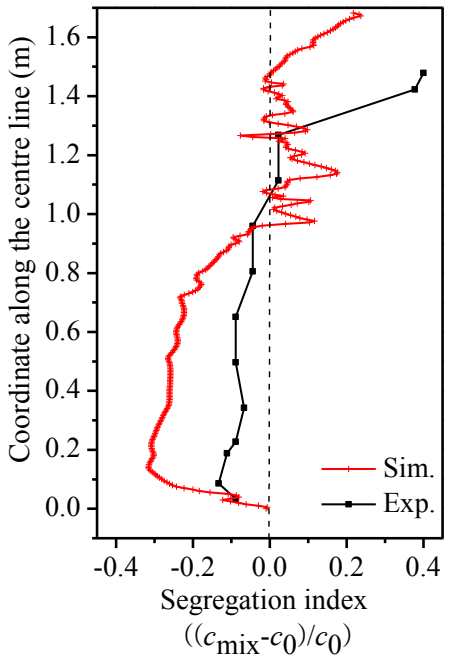

Figure 3.9: Comparison of the segregation index along the centerline between the simulation and the experiment.

The predicted macrosegregation pattern coincides qualitatively with the experiment result and fit to the typical segregation pattern of steel ingots. The segregation along the ingot centerline is compared with the experiment report [1], as shown in Figure 3.9. Both the experimental and simulated results show the negative segregation in the lower part and positive segregation in the upper part. However, the negative segregation in the lower part is predicted more severely than the experimental result. The overestimation of the negative segregation in the lower part by the model results from two aspects. One is the assumption of globular equiaxed morphology, which can cause significant overestimation of the

sedimentation-induced negative segregation. The other aspect is the lack of real process conditions and material property, especially in terms of the parameters for the nucleation of equiaxed crystals.

In the upper part of the ingot, the experiment result shows a large positive segregation in the hot top. The modeling result shows also a large positive segregation in the hot top, but a discontinuous distribution between negative and positive segregation can be identified just below the hot top. The predicted position of the hot top is higher than the experimentally indicated position. The reasons for the above discrepancy are from both experimental and modeling aspects. From the modeling aspect, the uncertainty about the thermal boundary conditions and the neglect of the formation of the shrinkage cavity in the top are mainly responsible for the discrepancy between the predicted and experimentally indicated hot top positions. From the experiment aspect, the distance between two sampling points is larger than 10 cm, and it might not provide sufficient measurement resolution. In the praxis, people often identified the discontinuous negative-positive segregation below the hot top [101]. The reason for this type of segregation distribution is due to the formation of a mini-ingot in the late stage of solidification. Further discussions of the formation and behavior of mini-ingot can be found in the Publication IV.

3.3.2 Simplified dendritic solidification model

As mentioned previously, the mixed columnar-equiaxed model has assumed a globular morphology for the equiaxed grain. This assumption underestimated the drag force between equiaxed grain and liquid melt which results in the overestimation of the equiaxed grain settling speed. In the bottom region, the settling equiaxed grain contains less solute. The more the equiaxed phase is, the serious the negative segregate is. Subsequently, the globular equiaxed model overestimates the negative segregation in the bottom region of the ingot. Therefore, some modifications should be made in order to take into account the influence of equiaxed dendritic on the drag force, etc. On the other hand, since the calculation time for this big ingot is huge, the improved model should not increase the calculation time so much. It is not a computationally efficient approach to embed the full dendritic model [141] into this model. Therefore, some simplifications were made to compromise the two aspects mentioned above. Here only the dendritic morphology of equiaxed crystal is considered.

An equiaxed dendrite is shown in Figure 3.10. Some important parameter definitions are as follows*:

1) The equiaxed dendrite envelope is defined as a smooth surface connecting the primary and secondary arm tips and contains both the solid dendrite and the interdendritic liquid. Therefore, there is four phases in a control volume: the solid dendrites in the equiaxed grain, the inderdendritic melt in the equiaxed grain, the extradendritic melt, and the columnar. The corresponding phase fractions are $\varepsilon_{\mathrm{s}}^{\mathrm{e}}$, $\varepsilon_{\mathrm{d}}^{\mathrm{e}}$, ε_{ℓ}, and ε_{c} with $\varepsilon_{\ell}+\varepsilon_{\mathrm{d}}^{\mathrm{e}}+\varepsilon_{\mathrm{s}}^{\mathrm{e}}+\varepsilon_{\mathrm{c}}=1$. For globular equiaxed crystals, $\varepsilon_{\mathrm{d}}^{\mathrm{e}}=0$.

2) The equiaxed envelope volume fraction, ε_{e}, is defined as $\varepsilon_{\mathrm{e}}=\varepsilon_{\mathrm{s}}^{\mathrm{e}}+\varepsilon_{\mathrm{d}}^{\mathrm{e}}$. The internal solid fraction within the porous dendrite envelope, $\varepsilon_{\mathrm{si}}$, is defined as $\varepsilon_{\mathrm{si}}=\varepsilon_{\mathrm{s}}^{\mathrm{e}}/\varepsilon_{\mathrm{e}}$. The total liquid fraction, ε_{f}, is defined as $\varepsilon_{\mathrm{f}}=\varepsilon_{\ell}+\varepsilon_{\mathrm{d}}^{\mathrm{e}}$.

3) The interfacial area concentration, S_{s} and S_{e}, denoting the surface areas of the solid/interdendritic liquid and dendrite envelope interfaces, respectively, divided by the total volume, V_0, of the control element.

There are some correlations between the dendritic and globular models:

$$\varepsilon_{\mathrm{f}}=f_{\ell}\ ,\ \varepsilon_{\mathrm{s}}^{\mathrm{e}}=f_{\mathrm{e}}\ ,\text{ and }\ \varepsilon_{\mathrm{c}}=f_{\mathrm{c}} \tag{3.1}$$

where, f_{ℓ}, f_{e}, and f_{c} represent the liquid, equiaxed, and columnar volume fraction, respectively, for non-dendritic solidification model.

As discussed above, the motivation to develop this model is to take into account the equiaxed dendritic structure without increasing the calculation time. Therefore, one simplification is made here: the internal solid fraction within the equiaxed envelope, $\varepsilon_{\mathrm{si}}$, was assumed to begin with a constant value, i.e. $\varepsilon_{\mathrm{si}}^{\mathrm{c}}$; when the solid dendritic volume fraction, $\varepsilon_{\mathrm{s}}^{\mathrm{e}}$, is bigger than $\varepsilon_{\mathrm{si}}^{\mathrm{c}}$, then it is identical to $\varepsilon_{\mathrm{s}}^{\mathrm{e}}$. Here $\varepsilon_{\mathrm{si}}^{\mathrm{c}}$ is assumed empirically.

* In order to avoid conflict, for dendritic model the phase volume fraction of phase *k* is indicated by ε_{k} which is f_{k} for globular model.

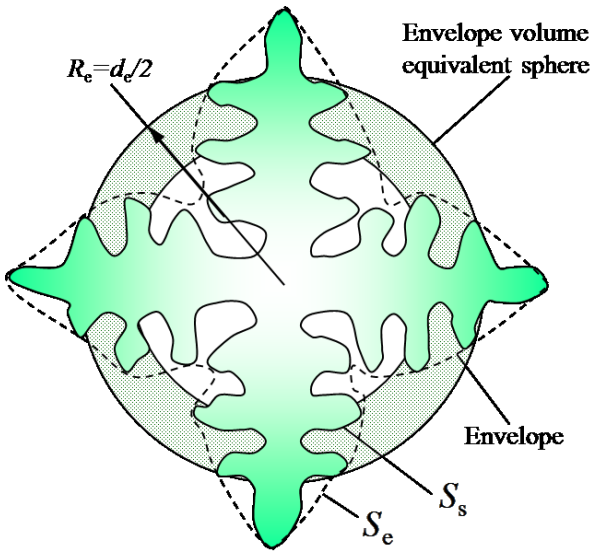

Figure 3.10: Schematic of the equiaxed dendritic structure and envelope.

All the parameters in the dendritic model are calculated directly from the globular model according to Eq. (3.1). Other quantities (e.g. ε_e and ε_d^e) are derived from ε_f and ε_s^e indirectly. Therefore, the simplified dendritic model, in general, is the same as the non-dendritic mixed columnar-equiaxed model. Here, only three modifications were made.

1) Drag law of equiaxed dendrite

In order to consider the influence of dendritic structure on the drag force, a drag low [156] which takes into account both the interdendritic and exterdendritic liquid, is employed. The total drag force in a unit volume can be written as:

$$F_{e\ell} = \frac{4\beta^2 \mu_\ell \varepsilon_f^2}{d_e^2} \quad \text{.....(3.2)}$$

where, μ_ℓ is the liquid viscosity; $d_e = \sqrt[3]{\frac{6\varepsilon_e}{\pi n_e}}$ is the diameter of an equivalent sphere having the same volume as the dendrite envelope, as shown in Figure 3.10; χ is the general correlation of χ_d and χ_ℓ [157]:

$$\chi = \frac{\chi_{\mathrm{d}}}{\left[(1-\varepsilon_{\ell})^{\mathrm{n}} + (\chi_d / \chi_{\ell})^{2\mathrm{n}}\right]^{1/2\mathrm{n}}} \tag{3.4}$$

where $n = 0.176\log 10(\chi_{\mathrm{d}}) + 0.275$, χ_{d} and χ_{ℓ} can be obtained as :

$$\chi_{\mathrm{d}} = \frac{3\sqrt{5}}{(1-\varepsilon_{\mathrm{si}})^{\frac{3}{2}}} \cdot \frac{S_{\mathrm{s}}}{\phi_{\mathrm{e}} S_{\mathrm{e}}} \tag{3.5}$$

$$\chi_{\ell} = \left\{ \frac{9}{2} \cdot \varepsilon_{\mathrm{e}} \frac{2 + 1.333\varepsilon_{\mathrm{e}}^{\frac{5}{3}}}{2 - 3\varepsilon_{\mathrm{e}}^{\frac{1}{3}} + 3\varepsilon_{\mathrm{e}}^{\frac{5}{3}} - 2\varepsilon_{\mathrm{e}}^{\frac{6}{3}}} \cdot \frac{1}{c_{\mathrm{p}}(\phi_{\mathrm{e}})} \cdot \frac{2\chi_{\mathrm{d}}^2\left[1 - \tanh(\chi_{\mathrm{d}})/\chi_{\mathrm{d}}\right]}{2\chi_{\mathrm{d}}^2 + 3\left[1 - \tanh(\chi_{\mathrm{d}})/\chi_{\mathrm{d}}\right]} \right\}^{0.5} \tag{3.6}$$

where $S_{\mathrm{e}} = \frac{n_{\mathrm{e}} \cdot \pi d_{\mathrm{e}}^2}{\phi_e} = \frac{6\varepsilon_{\mathrm{e}}}{\phi_{\mathrm{e}} d_{\mathrm{e}}}$, $S_{\mathrm{s}} = \frac{4}{\lambda_2}\varepsilon_{\mathrm{si}}^{\frac{1}{2}} \cdot \varepsilon_{\mathrm{e}}(1-\varepsilon_{\mathrm{si}}^6) + \cdot\varepsilon_{\mathrm{si}}^6 S_{\mathrm{e}}$, and the correction factor, $C_{\mathrm{p}}(\phi_{\mathrm{e}})$, account for the non-spherical shape of the dendrite envelope [156].

2) The columnar-to-equiaxed-transition (CET)

In the non-dendritic model, the columnar tip blocking mechanism described by Hunt [155] is implemented for CET. In the columnar tip elements, the tip growth velocity, v_{tip}, is set to zero as soon as the local volume fraction of equiaxed grain, f_{e}, exceeds the critical threshold of $f_{\mathrm{e,CET}}$ (e.g. 0.49), this is the so-called “hard blocking”.

For this simplified dendritic model, there is a similar “hard blocking” mechanism with the non-dendritic model. When the volume fraction of equiaxed envelope, ε_{e} , exceeds the critical threshold of 0.49, the columnar tip growth velocity is set to zero. Therefore the critical threshold is:

$$f_{\mathrm{e,CET}} = 0.49 \cdot \varepsilon_{\mathrm{si}} \tag{3.7}$$

which means when the calculated f_{e} reaches $0.49 \cdot \varepsilon_{\mathrm{si}}$, the columnar tips are blocked.

3) The packing limit of equiaxed grain

In the non-dendritic model, the momentum of the equiaxed phase is treated like that of a fluid. Hence, the solution of the corresponding conservation equation requires the definition of a viscosity of the equiaxed phase. This viscosity is caused by collisions between

individual rigid grains. It should increase with increasing solid volume fraction and crystal size because of stronger crystal interactions. The Ishii and Zuber's law [158] for solid/liquid mixture viscosity was employed:

$$\mu_{\mathrm{e}} = \frac{\mu_{\ell}}{f_{\ell}}((1 - f_{\mathrm{s}} / f_{\mathrm{s}}^{\mathrm{c}}))^{-0.25 \cdot f_{\mathrm{s}}^{\mathrm{c}}} - (1 - f_{\mathrm{s}}) \tag{3.8}$$

For $f_{\mathrm{s}} > f_{\mathrm{s}}^{\mathrm{c}}$, μ_{e} is infinitely large. This forces the macroscopic velocity gradients in the solid to vanish. Where the μ_{e} is the viscosity of equiaxed phase; f_{s} is the solid fraction; $f_{\mathrm{s}}^{\mathrm{c}}$ is the packing limit. In the non-dendritic model one has $f_{\mathrm{s}}^{\mathrm{c}} = 0.637$. Therefore, in this simplified dendritic model the packing limit is: $f_{\mathrm{s}}^{\mathrm{c}} = \varepsilon_{\mathrm{si}} \cdot 0.637$.

With above modifications, calculations of the same 2.45-ton ingot were made. The results are shown in Figure 3.11-3.12. As the parameter $\varepsilon_{\mathrm{si}}^{\mathrm{c}}$ is unknown, calculations of three cases with different $\varepsilon_{\mathrm{si}}^{\mathrm{c}}$ constant were compared. The case with $\varepsilon_{\mathrm{si}}^{c}$ = 1 indicates the globular (non-dendritic) equiaxed model. The macrosegregation pattern is the same for all cases (dendritic or non-dendritic): including the positive segregation zone in the top part, the cone shape negative segregation zone in the bottom region, and many quasi-A segregation bands. For simplified dendritic equiaxed cases, the cone shape negative segregation region has been prolonged. Figure 3.12 presents the centerline macrosegregation with different $\varepsilon_{\mathrm{si}}^{c}$. It is obviously found that the simplified dendritic equiaxed model predicted less serious negative segregation in the bottom region than the non-dendritic model. It demonstrates that the simplified dendritic model improves the accuracy of the calculation significantly.

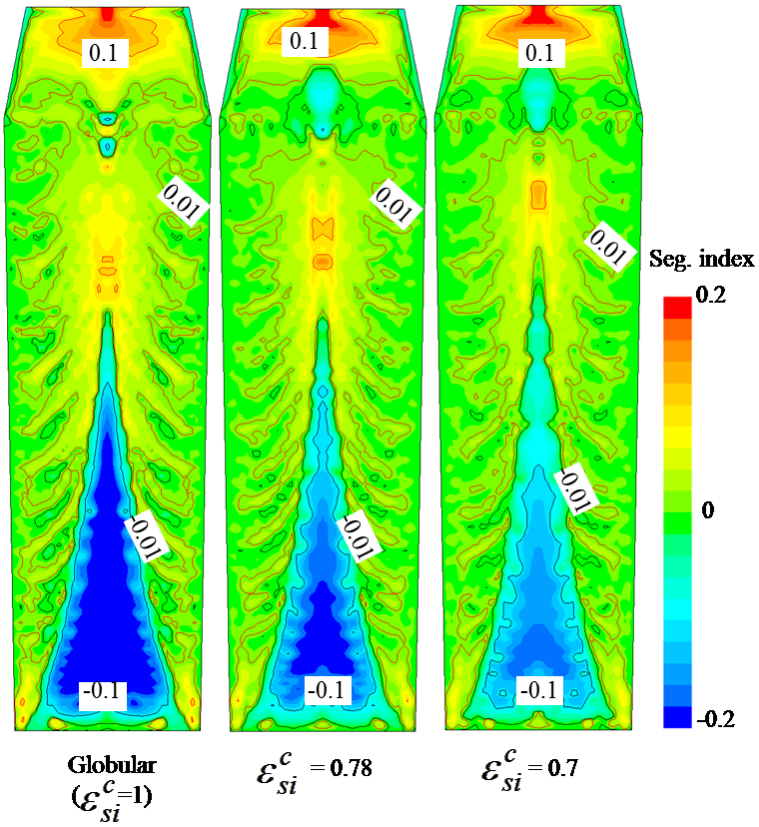

Figure 3.11: Predicted macrosegregation maps with different ε_{si}^{c}.

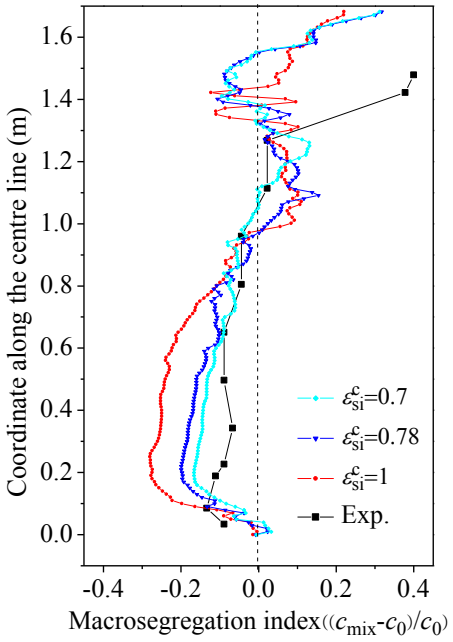

Figure 3.12: The comparison of centerline macrosegregation with different ε_{si}^{c}.

3.3.3 Improved model considering shrinkage cavity

A four-phase shrinkage model was established to predict the macrosegregation and the formation of shrinkage pipe in the 2.45 ton steel ingot. Four phases defined in this model are: the primary liquid phase (ℓ), the equiaxed phase (e), the columnar phase (c), and the air phase (a). The corresponding phase fraction is given by: f_ℓ , f_e , f_c and f_a with $f_\ell + f_\mathrm{e} + f_\mathrm{c} + f_\mathrm{a} = 1$. The solidification model is the same as the three-phase mixed columnar-equaixed model [10-11]. All the conservation equations for liquid, equiaxed, and columnar phases are the same as the three-phase mixed columnar-equiaxed model except that some exchange terms, between the air phase and other phases, have been added to the momentum and enthalpy conservation equations, respectively. The main part of model description can be found in the literature [8, 10-11, 151-152] and publication IV. Here only the conservation equations for air phase are described:

Mass:

$$\frac{\partial}{\partial t}\left(f_\mathrm{a}\rho_\mathrm{a}\right)+\nabla\cdot\left(f_\mathrm{a}\rho_\mathrm{a}\vec{u}_\mathrm{a}\right)=0 \tag{3.6}$$

Momentum:

$$\frac{\partial}{\partial t}\left(f_\mathrm{a}\rho_\mathrm{a}\vec{u}_\mathrm{a}\right)+\nabla\cdot\left(f_\mathrm{a}\rho_\mathrm{a}\vec{u}_\mathrm{a}\otimes\vec{u}_\mathrm{a}\right)=-f_\mathrm{a}\nabla p+\nabla\cdot\bar{\bar{\tau}}_\mathrm{a}+f_\mathrm{a}\rho_\mathrm{a}\vec{g}_\mathrm{a}+\vec{U}_{\ell\mathrm{a}}+\vec{U}_\mathrm{ca}+\vec{U}_\mathrm{ea} \tag{3.7}$$

Enthalpy:

$$\frac{\partial}{\partial t}\left(f_\mathrm{a}\rho_\mathrm{a}h_\mathrm{a}\right)+\nabla\cdot\left(f_\mathrm{a}\rho_\mathrm{a}\vec{u}_\mathrm{a}h_\mathrm{a}\right)=\nabla\cdot\left(f_\mathrm{a}k_\mathrm{a}\nabla\cdot T_\mathrm{a}\right)+Q_{\ell\mathrm{a}}+Q_\mathrm{ea}+Q_\mathrm{ca} \tag{3.8}$$

The exchange term $\vec{U}_\mathrm{ca}=-K_\mathrm{ca}\cdot\vec{u}_\mathrm{a}$, $\vec{U}_\mathrm{ea}=K_\mathrm{ea}\cdot(\vec{u}_\mathrm{e}-\vec{u}_\mathrm{a})$, and $\vec{U}_{\ell\mathrm{a}}=K_{\ell\mathrm{a}}\cdot(\vec{u}_\ell-\vec{u}_\mathrm{a})$. The symmetric model is employed to calculate the drag force between air and equixed phase.

$$K_\mathrm{ae}=\frac{3f_\mathrm{a}C_\mathrm{D}R_\mathrm{e}(f_\mathrm{a}\mu_\mathrm{a}+f_\mathrm{e}\mu_\mathrm{e})}{(d_\mathrm{a}+d_\mathrm{e})^2}, \tag{3.9}$$

where, d_a empirically assumed to be a constant value, 1.0×10^{-5} m; d_e is calculated by $d_e = \sqrt{\frac{6 f_e}{n_e \cdot \pi}}$. $K_{a\ell}$, K_{ac} are treated similarly. The exchange term $Q_{\ell a} = H_{\ell a} \cdot (T_\ell - T_a)$, where $H_{\ell a}$ is empirically assumed to be 107 W /m^3/K. Q_{ea}, Q_{ca} are treated similarly.

All the boundary conditions are the same as shown in Figure 3.7, except for the top surface where a constant pressure and constant temperature are applied.

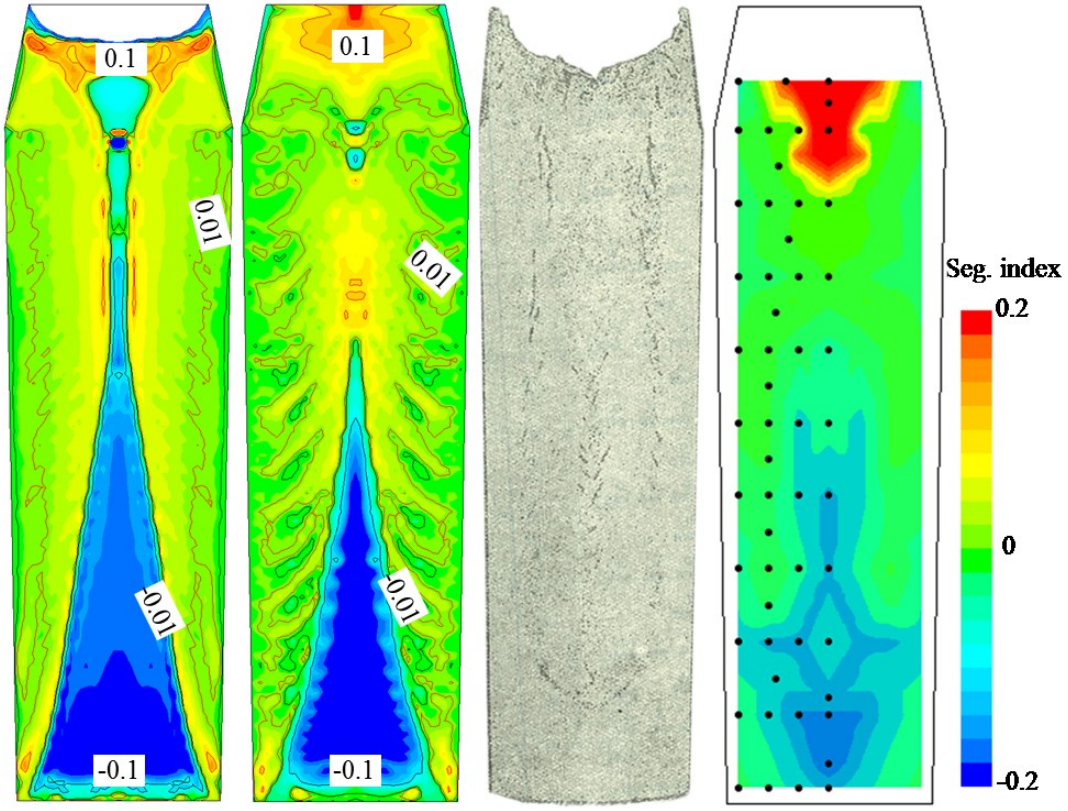

(a) (b) (c) (d)

Figure 3.13: The macrosegregation results for the 2.45-ton ingot: (a) simulation result of macrosegregation map with four-phase shrinkage model; (b) simulation result of macrosegregation map with three-phase mixed columnar-equiaxed model; (c) experimental etched surface; (d) experimentally measured macrosegregation.

Figure 3.13 compared macrosegregation patterns between simulations and experiment. Figure 3.13(a) and (b) compared the macrosegregation maps of four-phase shrinkage model and the three-phase mixed columnar-equiaxed model. Figure 3.13(c) shows the

experimental etched surface. Figure 3.13(d) indicates the experimentally measured macrosegregation distribution map. As we can see, although this four-phase shrinkage model successfully predicated the shrinkage pipe in the top region, which is favorable similar to the experiment one, the macrosegregation distribution is significantly different from the experiment one. Firstly, no oscillation of segregated band, the so-called A-segregation, is predicted by the four-phase shrinkage model, while both the mixed three-phase columnar-equiaxed model and the experimental results indicate the apparent A-segregation bands. Secondly, for the four-phase shrinkage model, in the upper part of the ingot there is a region of total equaixed zone where shows large negative segregattion. While both the experiment result and the three-phase mixed columnar-equaixed model show no negative segregation zone in the ¾ height of the ingot. Moreover, the experimental result shows the maximum positive segregation just beneath the shrinkage pipe and in the central of the ingot, while the four-phase shrinkage model predicts the maximum positive segregation in the region near the wall.

In summary, this new four-phase shrinkage model is still under development. The model still has some deficiencies, such as the calculation sometimes is unstable and even divergent. Much effort needs to be put into optimizing this model in the future, however it is not the objective of this thesis.

3.4 Segregates in a 25-ton steel ingot

A 25-ton steel ingot (Fe-0.44 wt.% C) was also studied. The ingot was chilled in an octagon mould. A 2D-axis symmetrical simulation was performed to approximate the solidification behavior in the octangon cross-section of the ingot. The configuration of this ingot, along with the necessary boundary and initial conditions, is described in Figure 3.14. Again, because the experiment was performed many decades ago and because of the lack of a precise process description, assumptions must be made for certain process parameters and boundary conditions. [41].

The same three-phase model as presented in section 3.1 was employed to simulate the macrosegregation in this 25-ton steel ingot. The grid size for each control volumes are between 1.5 cm x 1.5 cm and 3.2 cm x 3.2 cm, 2640 grids in the whole domain. The total solidification time is about 24000 second (6.7 hours). The calculation time step is between

0.01-0.02 s. The calculation was run in parallel on 8 CPUs (Intel Nehalem Cluster 2.93 GHz) with simulation time about 20 days.

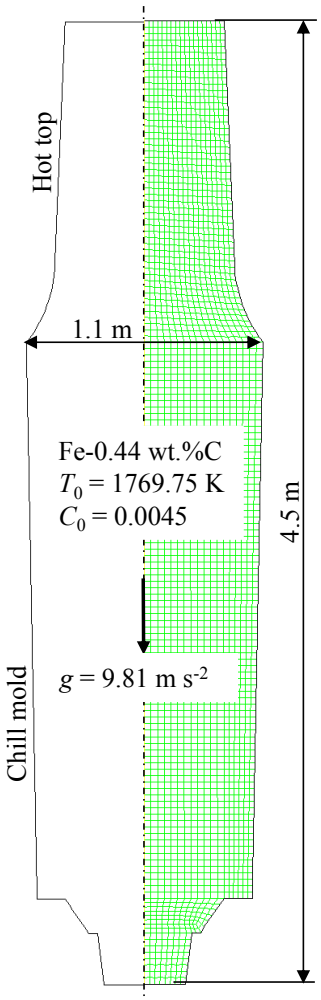

Figure 3.14: Configuration of a 25-ton steel ingot.

Figure 3.15 compares the macrosegregation results between the experiment and the simulation. It is easy to note that both the experiment and simulation results showing the positive macrosegregation in the top region, negative segregation in the bottom region, and a big positive segregation region in the central of the ingot. In addition, both of them show a small negative segregation region below the hot top region. However, due to the limiting amount of experimental points this experimentally measured macrosegregation cannot represent the exactly macrosegregation distribution. As we can see from Figure 3.15(a), the experimentally etched surface, some A-segregation bands are found between the middle radius region and the casting outer surface. However, there is no A-segregation predicted in

this simulation result. Li et al [151-152, 159] studied the influence of grid size on the prediction of the channel segregation formation, they deemed in order to predict the formation of channel segregation the computer grid size should not bigger than 1 cm. Therefore, simulation with finer grid should be made in the future in order to capture the appearance of A-segregation in this 25 ton steel ingot.

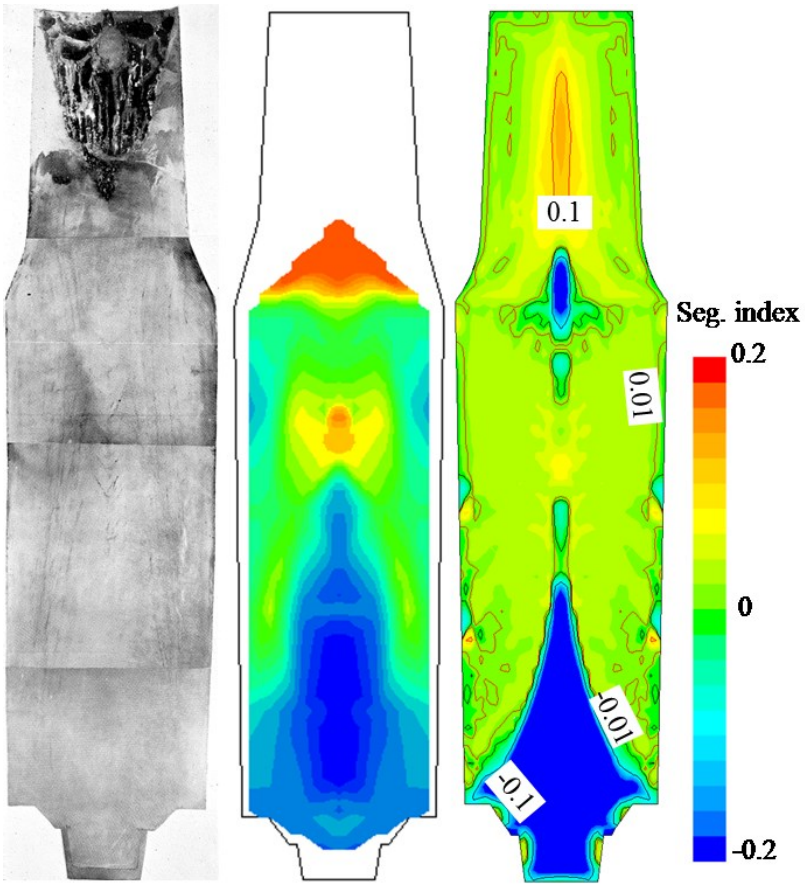

(a) (b) (c)

Figure 3.15: Macrosegregation result for the 25 ton ingot: (a) experimentally etched surface; (b) experimentally measured macrosegregation map; (c) simulated macrosegregation pattern.

Figure 3.16 illustrates the comparison of centerline macrosegregation between the experimental and simulated results. Some reasonable agreements are obtained from Figure 3.16: both the experimental and simulated results show the negative segregation in the lower part and positive segregation in the upper part, and negative segregation region

between ½ and ¾ height (just below the hot top) of the steel ingot. However, the negative segregation in the lower part is predicted more severely than the experimental result. Again, this overestimation of the negative segregation might result from two aspects: the assumption of globular equiaxed morphology; the lack of real process conditions and material property, especially in terms of the parameters for the nucleation of equiaxed crystals.

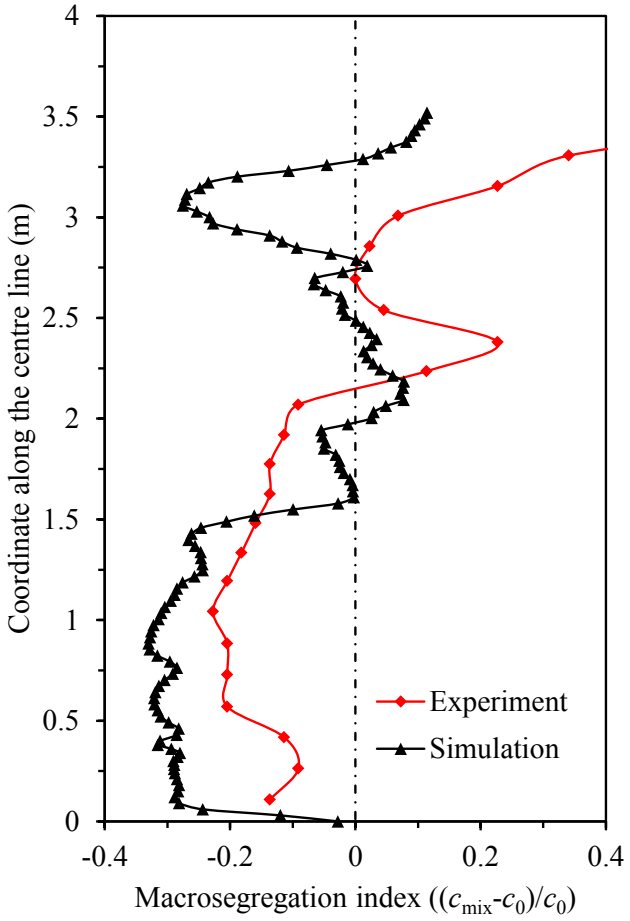

Figure 3.16: Comparison of centerline macrosegregation between experiment and simulation.

In addition, the predicted negative segregation region (below the hot top) shifts upwards, and the experimentally measured maximum positive segregation is larger than the simulated one. The reasons for the above discrepancy are due to the uncertainty of the thermal boundary conditions and the neglect of the formation of the shrinkage cavity in the top.

4 Conclusions

A two-phase columnar solidification model and a three-phase mixed columnar-equiaxed solidification model were used and improved to study macrosegregation phenomena in laboratory casting and industry steel ingots. Some segregation mechanisms were numerically analyzed. Main conclusions were drawn as follows.

1. Using a two-phase columnar solidification model to analyze channel segregates in a laboratory benchmark Sn-10 wt.% Pb.

   - Channel segregates were found to form in the bottom corner near the chilled wall with a predominately discontinuous lamellar-structured and rod-like morphology.

   - Significant difference in macrosegregation distribution was observed between the 2D calculation and 3D calculation. This difference, the 3D effect, is caused by the thermal and hydrodynamic influence of the front/back mold walls. The 3D effect is much less prominent in the thicker benchmark ($\geq$0.05 m), thus the 2D calculation suitably represents the thick-walled ($\geq$0.05 m) 3D benchmark but not the thinner 3D benchmark.

   - Verification of the current model was made by comparison with other modeling approaches and with the experiments of Hebditch and Hunt [17]. General quantitative agreements were obtained.

   - The mechanism leading to the formation of channel segregation in this laterally solidified Sn-10 wt.% Pb benchmark was also numerically studied. Both the initiation and growth of the channels were examined. The initiation of the channels is caused by flow perturbations in the mushy zone, which has been characterized by a mushy zone Rayleigh (R_a) number. For cases with channel segregation the

maximum R_a number must be larger than a critical value (0.12-0.24). The growth of the channel is the result of flow-solidification interactions. The sign of the flow-solidification interaction term, $\vec{u}_\ell \cdot \nabla c_\ell$, can be used to distinguish two solidification regions: a suppressed solidification region; and an accelerated solidification region. Channels can only occur in the suppressed solidification region, where an increase in local flow caused by a flow perturbation is reinforced by the resulting suppressed solidification. In this situation the flow becomes unstable and channels continue to grow.

2. Using a three-phase mixed columnar-equiaxed solidification model to predict macrosegregation in a 2.45 ton steel ingot.

   - The general segregation pattern was predicted as: cone shape negative segregation in the bottom region, positive segregation in the top region, and some A-segregation bands near the wall. The predicted macrostructure and macro-segregation results agree qualitatively with the experimentally reported pattern, although the quantitative discrepancy between the calculations and the experimental results is still significant.

   - Sedimentation of equiaxed grains was found playing a very important role in the formation of global segregation in the big steel ingot. For the case of mixed columnar-equiaxed solidification, varying the equiaxed nucleation parameters changes the area of the lower conic negative segregation zone correspondingly, but the lower and upper limits of the global segregation index are only slightly influenced.

   - Quasi A-segregates in the middle radius region were predicted. Flow instability causes the formation of quasi A-segregates, but both the appearance of equiaxed crystals and their interaction with the growing columnar dendrites strengthen the segregates significantly. The equiaxed phase is not a necessary condition for the formation of quasi A-segregates because similar segregation bands with less severity are also found during pure columnar solidification.

   - The discontinuous negative-positive segregation under the hot top was predicted. This type of segregation is caused by the formation of a mini-ingot and by the subsequent sedimentation of equiaxed crystals within the mini-ingot.

- The calculated quantitative result of segregation is sensitive to the numerical grid resolution. A very fine grid is required to predict the details of quasi A-segregates. A grid-independent result regarding the fine details of quasi A-segregates in such ingots is not attainable based on current hardware resources. However, the general segregation pattern, e.g., the positive segregation extreme, negative segregation extreme, and their locations, can be obtained using a relatively coarse grid (10 mm).

3. A simplified dendritic model for the 2.45-ton steel ingot.

   - The general macrosegregation pattern predicted by the simplified dendritic model is the same as the one predicted by the non-dendritic model: a positive segregation zone in the top part, a cone shape negative segregation zone in the bottom region, and many quasi-A segregation bands in the middle radius region.

   - By considering the influence of dendritic structure, less serious negative segregation in the bottom region is predicted. The modeling result is closer to the experimental one, therefore it is more reasonable.

4. A four-phase model to combine the shrinkage cavity and macrosegregation.

   - The four-phase shrinkage model successfully predicated the shrinkage pipe in the top region which is similar to the experiment one.

   - The predicted macrosegregation distribution by the four-phase model is significantly different from the experiment one.

   - This four-phase model has still some deficiency. For example the calculation sometimes is unstable and even divergent. Much effort should be made to optimize this model in future.

5. Using a three-phase mixed columnar-equiaxed solidification model to calculate a 25-ton steel ingot.

   - A reasonable agreement with the experimental result was obtained regarding to the general macrosegregation pattern and the centerline segregation distribution.

   - Some discrepancy still existed. The negative segregation in the lower part is quantitative predicted more severely than the experimental result. The predicted

negative segregation region (below the hot top) shifted upwards referring to the experiment result, and the experimental measured maximum positive segregation was larger than the simulated one.

- In addition, since the grid that used in this calculation was not finer enough, the A-segregation bands failed to predict in this simulation.

5 References

[1] Report on the heterogeneity of steel ingots, J. Iron Steel Inst., London, 1926, vol.113, pp.39-151

[2] S.D.Felicelli, J.C. Heinrich and D. R. Poirier, Simulation of freckles during vertical solidification of binary alloys, Metall. Trans. B, 1991, vol. 22B, pp. 847-859

[3] C. Beckermann and R. Viskanta, Mathematical modeling of transport phenomena during alloy solidification, Appl. Mech. Rev., 1993, vol. 46, pp. 1-27

[4] I. Vannier, H. Combeau, G. Lesoult, Numerical model for prediction of the final segregation pattern of bearing steel ingot. Mater. Sci. Eng. 1993, vol. 173 A, pp. 317-321

[5] C. Y. Wang, C. Beckermann, Equiaxed dendritic solidification with convection: Part I. Multiscale/multiphase modeling. Metall. Mater. Trans. A, 1996, vol. 27 A, pp. 2754-2764

[6] J. P. Gu, C. Beckermann, Simulation of convection and macrosegregation in a large steel ingot. Metall. Mater. Trans. A, 1999, vol. 30(5), pp. 1357-1366

[7] E. Pickering, Macrosegregation in steel ingots: The applicability of modeling and characterization techniques, ISIJ International, 2013, Vol. 53, pp. 935-949

[8] A. Ludwig, M. Wu, Modelling of globular equiaxed solidification with two-phase approach, Metall. Mater. Trans. A, 2002, vol. 33, pp. 3673-3683

[9] M. Wu, A. Ludwig, A. Polaczek, M. Fehlbier, and P. Sahm, Influence of convection and grain movement on globular equiaxed solifification, Int. J. Heat Mass Transfer., 2003, vol. 46, pp. 2819-2832

[10] M. Wu, A. Ludwig, A three-phase model for mixed columnar equiaxed solidification, Metall. Mater. Trans. A, 2006, vol. 37A, pp. 1613-1631

[11] M. Wu, A. Ludwig, Using a three-phase deterministic model for the columnar-to-equiaxed transition, Metall. Mater. Trans. A, 2007, vol. 38A, pp. 1465-1475

[12] M. Bellet, H. Combeau, Y. Fautrelle, D. Gobin, M. Rady, E. Arquis, O. Budenkova, B. Dussoubs, Y. Duterrail, A. Kumar, C.A. Gandin, B. Goyeau, S. Mosbah, M.Zaloz˘nik, Call for contributions to a numerical benchmark problem for 2D columnar solidification of binary alloys, Int. J. Therm. Sci., 2009, vol. 48, pp. 2013-2016

[13] Y. Fautrelle, Solidification of metallic alloys under the influence of various types of Ac magnetic field, Keynote lecture, ASIAN EPM 2005, in: Second Asian Workshop on Electromagnetic Processing of Materials, May 22-25, 2005, Shenyang (RP Chine)

[14] W.D. Griffiths, D.G. McCartney, The effect of electromagnetic stirring during solidification on the structure of Al–Si, Materials Science & Engineering A, 1996, vol. 216, pp. 47–60

[15] S. D. Felicelli, D. R. Poirier, A. F. Giamei, and J. C. Heinrich, Simulating convection and macrosegregation in superalloys, TOM, vol., 1997, pp. 21-25

[16] J. A. Dantzig, M. Rappaz, Solidification, EPFL Press, 2011

[17] D. J. Hebditch and J. D. Hunt, Observations of ingot macrosegregation on model systems, Metall. Trans. Vol. 5, 1974, pp.1557-1563

[18] H. Fredriksson and S. O. Nilsson, On the formation of macrosegregations in ingots, Metall. Trans. B, 1978, vol. 9B, pp. 111-120

[19] S.N. Tewari and R. Shah, Macrosegregation during Steady-State Arrayed Growth of Dendrites in Directionally Solidified Pb-Sn Alloys, Metall. Trans. A, 1992, vol. 23A, pp. 3383-3392.

[20] S.N. Tewari and R. Shah, Macrosegregation during dendritic arrayed growth of hypoeutectic Pb-Sn alloys: influence of primary arm spacing and mushy zone length, Metall. Meter. Trans. A, 1996, vol. 27A, pp. 1353-1362

[21] J. Spinellia, O. Rochab, A. Garciaa, The influence of melt convection on dendritic spacing of downward unsteady-State directionally solidified Sn-Pb alloys, Mater. Research, 2006, vol. 9, pp. 51-57.

[22] X. Wang and Y. Fautrelle, An investigation of the influence of natural convection on tin solidification using a quasi two-dimensional experimental benchmark, Int. J. Heat Mass Tran., 2009, vol. 52, pp. 5624-5633.

[23] T. Fujii, D. R. Poirier, and M. C. Flemings, Macrosegregation in a multicomponent low alloy steel, Metall. Trans. B, 1779, vol. 10B, pp.331-339.

[24] M. Rappaz and M. Rettenmayr, Simulation of solidification, Curr. Opin. Solid. St. M., 1998, vol. 3, pp. 275-282.

[25] M. D. Mat, O. J. Ilegbusi, Application of a hybrid model of mushy zone to macrosegregation in alloy solidification, Int. J. Heat Mass Tran., vol. 45, 2002, pp. 279-289

[26] P. B. Melou, B. Goyeau, M. Quintard, F. Fichot, D. Gobin, Average momentum equation for interdendritic flow in a solidifying columnar mushy zone, Int. J. Heat Mass Tran., 2002, vol. 45, pp. 3651-3665

[27] M.C. Flemings and G.E. Nereo, Macrosegregation: Part I, Trans. Met. Soc.AIME, 1967, vol. 239, pp. 1449-1461

[28] M.C. Flemings, R. Mehrabian, and G. E. Nereo, Macrosegregation: Part II, Trans. Met. Soc. AIME, 1968, vol. 242, pp. 41-49

[29] M.C. Flemings and G. E. Nereo, Macrosegregation: Part III, Trans. Met. Soc. AIME, 1968, vol. 242, pp. 50-56

[30] M. C. Flemings, Solidification Modeling, Past and Present, in 'Modeling of casting, welding and advanced solidification processes VIII', (ed. B. G. Thomas and C. Beckermann), 1998, pp. 1-13, Warrendale, PA, TMS

[31] S. D. Ridder, S. Kou, and R. Mehrabian, Effect of fluid flow on macrosegregation in axi-symmetric ingots, Metall. Trans. B, 1981, vol. 12B, pp.435-447.

[32] C. Beckermann, Modelling of macrosegregation: applications and future needs, Int. Mater. Rev., 2002, vol. 47 (5), pp. 243-261

[33] K. Nakajima, H. Zhang, K. Oikawa, M. Ohno and P. G. Jösson, Methodological progress for computer simulation of solidification and casting, ISIJ International, 2010, vol. 50 (12), pp. 1724-1734

[34] K. Suzuki and T. Miyamoto, Study on the formation of A segregation in steel ingot, Trans. Iron Steel Inst. Jpn, 1978, vol. 18, pp. 80-89

[35] J. A. Van Den Avyle, J. A. Brooks, A. C. Powell, Reducing defects in remelting processes for high-performance alloys, JOM, 1998, vol. 50, pp. 22-25

[36] M. B. Shafii, E. A. Dehkordi, M. E. Moghadam and M. M. Koochesfahani, Using nucleatiors to control freckles in unidirectional solidification, Exp.Therm. Fluid Sci., 2009, vol.33, pp. 1209–1215

[37] P. Auburtin, S. L. Cockroft, A. Mitchell, Liquid density inversions during the solidification of superalloys and their relationship to freckle formation in castings, in: J. Beech, H. Jones (Eds.), Solidification Processing 1997, The university of Sheffield, 1997, pp. 336-340

[38] K. Suzuki, K. Taniguchi, Mechanism of reducing A segregation in steel ingots, Trans. Iron Steel Inst. Jpn.1981, vol. 21, pp. 235-242

[39] K. Suzuki and T. Miyamoto, Influence of alloying elements on the formation of A segregation in steel ingot, Trans. Iron Steel Inst. Jpn, 1980, vol. 20, pp. 375-383

[40] J. J. Moore and N. A. Shah, Mechanisms of formation of A- and V-segregation in cast steel, Int. Mater. Rev., vol.28, 1983, pp. 338-356.

[41] E. Marburg, Accelerated solidification in ingots: its influence on ingot soundness, Trans. AIME, 1953, vol. 5, pp. 157-172

[42] A. F. Giamei and B. H. Kear, On the nature of freckles in nickel base superalloys, Metall. Mater. Trans. B, 1970, vol. 1, pp. 2185-2192

[43] M. I. Bergman, D.R. Fearn, J. Bloxham, M.C. Shannon, Convection and channel formation in solidifying Pb-Sn alloys, Metall. Mater. Trans. A, 1997, vol. 28A, pp. 859-866

[44] R. Mehrabian, M. Keane and M. C. Flemings, Interdendritic fluid flow and macrosegregation; influence of gravity, Metall. Trans. 1970, vol. 1, pp. 1209-1220

[45] R. J. McDonald and J. D. Hunt, Fluid motion through the partially solid regions of a casting and its importance in understanding A type segregation, Trans. Metall. Soc. AIME, 1969, vol. 245, pp. 1993-1997

[46] R. J. McDonald and J. D. Hunt, Convective fluid motion within the interdendritic liquid of a casting, Metall. Trans. 1970, vol. 1, pp. 1787-1788

[47] W.D. Bennon and F.P. Incropera, The evolution of macrosegregation in statically cast binary ingots, Metall. Trans. B, 1987, vol. 18B, pp. 611-616

[48] J.R. Sarazin and A. Hellawell, Channel formation in Pb-Sn, Pb-Sb, and Pb-Sn-Sb alloy ingots and comparison with the system NH4Cl-H2O, Metall. Trans. A, 1988, vol. 19A, pp. 1861-1871

[49] A.K. Sample and A. Hellawell, The mechanisms of formation and prevention of channel segregation during alloy solidification, Metall. Trans. A, 1984, vol. 15A, pp. 2163-2173

[50] A. C. Fowler, The formation of freckles in binary alloys, IMA Journal of Applied Mathematics, 1985, vol. 35, pp. 159-174

[51] M. Simpson, M. Yerebakan, and M.C. Flemings, Influence of dendrite network defects on channel segregate growth, Metall. Trans. A, 1985, vol. 16A, pp. 1687-1689

[52] J.C. Heinrich, S.D. Felicelli and D. R. Poirier, Vertical Solidification of Dendritic Binary Alloys, Comp. Meth. Appl. Mech. Eng., 1991, vol. 89, pp. 435-461

[53] H. Shahani, G. Amberg, and H. Fredriksson, On the formation of macrosegregation in unidirectionally solidified Sn-Pb and Pb-Sn alloys, Metall. Trans. A, 1992, vol. 23A, pp.2301-2311

[54] S.M. Copley, A.F. Giamei, S.M. Johnson, and M.F. Hornbecker, The original of freckles in unidirectionally solidified castings, Metall. Trans., 1970, vol. 1, pp. 2193-2204.

[55] P.K. Sung, D.R. Poirier, and S.D. Felicelli, Simulating the initiation of a channel during directional solidification of a superalloy, Metall. Mater. Trans. A, 2001, vol. 32A, pp. 202-207

[56] N. Mori and K. Ogi, Study on formation of channel-type segregation, Metall. Trans. A, 1991, vol 22A, pp. 1663-1672

[57] G. Quillet, A. Ciobanas, P. Lehmann, Y. Fautrelle, A benchmark solidification experiment on an Sn-10%wtBi alloy, Int. J. Heat Mass Tran., 2007, vol. 50, pp. 654-666

[58] L. Hachani, B. Saadi, X.Wang, A. Nouri, K. Zaidat, A. Bouzida, L. Derouiche, G. Raimondi, and Y. Fautrelle, Experimental analysis of the solidification of Sn-3 wt.% Pb alloy under natural convection, Int. J. Heat Mass Tran., 2012, vol. 55, pp. 1986-1996

[59] S. Peppin, H. Huppert, and M. Worster, Steady-state solidification of aqueous ammonium chloride, J. Fluid Mech., 2008, vol. 599, pp. 465-476

[60] B. Murray, A.Wheeler, and M. Glicksman, Simulations of experimentally observed dendritic growth behavior using a phase-field model, J. Cryst. Growth, 1996, vol. 154, pp. 386-400

[61] M. Zhang and T. Maxworthy, J. Fluid Mech., Experimental investigation of parallel shear flow, 2002, vol. 470, pp. 247-268

[62] C. F. Chen, Experimental study of convection in a mushy layer during directional solidification, J. Fluid Mech., 1995, vol. 293, pp. 81-98

[63] S. Boden, S. Eckert, B. Willers, and G. Gerbeth, X-Ray Radioscopic Visualization of the Solutal Convection during Solidification of a Ga-30 wt Pct In Alloy, Metall. Meter. TRANS. A, 2008, vol. 39A, pp. 613-623

[64] S. Boden, S. Eckert , G. Gerbeth, Visualization of freckle formation induced by forced melt convection in solidifying Ga-In alloys, Meter. Letters, 2010, vol. 64, pp. 1340-1343

[65] N. Shevchenko, S. Boden, S. Eckert and G. Gerbeth, Observation of segregation freckle formation under the influence of melt convection, IOP Conf. Series: Materials Science and Engineering 27, 2011. 012085

[66] N. Shevchenko, S. Eckert, S. Boden and G. Gerbeth, In situ X-ray monitoring of convection effects on segregation freckle formation, IOP Conf. Series: Materials Science and Engineering 33, 2012, 012035

[67] R. F. Katz and M. G. Worster, Simulation of directional solidification, thermochemical convection, and chimney formation in a Hele-Shaw cell, J. Comput. Phys., 2008, vol. 227, pp. 9823-9840

[68] P. Roux, B. Goyeau, D. Gobin, F. Fichot, M. Quintard, Chemical non-equilibrium modeling of columnar solidification, Int. J. Heat Mass Tran., 2006, vol.49, pp.4496-4510

[69] A. Kumar, B. Dussoubs, M. Založnik and H. Combeau, Effect of discretization of permeability term and mesh size on macro- and meso-segregation predictions, J. Phys. D: Appl. Phys., 2009, vol. 42, 105503

[70] D. Liu, B. Sang, X. Kang, and D. Li, Effect of Alloy Insert on Channel Segregation During Solidification of Sn-10 wt pct Bi Alloy, Metall. Mater. Trans. B, 2011, vol. 42B, pp.210-223

[71] W. Li, H. Shen and B. Liu, A response to numerical benchmark for solidification of binary alloys: macro-segregation with thermosolutal convection, China Foundry, 2012, vol. 9, pp. 171-177

[72] N. Ahmad, H. Combeau, J. L. Desbiolles, T. Jalanti, G. Lesoult, J. Rappaz, M. Rappaz and C. Stomp, Numerical simulation of macrosegregation: a comparison between finite volume method and finite element method predictions and a confrontation with experiments, Metall. Mater. Trans. A, 1998, vol. 29A, pp. 617-630

[73] H. Huang and D. R. Poirier, Computer simulation of directional solidification of binary alloy calculated under personal computer platform, Tamkang Journal of Science and Engineering, 2009. vol. 12 (3), pp. 239-248

[74] W. Liu, C. Xie, M. Bellet and H. Combeau, 2-dimensional FEM modeling of macrosegregation in the directional solidification with mesh adaptation, Acta Metall. Sin. (Engl. Lett.), 2009, vol. 22, pp. 233-240

[75] M. Založnik, A. Kumar, H. Combeau, An operator splitting scheme for coupling macroscopic transport and grain growth in a two-phase multiscale solidification model: Part II – Application of the model, Comp. Mater. Sci., 2010, vol.48, pp. 11-21

[76] A. Kumar, M. Založnik, H. Combeau, Study of the influence of mushy zone permeability laws on macro- and meso-segregations predictions, Int. J. Therm. Sci., 2012, vol. 54, pp. 33-47

[77] T. Sawada, K. Oikawa, and K. Anzai, Three-Dimensional simulation of channel segregation in lateral directional solidification, Steelsim 2009, Leoben Austria

[78] T. Sawada, K. Oikawa, and K. Anzai, Simplified three-dimensional macrosegregation simulation model and its application to directional solidification of Sn-Bi alloys, in: Modeling of casting, welding, and advanced solidification process-XII, ed. S. L. Cockcroft and D. M. Maijer, 2009, pp. 303-310

[79] S.D. Felicelli, D. R. Poirier, and J.C. Heinrich, Modeling Freckle Formation in Three Dimensions during Solidification of Multicomponent Alloys, Metall. Mater. Trans. B, 1998, vol. 29B, pp. 847-855

[80] S. D. Felicelli, J.C. Heinrich, D.R. Poirier, Three-dimensional simulations of freckles in binary alloys, J. Cryst. Growth, 1998, vol. 191, pp. 879-888

[81] J. Guo and C. Beckermann, Three-dimensional simulation of freckle formation during binary alloy solidification: effect of mesh spacing, Numer. Heat Tr. A-appl, 2003, vol. 44, pp. 559-576

[82] M. Medina, Y. D. Terrail, F. Durand, and Y. Fautrelle, Channel segregation during solidification and the effects of an alternating traveling magnetic Field, Metall. Mater. Trans. B, 2004, vol. 35B, pp. 743-754

[83] Y. Ebisu, A numerical method of macrosegregation using a dendritic solidification model, and its applications to directional solidification via the use of magnetic fields, Metall. Mater. Trans. B, 2011, vol. 42B, pp.341-369

[84] G. Quillet, A. Ciobanas, P. Lehmann and Y. Fautrelle, Meso-Segregations during Solidification in a Binary Alloy under the Influence of Convection, in: International Scientific Colloquium Modelling for Electromagnetic Processing Hannover, March 24-26, 2003, pp. 171-176

[85] T. M. Pollock and W. H. Murphy, The breakdown of single-crystal solidification in High refractory Nickel-Base Alloys, Metall. Mater. Trans. A, 1996, vol. 27A, pp. 1081-1094

[86] H. Yamada, T. Sakurai, T. Takemonchi and K. Suzuki, in Proc. Annual Meeting of AIME, Dallas, Tex., 1982, vol. A82-30, pp. 1-6

[87] S. Kou, D.R. Poirier, and M.C. Flemings, Macrosegregation in rotated remelted ingots, Metall. Trans. B, 1978, vol. 9B, pp. 711-719

[88] P. Auburtin, T. Wang, S. Cockcroft and A. Mitchell, Freckle formation and freckle criterion in superalloy castings, Metallurgical and Materials Transactions B, 2000, vol. 31, pp. 801-811

[89] M. G. Worster, Convection in mushy layers, Annual Review of Fluid Mechanics, 1997, vol. 29, pp. 91-122

[90] C. Beckermann, J. P. Gu, and W. J. Boettinger, Development of a freckle predictor via Rayleigh number method for single-crystal Nickel-base superalloy, Metall. Mater. Trans. A, 2000, vol.31, pp. 2545-2557

[91] J. C. Ramirez, C. Beckermann, Evaluation of a Rayleigh-number-based freckle criterion for Pb-Sn alloys and Ni-base superalloys, Metall. Mater. Trans. A, 2003, vol. 34A, pp. 1525-1536

[92] L. Yuan, P. D. Lee, A new mechanism for freckle initiation based on microstructural level simulation, Acta Mater. , 2012, vol. 60, pp. 4917-4926

[93] M.C. Flemings, Solidification processing, Metall. Trans., 1974, vol. 5, pp. 2121-2134

[94] M. C. Flemings, Principles of control of soundness and homogeneity of large ingots, Scand. J.Met., 1976, vol. 5, pp. 1-15

[95] B. M. Larsen, A review of factors underlying segregation in steel ingots, Trans. AIME, 1945, vol 162, pp. 414-437

[96] B. Gray, The effects of gravity in the solidification of steel, J. Iron Steel Inst., 1956, vol 182, pp. 366-374

[97] A. Olsson, R. West and H. Fredriksson, Macrosegregation in ingots, Scand. J. Metall., 1986, vol. 15, pp. 104-112

[98] A. Hultgren, A and V segregation in killed steel ingots, Scand. J. Metall., 1973, vol. 2, pp. 217-227

[99] L. H. Nelson, Solidification of steel in ingot molds, Trans. ASM, 1934, vol.22, pp. 193-226

[100] H. Combeau, A. Kumar, and M. Zalonik, Modeling of equiaxed grain evolution and macrosegregations development in steel ingots, Transactions Indian Institute of Metals, 2009, vol. 62, pp. 285-290

[101] H. Combeau, M. Zaloznik, S. Hans, and P. Richy, Prediction of macrosegregation in steel ingot: influence of the motion and the morphology of equiaxed grains, Metall. Mater. Trans. B, 2009, vol. 40B, pp.289-304

[102] J. R. Blank and F. B. Pickering, Effect of solidification in large ingots on segregation of non-metallic inclusions, in: The solidification of metals, 1968, London, the iron and steel institute, pp. 370-37

[103] H. Yamada, T. Takenouchi, T. Takahashi, M. Funazaki, T. Iwadate, and S. Nakada, Influence of alloying elements on the segregation of high purity CrMoV steel, Iron Steel Inst. Jap. Int. , 1995, vol. 35, pp. 686-692

[104] J. Wang, P. Fu, H. Liu, D. Li and Y. Li, Shrinkage porosity criteria and optimized design of a 100-ton 30Cr2Ni4MoV forging ingot, Mater. Design, 2012, vol. 35, pp. 446-456

[105] M. C. Schneider and C. Beckermann, Formation of macrosegregation by multicomponent thermosolutal convection during the solidification of steel, Metall. Mater. Trans. A, 1995, vol. 26A, pp. 2373-2388

[106] D. Liu, D. Li, and B. Sang, Numerical simulation of macrosegregation for an Fe-0.8 wt% C alloy, J. Mater. Sci. Technol., 2009, vol. 25, pp. 561-568

[107] D. Liu, X. Kang, P. Fu, and D. Li, Modeling of macrosegregation in steel ingot: influence of mold shape and melt superheat, Kovove Mater., 2011, vol. 49, pp. 143-153

[108] D. Liu, X. Kang, B. Sang, and D. Li, Numerical study of macrosegregation formation of ingot cast in normal sand mold and water-cooled sand mold, Acta Metall. Sin. (Engl. Lett.), 2011, vol. 24, pp. 54-64

[109] D. Liu, B. Sang, X. Kang, and D. Li, Numerical simulation of macrosegregation in large multiconcentration poured steel ingot, Int. J. Cast Met. Res., 2010, vol. 23, pp. 354-363

[110] A. Kumar, M. Zaloznik, and H. Combeau, Prediction of equiaxed grain structure and macrosegregation in an industrial steel ingot: comparison with experiment, Int. J. Adv. Eng. Sci. Appl. Math., 2010, vol. 2, pp.140-148

[111] H. Combeau, A. Kumar, M. Zaloznik, I. Poitrault, G. Lacagne, A. Gingell, T. Mazet, and G. Lesoult, Macrosegregation prediction in a 65 ton steel ingot, in: 1st international conference on ingot casting, rolling and forging, 2012, Brüssel-Saal

[112] A. Ishmurzin, Modelling and simulation of solidification of high grade steel ingot castings, Doctoral Thesis, Montanuniversität Leoben, Leoben, Austria, 2009

[113] G. Couturier and M. Rappaz, Effect of volatile elements on porosity formation in solidifying alloy, Modelling Simul. Mater. Sci. Eng., 2006, vol. 14, pp. 253-271

[114] R. P. Taylor, J. T. Berry and R. A. Overfelt, A critical evaluation of criteria function for use with shaped-casting modeling, MCWASP VIII, ed. B. Thomas, C. Beckermann, warrendale, PA, 1998, pp. 1055-1062.

[115] Y. K. Ko, V. Sahai, J. T. Berry, and R. A. Overfelt, Prediction of porosity in cast equiaxed alloy 718, MCWASP VII, ed. M. Cross, J. Campbell, Warendale, PA, 1995, pp. 731-738

[116] E. Niyama, T. Uchida, M. Morikawa and S. Saito, A method of shrinkage prediction and its application to steel casting practice, AFS Int. Cast Met. Res. J., 1982, pp. 52-63

[117] T. S. Piwonka and M. C. Flemings, Pore formation in solidification, Trans. AIME, 1966, vol. 236, pp. 1157-1165

[118] D. R. Poirier, K. Yeum, and A. L. Mapples, A thermodynamic prediction for microporosity formation in Aluminum-rich Al-Cu alloy, Metall. Trans. A, 1987, vol. 18A, pp. 1979-1987

[119] K. D. Carlson, Z. Lin, C. Beckermann, G. Mazurkevich, and M. C. Schneider, Modeling of porosity formation in aluminum alloys, in: MCWASP XI, eds C. Gandin and M. Bellet, 2006, pp. 627-634

[120] K. Kubo and R. D. Pehlke, Mathematical modeling of porosity formation in solidification, Metall. Trans. B, 1985, vol. 16B, pp. 359-366

[121] J. Huang and J. G. Conley, Simulation of microporosity formation in modified and unmodified A356 alloy castings, Metall. Mater. Trans. B, 1998, vol. 29B, pp. 1249-1260

[122] L. Nastac, Computational fluid dynamics modeling of macrosegregation and shrinkage in large-diameter steel roll castings, Metall. Mater. Trans. B, 2011, vol. 42B, pp.1231-1243

[123] S. Bounds, G. Moran, K. Pericleous, M. Cross and T.N. Croft, A computational model for defect prediction in shape castings based on the interaction of free surface flow, heat transfer and solidification phenomena, Metall. Mater. Trans. B, 2000, vol. 31B, pp. 515-526

[124] P. D. Lee and J. D. Hunt, Hydrogen porosity in directionally solidified aluminium-copper alloys: A mathematical model, Acta Mater., 2001, vol. 49, pp. 1383-1398

[125] K. Carlson, Z. Lin, R. Hardin and C. Beckermann, Modeling of porosity formation and feeding flow in steel casting, in: Proceeding of the 56 th SFSA technical and operating conference, Chicago, IL, 2002, pp.4.4

[126] K. D. Carlson, Z. Lin, C. Beckermann, G. Mazurkevich, and M. C. Schneider, Simulation of porosity formation in aluminum casting, in: MCWASP XI, eds Q. Wang, M. J. M. Krane, and P. D. Lee, 2006, pp. 133-142

[127] P. D. Lee, A. Chirazi and D. See, Modeling microporosity in aluminum-silicon alloys: a review, J. Light Metals, 2001, vol. 1, pp. 15-30

[128] A. Kuznetsov and K. Vafai, Development and investigation of three-phase model of the mushy zone for analysis of porosity formation in solidifying castings, Int. J. Heat Mass Tran., 1995, vol. 38, pp. 2557-2567

[129] A. S. Sabau, S. Viswanathan, Microporosity prediction in aluminum alloy castings, Metall. Mater. Trans. B, vol. 2002, 33B, pp. 243-255

[130] Ch. Pequet, M. Gremaud, and M. Rappaz, Modeling of microporosity, macroporosity, and pipe-shrinkage formation during the solidification of alloys using a mushy zone refinement method: applications to aluminum alloys, Metall. Mater. Trans., 2002, vol. 33A, pp. 2095-2106

[131] G. Couturier, J. Desbiolles, and M. Rappaz, A porosity model for multi-gas systems in multi-component alloys, in: MCWASP XI, eds. C. Gandin and M. Bellet, 2006, pp. 619-626

[132] G. Couturier and M. Rappaz, Modeling of porosity formation in multicomponent alloys in the presence of several dissolved gases and volatile solute elements, in: Simulation of aluminum shape casting processing: From alloy design to mechanical properties, edited by Q. Wang, M. J. Krane, and P. D. Lee, 2006

[133] T. Wang, M. Wu, A. Ludwig, M. Abondano, B. Pustal and A. Polaczek, Modelling the thermosolutal convection, shrinkage flow and grain movement of globular equiaxed solidification using a three phase model, Int. J. Cast Met. Res., 2005, vol. 18, pp. 221-228

[134] C. Beckermann, and R. Viskanta, Double-Diffusive Convection during Dendritic Solidification of a Binary Mixture, PhysicoChemical Hydrodynamics, 1988, vol.10, pp. 195-213

[135] C. Beckerman, C. Y. Wang, Incorporating Interfacial Phenomena in Solidification Models, JOM, 1994, vol. 46 (1), pp. 42-47

[136] C. Beckermann, C. Y. Wang, Equiaxed dendritic solidification with convection: Part III Comparisons with NH4CL-H2O experiments, Metall. Mater. Trams. A, 27A, 1996, pp. 2784-2795

[137] J. Ni, F. P. Incropera, Extension of the continuum model for transport phenomena occurring during metal alloy solidification-I. The conservation equations, Int. J. Heat Mass Transfer, 1995, vol. 38, pp. 1271-1284

[138] A. Ludwig, M. Pretzler, F. Mayer, A. Ishmurizin, M. Wu, A way of coupling ternary phase diagram information with multiphase solidification simulatins, Mater. Sci. Eng. A, 2005, vol. 413-414, pp. 485-489

[139] M. Wu, L. Könözsy, A. Ludwig, W. Schützenhöfer, and R. Tanzer, On the formation of macrosegregations in steel ingot castings, Steel research int., 2008, vol. 79, pp. 56-63

[140] L. Könözsy, A. Ishmurzin, F. Mayer, M. Grasser, M. Wu, A. Ludwig, Numerical Investigation of Grid Influence on the Formation of Macrosegregation, Int. J. Cast Metals Research, 2009, vol. 22, pp.175-178

[141] M. Wu and A. Ludwig, Modeling equiaxed solidification with melt convection and grain sedimentation-I: Model description, Acta Materialia, 2009, vol. 57, pp. 5621-5631

[142] M. Wu and A. Ludwig, Modeling equiaxed solidification with melt convection and grain sedimentation-II: Model verification, Acta Materialia, 2009, vol. 57, pp. 5632-5644

[143] M. Wu, A. Fjeld, and A. Ludwig, Modelling mixed columnar-equiaxed solidification with melt convection and grain sedimentation – Part I: Model description, Comp. Mater. Sci., 2010, vol. 50, pp. 32-42

[144] M. Wu, A. Fjeld, and A. Ludwig, Modelling mixed columnar-equiaxed solidification with melt convection and grain sedimentation – Part II: Illustative modeling results and parameter studies, Comp. Mater. Sci., 2010, vol. 50, pp. 43-58

[145] F. Mayer, M. Wu, A. Ludwig, On the formation of centerline segregation in continuous slab casting of steel due to bulging and/or feeding, steel, research int., 2010, vol . 81, pp. 660-667

[146] L. Könözsy, A. Ishmurzin, M. Grasser, M. Wu, A. Ludwig, R. Tanzer, W. Schützenhöfer, Columnar to equiaxed transition during ingot casting using ternary alloy composition, Mater. Sci. Forum, 2010, vol. 649, pp.349-354

[147] M. Wu, J. Domitner, and A. Ludwig, Using a two-phase columnar solidification model to study the principle of mechanical soft reduction in slab casting, Metall. Mater. Trans. A, 2012, vol. 43, pp. 945-964

[148] M. Ahmadein, M. Wu, J. H. Li, P. Schumacher, A. Ludwig, Prediction of the As-Cast Structure of Al-4.0 wt Pct Cu Ingots, Metall. Mater. Trans. A, 2013

[149] A. Ludwig, M. Grasser, M. Wu, A. Kuhn, J. Riedle, About the Formation of Macrosegregations During Continuous Casting of Sn-Bronze, Int. J. Fluid Dynamics Mater. Proc., 2006, vol. 1, pp. 285-300

[150] A. Ludwig, M. Wu, Modelling the columnar-to-equiaxed transition with a 3-phase Eulerian approach, Mater. Sci. Eng. A, 2005, vol. 413-414, pp. 109-114

[151] J. Li, M. Wu, J. Hao, A. Ludwig, Simulation of channel segregation using a two-phase columnar solidification model – Part I: Model description and verification, Comp. Mater. Sci., 2012, vol. 55, pp. 407-418

[152] J. Li, M. Wu, J. Hao, A. Ludwig, Simulation of channel segregation using a two-phase columnar solidification model – Part II: Mechanism and parameter study, Comp. Mater. Sci., 2012, vol. 55, pp. 419-429

[153] R.B. Bird, W.E. Steward, E.N. Lightfoot, Transport Phenomena, John Wiley & Sons, New York, 1960

[154] V. Felice, K. Tveito, M. Založnik, H. Combeau, and M. Hamdi, Three-dimensional study of macro- and mesosegregation formation in a rectangular cavity cooled from one vertical side, in MCWASP XIII, Schladmin, 2012, IOP Conf. Series: Materials Science and Engineering, 2012, vol. 33, 012088

[155] J. D. Hunt, Steady State Columnar and Equiaxed Growth of Dendrites and Eutectic, Mater. Sci. Eng., 1984, vol. 65, pp. 75-83

[156] C. Wang, S. Ahuja, C. Beckermann, and H. Groh, Multiparticle interfacial drag in equiaxed solidification, Metall. Mater. Trans. B, 1995, vol. 26B, pp. 111-119

[157] G. Neale, N. Epstein, and W. Nader, Creeping flow relative to permeable spheres, Chem, Eng. Sci., 1973, vol. 28, pp.1865-1874

[158] M. Ishii and N. Zuber, Drag coefficient and relative velocity in bubble droplet or particulate flows, AIChE J., 1979, vol. 25, pp. 843-855

[159] J. Li, M. Wu, A. Ludwig, A. and Kharicha, Modelling macrosegregation in a 2.45 ton steel ingot, in: MCWASP XIII, Schladming, Austria, 17-22 June (2012), Eds.: A. Ludwig, M. Wu, A. Kharicha, IOP Conf. Series: Mater. Sci. Eng. 33 (2012) 012091

6 Publications

6.1 Publications attached to this thesis

I. Simulation of channel segregation using a two-phase columnar solidification model – Part I: Model description and verification

J. Li, M. Wu, J. Hao, A. Ludwig

Comp. Mater. Sci. 55 (2012) 407-418

II. Simulation of channel segregation using a two-phase columnar solidification model – Part II: Mechanism and parameter study

J. Li, M. Wu, J. Hao, A. Ludwig

Comp. Mater. Sci. 55 (2012) 419-429.

III. Study of the channel segregation using a two-phase columnar solidification model

J. Li, M. Wu, J. Hao and A. Ludwig

In: The 3rd International Conference on Advances in Solidification Processes, IOP Conf. Series: Materials Science and Engineering 27 (2011) 012055 doi:10.1088/1757-899X/27/1/012055

IV. Simulation of macrosegregation in a 2.45-ton steel ingot using a three-phase mixed columnar-equiaxed model

J. Li, M. Wu, A. Ludwig, and A. Kharicha

Int. J. Heat Mass Transfer, under revision, June 2013

V. Modelling macrosegregation in a 2.45 ton steel ingot

J. Li, M. Wu, A. Ludwig and A. Kharicha

in: MCWASP XIII, Schladming, Austria, 17-22 June (2012), Eds.: A. Ludwig, M. Wu, A. Kharicha, IOP Conf. Series: Mater. Sci. Eng. 33 (2012) 012091

VI. Multiphase modelling of the macrosegregation in ingot castings

M. Wu, J. Li, A. Kharicha, and A. Ludwig

ICRF-2012 (1st Int. Conf. on Ingot Casting, Rolling and Forging), Aachen, Germany 3-7 June (2012) CD-ROM proc., 1-10.

6.2 Publications not attached to this thesis

VII. Modeling diffusion-governed solidification of ternary alloys – Part 1: Coupling solidification kinetics with thermodynamics

M. Wu, J. Li, A. Ludwig, and A. Kharicha

Comp. Mater. Sci. In Press http://dx.doi.org/10.1016/j.commatsci.2013.05.015.

VIII. Using a three-phase mixed columnar equiaxed solidification modelt o study macrosegregation in ingot casting: perspective and limitations

M. Wu, J. Li, A. Kharicha, A. Ludwig,

In LMPC(Liquid Metal Processing and Casting Conference) sep. 22-25, 2013, Austin, Texas, USA, Manuscript has been accepted for publication in a TMS proceedings, pp: 1-10.

Publication I

Simulation of channel segregation using a two-phase columnar solidification model

Part I: Model description and verification

Jun Li, Menghuai Wu, Jing Hao and Andreas Ludwig

Computational Materials Science

Volume 55, 2012, pp. 407-418

Simulation of channel segregation using a two-phase columnar solidification model

Part I: Model description and verification

J. Li[1,2], M. Wu[1,2*], J. Hao[1] and A. Ludwig[1]

[1]Simulation and Modeling of Metallurgical Processes, Dept. of Metallurgy, Univ. of Leoben,

[2]Christian Doppler Lab for Advanced Simulation of Solidification and Melting, Dept. of Metallurgy, Univ. of Leoben, A-8700 Leoben, Austria

∗ Corresponding author: menghuai.wu@unileoben.ac.at

Tel: 0043-3842-4023103; Fax: 0043-3842-4023102

Abstract

A numerical investigation on the formation of channel segregation using a two-phase columnar solidification model is presented in this two-part paper. Part I includes a model summary and model verification and Part II presents an in-depth discussion and parameter study on the formation mechanisms of channel segregation. The two phases considered in the model are the liquid melt and solid columnar phase. The morphology of the columnar dendrite trunks is approximated by step-wise growing cylinders with constant primary dendrite arm spacing. The columnar dendrites grow from the mold wall following the liquidus isotherm. The growth kinetics of the columnar trunks is governed by diffusion of the rejected solute surrounding the columnar trunks near the solid-liquid interface. The

conservation equations for mass, momentum, species and enthalpy are solved for each phase. The permeability of the two-phase mushy zone is treated with the Blake-Kozeny approach. The model is applied in 2D and 3D simulations of segregation in a Sn-10 wt.% Pb benchmark ingot, as defined by Bellet et al. [1]. The 3D calculations show channel segregation patterns of predominantly discontinuous lamellar structure with a few rod-like channels. A series of 3D simulations with increasing thickness clarify that, with thickness greater than 0.05 m, the influence of the front and back mold walls on the center plane segregation becomes negligible. Thus, the segregation pattern on the center plane in the 3D case can be sufficiently reproduced by computationally inexpensive 2D calculations. Verification was made by comparison with published models and experimental results.

Key words: macrosegregation; channel; columnar solidification; multiphase flow.

1 Introduction

Channel segregation is one of the most frequently observed segregation patterns in large steel ingots, vacuum-arc remelting or electro-slag remelting ingots [2-3] and similar castings. These segregation defects are often referred to as ‘A’ segregate [4-5] or lamellar- or plume-structured segregate [6-7] in large steel ingots and ‘freckles’ [8-9] in vertically solidified castings.

In the last decades numerous experimental studies in the area of solidification have contributed to the understanding of channel segregation formation [10-12]. Mcdonald and Hunt [10-11] built an ammonium chloride water system to study the effect of growth conditions and convection on ‘A’ segregate, and were the first to observe that the formation of ‘A’ segregate was directly caused by the extensive fluid motion in the interdendritic region. Sarazin and Hellawell [12] studied channel segregation in three alloy systems (binary Pb-Sn and Pb-Sb, and ternary Pb-Sn-Sb) during unidirectional solidification in base-chilled ingots and found that the channels originate from flow perturbations, which can be characterized with the Rayleigh number.

Numerical models [13-14] have also significantly contributed to the understanding of macrosegregation, complimenting experimental investigations and providing a view into these opaque flow systems. Shahani et al. [15] studied the effect of natural convection on the formation of macrosegregation in the case of unidirectional solidification of Sn-Pb and

Pb-Sn alloys. Their final simulation results indicated a pattern of channel segregates, but their simulations did not provide insight into how channels are formed. Schneider and Beckermann [16] studied the combined effects of microsegregation, mushy zone permeability, thermosolutal convection and contraction flow on macrosegregation during solidification of a Pb-20 wt.% Sn alloy and found that a higher mushy zone permeability causes longer and more vertically oriented channels, while a lower permeability causes shorter and more horizontally oriented channels. Further studies proposed numerical methods and models [14, 17-19] to simulate macrosegregation of Pb-Sn alloy systems based on the benchmark of Hebditch and Hunt [20]. To date most numerical investigations of channel segregates have been limited to 2D, with only a few computational attempts made on full 3D geometries [18].

The formation of channel segregates is a multiphase and multiscale problem suitably treated with a simplified version of the authors' mixed columnar-equiaxed solidification model [21-22]. In the current paper the presence of equiaxed crystals is neglected. This volume-average model stems from the pioneering work in the field of multiphase solidification by Beckermann el al. [23-25]. Macrosegregation in a Sn-10 wt.% Pb benchmark ingot, as described by Bellet et al. [1], is simulated in 3D and 2D. Comparisons between the model geometries are made along with a grid-sensitivity study to ensure calculation accuracy. Model verification is discussed in comparison with modeling and experimental results available in the literature.

2 Model description

A brief outline of the two-phase columnar solidification model is given here; additional model details can be found in a previous publication [26]. Conservation equations, sources and exchange terms, and auxiliary equations are summarized in Table 1. The main assumptions of the model include:

1) The two phases in the model are the liquid melt and the solid columnar dendrite trunks.

2) The morphology of the columnar dendrite trunks is approximated by step-wise growing cylinders positioned in a staggered arrangement with constant primary dendritic arm spacing, λ_1.

3) The columnar trunks grow from the casting surface when constitutional undercooling is met and solidification follows the liquidus isotherm.

4) The liquid-to-solid mass transfer (solidification/melting) rate, $M_{\ell s}$, is calculated as a function of the growth velocity of the columnar trunks, v_{R_c}, which is governed by diffusion of the solute in the interdendritic melt around each cylindrical trunk.

5) Volume-averaged concentrations (c_ℓ, c_s) are calculated and macrosegregation is characterized by the mixture concentration, c_{mix}. Thermodynamic equilibrium is assumed at the liquid-solid interface, which dictates the liquid-solid interface concentrations (c_ℓ^*, c_s^*). Back diffusion in the solid is neglected ($D_s = 0$). The concentration difference ($c_\ell^* - c_\ell$) is the driving force for the growth of columnar trunks [21].

6) A linearized binary Sn-Pb phase diagram with a constant solute redistribution coefficient *k* and a constant liquidus slope *m* is used.

7) Interdendritic flow resistance in the mushy zone is calculated via a permeability law according to the Blake-Kozeny approach [27].

8) Solidification shrinkage is not accounted for and thermosolutal convection is modeled with the Boussinesq approach.

The current model differs from some previous models [13-19, 23-25]. Firstly, The energy conservation is treated in two-phase form, implying that the temperatures of the solid and liquid are locally different, but an 'infinite' volumetric heat transfer between the two phases ($H^* = 10^9$ $Wm^{-2}K^{-1}$) is applied to level out the temperature difference. An alternative method to treat the energy conservation is to use a mixture form of energy equation [14, 18-19]. The advantage of the two-phase form over the mixture form is that more freedoms are provided for handling the interphase enthalpy exchange, release of latent heat, and boundary conditions. The drawback of the two-phase form is that the calculation cost is relatively high.

Secondly, the meaning of the momentum exchange due to solidification-induced mass transfer, $\vec{U}_{\ell s}^{M}$, is different from the one as defined in the literature [23, 25, 28], where $\vec{U}_{\ell s}^{M}$ was the momentum flux across the solid-interface due to the solidification-induced

expansion/shrinkage (ignorable when the density difference between the liquid and solid phases is small). In the current model $\vec{U}_{\ell s}^{M}$ is calculated by the mass transfer rate ($M_{\ell s}$) timing an interphase velocity ($\vec{u}_{\ell-s}$) [29]. In the case of solidification, the interphase velocity $\vec{u}_{\ell-s}$ is equal to $\vec{u}_{\ell}$. As schematically shown in Fig. 1, when the melt flows passing by a stationary growing columnar trunk (cylinder), a non-slip boundary condition applies at the liquid-solid interface, and far-field velocity of the melt is $\vec{u}_{\ell}$ (intrinsic velocity). A flow boundary layer adjacent to the columnar trunk is developed. It is further assumed that the velocity profile in the boundary layer moves in the parallel direction to the growth of the columnar trunk. In a time interval of *dt*, the volume-averaged mass transfer due to solidification is $M_{\ell s} \cdot dt$. The corresponding momentum loss in the adjacent melt is $M_{\ell s} \cdot dt \cdot \vec{u}_{\ell}$. Therefore, the momentum transfer rate due to phase change $\vec{U}_{\ell s}^{M}$ is equal to $M_{\ell s} \cdot \vec{u}_{\ell}$. In the case of melting, $\vec{u}_{\ell-s}$ =0.

Table 1. Conservation equations, sources and exchange terms, auxiliary equation.

Conservation equations

Mass:

$$\frac{\partial}{\partial t}(f_{\ell}\rho_{\ell}) + \nabla \cdot (f_{\ell}\rho_{\ell}\vec{u}_{\ell}) = -M_{\ell s} \tag{1}$$

$$\frac{\partial}{\partial t}(f_{s}\rho_{s}) = M_{\ell s}$$

Momentum:

$$\frac{\partial}{\partial t}(f_{\ell}\rho_{\ell}\vec{u}_{\ell}) + \nabla \cdot (f_{\ell}\rho_{\ell}\vec{u}_{\ell} \otimes \vec{u}_{\ell}) = -f_{\ell}\nabla p + \nabla \cdot \bar{\bar{\tau}}_{\ell} + f_{\ell}\rho_{\ell}\vec{g} - \vec{U}_{\ell s}^{M} - \vec{U}_{\ell s}^{D} \tag{2}$$

where $\bar{\bar{\tau}}_{\ell} = \mu_{\ell}\left(\nabla \cdot (f_{\ell}\vec{u}_{\ell}) + (\nabla \cdot (f_{\ell}\vec{u}_{\ell}))^{T}\right)$

Species:

$$\frac{\partial}{\partial t}\left(f_{\ell}\rho_{\ell}c_{\ell}\right) + \nabla \cdot \left(f_{\ell}\rho_{\ell}\vec{u}_{\ell}c_{\ell}\right) = -C_{\ell s}^{M} \tag{3}$$

$$\frac{\partial}{\partial t}\left(f_{s}\rho_{s}c_{s}\right) = C_{\ell s}^{M}$$

Enthalpy:

$$\frac{\partial}{\partial t}\left(f_{\ell}\rho_{\ell}h_{\ell}\right) + \nabla \cdot \left(f_{\ell}\rho_{\ell}\vec{u}_{\ell}h_{\ell}\right) = \nabla \cdot (f_{\ell}k_{\ell}\nabla \cdot T_{\ell}) + Q_{\ell}^{M} - Q_{\ell s}^{D} \tag{4}$$

$$\frac{\partial}{\partial t}\left(f_{s}\rho_{s}h_{s}\right) = \nabla \cdot (f_{s}k_{s}\nabla \cdot T_{s}) + Q_{s}^{M} + Q_{\ell s}^{D}$$

where $h_\ell = \int_{T_{\text{ref}}}^{T_\ell} c_{\text{p}}^{\ell} dT + h_\ell^{\text{ref}}$ and $h_{\text{s}} = \int_{T_{\text{ref}}}^{T_{\text{s}}} c_{\text{p}}^{\text{s}} dT + h_{\text{s}}^{\text{ref}}$

Solidification net mass transfer

Mass transfer: $M_{\ell \text{s}} = v_{R_{\text{c}}} \cdot S_{\text{A}} \cdot \rho_{\text{s}} \cdot \Phi_{\text{imp}}$ (5)

Col. trunk growth velocity: $v_{R_{\text{c}}} = \frac{dR_{\text{c}}}{dt} = \frac{D_\ell}{R_{\text{c}}} \cdot \frac{\left(c_\ell^* - c_\ell\right)}{\left(c_\ell^* - c_{\text{s}}^*\right)} \cdot \ln^{-1}\left(\frac{R_{\text{f}}}{R_{\text{c}}}\right)$ (6)

Diameter of col. trunks: $d_{\text{c}} (= 2R_{\text{c}}) = \lambda_1 \cdot \sqrt{\frac{\sqrt{12} \cdot f_{\text{s}}}{\pi}}$ (7)

Far field radius of col. trunks: $R_{\text{f}} = \frac{1}{\sqrt{3}} \cdot \lambda_1$ (8)

Col. surface concentration: $S_{\text{A}} = \frac{2 \cdot d_{\text{c}} \cdot \pi}{\sqrt{3} \cdot \lambda_1^2}$ (9)

Growing surface impingement: $\Phi_{\text{imp}} = \begin{cases} 1 & d_{\text{c}} \le \lambda_1 \\ 2\sqrt{3} \cdot f_\ell / \left(2\sqrt{3} - \pi\right) & d_{\text{c}} > \lambda_1 \end{cases}$ (10)

Source and exchange terms

Momentum transfer: $\vec{U}_{\ell \text{s}}^{\text{M}} = \begin{cases} \vec{u}_\ell \cdot M_{\ell \text{s}} & \text{solidification} \\ 0.0 & \text{melting} \end{cases}$ $\vec{U}_{\ell \text{s}}^{\text{D}} = \frac{f_\ell^2 \cdot \mu_\ell}{K} \cdot (\vec{u}_\ell - \vec{u}_{\text{s}})$ (11)

where $K = \lambda_2^2 \cdot \frac{f_\ell^3}{180 \cdot (1 - f_\ell)^2}$

Species transfer: $C_{\ell \text{s}}^{\text{M}} = \begin{cases} k \cdot c_\ell^* \cdot M_{\ell \text{s}} & \text{solidification} \\ c_{\text{s}} \cdot M_{\ell \text{s}} & \text{melting} \end{cases}$ (12)

Enthalpy transfer and latent heat: $Q_\ell^{\text{M}} = \left(\Delta h_{\text{f}} \cdot f_\ell - h_\ell\right) \cdot M_{\ell \text{s}}$ $Q_{\ell \text{s}}^{\text{D}} = H^* \cdot (T_\ell - T_{\text{s}})$ (13)

$Q_{\text{s}}^{\text{M}} = \left(\Delta h_{\text{f}} \cdot f_{\text{s}} + h_{\text{s}}\right) \cdot M_{\ell \text{s}}$ where $H^* = 10^9$ $\text{Wm}^{-2}\text{K}^{-1}$

Auxiliary equation

Mixture concentration: $c_{\text{mix}} = \left(c_\ell \cdot \rho_\ell \cdot f_\ell + c_{\text{s}} \cdot \rho_{\text{s}} \cdot f_{\text{s}}\right) / \left(\rho_\ell \cdot f_\ell + \rho_{\text{s}} \cdot f_{\text{s}}\right)$ (14)

Additionally, the mass and species exchanges between the liquid and solid phases are modelled in a different way as the previous models [23, 25, 28]. Species balance in an

'isolated' volume element enveloped by a fictitious cylinder with a radius of R_f is schematically shown in Fig. 2. Each part of species transfer (due to solute partitioning at the solid-liquid interface, diffusion in the liquid region) is expressed with symbols ***A*** to ***F***. For the simplicity of the discussion, no flow is considered, hence the species must be conserved: $d\left(f_\ell \rho_\ell c_\ell + f_s \rho_s c_s\right)/dt = 0$, i.e.

$$\boldsymbol{A} + \rho_s c_s^* \frac{df_s}{dt} - \boldsymbol{B} + \boldsymbol{F} - \rho_\ell c_\ell^* \frac{df_s}{dt} + \boldsymbol{D} = 0. \tag{15}$$

As $\boldsymbol{A} = \boldsymbol{B}$ and $\boldsymbol{E} = \boldsymbol{D} + \boldsymbol{F}$, then

$$\boldsymbol{E} = \rho_\ell \left(c_\ell^* - c_s^*\right) \frac{df_s}{dt}. \tag{16}$$

Replace ***E*** and $\frac{df_s}{dt}$ in Eq. (16) with the expressions in Fig. 2, we have

$$\rho_\ell S_A D_\ell \frac{\left(c_\ell^* - c_\ell\right)}{R_c} \ln^{-1}\left(\frac{R_f}{R_c}\right) = \rho_\ell \left(c_\ell^* - c_s^*\right) \cdot v_{R_c} \cdot S_A. \tag{17}$$

The formulations for the columnar trunk growth velocity (Eq. (6)) and the solidification net mass transfer rate (Eq. (5)) are obtained. It is clear that the growth of the columnar trunk is governed by diffusion of species around the growing columnar trunk. This diffusion happens only in the melt region.

The interfacial net species transfer due to solidification is: $C_{\ell s}^M = M_{\ell s} \cdot c_s^*$. No additional diffusive species transfer is necessarily considered, as there is no net species flux across the

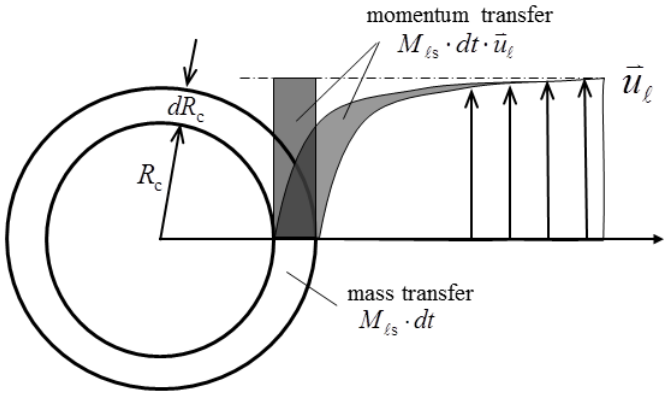

Figure 1: Schematic of the velocity profile adjacent to a growing columnar trunk and momentum transfer due to solidification mass transfer.

liquid-solid interface without solidification. For remelting, the interfacial net species transfer is modelled according to Beckermann and co-author [25]: $C_{\ell s}^{M} = M_{\ell s} \cdot c_s$.

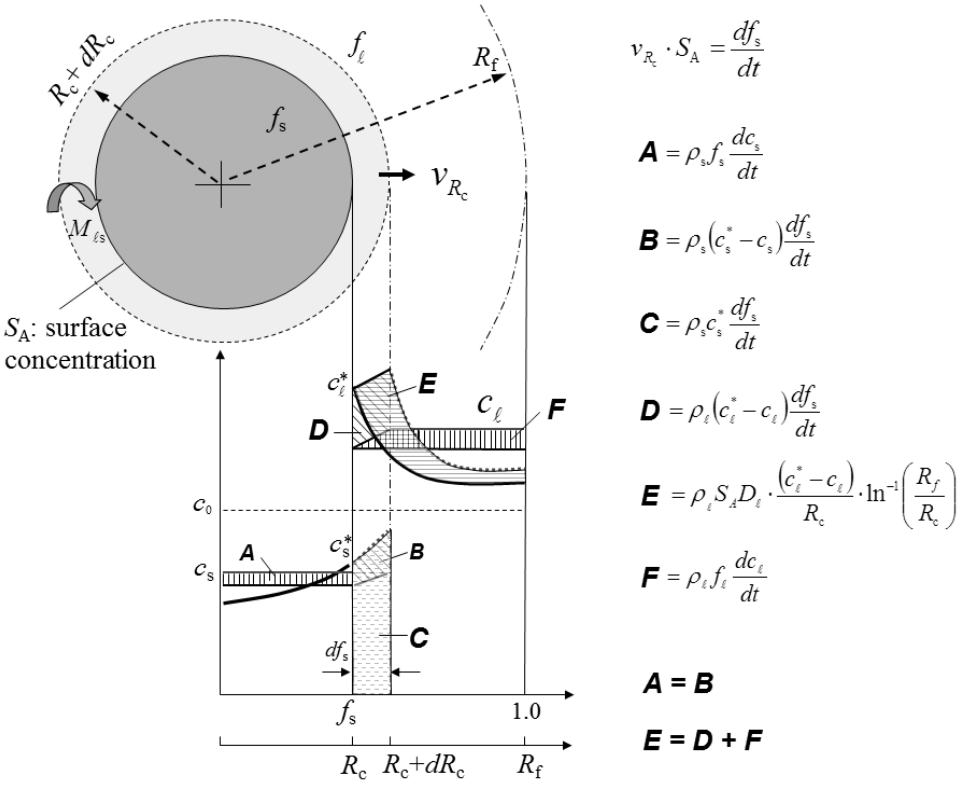

Figure 2: Schematic of interfacial mass and species transfer. Species conservation is considered in an 'isolated' volume element enveloped by a fictitious cylinder with a radius of R_f.

The conservation equations in Table 1 are numerically solved using FLUENT* 6.3.26 [29], which uses a control-volume finite difference numerical method. All phases share a single pressure field, p, which is solved via a pressure correction equation obtained from the sum of the normalized mass continuity equations using the phase coupled SIMPLE (PC-SIMPLE) algorithm. For each time-step, up to 60 iterations are necessary to reach solution convergence as determined by a decrease of the normalized residuals of f_ℓ and $\vec{u}_\ell$ below 10^{-4}, of c_ℓ and c_s below 10^{-5}, and of h_ℓ and h_s below 10^{-7}. Choice of a time step that ensures a high accuracy solution must be determined empirically by test simulations. In this study all calculations are run with a time-step of 0.0005 s. All simulations are run in parallel on 8 CPUs (Intel Nehalem Cluster 2.93 GHz), with simulation times close to three months for the 3D case and 7-15 days for the 2D cases, depending on mesh size.

3 Benchmark configuration

Benchmark simulations are carried out for one 2D and two 3D configurations. A sketch of the 2D benchmark configuration described by Bellet et al. [1] is shown in Fig. 3, labeled with boundary and initial conditions. Due to the geometric and heat extraction symmetry of the Bellet ingot, half of the ingot is modeled and a symmetry boundary condition is defined at the left boundary. The 3D geometries have the same cross-sectional dimensions as shown in Fig. 1 with a thickness of 0.03 in one case and 0.05 in the second case. The casting alloy is Sn-10 wt.% Pb. In the 2D model heat is extracted from one vertical wall and a symmetry boundary condition is imposed at the centerline. At time $t = 0$, the mold is filled with melt at uniform temperature and composition. The mold walls have a constant temperature, T_{EXT}, and a constant heat transfer coefficient, h, is applied between the casting and the mold. The 3D simulations have the same boundary conditions as the 2D case with non-slip front and back walls treated with a convective cooling boundary condition where $h = 50$ W m^{-2} K^{-1} and $T_{EXT} = 298$ K. The calculation was run to the end of solidification at ca. 490 s. Thermo-physical properties, boundary conditions and numerical parameters are given in Table 2.

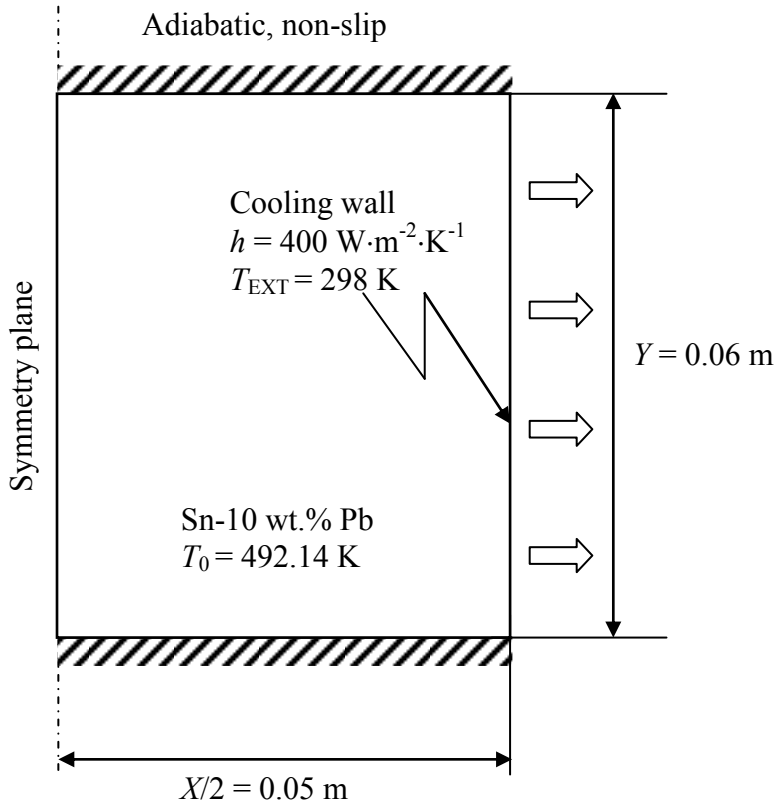

Figure 3: Benchmark geometry with boundary and initial conditions.

Table2. Thermo-physical properties and model parameters.

Property	Symbol	Units	Quantity
Nominal concentration	c_0	wt.% Pb	10.0
Melting point at $c = 0$	T_m	K	505
Eutectic composition	c_e	wt.% Pb	38.1
Eutectic temperature	T_e	K	456
Liquidus slope	m	K (wt.%)$^{-1}$	-1.286
Equilibrium partition coefficient	k	-	0.0656
Reference density	ρ_{ref}	kg·m^3	7000
Specific heat	c_p^{ℓ}, c_p^s	J kg^{-1} K^{-1}	260
Thermal conductivity	k_{ℓ}, k_s	W m^{-1} K^{-1}	55.0
Latent heat	Δh_f	J kg^{-1}	6.1×10^4
Viscosity	μ_{ℓ}	Kg m^{-1} s^{-1}	1.0×10^{-3}
Liquid thermal expansion coefficient	β_T	K^{-1}	6.0×10^{-5}
Liquid solutal expansion coefficient	β_C	wt.%$^{-1}$	-5.3×10^{-3}
Primary dendritic arm spacing	λ_1	m	1.3×10^{-3}
Second dendritic arm spacing†	λ_2	M	3.25 (or 4.55) $\times 10^{-4}$
Diffusion coefficient (liquid)	D_{ℓ}	m^2 s^{-1}	1.0×10^{-8}
Initial temperature	T_0	K	492.14
Heat transfer coefficient	h	W m^{-2} K^{-1}	400
External temperature	T_{EXT}	K	298
Dimension of the 2D cavity	$X \times Y$	m	0.1×0.06
Grid size*		m	0.25 (or 0.5, 1, 2) $\times 10^{-3}$

*Parameters varied in parameter study.

4 Simulation results

4.1 Evolution of 3D channels

Transient simulation results for the 3D benchmark with 0.03 m thickness at 100 s are shown in Fig. 4. In Fig. 4(a), melt velocity vectors are shown in two planes (a vertical plane and a horizontal plane with a distance of 0.01 m from the bottom) and liquid volume fraction isolines are shown in the vertical plane. In Fig. 4(b), c_{mix} isolines, flow streamlines, and the Pb solute mixture concentration, c_{mix}, are shown.

As seen in Fig. 4(a), when the liquid fraction is larger than 0.4, the flow is relatively strong while in the region where the liquid fraction is less than 0.3 velocities are negligible, less than 0.0003 m s^{-1}. The low velocity regions correlate with the dendritic mushy zone where the liquid fraction is smaller than 0.3. For the alloy Sn-10 wt.% Pb, the interdendritic melt, enriched with Pb, has a higher density than the bulk melt, and both the thermal and solute buoyancy forces lead to a downward flow along the solidification front. This forms a large clockwise circulation in the domain, as the streamlines in Fig. 4(b) show. In the right bottom region of the vertical plane, the flow channels which have formed can be seen. As the channels form, the flow (streamlines) is significantly diverted. This diversion is a result of the relatively higher volume fraction of liquid (and thus higher permeability) within a channel in comparison to the channel-wall region. The interdendritic melt will preferentially take its path along the channel, and the streamlines are periodically diverted from one channel, through the channel walls, to the neighboring channels.

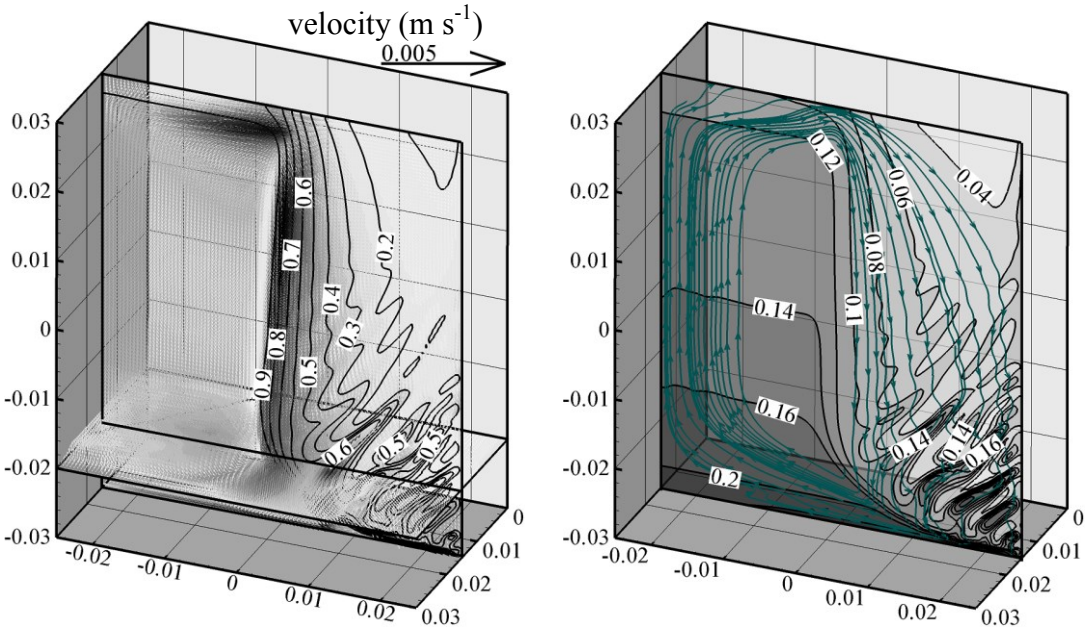

(a) velocity & liquid fraction (b) c_{mix} & streamlines

Figure 4: Transient 3D simulation results at 100 s are shown: (a) velocity vectors in two planes (a vertical plane and a horizontal plane 0.01 m from bottom) and liquid volume fraction isolines with labeled values in the vertical center plane; (b) in the vertical plane, c_{mix} in gray scale (dark for the highest and light for the lowest value), c_{mix} isolines labeled with corresponding values, and streamlines of the melt flow.

Figs. 5 (a)-(f) show snapshots of the evolution of solidification at t = 30, 50, 100, 150, 200 and 400 s for the 3D benchmark with 0.03 m thickness. In each frame the liquid fraction distributions are shown in a vertical center plane and horizontal plane as in Fig. 2(a). Isosurfaces (yellow) of liquid volume fraction (f_ℓ = 0.35) are also shown to demonstrate the evolution of the flow channels. The regions bounded by the isosurfaces, where f_ℓ is larger than 0.35, represent the flow channels. At 30 s the channels have formed in the right bottom region adjacent to the chill wall, but they are not well pronounced. At 50 s, the number of channels near the chilled wall region has grown and a portion of these are already fully developed. After 200 s the channels become relatively stable and fixed, with very little additional growth. The channels are generally 3D in nature, most of them are lamellar-structured, discontinuous, while a few of them are rod-like. They occur only in the right bottom region, which is roughly a quarter of the whole calculation domain. The

channel spacing (distance between neighboring channels) is nearly constant, varying slightly over time during solidification.

The sequence of global solidification snapshots in Fig. 5 show that in the upper part of the ingot the solidification front, approximated with the isosurface of f_ℓ = 0.35, sweeps across the domain much faster than in the bottom region. This is caused by the downward flow in the mushy zone, which transports the Pb-rich interdendritic melt from the upper to the lower region; hence the liquidus temperature decreases in the lower region. As a consequence, the solidification rate in the lower region is retarded.

The macrosegregation profile of the solidified ingot in the vertical center plane is shown in Fig. 6. Negative segregation, with c_{mix} as small as 0.04, is predicted in the upper-right region and positive segregation, with c_{mix} as large as 0.32, is predicted in the lower-left region. The channel segregation pattern is clearly shown in the lower right region. The pattern of the segregates (inclined angle, channel spacing, number of the channels) corresponds to the flow patterns that develop during solidification (Fig. 5).

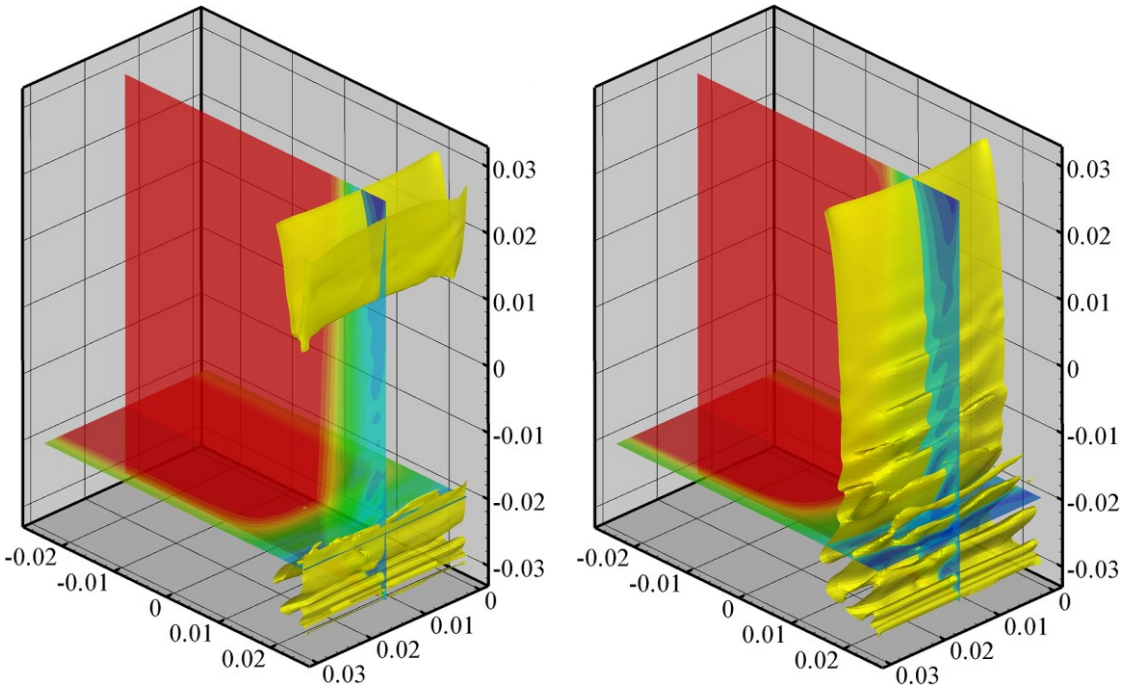

(a) 30 s (b) 50 s

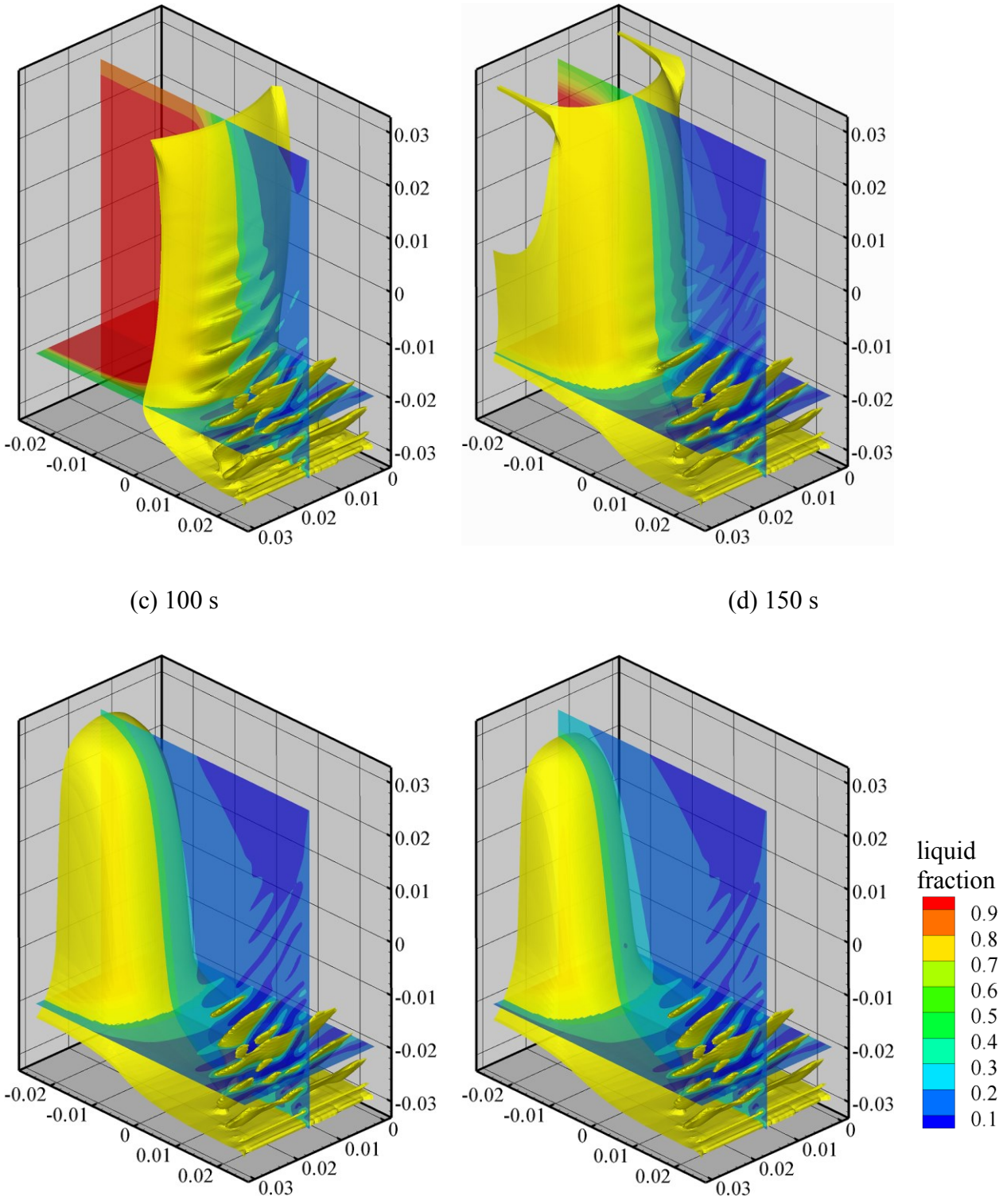

(c) 100 s (d) 150 s

(e) 200 s (f) 400 s

Figure 5: Evolution of solidification in the 3D benchmark with 0.03 m thickness at (a) 30 s, (b) 50 s, (c) 100 s, (d) 150 s, (e) 200 s, and (f) 400 s. The liquid volume fraction in two planes (a vertical center plane and a horizontal plane with 0.01 m from bottom) is shown in color scale. The isosurfaces (yellow) of liquid volume fraction (f_ℓ = 0.35) are also shown to demonstrate the evolution of the flow channels.

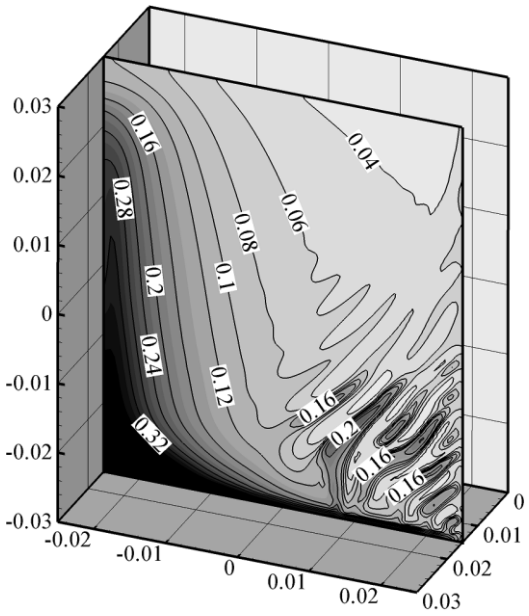

Figure 6: Distribution of the Pb mixture concentration, c_{mix}, at the end of solidification is shown in gray scale (dark for the highest and light for the lowest value) along with labeled c_{mix} isolines.

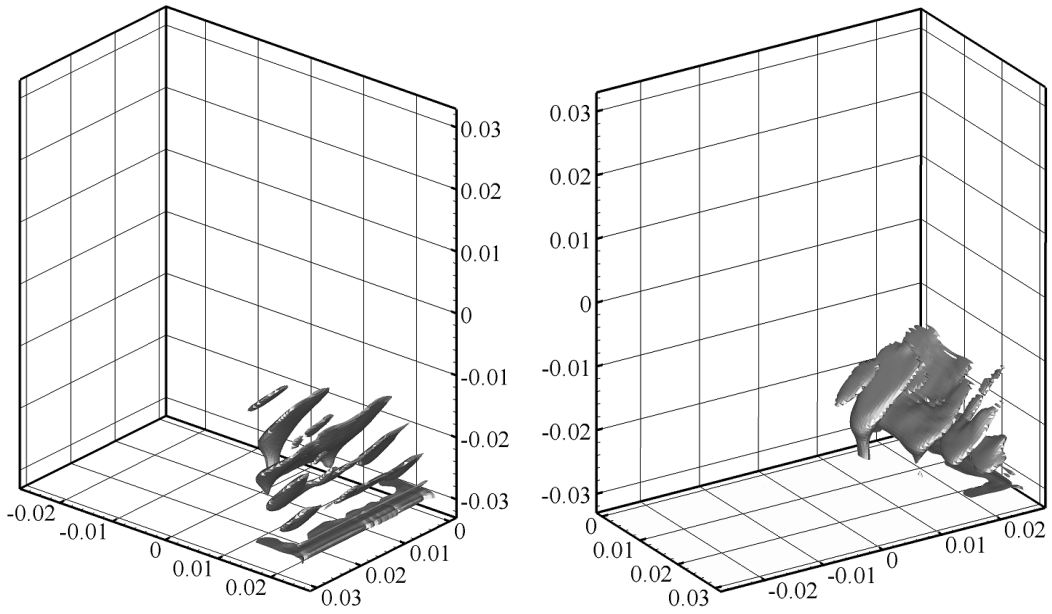

Figure 7: The isosurface of Pb segregation ratio, as defined by $(c_{mix} - c_0)/c_0 = 1.5$ from two viewing angles.

Fig. 7 shows the final channel segregation pattern in 3D from two angles. The isosurface of segregation ratio, as defined by $(c_{mix} - c_0)/c_0 = 1.5$, is displayed. The channel segregates are predominately lamellar-structured with some rod-like morphology, which is in agreement

with 3D channel segregation previously described in the literature [6-7]. In the current benchmark, the channel segregation pattern is observed only in the lower right region and shows an upward slanting pattern with an angle of 40-60 degree from the horizontal plane. The average thickness of the channels is 0.002 m, the channel spacing is 0.004 m and the length of the largest channel is approximately 0.019 m.

4.2 Comparison of 3D and 2D calculations

Transient results at 200 s for the 3D and 2D benchmark cases are compared in Fig. 8. Fig. 8(a) shows the c_{mix} distribution in the center plane of the 3D benchmark with 0.03 m thickness and Fig. 8(b) presents the corresponding 2D c_{mix} distribution. The 3D and 2D calculations predict similar channel segregation patterns, however, the severity of the macrosegregation of these two cases is significantly different. For example, the maximum Pb concentration in the lower left region of the 3D benchmark is 0.32, much higher than the maximum Pb concentration of 0.24 in the same region of the 2D case. This difference is called the 3D effect. The front and back walls of the 3D benchmark with finite thickness of 0.03 m have significant influence on the internal flow intensity, hence on the transport of segregated solute elements. To show the diminishing 3D effect as casting thickness increases, a corresponding 3D benchmark with a thickness of 0.05 m was simulated, and is shown in Fig. 8(c). It is found that with a casting thickness of 0.05 m the c_{mix} distribution in the center plane (Fig. 8(c)) is almost identical to the 2D result (Fig. 8(b)), with respect to both the channel segregation pattern and the severity of the macrosegregation. Fig. 9 compares the 2D and 3D c_{mix} distribution profiles along three paths as marked in Fig. 8(b). The difference in distribution between the 2D and the 3D with thickness of 0.03 m is significant. However, the difference between the 2D and the 3D with thickness of 0.05 m is minor. The 3D effect decreases for the benchmark with larger thickness, i.e. the segregation pattern on the center plane of the 3D case can be reproduced by a 2D calculation. Based on this conclusion, the analysis and discussion in the following sections are based on 2D simulations.

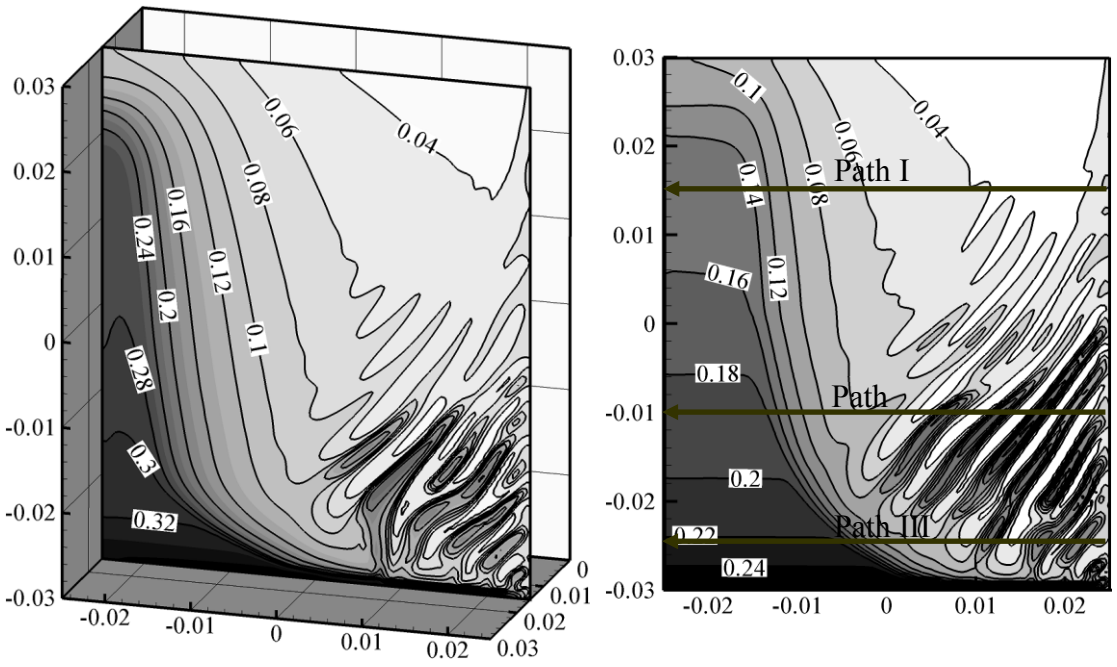

(a) (b)

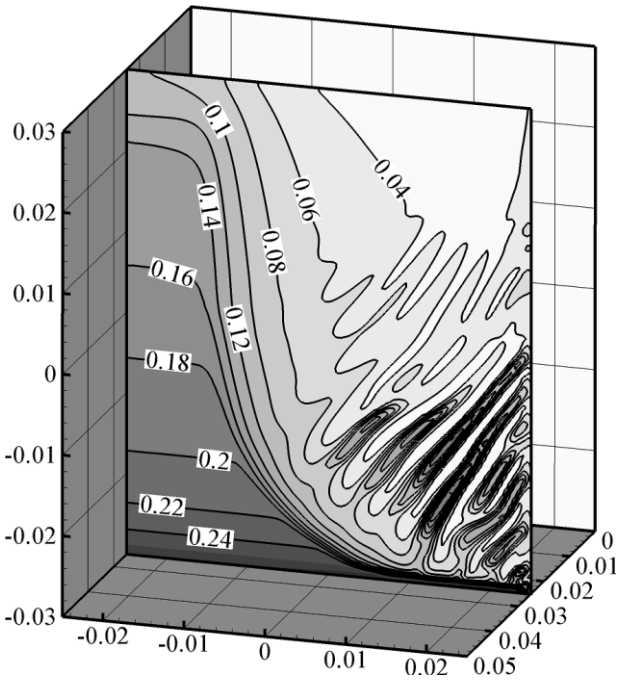

(c)

Figure 8: Comparison of c_{mix} at t = 200 s for (a) center plane of 3D benchmark with thickness of 0.03 m; (b) 2D benchmark; and (c) center plane of 3D benchmark with thickness of 0.05 m. c_{mix} is shown in gray scale (dark for the highest and light for the lowest value) with labeled c_{mix} isolines.

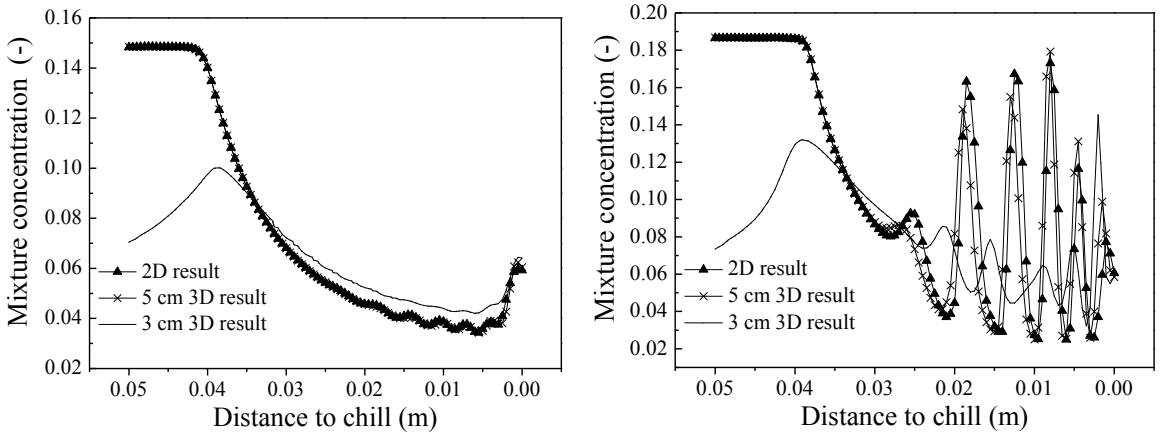

(a) (b)

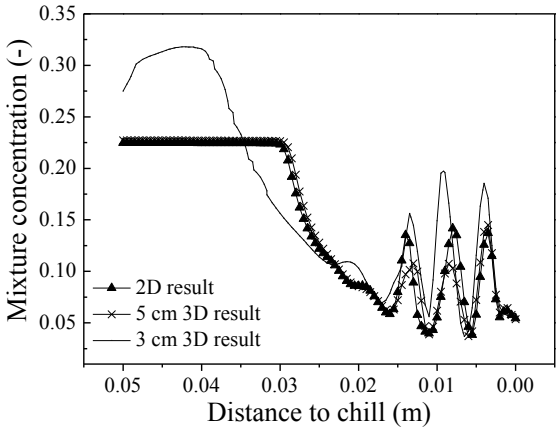

(c)

Figure 9: Comparison of c_{mix} distributions of the 2D and 3D cases along paths I to III as marked in Fig. 8(b). (a) Path I, on the center plane, 0.045 m from the bottom; (b) Path II, in the center plane, 0.02 m from the bottom; (c) Path III, in the center plane, 0.005 m from the bottom.

5 Verifications

5.1 Grid sensitivity

A grid study was carried out on four grids with cell sizes of 0.25, 0.5, 1 and 2 mm respectively. For this study the secondary dendrite arm spacing (3.25×10^{-4} m) and other

physical and process parameters are kept constant. Fig. 10 shows the liquid fraction and Fig. 11 the Pb solute mixture concentration, c_{mix}, at 200 s for each grid size. The temperature isotherms are nearly identical for all cases, thus the grid with 2 mm cell size is fine enough to resolve the temperature field. The liquid volume fraction and segregation patterns are more sensitive to cell size, especially in the lower right corner region where the channel segregates appear. Firstly, the coarse grid calculation has only one to two channels close to the lower right corner, while the fine grid calculation has more channels in a broader region near the lower right corner. The trend shows that simulations with finer grids predict more channels. Additionally, as cell size decreases the size of the channel and the channel spacing (distance between the neighboring channels) become smaller and the length of the channels becomes longer.

When the cell size is smaller than 0.5 mm, the difference in segregation pattern from case to case is not as great as cases with grid size larger than 0.5 mm--a significant finding of the current study. To further quantify the influence of grid size on the segregation pattern, the estimated average channel length and channel spacing as a function of mesh size are compared in Fig. 12. The channel spacing decreases with grid refinement, while the average length of the channel increases. It is noted that there is only a slight difference in channel size between the 0.5 mm grid and 0.25 mm grid. The average channel length appears to be approaching a constant of 20.5 mm, and the average channel spacing is approaching a constant of 6 mm.

Fig. 13 shows the influence of mesh size on the c_{mix} distribution profile along the path IV as marked in Fig. 11(a). The c_{mix} curves for each grid coincide in the no-channel region, i.e. at 0.025 m or further from the chilled surface. In the region with channel segregates, close to the chilled surface, the c_{mix} curves differ, particularly when the grid size is larger than 0.5 mm. However, the difference between the c_{mix} curves of the fine grids (e.g. 0.25 and 0.5 mm) is quite small. According to Kumar et al [14], the grid should be fine enough to resolve the flow through the channel, i.e. at least 3 grid points (volume elements) should be located in each channel. As shown in Fig. 13, there are 6 grid points in each channel for the case of grid resolution of 0.5 mm, and 12 grid points in each channel for the case of grid resolution of 0.25 mm.

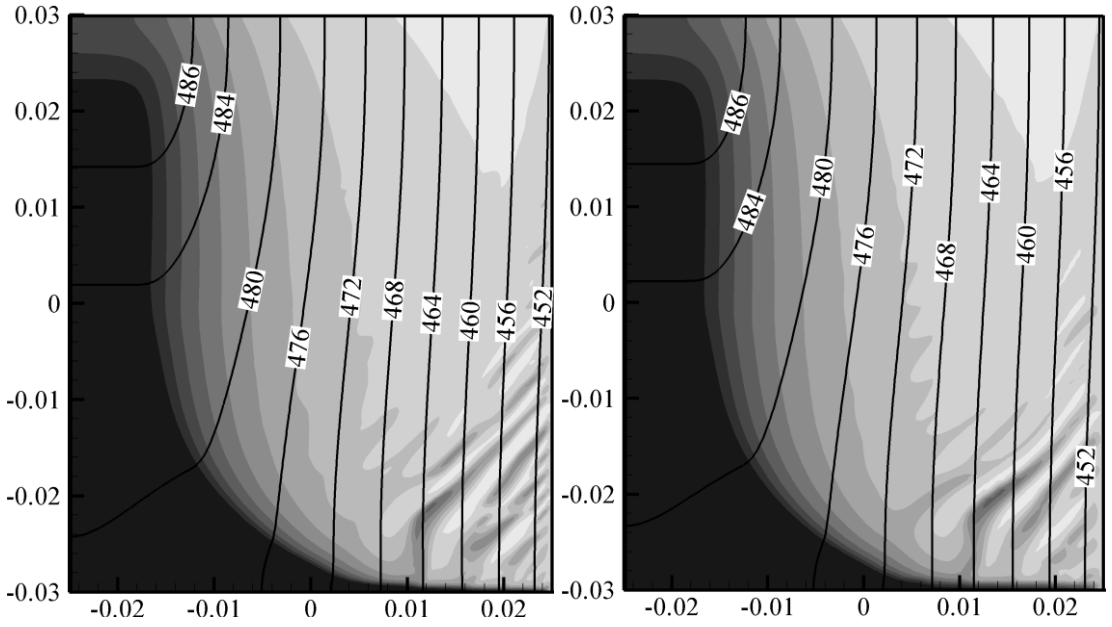

(a) 0.25 mm

(b) 0.5 mm

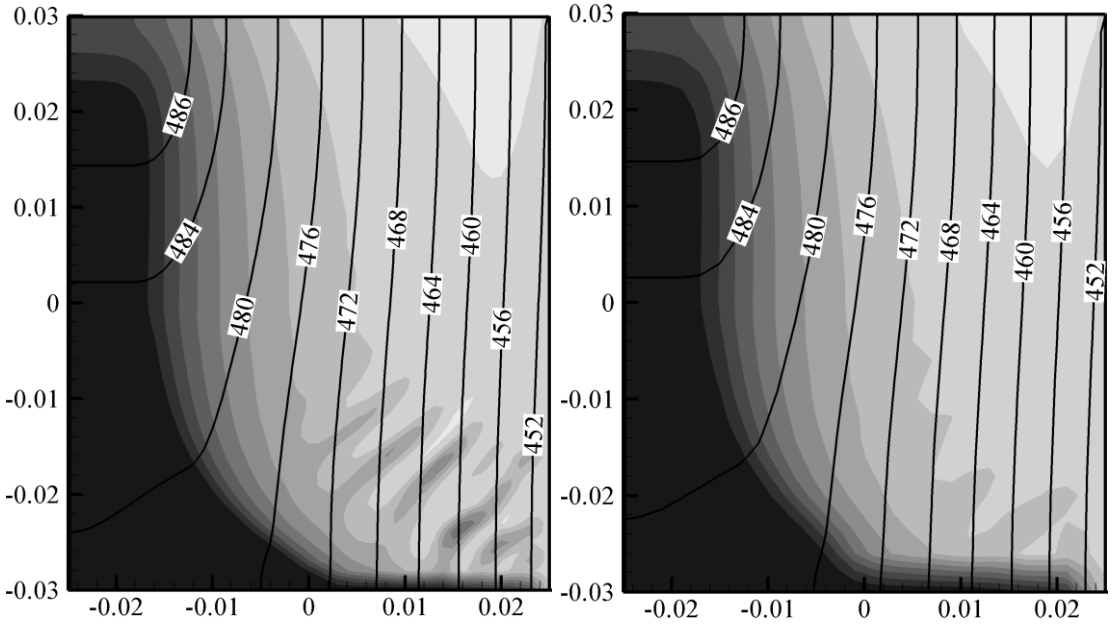

(c) 1 mm

(d) 2 mm

Figure 10: Grid sensitivity of the temperature field and volume fraction of liquid at 200 s. The volume fraction of liquid is shown in gray scale (dark for the highest and light for the lowest value), overlaid with isotherms of the temperature [K] for (a) grid size is 0.25 mm; (b) 0.5 mm; (c) 1 mm; and (d) 2 mm.

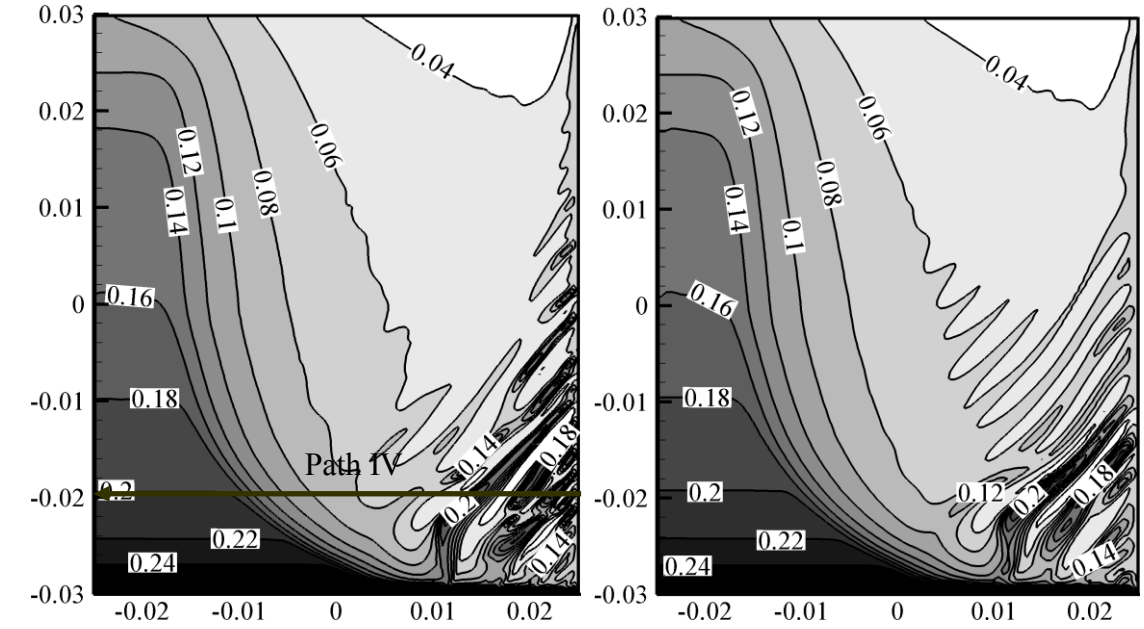

(a) 0.25 mm (b) 0.5 mm

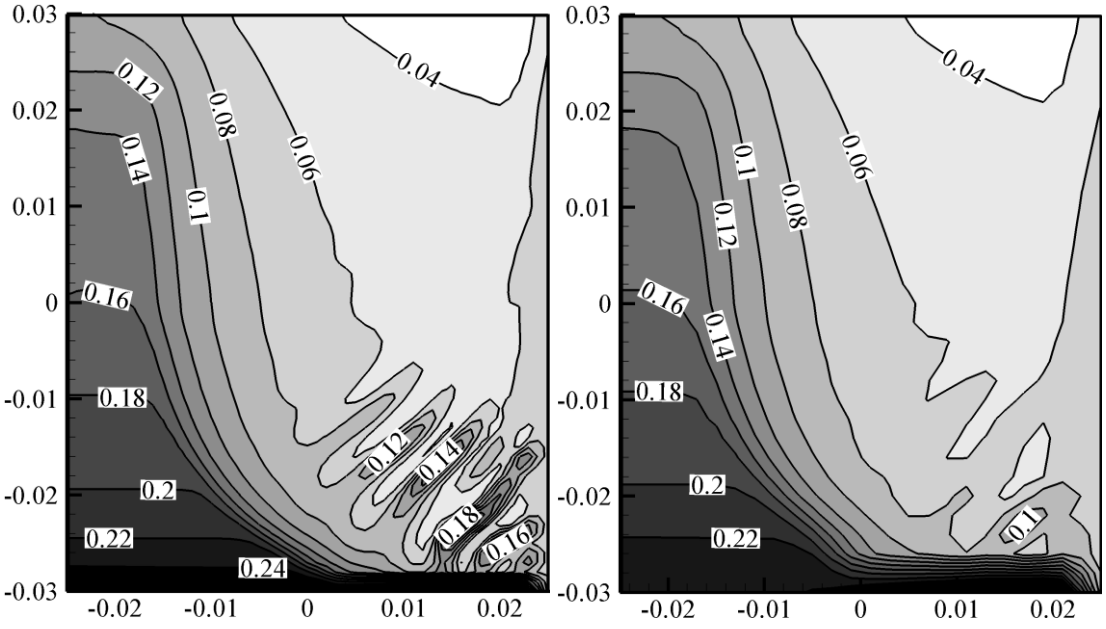

(c) 1 mm (d) 2 mm

Figure 11: Grid sensitivity of macrosegregation at 200 s. The Pb mixture concentration, c_{mix}, is shown in gray scale with dark for the highest and light for the lowest value and overlaid with c_{mix} isolines for grid size of (a) 0.25 mm; (b) 0.5 mm; (c) 1 mm; and (d) 2 mm.

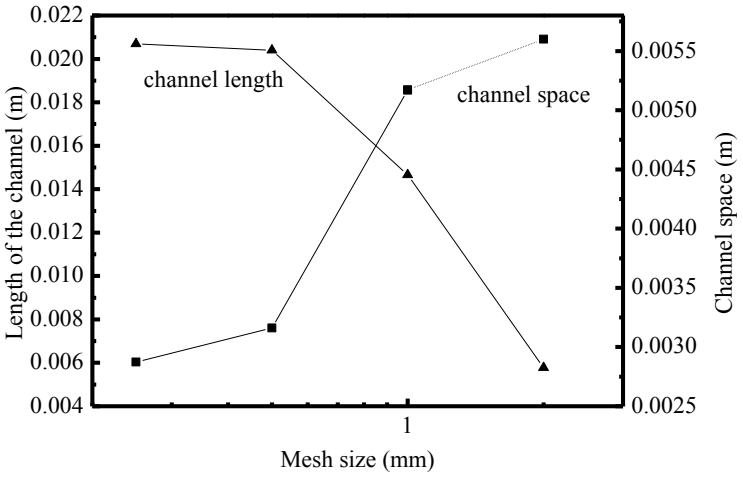

Figure 12: The predicted average length and spacing of channels as function of the mesh size.

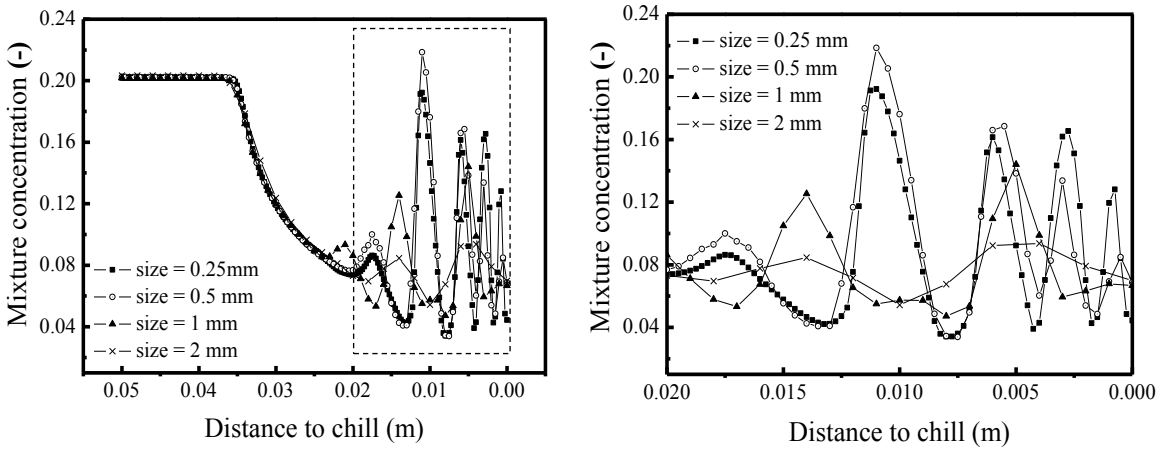

(a) (b)

Figure 13: Influence of the mesh size on the c_{mix} distribution profile along the path IV as marked in Fig. 11(a): (b) zoomed-in view of the right part region of (a).

Based on the above findings, it is anticipated that a quasi grid-independent result is reached with a grid size of 0.5 mm for the current benchmark. The characteristic parameters (average channel spacing, length and the severity of the segregation) will approach constant values, however the fine details of the c_{mix} distribution contours will change slightly with further refinement of the grid size.

5.2 Comparison with other numerical modeling results

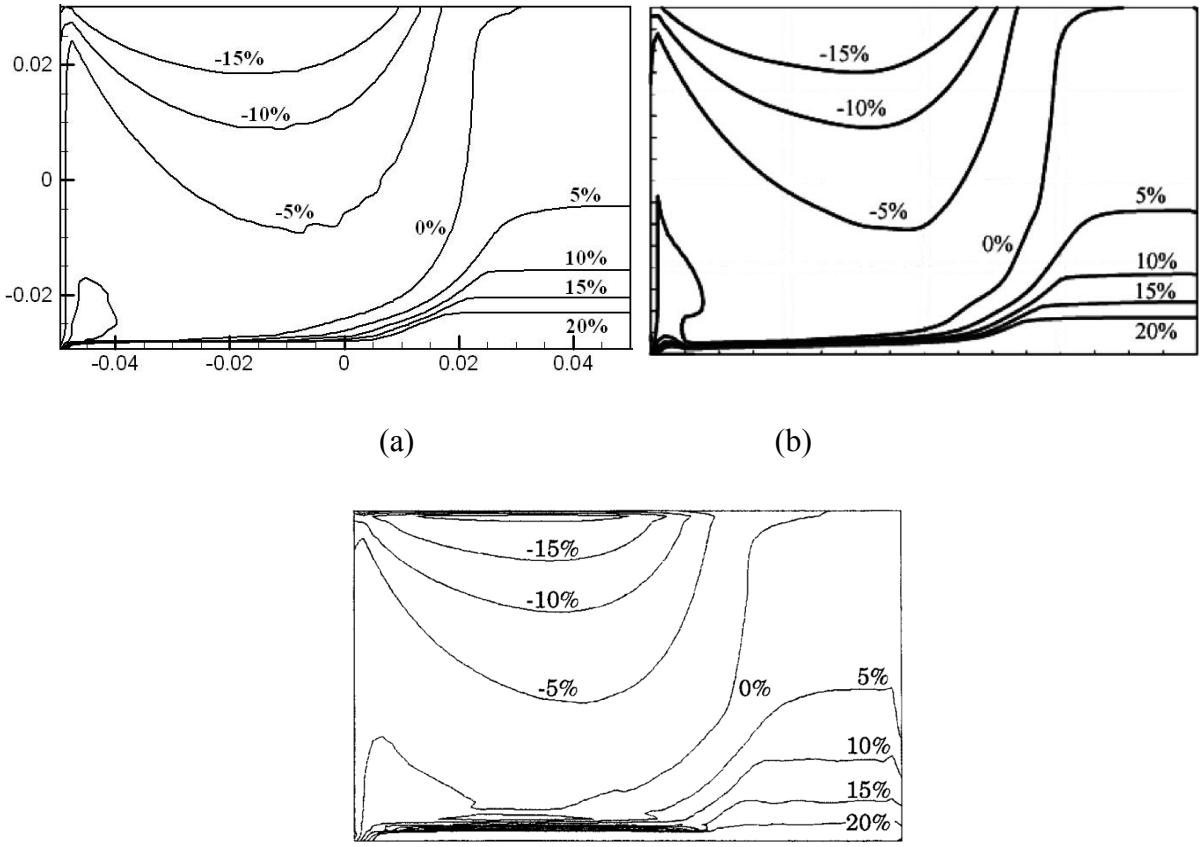

Figure 14: Predicted segregation patterns in the Sn-5 wt.% Pb benchmark at 400 s: (a) the current model; (b) chemical non-equilibrium model in [30] and (c) FEM model in [17].

A simulation using the current finite volume numerical model with a 2D (0.1×0.06 m^2) benchmark geometry with alloy Sn-5 wt.% Pb is compared to the same benchmark studied by Ahmad [17] with a finite element model and by Roux [30] with a chemical non-equilibrium model. In this benchmark, heat is extracted from the left vertical wall with a heat transfer coefficient of 300 W·m^{-2}·K^{-1}. At $t = 0$ the domain is filled with a liquid binary metal at a uniform temperature and composition. A detailed model description, material properties and process parameters can be found in Reference [17] and [30]. Fig. 14 shows a comparison of the c_{mix} distribution for the current model, the non-equilibrium model [30] and the FEM model [17], at 400 s of solidification. The current model (Fig. 14(a)) is in very good agreement with the non-equilibrium model (Fig. 14(b)), and shows reasonable

agreement with the FEM model (Fig. 14(c)). All three models predict a high solute enrichment with a strong concentration gradient in the lower right of the domain.

5.3 Experimental verification

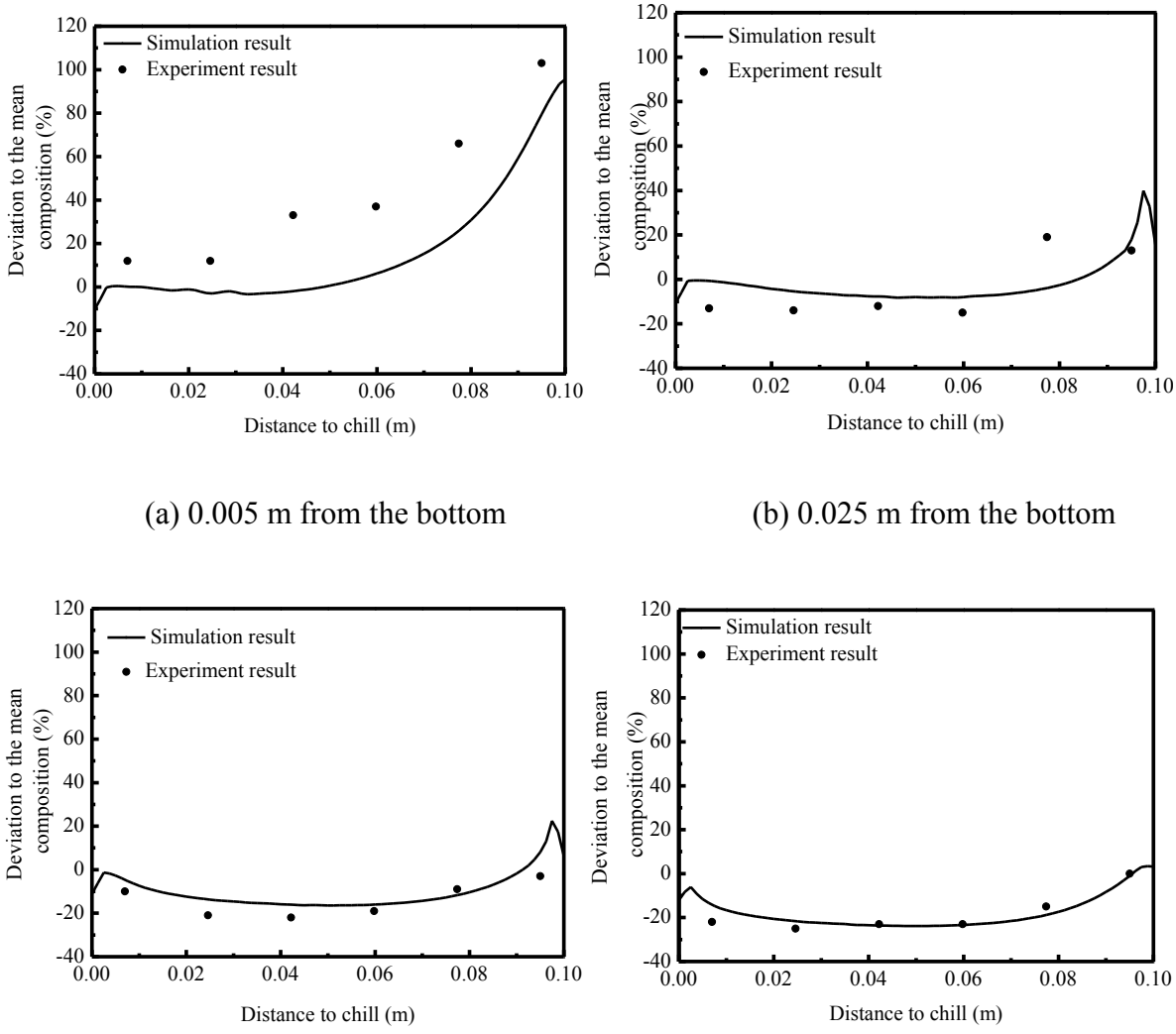

(a) 0.005 m from the bottom

(b) 0.025 m from the bottom

(c) 0.045 m from the bottom

(d) 0.055 m from the bottom

Figure 15: Relative Pb mass fraction variations, $((c_{\text{mix}} - c_0)/c_0) \times 100$, for the Sn-5 wt.% Pb benchmark at the end of solidification as a function of the distance from the cooling wall. These profiles correspond to four heights of the cavity at (a) 0.005 m, (b) 0.025 m, (c) 0.045 m, and (d) 0.055 m from the bottom.

The current model is also evaluated by comparing the modeling results with the results of Hebditch and Hunt [20], as shown in Fig. 15. The variation of relative Pb average mass

fraction (displayed as percentage of the mean composition) are plotted as a function of the distance to the cooling wall along 4 paths, namely 0.005 m, 0.025 m, 0.045 m and 0.055 m from the bottom. Agreement is fairly good, especially in the upper part of the cavity along the paths of 0.045 m and 0.055 m, where negative segregation is observed. The Pb mass fraction differs near the bottom of the cavity (0.005 m), where a strong positive segregation is observed at the end of the solidification. The Pb composition from the experiment is higher than the predicted result from the simulation, however this is to be expected since the simulation is 2D while the experimental geometry is of course 3 dimensional with a very thin thickness (0.013 m). The experimental result has strong 3D effects, so the value of the composition should be higher than the corresponding 2D results. Recalling the comparison of 2D and 3D simulation results in Fig. 8, the predicted maximum positive segregation in the low corner last-to-solidify region is significantly higher for the 3D case. The 3D effect is significant for the 3D experimental benchmark with a 0.013 m thickness.

6 Discussion

A two-phase columnar solidification model was used to simulate the formation of channel segregates and expand the understanding of the mechanisms that lead to channel segregation. Solidification of a reference Sn-Pb benchmark, as defined by Bellet et al. [1], was calculated. The main findings are as follows.

1) The 3D simulations show the transient development of the channel segregation. In the current alloy system the thermo-solutal buoyancy drives the clockwise circulation flow, i.e. the segregated interdendritic melt is heavier than the bulk melt and sinks downward along the solidification front. Channel segregates form in the bottom corner near the chilled wall with a predominately discontinuous lamellar-structured morphology and some rod-like formation.

2) Significant differences in c_{mix} distribution are observed between the 2D calculation and the center plane of the 3D calculation with 0.03 m thickness. This difference, the 3D effect, is caused by the thermal and hydrodynamic influence of the front/back mold walls. The 3D effect is much less prominent in the thicker benchmark (≥ 0.05 m), thus the 2D calculation suitably represents the thick-walled (≥ 0.05 m) 3D benchmark but not the thinner 3D benchmark. As a corollary, caution must be used when comparing 2D modeling results with 3D experiments. Despite

this, the efficient computation time of a 2D simulation makes them a worthy analysis tool.

3) To ensure calculation accuracy, the influence of grid size on channel segregation formation was evaluated. In the current benchmark, a quasi grid-independent result can be achieved with a cell size less than 0.5 mm. This quasi grid-independence means that the characteristic parameters (average channel spacing, length and severity of the segregation) tend to converge to constant values, although the fine features of the c_{mix} contours change slightly with further refinement of the grid. The current mesh resolution (0.25 mm) may not be fine enough to produce grid-converged result of the fine channel segregates details, but the most important features regarding the formation of channel segregates can be resolved with the current mesh resolution. This finding coincides with the statement of Kumar et al [14].

4) Verification of the current model was made by comparison with other modeling approaches [17, 30] and with the experiments of Hebditch and Hunt [20]. General quantitative agreements were obtained, however, these models and experiments have not been able to describe details of the channel segregates in 3D. A more detailed comparison of the current model is possible with the experimental work by Sawada et al.[18] who presented a stereoscopic structure of the channel segregates with X-ray CT method on a Sn-20wt.%Bi benchmark ($0.1 \times 0.11 \times 0.03$ m^3). In this experiment, the channels were more rod-like than lamellar. In the current modeling result, mostly lamellar structure is observed. This discrepancy may arise from 1) differences in alloy system, benchmark geometry and boundary conditions or 2) from the uncertainties of model assumptions and model parameters, such as the assumption of the isotropic permeability of the mushy zone, the limitation of the volume average technique, etc. To clarify this issue, further experiments are planned in collaboration with Y. Frautrelle et al. [31] based on the same Sn-Pb benchmark.

Part II of this investigation presents an in-depth discussion and parameter study on the formation mechanisms of channel segregation.

Nomenclature

c_0	initial concentration of the alloy	-
c_ℓ, c_s	species concentration	-
c_ℓ^*, c_s^*	interface equilibrium species concentration	-
$C_{\ell\mathrm{s}}^\mathrm{M}$	species exchange due to phase change	$\mathrm{kg \cdot m^{-3} \cdot s^{-1}}$
c_mix	mixture concentration	-
$c_\mathrm{p}^\ell, c_\mathrm{p}^\mathrm{s}$	specific heat	$\mathrm{J \cdot kg^{-1} \cdot K^{-1}}$
D_ℓ	diffusion coefficient	$\mathrm{m^2 \cdot s^{-1}}$
d_c	diameter of columnar trunk	m
f_ℓ, f_s	volume fraction	-
$\bar{g}$	gravity	$\mathrm{m \cdot s^{-2}}$
H^*	volume heat exchange rate between solid and liquid phases	$\mathrm{W \cdot m^{-3} \cdot K^{-1}}$
h	heat transfer coefficient	$\mathrm{W \cdot m^{-2} \cdot K^{-1}}$
h_ℓ, h_s	enthalpy	$\mathrm{J \cdot kg^{-1}}$
$h_\ell^\mathrm{ref}, h_\mathrm{s}^\mathrm{ref}$	enthalpy at reference temperature	$\mathrm{J \cdot kg^{-1}}$
Δh_f	latent heat (heat of fusion)	$\mathrm{J \cdot kg^{-1}}$
K	permeability	$\mathrm{m^2}$
k	solute partition coefficient	-
k_ℓ, k_s	thermal conductivity	$\mathrm{W \cdot m^{-1} \cdot K^{-1}}$
$M_{\ell\mathrm{s}}$	solidification mass transfer rate	$\mathrm{kg \cdot s^{-1} \cdot m^{-3}}$
m	liquidus slope of the binary phase diagram	$\mathrm{K\ (wt.\%)^{-1}}$
p	pressure	Pa
$Q_{\ell\mathrm{s}}^\mathrm{D}$	energy exchange by heat transfer	$\mathrm{J \cdot m^{-3} \cdot s^{-1}}$
$Q_\ell^\mathrm{M}, Q_\mathrm{s}^\mathrm{M}$	energy source term due to phase change	$\mathrm{J \cdot m^{-3} \cdot s^{-1}}$
R_c	radius of columnar trunk	m
R_f	far field radius of columnar trunk	m
S_A	columnar surface concentration	$\mathrm{m^{-1}}$

T, T_ℓ, T_s	temperature	K
T_{ref}	reference temperature for enthalpy definition	K
T_{EXT}	External temperature	K
t	time	s
$\vec{U}_{\ell s}^{D}$	momentum change due to drag force	$kg \cdot m^{-2} \cdot s^{-2}$
$\vec{U}_{\ell s}^{M}$	momentum exchange due to phase change	$kg \cdot m^{-2} \cdot s^{-2}$
$\vec{u}_\ell$	velocity vector of the melt	$m \cdot s^{-1}$
v_{R_c}	columnar trunk growth velocity	$m \cdot s^{-1}$
Φ_{imp}	columnar growing surface impingement	-
λ_1	primary dendrite arm spacing of columnar	m
λ_2	second dendrite arm spacing of columnar	m
ρ_ℓ, ρ_s	density	$kg \cdot m^{-3}$
μ_ℓ	viscosity	$kg \cdot m^{-1} \cdot s^{-1}$
$\bar{\bar{\tau}}_{ls}$	stress-strain tensors	$Kg \cdot m^{-1} \cdot s^{-2}$

Subscripts ℓ, s indicate liquid and solid phases.

Acknowledgments

The authors would like to thank Prof. H. Combeau from CNRS-Nancy and Prof. Y. Frautrelle from CNRS-SIMAP-EPM, France for contributing discussions on the current modeling results. Financial support for this project is provided by the Austrian Federal Ministry of Economy, Family and Youth and the National Foundation for Research, Technology and Development. Author Jun Li would like to thank the China Scholarship Council for financial support.

References

[1] M. Bellet, H. Combeau, Y. Fautrelle, D. Gobin, M. Rady, E. Arquis, O. Budenkova, B. Dussoubs, Y. Duterrail, A. Kumar, C.A. Gandin, B. Goyeau, S. Mosbah, M. Založnik, Int. J. Therm. Sci. 48 (2009) 2013-2016.

[2] K. Suzuki and T. Miyamoto, Transactions ISIJ 18 (1978) 80-89.

[3] J. A. Van Den Avyle, J. A. Brooks and A. C. Powell, JOM 50 (1998) 22-25.

[4] K. Suzuki and K. Taniguchi, Trans. Iron Steel Inst. Jp. 21 (1981) 235-242.

[5] K. Suzuki and T. Miyamoto, Trans. Iron Steel Inst. Jp. 20 (1980) 375-383.

[6] J. J. Moore and N. A. Shah, Inter. Metals Reviews 28 (1983) 338-356.

[7] E. Marburg, Transactions AIME 5 (1953) 157-172.

[8] S.N. Tewari and R. Shah, Metall. Trans. A 23A (1992) 3383-3392.

[9] M.I. Bergman, D. R. Fearn, J. Bloxham, and M. C. Shannon, Metall. Mater. Trans. A 28A (1997) 859-866.

[10] R. J. Mcdonald and J. D. Hunt, Trans. Metall. Society of AIME 245 (1969) 1993-1997.

[11] R. J. McDonald and J. D. Hunt, Metall. Trans. 1 (1970) 1787-1788.

[12] J. R. Sarazin and A. Hellawell, Metall. Trans. A 19A (1988) 1861-1871.

[13] G. Quillet, A. Ciobanas, P. Lehmann and Y. Fautrelle, Int. Sci. Colloquium Modelling for Electromagnetic Processing, Hannover, March 24-26. 2003, 171-176.

[14] Kumar, B. Dussoubs, M. Založnik and H. Combeau, J. Phys. D: Appl. Phys. 42 (2009) 105503-105515.

[15] H. Shahani, G.Amberg, and H. Fredriksson, Metall. Trans. A 23A (1992) 2301-2311.

[16] M. C. Schneider and C. Beckermann, Int. J. Heat Mass Transfer 38 (1995) 3455-3473.

[17] N. Ahmad, H. Combeau, J. Desbiolles, T. Jaldanti, G. Lesoult, J. Rappaz, M. Rappaz, C. Stomp, Metall. Mater. Trans. A 29A (1998) 617-630.

[18] T. Sawada, K. Oikawa and K. Anzai, in: S. L. Cockroft, D.M. Maijer, (Eds.), Modeling of Casting, Welding and Advanced Solidification Processes XII, TMS, Warrendale, PA, USA, 2009, 303-309.

[19] M. Zaloznik and H. Combeau, in: S. L. Cockroft, D.M. Maijer, (Eds.), Modeling of Casting, Welding and Advanced Solidification Processes XII, TMS, Warrendale, PA, USA, 2009, 253-260.

[20] D. J. Hebditch and J. D. Hunt, Metall. Trans. 5 (1974) 1557-1564.

[21] M. Wu, A. Ludwig, Metall. Mater. Trans. A 37A (2006) 1613-1431.

[22] M. Wu, A. Ludwig, Metall. Mater. Trans. A 38A (2007) 1465-1475.

[23] J. Ni and C. Beckermann, Metall. Trans. B 22B (1991) 349-361.

[24] Y. Wang and C. Beckermann, Metall. Mater. Trans. A 27A (1996) 2754-2764.

[25] Beckermann and R. Viskanta, Appl. Mech. Rev. 46 (1993) 1-27.

[26] Ludwig, M. Grasser, M. Wu, A. Kuhn, J. Riedle, Int. J. Fluid Dynamics Mater. Proc. 1 (2006) 285-300.

[27] R.B. Bird, W.E. Steward, E.N. Lightfoot, Transport Phenomena, John Wiley & Sons, New York, 1960.

[28] M. Zaloznik, H. Combeau, Comp. Mater. Sci. 48(2010) 1-10.

[29] Fluent 6.3.26 User's Guide, chapter 18, 2009.

[30] P. Roux, B. Goyeaau, D. Gobin, F. Fichot and M. Quintard, Int. J. Heat Mass Trans. 49 (2006) 4496-4510.

[31] Y. Frautrelle, CNRS-SIMAP-EPM, France, personal communication, 2011.

Publication II

Simulation of channel segregation using a two-phase columnar solidification model

Part II: Mechanism and parameter study

Jun Li, Menghuai Wu, Jing Hao, Abdellah Kharicha and Andreas Ludwig

Computational Materials Science

Volume 55, 2012, pp. 419-429

Simulation of channel segregation using a two-phase columnar solidification model

Part II: Mechanism and parameter study

J. Li[1,2], M. Wu[1,2]*, J. Hao[1], A. Kharicha[1] and A. Ludwig[1]

[1]Simulation and Modeling of Metallurgical Processes, Dept. of Metallurgy, Univ. of Leoben,

[2]Christian Doppler Lab for Advanced Simulation of Solidification and Melting, Dept. of Metallurgy, Univ. of Leoben, A-8700 Leoben, Austria

∗ Corresponding author: Menghuai.wu@unileoben.ac.at

Tel: 0043-3842-4023103; Fax: 0043-3842-4023102

Abstract

In Part II of this investigation the two-phase columnar solidification model, described in Part I, is applied to study channel segregation in a Sn-10 wt.% Pb benchmark. Channel segregation originates from the thermo-solutal convection and the flow perturbations. The onset of a flow perturbation and subsequent channel segregation was previously analyzed with a mushy zone Rayleigh number by Beckermann et al. [Worster, Ann. Rev. Fluid Mech., 1997; Beckermann et al., Metall. Mater. Trans. A., 2000]. The current study has

justified the Rayleigh number as a qualitative indicator for characterizing the origin of segregation channels. Numerical parameter study has shown that an enhanced mushy zone Rayleigh number by increasing the secondary dendrite arm spacing and/or solutal expansion coefficient is prone to the formation of the channel segregation. Newly formed channels are sustained via growth under certain preferential conditions of the resulting flow-solidification interactions, which can be characterized by a flow-solidification interaction term, $\bar{u}_\ell \cdot \nabla c_\ell$. Depending on the flow direction, the sign of this term can be positive or negative. Channels occur only in the region where the flow-solidification interaction term is negative. With a negative flow-solidification interaction term the increase in flow velocity due to a flow perturbation suppresses the local solidification rate, promoting the growth of the channel. In return the growing channel strengthens the flow perturbation, and the flow-solidification interaction term becomes more negative; thus the channel continues to grow and becomes stable. The current model indicates that remelting is not a necessary condition for channel segregation.

Key words: macrosegregation; channel; columnar solidification; multiphase flow.

1 Introduction

Channel segregates, e.g. A-segregates in large steel ingots and freckles in unidirectionally solidified castings, are the consequence of thermal-solutal convection and the resulting flow interaction with the solidifying mushy zone [1-6]. Due to the engineering significance of alloy quality and durability, the formation mechanism of channel segregates has been the central focus of much theoretical and experimental research for many decades [4-12]. As large-scale computational power continues to become more accessible and affordable, numerical studies have also become a significant contributor to the investigation of channel segregates in the last decade [3, 12-17].

The formation of channel segregates in a casting is dependent on the flow conditions present during solidification. The initial formation of channel segregates is believed to be the result of convection instability in the mushy zone near the primary dendrite tips [6]. For an alloy with a partition coefficient less than one ($k < 1$), the interdendritic melt becomes enriched with solute elements, which causes a change in the local melt density. Thus, the density of the interdentric melt is a function of both concentration and temperature.

Depending on the thermal and solutal expansion coefficients and the solidification direction, varying thermo-solutal convection patterns in the mushy zone can develop as shown in Fig 1.. In the majority of engineering casting situations convection usually occurs as in Fig. 1(b-d).

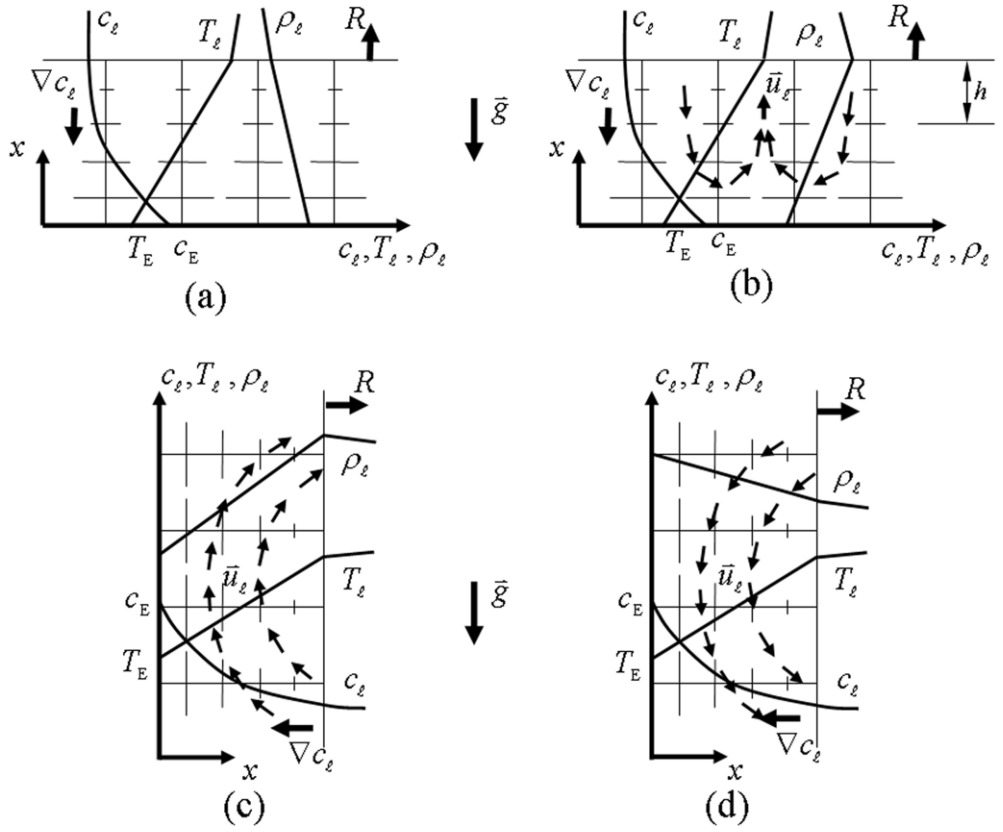

Figure 1: Schematic of a solidifying mushy zone at a prescribed solidification velocity R. The density of the saturated interdendritic melt, ρ_ℓ, changes with the thermal and solutal concentration fields (T_ℓ, c_ℓ). Depending on their expansion coefficients and the direction of gravity $\vec{g}$, the following flow patterns are induced: (a) unidirectional solidification with denser melt in the bottom of the mush; (b) unidirectional solidification with the densest melt near the solidification front; (c) lateral solidification with the densest melt near the solidification front; (d) and lateral solidification with denser melt in the deeper mushy zone.

According to Worster [7] the onset of convection instability and channel formation can be analyzed in terms of the mushy zone Rayleigh number R_a, defined as the ratio of the thermo-solutal buoyancy force to the opposing friction force associated with the mush permeability. Beckermann and co-workers [12] have extended the previous definition of R_a

by incorporating a more precise consideration of the solidification kinetics and the variable permeability of the mush:

$$R_a(h) = \frac{((\rho_0 - \rho_\ell)/\rho_0)\bar{g}\bar{K}h}{\alpha\nu}. \quad (1)$$

In this expression the R_a number is a function of the position h in the mushy zone, where h measures the depth of the mush from the primary dendrite tip, shown in Fig. 1(b). The α and ν are thermal diffusivity and kinematic viscosity, ρ_0 is the reference density corresponding to the liquidus temperature and $\bar{K}$ is the mean permeability. It was found that if the maximum R_a in the mushy zone exceeded a critical number, 0.25, freckles tend to form.

Given that R_a varies significantly with thermal parameters such as the temperature gradient G and the solidification velocity R, Beckermann's definition of the R_a criterion can also be approximated as

$$\frac{1}{R^{n'}G^{n''}} < \text{constant}, \quad (2)$$

where n' and n'' are 1/2 and 1/5, respectively. When the above condition is fulfilled, channel segregates will not form. Other experimental researchers have also proposed similar criteria, with varying exponents and constants. For example, in an NH_4Cl-H_2O system, the exponents n' and n'' were found to be 1 and 1 [11]; Pollock and Murphy suggested 1/2 and 1/4 for the Ni-based superalloys [18]; and Suzuki and Miyamoto used 2.1 and 1 for large steel ingots [8-9]. As G and R are important, but not the only factors influencing channel segregation, the above discrepancy suggested further investigation as worthwhile.

The onset of convection instability is not a sufficient condition to ensure the formation of channels; the channels must be stabilized by the resulting flow-solidification interaction. The coupling between the interdendritic flow and solidification is a key factor for channel growth. Solidification of the mushy zone can be accelerated at one location, or suppressed (even leading to remelting) at another location by the flow [4-5, 12]. For the unidirectional solidification case in Fig. 1(b), the segregated melt is lighter, tends to rise and induces a convection cell. The rising melt, bringing the segregated melt upwards, suppresses

solidification and/or encourages localized remelting such that a pencil-like plume (chimney) forms, leading to the formation of freckles as observed in many super-alloy castings. For the lateral solidification cases of Fig. 1(c) and (d), flow perturbation can occur at different positions (height). However, the flow perturbation can only create stable channels in some preferential regions. Meherabian and co-authors proposed an analytical correlation between the solidification rate and the flow velocity, $\vec{u}_\ell$, [4-5] based on Flemings' local solute redistribution equation [1],

$$\frac{\partial f_\ell}{\partial T} = -\left(\frac{1-\beta}{1-k}\cdot\frac{f_\ell}{c_\ell^*}\cdot\frac{\partial c_\ell^*}{\partial T}\right)\left(1+\frac{\vec{u}_\ell\cdot\vec{G}}{\dot{T}}\right). \tag{3}$$

Here β = ($(\rho_s - \rho_\ell)/\rho_s$), the solidification shrinkage, and c_ℓ^* is the thermodynamic equilibrium concentration, assumed to be equal to the local melt concentration, c_ℓ. The sign of the first term in parenthesis on the right hand side of Eq. (3) is always negative regardless of *k*, and the sign of the cooling rate $\dot{T}$ is always negative. Therefore, the sign of $\partial f_\ell/\partial T$, determining the acceleration or suppression (even remelting) of solidification, depends on the sign and magnitude of the term $\vec{u}_\ell\cdot\vec{G}$. This analysis predicts that a stable channel will form when $\vec{u}_\ell\cdot\vec{G} > |\dot{T}|$, which causes $\partial f_\ell/\partial T$ to be negative. In other words, a sufficiently strong interdendritic flow in the direction of the temperature gradient will cause remelting of dendrites and an open channel will form. If $\vec{u}_\ell\cdot\vec{G}$ < 0, i.e. flow is in the direction opposite to the temperature gradient and $\partial f_\ell/\partial T$ is positive, hence there is no possibility for stable channel to form. A third, intermediate case arises if $|\dot{T}| > \vec{u}_\ell\cdot\vec{G} > 0$, i.e. interdendritic flow is in the direction of temperature gradient and $\partial f_\ell/\partial T$ is still positive, but is reduced by the flow. In other words, solidification still proceeds with decreasing temperature, but the solidification rate is locally suppressed by the flow. In this intermediate case channels might form.

Eq. (3) can be applied to qualitatively analyze the potential formation of channel segregates. For example, in the lateral solidification case of Fig. 1(c), the interdendritic melt, with a relatively higher concentration of solute element, is lighter and tends to rise and escape from the mushy zone in the upper part of the casting. The escaping melt suppresses solidification and may cause localized remelting, such that channels form, leading to the A-segregation observed in many steel ingots. Channels are not able to form in the bottom

region in such a configuration. In the lateral solidification of Fig. 1(d) where the interdendritic melt is denser, channels form in the bottom region, as demonstrated in the current Sn-Pb benchmark (Part I).

Part II of this investigation examines the formation mechanism of channel segregates in the Sn-10 wt. % Pb benchmark using a two-phase columnar solidification model [19-20]. The current model differs from previous channel segregation models by including diffusion of the solute element in the interdendritic melt as a governing factor of solidification. Therefore, the significance of the diffusivity of the solute element is also discussed. An in-depth parameter study of the R_a number, by varying the mush permeability, is presented. The benchmark studied is similar to the lateral solidification case of Fig. 1(d), however the conclusions from this study can be applied to the case of Fig. 1(c).

2 Growth of channels

2.1 Flow-solidification interaction

After the initial formation, a channel may either continue to grow or disappear depending on the flow-solidification interaction in the two-phase mushy zone. Following the work of Meherabian and co-authors [4], a correlation of the local solidification rate ($M_{\ell c}$) to the flow velocity ($\bar{u}_\ell$) is established to better capture the phenomena of channel segregation in the situation of diffusion-governed solidification. The mass and species conservation equations for the two-phase columnar solidification model are summarized in Table 1 of Part I. A detailed description of the model is presented in the authors' previous publications [19-20]. The current model includes the following key assumptions [21]:

1) The flow is driven by thermo-solutal buoyancy. The solidification shrinkage is neglected, i.e., both solid and liquid have the same and constant density ($\rho_s = \rho_\ell = \rho$), with a Boussinesq approach used to treat thermo-solutal convection;

2) Solidification is modeled with a columnar dendritic morphology. The columnar dendrite is approximated by step-wise growing cylinders with constant (primary arm) spacing, and the growth rate of the columnar phase is governed by diffusion around the cylindrical trunk;

3) Species partitioning occurs at the liquid-solid interface, $\partial(f_s \rho_s c_s)/\partial t = c_s^* \rho_s \, \partial f_s/\partial t$, where c_ℓ^* and c_s^* are thermodynamic equilibrium concentrations at the liquid-solid interface;

4) At the macroscopic scale (global species transport) diffusion is neglected ($D_\ell = 0$, $D_s = 0$), while at the microscopic scale diffusion in the interdendritic melt is considered ($D_\ell \neq 0$) and back diffusion in the solid is ignored ($D_s = 0$);

5) The solidified phase is stationary: $\vec{u}_s = 0$.

The species conservation equation is written as

$$c_s^* \rho_s \frac{\partial f_s}{\partial t} + \rho_\ell c_\ell \frac{\partial f_\ell}{\partial t} + \rho_\ell f_\ell \frac{\partial c_\ell}{\partial t} + \nabla \cdot (f_\ell \rho_\ell c_\ell \vec{u}_\ell) = 0 . \tag{4}$$

Substituting the mass conservation equation into Eq. (4) the time derivative of the liquid concentration is

$$\frac{\partial c_\ell}{\partial t} = -\frac{(c_\ell - c_s^*)}{f_\ell} \cdot \frac{\partial f_\ell}{\partial t} - \vec{u}_\ell \cdot \nabla c_\ell \ . \tag{5}$$

Taking the time derivative of $T = T_f + m c_\ell^*$, the changing liquid interface concentration is

$$\frac{\partial c_\ell^*}{\partial t} = \frac{1}{m} \frac{\partial T}{\partial t} \ . \tag{6}$$

Subtracting Eq. (5) from Eq. (6) results in the local rate of change of ($c_\ell^* - c_\ell$)

$$\frac{\partial (c_\ell^* - c_\ell)}{\partial t} = \frac{(c_\ell - c_s^*)}{f_\ell} \frac{\partial f_\ell}{\partial t} + \frac{1}{m} \frac{\partial T}{\partial t} + \vec{u}_\ell \cdot \nabla c_\ell . \tag{7}$$

In the LHS of Eq. (7), $(c_\ell^* - c_\ell)$ is the driving force for solidification/melting, which governs the solidification/melting rate, $M_{\ell c}$ [19-21].

The local solidification/melting rate is the result of three contributions, corresponding to the three right hand side (RHS) terms of Eq. (7). The first RHS term is the contribution of the solidification-induced solute enrichment of the interdendritic melt, the sign of which is always negative for solidification. The solidification rate decreases with solute enrichment

of the interdendritic melt. The second RHS term is the contribution of the cooling rate, the sign of which is always positive, i.e., the solidification rate increases with enhanced cooling. These first two terms are relatively stable during solidification and are not considered critical factors in channel formation.

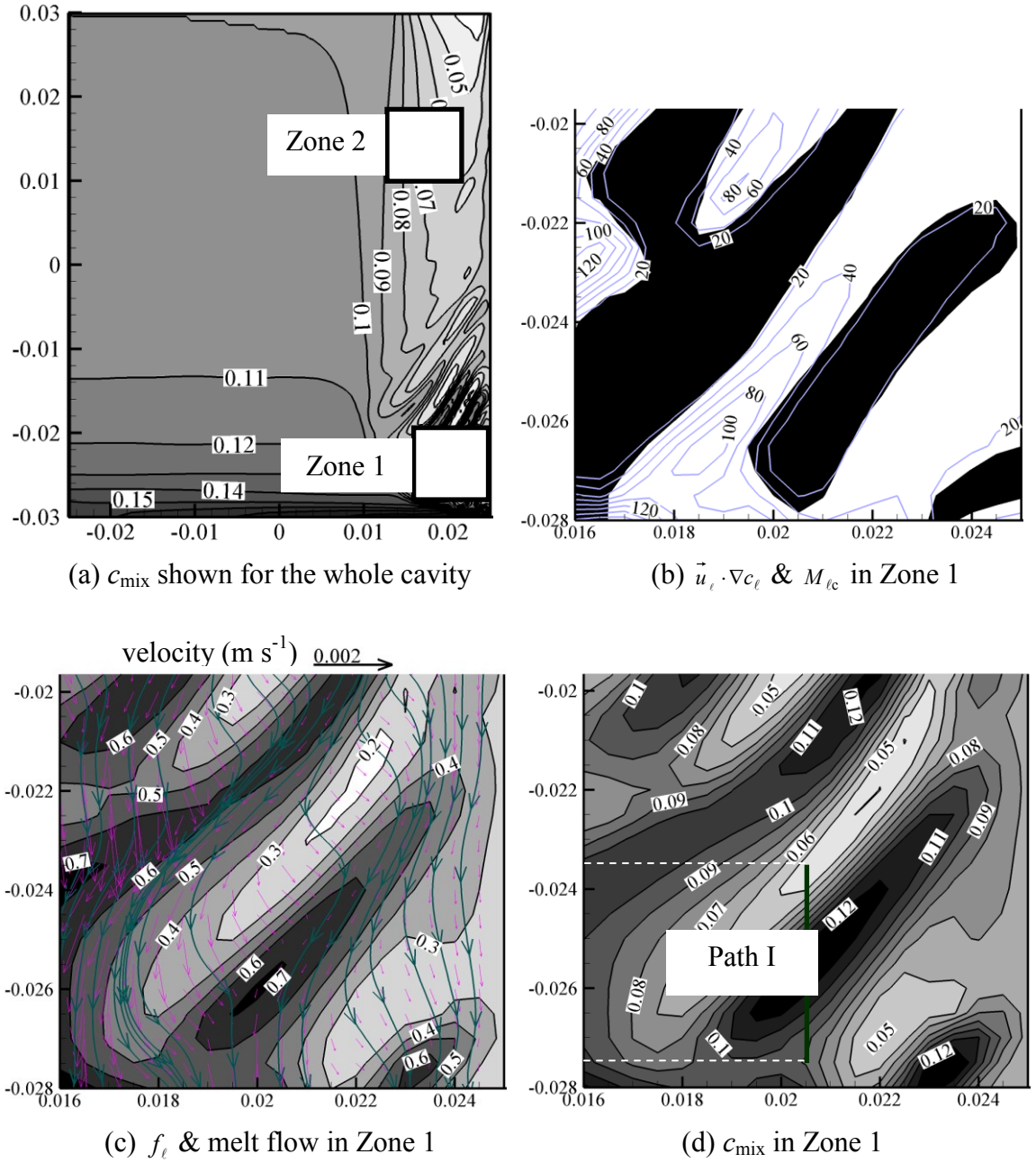

(a) c_{mix} shown for the whole cavity

(b) $\vec{u}_\ell \cdot \nabla c_\ell$ & $M_{\ell c}$ in Zone 1

(c) f_ℓ & melt flow in Zone 1

(d) c_{mix} in Zone 1

Figure 2: Analysis of the formation of the channel segregation at t = 40 s: (a) mixture concentration (c_{mix}) distribution in the cavity is shown in gray scale and isolines; (b) contours of the flow-solidification interaction term ($\vec{u}_\ell \cdot \nabla c_\ell$) in white (positive) and black (negative) overlaid by the mass transfer rate ($M_{\ell c}$) isolines; (c) liquid volume fraction (f_ℓ) contours and f_ℓ isolines overlaid by vectors of liquid velocity and streamlines; and (d) c_{mix} contour and its isolines.

The third RHS term in Eq. (7), $\bar{u}_\ell \cdot \nabla c_\ell$, is a flow-solidification interaction term, which is the most critical for the formation of the channel. Depending on the interdendritic flow, the sign of this term can be positive or negative. Local solidification behavior depends on the sign of the flow-solidification interaction term. In a region where the melt flows in the same direction as the concentration gradient, the flow-solidification interaction term is positive. The local increase in flow velocity due to a flow perturbation accelerates solidification and as a consequence of the locally accelerated solidification the flow permeability (K) becomes relatively smaller than that of neighboring zones and the interdentric flow slows down. In other words, the increase in flow velocity induced by a flow perturbation is throttled through the enhanced solidification. In the same sense, the local decrease in flow veloctiy due to a perturbation is reinforced by the decreased solidification rate. The region with a positive flow-solidification interaction term is an accelerated solidification region where flow perturbations are throttled through the flow-solidification interaction and channels do not form.

In regions where the melt flows in the opposite direction of the concentration gradient, the flow-solidification interaction term is negative. The local increase in flow velocity due to a flow perturbation supresses the solidification rate. This region with a relatively lower solid fraction has a larger permeability and the flow becomes stronger. In other words, the local increase in flow velocity due to a flow perturbation is reinforced by the suppressed solidification. In the same sense, a local decrease in flow velocity due to a flow perturbation is further decreased by the increased solidification rate. As a consequence of the flow-solidification interaction, the magnitude of the initial flow perturbation is increased. The region with a negative flow-solidification interaction term is a suppressed solidification region where channels form.

The above hypothesis on channel formation is verified by the current modeling results, as detailed in Figs. 2 to 4. The results shown here are obtained from a 2D simulation of Sn-10 wt. % Pb benchmark (0.05×0.06 m^2). Heat is extracted from the vertical (right) wall, and solidification proceeds laterally from the right towards the plane of symmetry. The two-phase columnar solidification model, computational domain, material properties and process parameters, were described in Part I of this study.

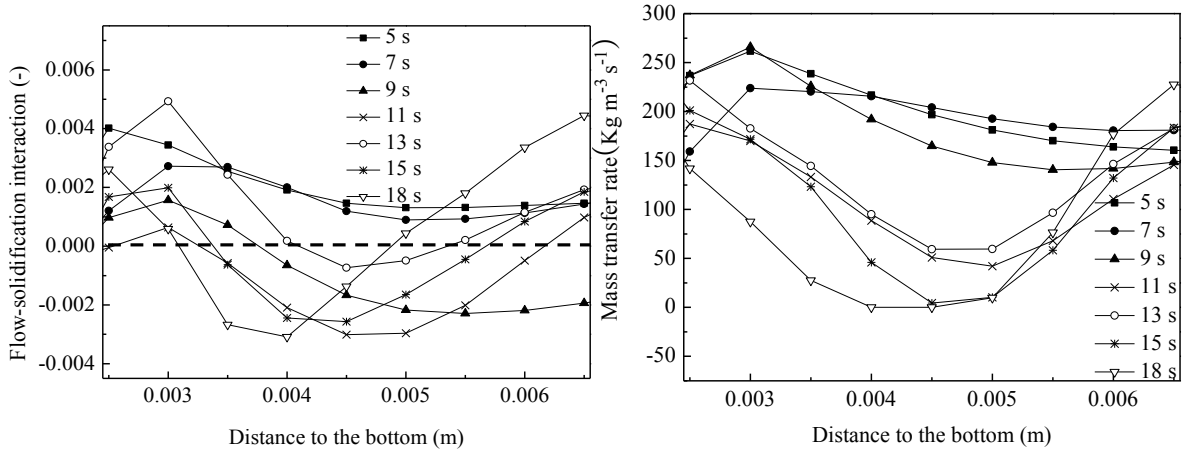

(a) flow-solidification interaction term ($\vec{u}_\ell \cdot \nabla c_\ell$) (b) mass transfer rate ($M_{\ell c}$)

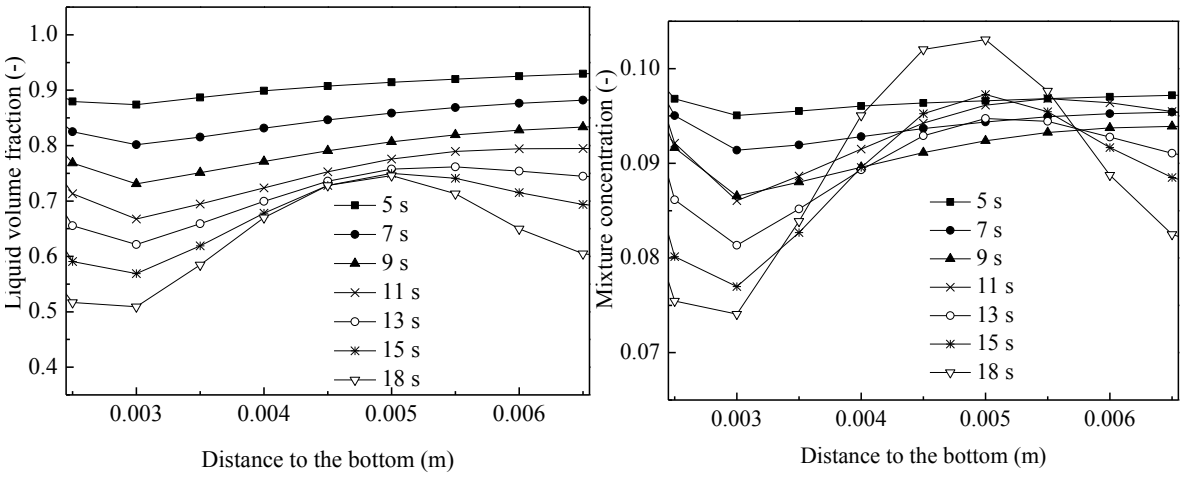

(c) liquid fraction (f_ℓ) (d) mixture concentration (c_{mix})

Figure 3 : Analysis of the evolution of channels and channel segregates along Path I as marked in Fig. 2(d) in terms of (a) $\vec{u}_\ell \cdot \nabla c_\ell$, (b) $M_{\ell c}$, (c) f_ℓ and (d) c_{mix}.

The dynamic evolution of the channel is further analyzed in Fig. 3 by tracking the flow-solidification interaction term ($\vec{u}_\ell \cdot \nabla c_\ell$), mass transfer rate ($M_{\ell c}$), liquid volume fraction (f_ℓ) and mixture concentration (c_{mix}) along a vertical path in the simulation domain. The path (Path I, as marked in Fig. 2(d)) crosses one channel, from 0.0025 m to 0.0065 m (distance from the bottom). The formation of the channel can be analyzed by f_ℓ and c_{mix} curves, when they become arched-upwards. Generally, the curves of $\vec{u}_\ell \cdot \nabla c_\ell$ are quite similar to the curves of $M_{\ell c}$, Fig. 3 (a) and (b), indicating a strong interaction between the flow and the

mass transfer. This further verifies that among the three RHS terms of Eq. (7) the flow-solidification interaction term is the most critical in determining the variation of $M_{\ell c}$. If the flow-solidification interaction term is not negative (e.g. before 7 s), channels are not prone to form. At 9 s, the flow-solidification interaction term is negative in the upper section of Path I--solidification is suppressed leading to a reduction of $M_{\ell c}$.

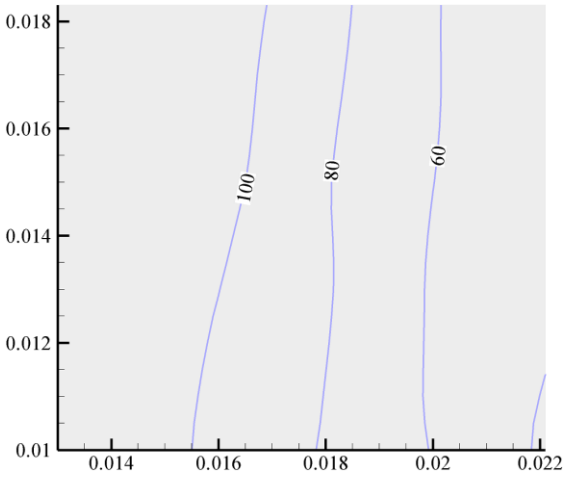

(a) $\vec{u}_\ell \cdot \nabla c_\ell$ & $M_{\ell c}$ in Zone 2

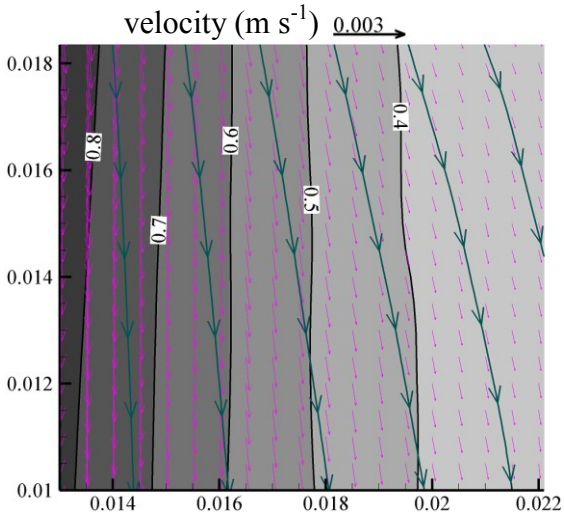

(b) f_ℓ & melt flow in Zone 2

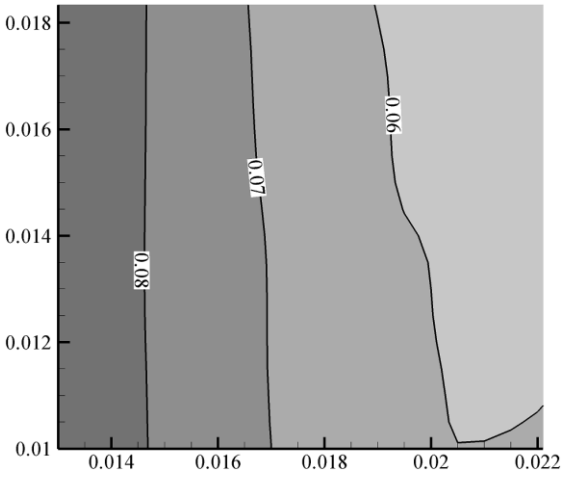

(c) c_{mix} in Zone 2

Figure 4: Analysis of the channel-free zone (Zone 2 of Fig. 2(a)) at t = 40 s. (a) contours of $\vec{u}_\ell \cdot \nabla c_\ell$ in white (positive) and black (negative) overlaid with $M_{\ell c}$ isolines, $\vec{u}_\ell \cdot \nabla c_\ell$ is positive everywhere; (b) f_ℓ contours and isolines overlaid by liquid velocity vectors and streamlines; (c) c_{mix} contours and isolines.

However, the arching of the f_ℓ curve, an indicator of channel formation, is not yet evident. Up to 13 s the flow-solidification interaction term stays locally negative in a somewhat oscillatory manner, the $M_{\ell c}$ curves become concave-downwards, and the onset of channel formation can be identified from the f_ℓ curve and c_{mix} curve. At 15 s in the suppressed solidification region $M_{\ell c}$ is only 9 $\text{kg.m}^{-3}.\text{s}^{-1}$, about 200 $\text{kg.m}^{-3}.\text{s}^{-1}$ smaller than the neighboring regions. As the difference in solidification rate between the suppressed solidification area and neighboring regions becomes greater, the channel becomes larger and more stable. Again, during the entire solidification process, $M_{\ell c}$ is never negative--formation of the channel appears to be entirely due to the change in the solidification rate caused by flow instability.

As proof of the aforementioned hypothesis, that channels cannot form in the solidification-accelerated region, the solidification process in the accelerated solidification region is also examined, as shown in Fig. 4. The flow-solidification interaction term $\vec{u}_\ell \cdot \nabla c_\ell$ is positive everywhere in Zone 2. Any increase in flow due to local flow perturbations will be throttled by the accelerated solidification. The f_ℓ isolines and the flow streamlines are smooth and undisturbed, thus, channels do not appear in this region.

Recently, Sawada and co-authors [22] studied the mechanism of channel segregation in vertical directional solidification with a Pb-10 wt.% Sn alloy, and reported a similar conclusion regarding the accelerated and suppressed solidification zones.

2.2 Significance of the finite diffusion in the interdendritic melt

Equations (3) and (7) differ in the treatment of diffusion of the solute element in the interdentritc melt. Eq. (3) is derived on the assumption of infinite diffusion of the solute element in the interdendritic melt while Eq. (7) includes this diffusion. When an assumption of infinite diffusion in the interdendritic melt is applicable (i.e. $c_\ell = c_\ell^*$), one can use the definition of the flow-solidification interaction term $\vec{u}_\ell \cdot \vec{G}$ instead of $\vec{u}_\ell \cdot \nabla c_\ell$ to analyze channel formation. For many engineering cases of solidification, infinite diffusion in the interdendritic melt represents a reasonable approximation and the term $\vec{u}_\ell \cdot \vec{G}$ has been successfully used to analyze channel formation [4-5]. However, when the influence of

the interdendritic diffusion is significant, an analysis based on the term $\vec{u}_\ell \cdot \nabla c_\ell$ is more reliable.

Fig. 5 shows the evolution of the flow-solidification term, which was defined in two ways, i.e. $\vec{u}_\ell \cdot \nabla c_\ell$ and $\vec{u}_\ell \cdot \vec{G}$, along the same path. As expected, the evolution of the $\vec{u}_\ell \cdot \vec{G}$ curves and $\vec{u}_\ell \cdot \nabla c_\ell$ curves show quite similar behavior. Small differences exist in the curves, particularly in the lower region of the benchmark, however the oscillation frequencies between the positive and negative values show the same trend. This indicates that the flow-solidification interaction term ($\vec{u}_\ell \cdot \vec{G}$), based on the infinite diffusion assumption, is a good approximation for a qualitative investigation on the formation of the channel segregation for the current benchmark.

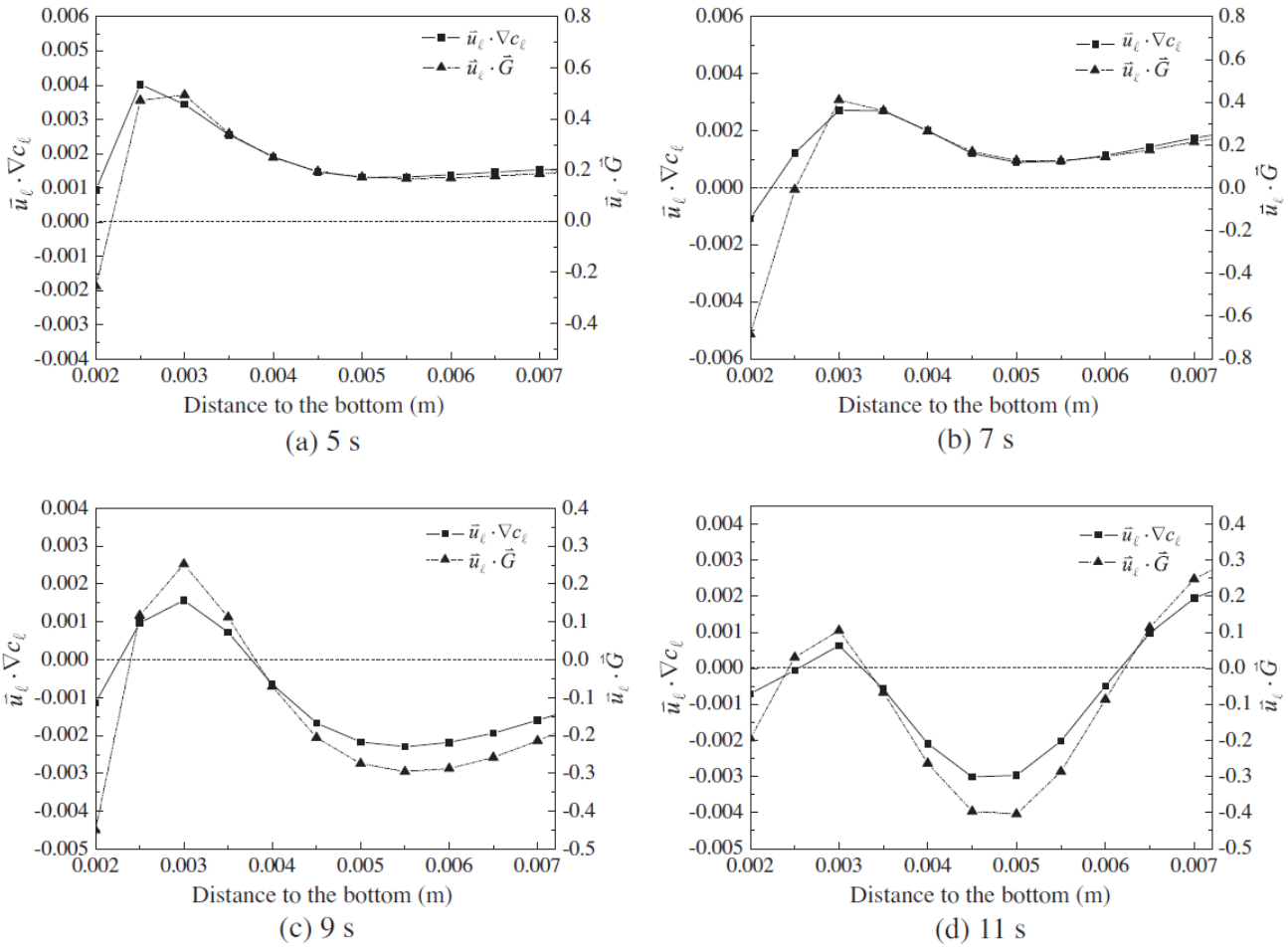

Figure 5: Evolution of the flow-solidification interaction term, which is defined by $\vec{u}_\ell \cdot \nabla c_\ell$ and $\vec{u}_\ell \cdot \vec{G}$. The curves are plotted along the path I as marked in Fig. 2(d). (a) 5 s; (b) 7 s; (c) 9 s; (d) 11 s.

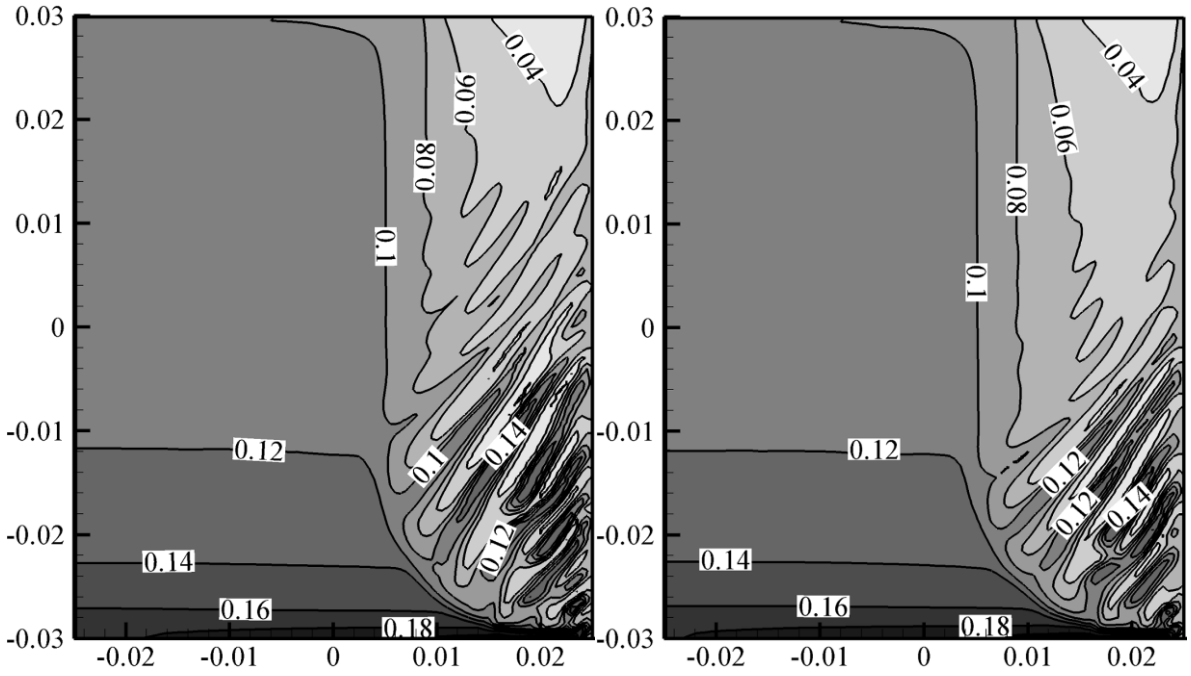

(a) $D_\ell = 1.0 \times 10^{-7}\ \mathrm{m^2 \cdot s^{-1}}$ (b) $D_\ell = 1.0 \times 10^{-8}\ \mathrm{m^2 \cdot s^{-1}}$

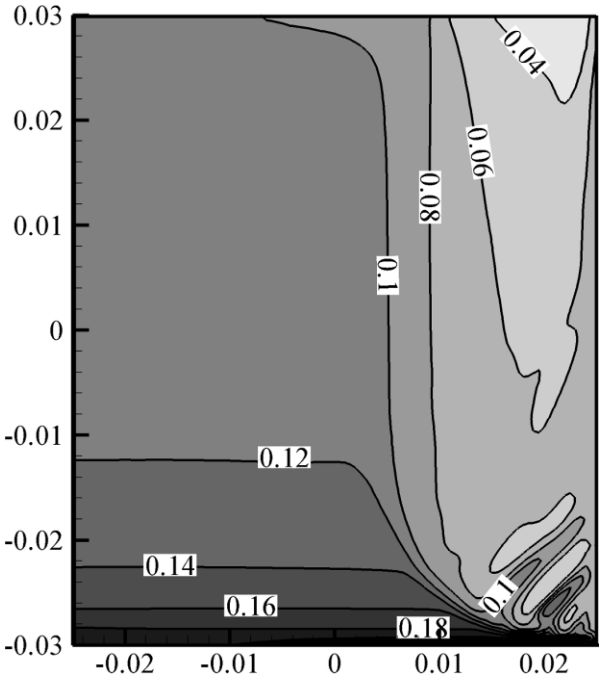

(c) $D_\ell = 1.0 \times 10^{-9}\ \mathrm{m^2 \cdot s^{-1}}$

Figure 6: Influence of the liquid diffusion coefficient D_ℓ on the channel segregation. Results at the moment 70 s are shown. c_{mix} map is overlaid with c_{mix} - isotherm. (a) $D_\ell = 1.0 \times 10^{-7}\ \mathrm{m^2 \cdot s^{-1}}$; (b) $D_\ell = 1.0 \times 10^{-8}\ \mathrm{m^2 \cdot s^{-1}}$; (c) $D_\ell = 1.0 \times 10^{-9}\ \mathrm{m^2 \cdot s^{-1}}$.

To verify the significance of solute diffusion in the interdendritic melt, further simulations were made by varying D_ℓ from (a) 1.0×10^{-7}, (b) 1.0×10^{-8}, (c) 1.0×10^{-9} $m^2 \cdot s^{-1}$. As shown in Fig. 6, the tendency for channel segregation to occur (the amount of channels, the area where the channels occur, and the severity of segregation) increases as D_ℓ increases. The case with $D_\ell = 1.0 \times 10^{-7}$ is closest to the assumption of infinite diffusion, where channel segregation is slightly overestimated. When the diffusivity is very small, 1.0×10^{-9}, channel formation is inhibited. This indicates that the validity of $\vec{u}_\ell \cdot \vec{G}$ for the investigation of channel formation is limited to alloys with large solute diffusivity in the interdendritic melt.

3 Onset of channels

3.1 Parameter study

As previously studied, the onset of channel formation can be characterized by the Rayleigh number [7, 12], i.e. the ratio of the thermo-solutal buoyancy force to the friction force associated with mushy zone permeability. The mushy zone permeability is proportional to the square of secondary dendrite arm spacing, $K \propto \lambda_2^2$, and the key parameters for the buoyancy force are the expansion coefficients β_c and β_T.

Thus, the sensitivity of the channel segregation to Rayleigh number is investigated by varying λ_2 and β_c, as listed in Table 1. All other physical and process parameters are kept constant.

Fig. 7 and Fig. 8 compare the simulation results of four cases by varying λ_2. As λ_2 increases resistance to the interdendritic flow decreases and heat and mass transfer are enhanced. As shown by the isotherms in Fig. 7 the heat extraction in Case 13 (large λ_2) appears to be faster than that in Case 2 (small λ_2). At t = 150 s the temperature near the plane of symmetry of Case 13 is lower than that of Case 2, and the isotherms move slightly faster toward the plane of symmetry as λ_2 increases.

The influence of λ_2 on f_ℓ and c_{mix} is more evident than the influence of λ_2 on heat transfer. When λ_2 is small (< 100 μm) the friction resistance of the dendrites is high enough to

maintain a stable interdendritic liquid flow; channels and channel segregation are not observed, as shown in Fig. 7(a) and Fig. 8(a). Channels and channel segregation occur only when λ_2 is sufficiently large ($\geq$ 260 μm), as shown in Fig. 7(b)-(d) and Fig. 8(b)-(d). The number of the channels found in the calculation domain is dependent on λ_2. For λ_2 equal to 260, 455, and 650 μm, the number of channels formed is 4, 7 and 11, respectively. The length of the channels is also influenced by λ_2. With a larger λ_2, the channels extend (penetrate) deeper into the mushy zone. For Case 13 (λ_2 = 650 μm) the channel segregation zone occupies more than half of the mold cavity. Based on these results, it can be concluded that a large Rayleigh number promotes channel formation.

Table 1. Numerical parameter study by varying λ_2 and β_c.

Simulation case	λ_2 (μm)	β_c	$R_{a,\,Max}$*	Channel or not
1	32.5	-1.06	0.02	No
2	65	-0.53	0.05	No
3	97.5	-0.53	0.11	No
4	65	-1.06	0.12	No
5	130	-0.53	0.24	Yes
6	97.5	-1.06	0.28	Yes
7	65	-2.65	0.32	Yes
8	65	-5.3	0.54	Yes
9	195	-0.53	0.68	Yes
10	260	-0.53	1.25	Yes
11	325	-0.53	2.05	Yes
12	455	-0.53	7.04	Yes
13	650	-0.53	13.22	Yes

*Maximum Rayleigh number ($R_{a,\,Max}$) being reached during the initial stage (10 s).

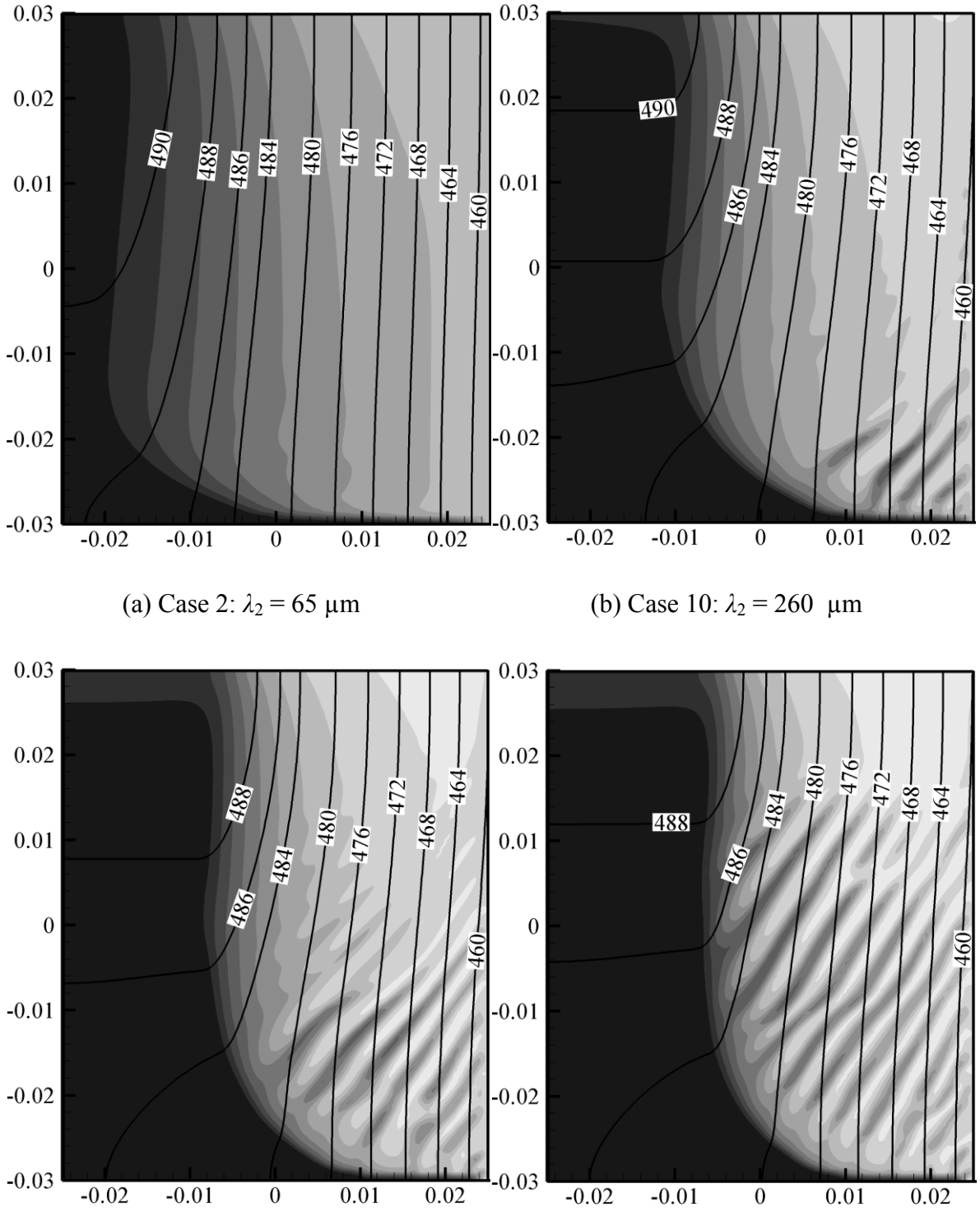

(a) Case 2: λ_2 = 65 μm

(b) Case 10: λ_2 = 260 μm

(c) Case 12: λ_2 = 455 μm

(d) Case 13: λ_2 = 650 μm

Figure 7: Influence of λ_2 on f_ℓ and T at t = 150 s, where f_ℓ is shown in gray scale (dark for 1 and light for 0) and T is shown in isothermals. (a) Case 2: λ_2 = 65 μm; (b) Case 10: λ_2 = 260 μm; (c) Case 12: λ_2 = 455 μm; (d) Case 13: λ_2 = 650 μm.

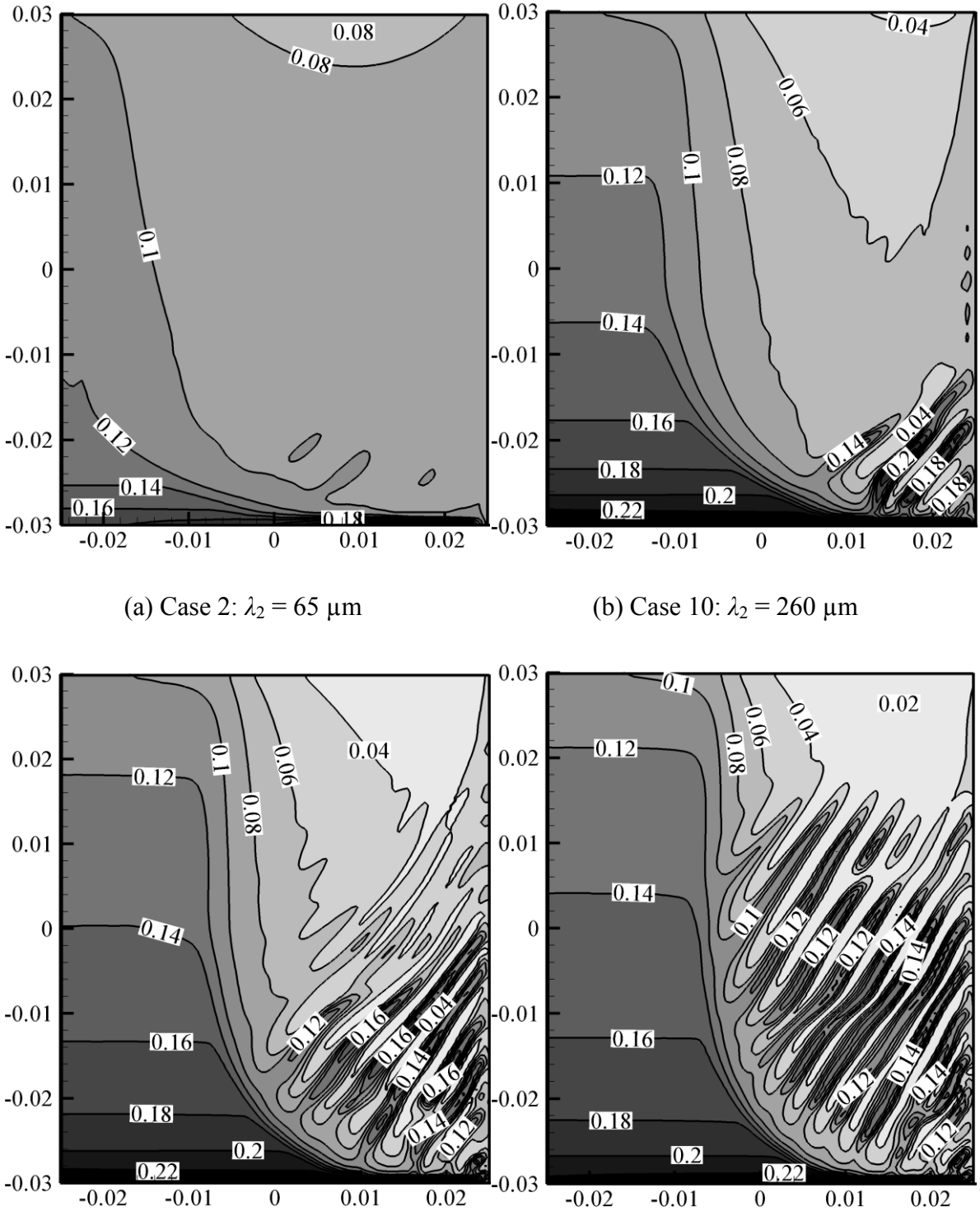

(a) Case 2: λ_2 = 65 µm

(b) Case 10: λ_2 = 260 µm

(c) Case 12: λ_2 = 455 µm

(d) Case 13: λ_2 = 650 µm

Figure 8: Influence of λ_2 on c_{mix}, shown in gray scale and isolines (t = 150 s). (a) Case 2: λ_2 = 65 µm; (b) Case 10: λ_2 = 260 µm; (c) Case 12: λ_2 = 455 µm; (d) Case 13: λ_2 = 650 µm.

Examining the global maximum c_{mix}, which occurs in the lower left (near the plane of symmetry), and the global minimum $c_{mix,}$ which occurs in the upper right region near the casting surface, shows that the minimum c_{mix} and maximum c_{mix} are also strongly influenced by λ_2 (Fig. 9). Two situations spanning the range of λ_2 must be distinguished. Firstly, when λ_2 is small (< 130 μm) when very few or no channels appear, the maximum c_{mix} increases while the minimum c_{mix} decreases with increasing λ_2. This is due to the significantly enhanced global flow in the mold cavity, caused by the increased permeability of the mushy zone. A stronger flow means enhanced transport of segregated interdendritic melt, hence stronger macrosegregation. Secondly, when λ_2 is large (≥ 195 μm) and a greater number of channels appear, both maximum c_{mix} and minimum c_{mix} decrease with increasing λ_2. The reason for the decrease of the global maximum c_{mix} is due to the entrapment of the solute element by the segregation in the channels. The minimum c_{mix} occurs in the upper right region near the casting surface, an area less influenced by the channel formation. Therefore, the minimum c_{mix} continues to decrease with the enhanced global flow intensity in the mold cavity.

To further quantify channel segregation and characterize channel features the following parameters are defined: maximum channel length (l), channel space (δ), and channel inclination angle (θ), as schematically shown in Fig. 10. The severity of segregation across a channel is evaluated by a channel segregation severity index (Γ), defined as

$$\Gamma = \frac{c_{mix}^{max} - c_{mix}^{min}}{c_0} \times 100\%, \tag{9}$$

where, c_{mix}^{max} is the local maximum of c_{mix} within the channel, c_{mix}^{min} is the local minimum of c_{mix} between two neighboring channels and c_0 is the nominal concentration. The local maximum and minimum concentrations used in Eq. (9) are distinguished from the global maximum and minimum concentrations discussed in the previous section. Determination of the segregation parameters (l, δ and θ) from the current simulation results, for instance in Fig. 8, is done by a visual measurement. The values of δ and θ are averaged for each simulation case. The current discussion serves only as qualitative evaluation of the dependency of the segregation parameters on λ_2.

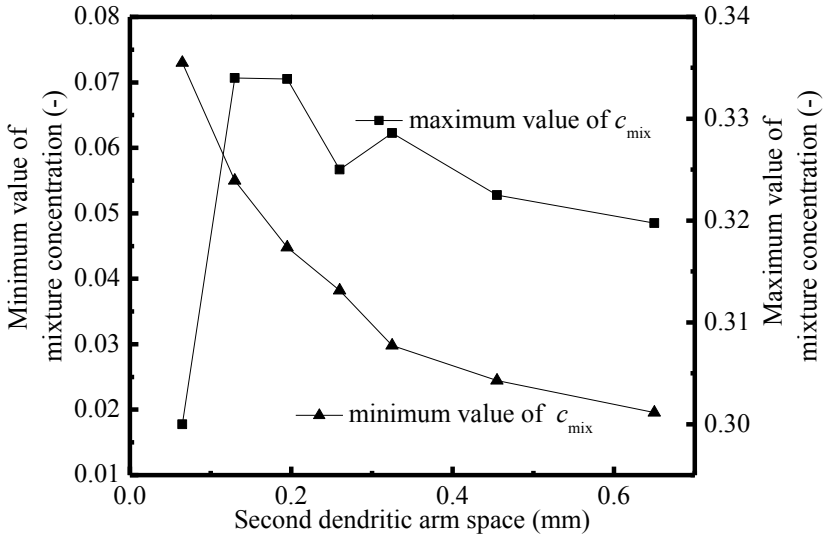

Figure 9: The influence of λ_2 on the global maximum and the minimum value of mixture concentration (c_{mix}) in the computational domain.

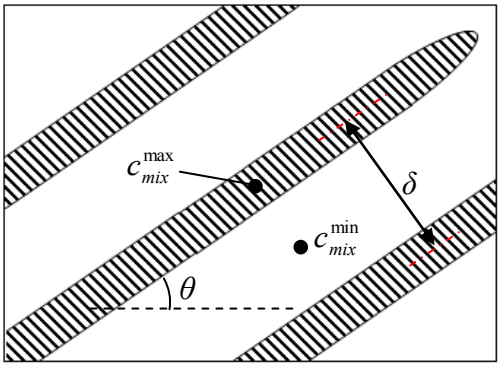

Figure 10: Schematic definition of channel segregation parameters. The shaded regions indicate the channels.

The influence of λ_2 on the above segregation parameters is shown in Fig. 11 and Fig. 12. The channel spacing, δ, decreases and the maximum channel length, l, increases with increasing λ_2. The channel inclination angle increases with increasing λ_2, while the channel segregation severity index, Γ, initially increases and then decreases. Thus, channel segregation tends to occur for the cases of large λ_2, but the severity of segregation is reduced with further increase of λ_2. Precise evaluation of the above dependencies is out of the scope of the current study and requires further investigations.

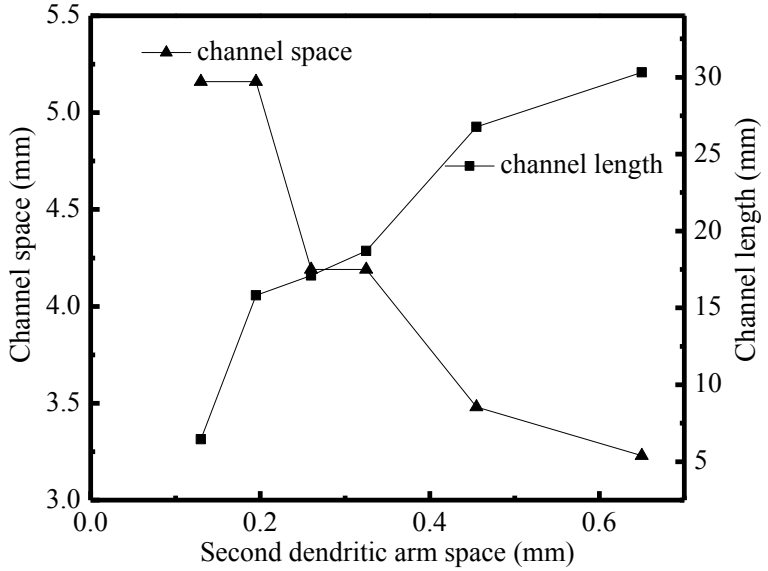

Figure 11: Influence of λ_2 on channel spacing, δ, and maximum channel length, l.

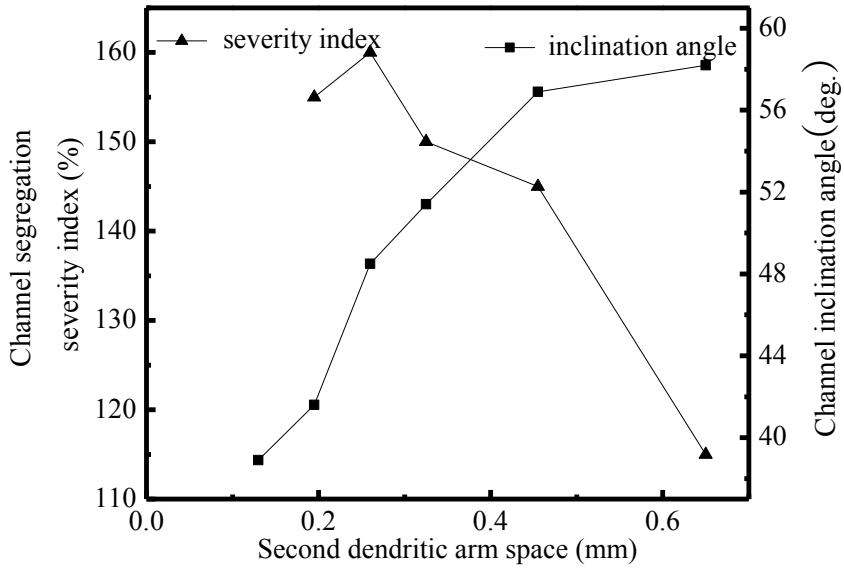

Figure 12: Influence of λ_2 on channel inclination angle, θ, and channel segregation severity index, Γ.

3.2 Local Rayleigh number

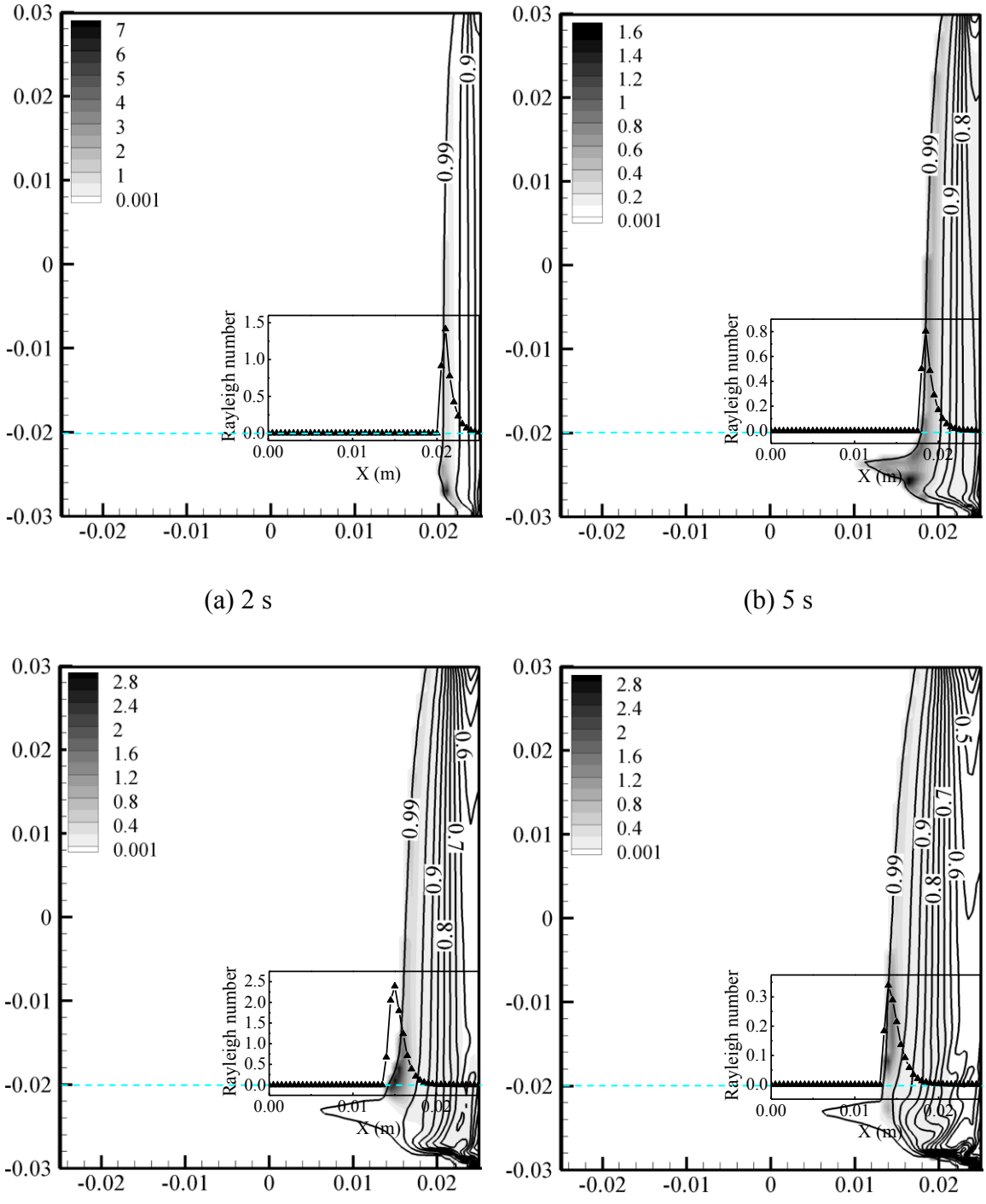

(a) 2 s

(b) 5 s

(c) 10 s

(d) 15 s

Figure 13: R_a number distribution in the solidifying mushy zone: (a) at 2 s; (b) at 5 s; (c) at 10 s; (d) 15 s. The R_a number distribution is shown in grey scale, overlaid with the liquid volume fraction f_ℓ. The inserted diagrams show the R_a number distribution profiles along the marked horizontal lines. This simulation is performed with $\lambda_2 = 455$ μm.

The local R_a number in the mushy zone (Eq. (1)) and its correlation to the formation of channel segregation are examined via Fig. 13. The h in Eq. (1) is estimated by $\left(T_{\text{liquidus}} - T\right)/G$, and the average permeability $\overline{K}$ is replaced by the local K. Distribution of the R_a number in the mushy zone is shown in Fig. 13. The R_a number initially increases in the mushy zone with increasing distance from the liquidus isotherm (h), reaching its maximum at a position very close to the solidification front (liquidus isotherm), where the solid fraction is about 0.03. As h further increases the R_a number decreases in the deep mushy zone, implying that the onset of flow instability may occur very close to the solidification front in the mushy zone. If there is any possibility for a channel to form, it will form in the front of the mushy zone. Upon initial channel formation, the channel continues to 'grow' via the flow-solidification interaction. This 'growth' does not occur by re-melting of the already-solidified phase, it is due to the change of the solidification rate in the immediate neighboring regions.

Uncertainty over a precise definition of a critical R_a number for channel formation has prevented us from using this criterion to predict channel formation directly. Table 1 summarizes the maximum Rayleigh number ($R_{a,Max}$) of each simulation case during initial stage of solidification. This $R_{a,Max}$ number can be used as an indicator to analyze the tendency of channel formation. The larger the $R_{a,Max}$, the more likely a channel will form. If $R_{a,Max}$ is correlated with the event of channel formation (yes or no), it is found that the cases with channel segregation must have a $R_{a,Max}$ larger than a critical value. This critical value is likely to fall in a range between 0.12 and 0.24, which is coincidently similar to the value as suggested by Beckermann and co-authors (0.25) [12], although here a different casting configuration and alloy are used. Normally, this critical number is dependent on the alloy even on the casting configuration.

A more precise critical $R_{a,Max}$ number could be identified through additional studies of Case 4 and Case 5, however this would not be entirely straightforward. Case 4 without channels and Case 5 with clearly identified channels can only be visually distinguished-these differences cannot, under the current analysis, be quantitatively expressed. Secondly, the maximum $R_{a,Max}$ number recorded in Table 1 does not represent the value at the exact position and moment of channel formation. This value cannot be used as criterion to predict the position of the channel initialization. Additionally, as previously discussed (Section 2.1), the flow-solidification interaction plays a significant role in the channel formation as well. In the upper-right region of the benchmark where the flow-solidification interaction term

$\vec{u}_\ell \cdot \nabla c_\ell$ is positive, a channel would not form even the critical $R_{a,Max}$ number is reached. Therefore, both the $R_{a,Max}$ number and the flow-solidification interaction term $\vec{u}_\ell \cdot \nabla c_\ell$ should be considered when analyzing the formation mechanism of the channel segregation.

4 Conclusions

In Part II of this two-part investigation the mechanism leading to the formation of channel segregation in a laterally solidified Sn-10 wt. % Pb benchmark was numerically studied. Both the initiation and growth of the channels were examined. The former is caused by flow perturbations in the mushy zone, which has been characterized by a mushy zone Rayleigh (R_a) number [6-7, 12] and the latter is the result of flow-solidification interactions [4-5].

The parameter studies have verified the use of the R_a number as a qualitative indicator for initialization of channel segregation. The cases with high R_a number, obtained by increasing the secondary dendrite arm spacing λ_2 and the solutal expansion coefficient β_c, are prone to channel segregation. A further step is taken to correlate the maximum Rayleigh number ($R_{a,Max}$) with the event of channel formation. For cases with channel segregation $R_{a,Max}$ must be larger than a critical value, determined to be in a range between 0.12 and 0.24. Coincidently, this $R_{a,Max}$ is similar to the value as found by Beckermann and co-authors (0.25) [12]. The above critical value of $R_{a,Max}$ cannot be used for firm quantitative prediction of channel formation as it does not represent the value at the exact position and moment of channel formation. Further studies are needed to identify a well-defined critical $R_{a,Max}$.

The R_a criterion alone is not a sufficient condition to predict channel segregation; the growth and stability of the channels must be determined by the resulting interdendritic flow-solidification interaction. With the assumption of the infinite solute diffusion in the interdendritic melt, Meherabian and co-authors proposed a flow-solidification interaction term, $\vec{u}_\ell \cdot \vec{G}$, to qualitatively analyze channel formation [1, 4-5]. The justification of using this term when solute diffusivities in the interdendritic melt are large is verified by the current model. The reported numerical parameter studies have demonstrated the influence of solute diffusivity in channel formation. For low solute diffusivity, the definition of the

flow-solidification interaction term $\vec{u}_\ell \cdot \nabla c_\ell$ should be used to avoid overestimation of channel segregation by the assumption of the infinite diffusion.

The sign of the flow-solidification interaction term, $\vec{u}_\ell \cdot \nabla c_\ell$, can be used to distinguish two solidification regions: a suppressed solidification region, where the sign of the flow-solidification interaction term is negative (flow is in the opposite direction of the liquid concentration gradient); and an accelerated solidification region, where the sign of the flow-solidification interaction term is positive (flow is in the same direction of the liquid concentration gradient). Channels can only occur in the suppressed solidification region, where an increase in local flow caused by a flow perturbation is reinforced by the resulting suppressed solidification. In this situation the flow becomes unstable and channels continue to grow. Channels do not form in the accelerated solidification region, where an increase in local flow intensity due to a flow perturbation is throttled by the resulting accelerated solidification. In this latter case flow perturbation is stabilized by flow-solidification interactions.

In the current benchmark simulation, remelting does not occur during channel formation, indicating that remelting is not a necessary condition for channel formation, which confirms a recent finding of Sawada et al. [22].

Acknowledgments

The authors acknowledge the discussions of the modeling results with Prof. H. Combeau from CNRS-Nancy and Prof. Y. Fautrelle from CNRS-SIMAP-EPM, France. The financial support by the Austrian Federal Ministry of Economy, Family and Youth and the National Foundation for Research, Technology and Development is gratefully acknowledged. Jun Li would like to thank the support from the China Scholarship Council.

References

[1] M.C. Flemings, G.E. Nereo, Trans. TMS-AIME 239 (1967) 1449-1461.

[2] R.J. McDonald, J.D. Hunt, Trans. TMS-AIME 245 (1969) 1993-1997.

[3] A. Kumar, B. Dussoubs, M. Založnik, H. Combeau, J. Phys. D: Appl. Phys. 42 (2009) 105503-105515.

[4] R. Meherabian, M. Keane, M. C. Flemings, Metall. Trans. 1 (1970) 1209-1220.

[5] J. J. Moore, N. A. Shah, Inter. Metals Reviews 28 (1983) 338-356.

[6] A.K. Sample, A. Hellawell, Metall. Trans. A 15 (1984) 2163-2173.

[7] M. G. Worster, Ann. Rev. Fluid Mech. 1 (1997) 91-122.

[8] K. Suzuki, T. Miyamoto, Trans. Iron Steel Inst. Jpn 14 (1974) 296-305.

[9] K. Suzuki, T. Miyamoto, Trans. Iron Steel Inst. Jpn 18 (1978) 80-89.

[10] W. H. Yang, J. J. deBarbadillo, K. Morita, T. Suzuki, W. Chen, K. M. Chang, JOM 56 (2004) 56-61.

[11] S. M. Copley, A. F. Giamei, S. M. Johnson, M. F. Hornbecker, Metall. Trans. 15A (1970) 2163-2173.

[12] C. Beckermann, J.P. Gu, W.J. Boettinger, Metall. Mater. Trans. A 31 (2000) 2545-2525.

[13] T. Sawada, K. Oikawa, K. Anzai, in: S.L. Cockroft, D. M. Maijer, (Eds.), Modeling of Casting, Welding and Advanced Solidification Processes XII, TMS, Warrendale, PA, USA, 2009, pp. 303-310.

[14] G. Guillemont, C. Gandin, M. Bellet, J. Crystal Growth 303 (2007) 58-68.

[15] M. Medina, Y. D. Terrail, F. Durand, Y. Fautrelle, Metall. Mater. Trans. B 35 (2004) 743-754.

[16] J. Guo, C. Beckermann, Numer. Heat Tr. A-Appl. 44 (2003) 559-576.

[17] E. Yoshio, Metall. Mater. Trans. B 42 (2011) 341-369.

[18] T.M. Pollack, W.H. Murphy, Metall. Mater. Trans. A 27 (1996) 1081-1094.

[19] M. Wu, A. Ludwig, Metall. Mater. Trans. A 37 (2006) 1613-1631.

[20] M. Wu, A. Ludwig, Metall. Mater. Trans. A 38 (2007) 1465-1475.

[21] M. Wu, L. Könözsy, A. Ludwig, W. Schützenhöfer, R. Tanzer, Steel Res. Int. 79 (2008) 56-63.

[22] T. Sawada, K. Oikawa, K. Anzai, F. Takahashi, K. Kajikawa, H. Yamada, J. JFS 82 (2010) 142-148.

Publication III

Study of the channel segregation using a two-phase columnar solidification model

Jun Li, Menghuai Wu, Jing Hao and Andreas Ludwig

In: the 3rd International Conference on Advances in Solidification Processes, in Aachen/Rolduc, June 7-10, 2011

IOP Conference Series: Materials Science and Engineering

Volume 27 012055 doi:10.1088/1757-899X/27/1/012055

Study of the channel segregation using a two-phase columnar solidification model

J Li, M Wu, J Hao and A Ludwig

Simulation and Modelling of Metallurgical Processes, Department of Metallurgy, University of Leoben, A-8700 Leoben, Austria

E-mail: jun.li@stud.unileoben.ac.at

Abstract

A two-phase columnar solidification model was used to study the formation mechanism of the channel segregation in a Sn-10 wt.% Pb benchmark ingot. The two phases considered in the current model are the melt and columnar phase. The morphology of the columnar dendrite trunks is approximated as step-wise cylinders with constant primary dendrite arm spacing. The growth kinetics of the columnar trunks is governed by the diffusion of the rejected solute element surrounding the columnar trunks. From the 3D modelling result one can 'visualize' the dynamic formation sequence of the channel segregation. The final channel segregation pattern shows a discontinuous, and lamellar- or plume-structure. The formation mechanism of the channels is due to the disturbed flow, which can accelerate and retard the local solidification rate in the mushy zone and near the solidification front. This study has also verified that the channel segregation can form in the condition without remelting, namely, remelting is not a necessary condition for channel segregation.

1 Introduction

Channel segregation is one of the most frequently observed segregation pattern in different casting processes, such as large steel ingots, vacuum-arc remelting or electro-slag remelting ingots, etc. [1-2]. The generally termed channel segregation is often called as 'A-segregate' in large steel ingot [3], or 'freckles' in directionally solidified turbine blade [4]. In the early literature the 'A-segregate' was also termed as lamellar- or plume-shaped segregation [5-6].

People have experimentally studied the formation mechanism of the channel segregation for several decades [7-8]. Recently, numerical models [9-13] provided an alternative method to investigate the mechanism of channel segregation. A widely accepted explanation to the formation of the channel segregation is [5]: it is the perturbed fluid flow of the solute-rich interdendritic melt which causes the remelting of the dendritic fragments in the mush zone, hence to form the channel. Therefore, people generally believe that the channel originate from and develop with remelting.

Modelling of channel segregation is a multiphase and multiscale problem. The most promising model is the multiphase volume-averaging approach pioneered by Beckermann and co-workers [14-15]. The two-phase columnar solidification model used here is a simplified version of the mixed columnar-equiaxed solidification model, which were developed by two of the current authors [16-18], by ignoring the appearance of the equiaxed phase. Details of the numerical model for the columnar solidification are described elsewhere [19].

2 Model description

Figure 1 shows a 2D configuration of the benchmark ingot (Sn-10 wt.% Pb), together with necessary boundary and initial conditions. Both 3D and 2D calculations are made. For the 3D simulation all the boundary conditions are the same as the 2D case except for the front and back walls for which we applied the non-slip condition for the fluid flow calculation, and a convective cooling condition for the heat transfer coefficient, h, equal to 50 W m^{-2} K^{-1} with an external temperature (T_{EXT}) of 298 K. All the thermo-physical properties, boundary conditions and numerical parameters used in this study are given in literature [20].

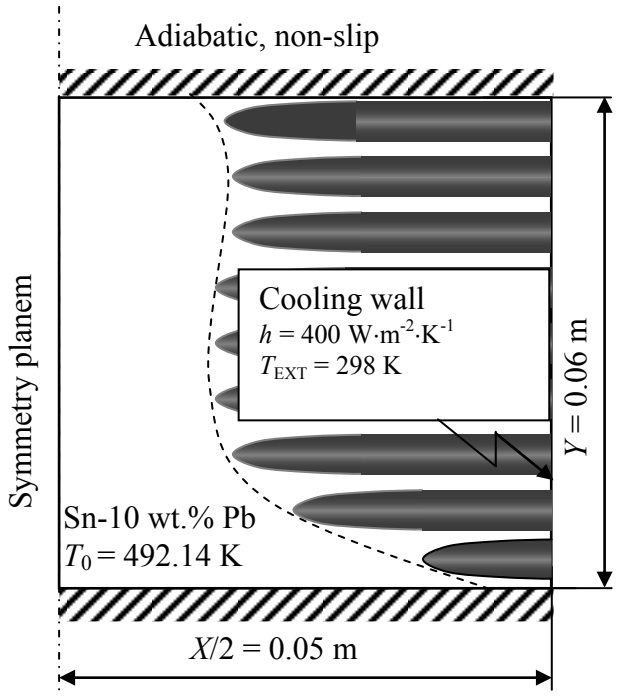

Figure 1: Configuration of the benchmark with boundary and initiation conditions.

Details of the numerical model for columnar solidification are described elsewhere [17, 19]. A brief outline of the model assumptions is given below.

1) Two phases are included in the model: the melt and the columnar dendrite trunks.

2) The morphology of the columnar dendrite trunks is approximated by step-wise cylinders, and the primary dendrite arm spacing, λ_1 , is constant. The arrangement of the cylindrical columnar trunks is assumed to be staggered.

3) The columnar trunks initially grow from the casting surface when constitutional undercooling is achieved. Solidification front coincides with the liquidus isotherm.

4) The liquid-to-solid mass transfer (solidification/melting) rate, $M_{\ell s}$, is calculated based on the radial growth velocity of the columnar trunks, v_{R_c} , which is governed by diffusion of solute element in the interdendritic melt surrounding each cylindrical trunk.

5) A linearly binary Sn-Pb phase diagram with a constant solute redistribution coefficient, *k*, and a constant liquidus slope, *m*, is used.

3 Simulation results and discussions

3.1 3D solidification results

Examples of the transient 3D simulation result at 100 seconds are shown in Figure 2(a)-(b). In Figure 2(a), the velocity vectors were shown in two planes (a vertical central plane and a horizontal plane with a distance of 0.01 m from the bottom), together with liquid volume fraction isolines. Figure 2(b) predicted the c_{mix} in gray scale (dark for the highest and light for the lowest value) with c_{mix}-isolines in the vertical central plane and the streamlines (arrows for flow direction) of the melt flow are also overlaid in this plane. For the alloy considered in the simulations (Sn-10 wt.% Pb), the interdendritic melt enriched with Pb solute element has a higher density than the bulk melt, and both the thermal and solute buoyancy forces lead to a downward flow along the solidification front. The resultant solute-enriched melt tends to create a downward flow near the solidification front, subsequently to form a clockwise circulation in the whole cavity, as seen in Figure 2(b). The liquid flow is obviously seen in the region where the liquid fraction is bigger than 0.4, while in the region where the liquid fraction is smaller than 0.3 the liquid velocity is unapparent. It means that the liquid melt can hardly flow through the dendritic mushy region where the liquid fraction is smaller than 0.3. When channels are initiated in the mush zone, the velocity fields (see paths of the streamlines) will be significantly changed. As the liquid volume fraction inside the channel is higher than in the neighboring regions, the permeability of the channels is relatively higher. Therefore, the interdendritic melt would take preferentially its path along the channel, and the streamlines are periodically diverted.

Transient development of the flow channels during solidification can be ‘visualized’ in Figure 3. The iso-surfaces of liquid volume fraction (f_ℓ = 0.35) are plotted. The regions enveloped in these iso-surfaces, where f_ℓ is bigger than 0.35, indicate the channels. The channels are 3D in nature, discontinuous, and lamellar-structured. They occur only in the right bottom region, which takes only a quarter of the whole calculation domain. The channels originate from the region adjacent to the cooling wall, and develop with a certain

angle (about 40 - 60 degrees to the horizontal plane). The channel space (distance between neighboring channels) is almost constant, or slightly adjusted with the time during solidification.

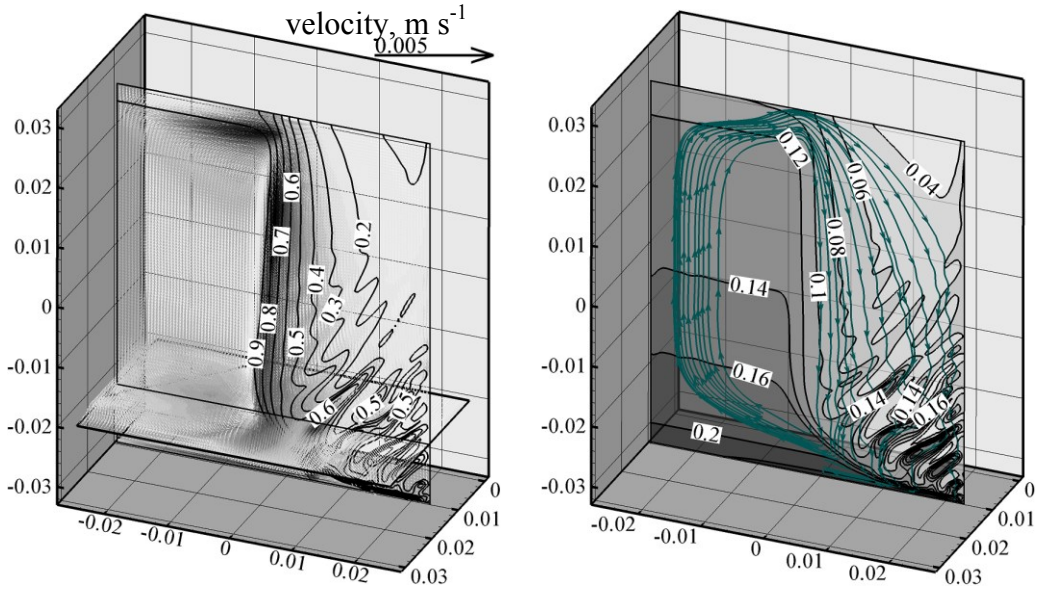

(a) velocity & liquid fraction (b) c_{mix} & streamlines

Figure 2: 3D results at 100 s. (a) velocity vectors shown in two planes (a vertical central plane and a horizontal plane with 0.01 m from bottom), together with liquid volume fraction isolines in the vertical central plane; (b) predicted c_{mix} in gray scale and c_{mix}-isolines in the vertical central plane, the streamlines (arrows for flow direction) of the melt flow are also overlaid in this plane.

The global solidification sequence shows that in the upper part of the ingot the solidification front, approximated with the iso-surface of f_ℓ = 0.35, sweeps much faster than in the bottom region. The explanation for this is that the downward flow in the mushy zone transports the Pb-rich interdendritic melt from the upper to the bottom region; hence the liquidus temperature in the upper region is increased and in the bottom region is depressed. As a consequence the solidification rate in the upper region is accelerated, and in the bottom region is retarded.

The final macrosegregation profile of this ingot is predicted and shown in Figure 4. Globally, negative segregation is predicted in the upper-right region, and positive segregation is predicted in the low-left region. The minimum and maximum values of c_{mix}

in this calculation are 0.03 and 0.35 of Pb in mass fraction, respectively. Channel segregation pattern is clearly seen. The structure of the channel segregates (inclined angle, channel space, number of the channels) corresponds to the previous analysis of Figure 3.

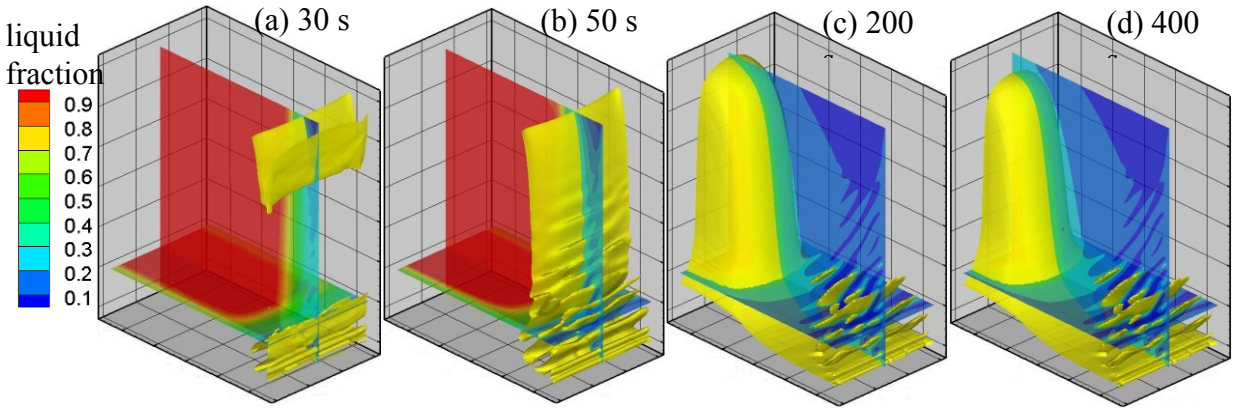

Figure 3: Predicted 3D solidification sequence from (a) 30 s to (d) 400 s. The liquid volume fraction in two planes (a vertical central plane and a horizontal plane with a distance of 0.01 m from the bottom) is shown in colour scale. The iso-surfaces of liquid volume fraction (f_ℓ = 0.35) are shown to demonstrate the formation sequence of the flow channels.

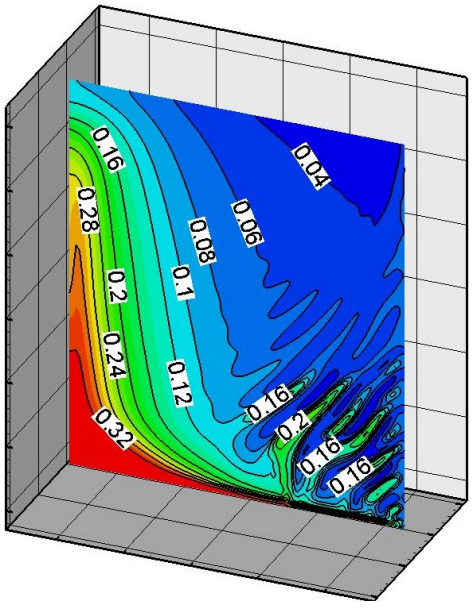

Figure 4: Distribution of mixture mass fraction of Pb at the end of the solidification.

3.2 The formation mechanism of the channel segregation

In the current columnar solidification model, if we further assume that the diffusion within a local volume in the interdendritic melt region is infinitive, then we have [21],

$$\frac{\partial c_\ell}{\partial t} = -(1-k)\frac{c_\ell}{f_\ell}\frac{\partial f_\ell}{\partial t} - \vec{u}_\ell \cdot \nabla c_\ell . \tag{1}$$

From $T = T_\mathrm{f} + m c_\ell^*$, we get

$$\frac{\partial c_\ell^*}{\partial t} = \frac{1}{m}\frac{\partial T}{\partial t} \tag{2}$$

Eq. (3) minus Eq. (2),

$$\frac{\partial (c_\ell^* - c_\ell)}{\partial t} = (1-k)\frac{c_\ell}{f_\ell}\frac{\partial f_\ell}{\partial t} + \frac{1}{m}\frac{\partial T}{\partial t} + \vec{u}_\ell \cdot \nabla c_\ell . \tag{3}$$

In the LHS of Eq. (3), $\left(c_\ell^* - c_\ell\right)$ is the driving force for solidification/melting, which governs the solidification/melting rate, $M_{\ell \mathrm{c}}$ [17]. Therefore, the local solidification/melting is actually induced by three contributions, corresponding to the three RHS terms of Eq. (3). The 1st RHS term is the contribution of the solidification-induced solute enrichment of the interdendritic melt, the sign of which is always negative with the progress of solidification. The solidification rate decreases with the enrichment of solute in the interdendritic melt. The 2nd RHS term is the contribution of cooling rate, the sign of which is always positive. It means that the solidification rate increases with enhanced cooling. The 3rd term is what we called perturbation term, $\vec{u}_\ell \cdot \nabla c_\ell$. Its sign can be positive or negative, depending on the interdendritic flow, as schematically shown in Figure 5. In the mush zone, where the melt flows in the direction of the concentration gradient, the above term is positive. It means that the local solidification rate is accelerated; hence this zone is called as solidification-accelerated zone. On the contrary, in the mush zone, where the melt flows in the opposite direction of the concentration gradient, the above term is negative. It means that the local solidification rate is retarded; hence this zone is called as solidification-retarded zone. The physical explanation to the contribution of the perturbation term is as follows. The

interdendritic melt flow modifies the local concentration of the melt, c_ℓ, which in turn changes the driving force for the solidification $\left(c_\ell^* - c_\ell\right)$.

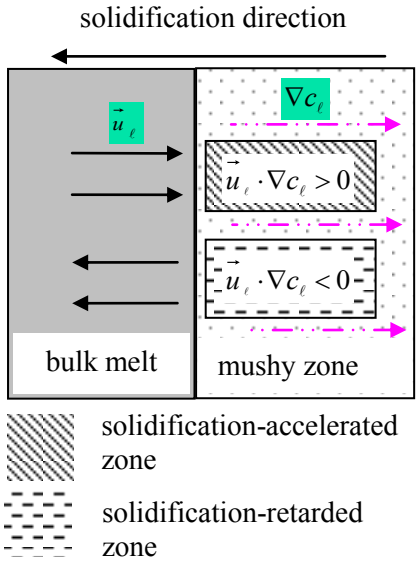

Figure 5: Schematic of the solidification-accelerated and solidification-retarded zones.

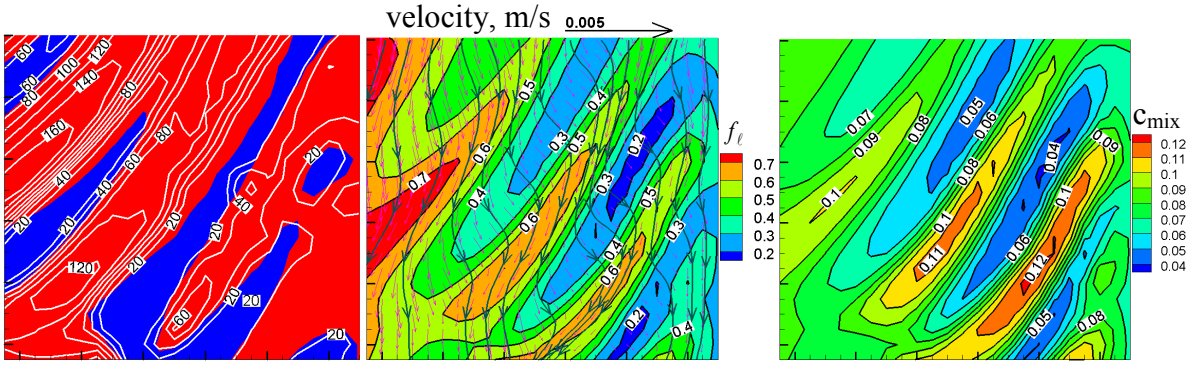

Figure 6: Analysis of the formation mechanism of the channel segregation. Only the relevant simulation results zoomed in the right bottom of the mould cavity are shown (t = 40 s). (a) Contour of $\vec{u}_\ell \cdot \nabla c_\ell$ in red (positive) and blue (negative), overlaid by the isolines of mass transfer rate, $M_{\ell c}$. (b) Contour of liquid fraction, overlaid by the vectors of liquid velocity and the streamlines (black). (c) Contour of c_{mix} in mass fraction.

Channel segregations occur in the solidification-retarded zone. In this zone, the increase rate of the volume fraction solid, f_s, is lowered down by the retarded solidification, hence to induce a relative low f_s in comparison to the neighboring zones where the perturbation

term is positive. The relative lower f_s in this zone will enhance the flow, as the permeability increases with the decrease of f_s. Further on, the perturbation term would become more negative due to the enhanced flow (Eq. (3)), and the local solidification rate becomes even smaller. As a consequence, the ratio of the local f_s to the f_s of its neighboring zones becomes smaller and smaller, hence a channel is initiated. This mechanism is verified by the current modeling results, as detailed in Figure 6. In this figure the red colour indicates the positive value of $\vec{u}_\ell \cdot \nabla c_\ell$, and the blue shows the negative value of $\vec{u}_\ell \cdot \nabla c_\ell$. The blue zones where the values of the perturbation term $\vec{u}_\ell \cdot \nabla c_\ell$ are negative (in another word, the direction of interdendritic velocity vector, $\vec{u}_\ell$, and the liquid concentration gradient vector, ∇c_ℓ, is opposite) are the solidification-retarded zones. As discussed above, the solidification rate in these solidification-retarded zones is decreased by the flow, hence the value of solidification (mass transfer) rate, $M_{\ell c}$, in these solidification-retarded zones are very small, namely, 20 - 40 $kg \cdot s^{-1} \cdot m^{-3}$. In comparison, the solidification rate, $M_{\ell c}$, is very high (as high as 160 $kg \cdot s^{-1} \cdot m^{-3}$) in the solidification-accelerated (red) zones. As a consequence, channels are initiated from the solidification-retarded (blue) zones. One interesting finding is that the channels occur without evidence of remelting, i.e. $M_{\ell c} \geq 0$. Additionally, it is noted that the streamlines change their direction abruptly when they reached the channels. The streamlines are diverted in the direction of the channels.

Moore and Shah [5] have also discussed the above mechanism of channel segregation. Recently, Sawada et al [22] have studied the mechanism of the channel segregation in the vertical directional solidification with a Pb-10 wt.% Sn alloy, and got a similar conclusion about the solidification accelerated and retarded regions.

4 Conclusion

The 3D simulations with a two-phase columnar solidification model have ‘visualized’ the transient development of the channel segregation in the benchmark ingot (Sn-10 wt.% Pb). Channel segregation appears near the wall-bottom corner. The final channel segregation pattern shows a discontinuous, and lamellar- or plume-structure.

It is verified by the current model that the remelting is not the necessary condition for the formation of channel segregation. Although remelting is not predicted in the current benchmark, the channel segregation still appears.

The origin of the channels is due to the flow perturbation. The numerical study has shown the strong co-relation of the local solidification rate to the perturbation term, $\vec{u}_\ell \cdot \nabla c_\ell$. If the perturbation term becomes negative locally, the solidification rate will be significantly retarded there, hence to promote the initiation of a channel. In return the newly initiated channel will strengthen the flow perturbation, the perturbation term becomes more negative, and the channel becomes more stable.

Acknowledgments

The author (Jun Li) would like to thank the support from the China Scholarship Council.

References

[1] Suzuki K and Miyamoto T 1978 Transactions ISIJ 18 80-9

[2] Van den Avyle J A, Van D A, Brooks J A and Powell A C 1998 JOM 50 22-5

[3] Suzuki K and Taniguchi K 1981 Transactions ISIJ 21 235-42

[4] Beckermann C, Gu J P and Boettinger W J 2000 Metall. Mater. Trans. A 31A 2545-57

[5] Moore J J and Shah N A 1983 Inter. Metals Reviews 28(6) 338-356

[6] Marburg E 1953 Transactions AIME 5 157-72

[7] McDonald R J and Hunt J D 1970 Metall. Trans. 1 1787-8

[8] Sample A K and Hellawell A 1984 Metall. Trans. A 15A 2163-73

[9] Kumar A, Dussoubs B, Založnik M and Combeau H 2009 J. Phys. D: Appl. Phys. 42 105503-15

[10] Shahani H, Amberg G, and Fredriksson H 1992 Metall. Trans. A 23A 2301-11

[11] Schneider M C and Beckermann C 1995 Int. J. Heat Mass Transfer 38 3455-73

[12] Ahmad N, Combeau H, Desbiolles J, Jaldanti T, Lesoult G, Rappaz J, Rappaz M and Stomp C 1998 Metall. Mater. Trans. 29A 617-30

[13] ZaložnikM and Combeau H 2009 McWASP XII, TMS editors Cockroft S L and Maijer D M (Warrendale, PA, USA) 253–60

[14] Ni J and Beckermann C 1991 Metall. Trans. B 22B 349-61

[15] Wang C Y and Beckermann C 1996 Metall. Mater. Trans. A 27A 2754-64

[16] Ludwig A and Wu M 2005 Mater. Sci. Eng. A 413-414 109-114

[17] Wu M and Ludwig A 2006 Metall. Mater. Trans. A 37A 1613-31

[18] Wu M and Ludwig A 2007 Metall. Mater. Trans. A 38A 1465-75

[19] Ludwig A, Grasser M, Wu M, Kuhn A and Riedle J 2006 Int. J. Fluid Dynamics Mater. Proc. 1 285-300

[20] Bellet M, Combeau H, Fautrelle Y, Gobin D, Rady M, Aruis E, Budenkova O, Dussoubs B, Duterrail Y, Kumar A, Candin C A, Goyeau B, Mosbah S and Založnik M 2009 Int. J. Therm. Sci. 48 2013-16

[21] Wu M, Könözsy L, Ludwig A,Schützenhöfer W,Tanzer R 2008 Steel Research Int 79 56-63

[22] Sawada T, Oikawa K, Anzai K, Takahashi F, Kajikawa K and Yamada H 2010 J. JFS 82 142

Publication IV

Simulation of macrosegregation in a 2.45-ton steel ingot using a three-phase mixed columnar-equiaxed model

Jun Li, Menghuai Wu, Andreas Ludwig, Abdellah Kharicha

International Journal of Heat and Mass Transfer

Under revision, June 2013

Simulation of macrosegregation in a 2.45-ton steel ingot using a three-phase mixed columnar-equiaxed model

Jun Li[a,b], Menghuai Wu[a,b*], Andreas Ludwig[b], Abdellah Kharicha[a,b]

[a] Christian Doppler Lab for Adv. Process Simulation of Solidification and Melting,

[b] Chair of Simulation and Modeling of Metall. Processes, Univ. of Leoben, Austria

*Corresponding author. Tel.: +43 38424023103; Fax: +43 38424023102.

Email address: menghuai.wu@unileoben.ac.at

Abstract

A three-phase mixed columnar-equiaxed solidification model is used to calculate the macrosegregation in a 2.45 ton steel ingot. The main features of mixed columnar-equiaxed solidification in such an ingot can be quantitatively modelled: growth of columnar dendrite trunks; nucleation, growth and sedimentation of equiaxed crystals; thermosolutal convection of the melt; solute transport by both convection and crystal sedimentation; and the columnar-to-equiaxed transition (CET). The predicted as-cast macrostructure and the segregation pattern are in qualitative agreement with the reported experimental results. Parameter study on the numerical grid size and the nucleation of the equiaxed crystals are performed, and some segregation mechanisms are numerically analyzed. Discontinued positive-negative segregation just below the hot top is predicted because of the formation of a local mini-ingot and the subsequent sedimentation of equiaxed grain within the mini-ingot. Quasi A-segregates in the middle radius region between the casting outer surface and the centreline are also found. The quasi A-segregates originate from the flow instability, but both the appearance of equiaxed crystals and their interaction with the growing columnar

dendrite tips significantly strengthen the segregates. The equiaxed phase is not a necessary condition for the formation of quasi A-segregates. The quantitative discrepancy between the predicted and experimental results is also discussed.

Key words: macrosegregation; ingot; multiphase modelling; crystal sedimentation; solidification.

1 Introduction

Macrosegregation, or compositional heterogeneity, is a very common and serious defect in large steel ingots. This compositional heterogeneity occurs due to the relative motion between the liquid and solid phases during solidification. This relative motion can arise from thermosolutal convection, shrinkage-induced feeding flow, flotation and sedimentation of free moving crystals, mechanical or electromagnetic stirring, flow induced by pore or gas bubble formation, deformation of the solid skeleton, and capillary force-induced flow [1]. A lot of experiments were done to study the macrosegregation in steel ingots [2-4]. The typical segregation pattern in a steel ingot consists of a positive segregation in the upper region, a conic negative segregation in the lower region, V-segregates along the centreline, and A-segregates in the middle radius region between the casting outer surface and the centreline [5-6].

Since the first modelling attempt by Flemings et al. [7-8], several macrosegregation models have been developed [9-12]. Gu and Beckermann [12] were the first to apply a fully coupled, multicomponent solidification model, with melt convection to a large industry-scale ingot ($1.016 \times 2.08 \times 2.819$ m^3); their simulation qualitatively agreed with the positive segregation observed in the upper region of the ingot. However, because the sedimentation of free equiaxed crystals was neglected, they could not properly predict the negative segregation at the lower region of the ingot. Ludwig et al. [13] presented a new method of coupling a ternary phase diagram with a multiphase process simulation. Their model was applied to a continuous bronze casting, and a reasonable result was obtained. Combeau et al. [14-15] presented a two-phase (solid and liquid) model to study the influences of both motion and morphology of equiaxed grains on a 3.3-ton, large steel ingot. Some progress was made towards predicting the behaviour at the negative segregation zone in the lower region of the ingot, and this model is in good agreement with the experimental results.

However, these researchers did not distinguish the columnar phase from the equiaxed phase; both of which are present and interact with each other during solidification.

Researchers have been investigating the mechanism of formation for A-segregation (channel segregation) for decades, and various mechanisms have been suggested [4, 16-17]. The most accepted mechanism supports that the main factor in producing A-segregation is the fluid flow of the segregated melt within the mushy zone, which is primarily controlled by both the alloy composition and the thermal conditions prevailing during the solidification process.

Wu et al. [18-19] developed a mixed columnar-equiaxed model, which directly accounts for the nucleation and growth of equiaxed globular grains, the growth of columnar dendrite trunks, and the effect of both equiaxed grain sedimentation and melt convection. The previous studies successfully predicted both the conic negative segregation in the lower region of the ingot and the columnar-to-equiaxed-transition (CET). However, due to both the complexity of the model and limited computational capabilities, the previous studies were only based on the laboratorial scale of steel ingots. In this study, the previous model is modified to study macrosegregation in a 2.45-ton, large-end-up, industry steel ingot that was reported in the literature [3].

2 Model description

Details of the three-phase mixed columnar-equiaxed solidification model can be found in the literature [18-21]. Here, only a brief outline of the model and the assumptions made are given.

1) Three phases are defined: the primary liquid phase (ℓ), the equiaxed phase (e), and the columnar phase (c). The corresponding phase fractions are f_ℓ, f_e and f_c with $f_\ell + f_\mathrm{e} + f_\mathrm{c} = 1$. Both the liquid and equiaxed phases are moving phases, for which the corresponding Navier-Stokes equations are solved. The columnar phase is assumed to adhere to the wall, thus a momentum equation for the columnar phase is not considered.

2) Columnar dendrites are approximated by cylinders extending from the mould wall towards the casting centre. The advance of the columnar tip front is tracked during the solidification.

3) Equiaxed grains are approximated as spheres. However, to calculate the drag force, the morphology of the equiaxed grains is modelled as octahedra.

4) A three-parameter heterogeneous nucleation law is used for the nucleation of equiaxed grains. Neither fragmentation nor grain attachment is currently considered.

5) The growth of both the columnar trunk and the equiaxed grain are governed by diffusion; the concentration difference ($c_\ell^* - c_\ell$) is the driving force for the growth of columnar trunks and equiaxed grains. Back diffusion in the solid is also considered for both equiaxed and columnar phases.

6) Volume-averaged concentrations (c_ℓ, c_s) are calculated, and macrosegregation is characterised by the concentration of the mixture, c_{mix}. Thermodynamic equilibrium is assumed at the liquid-solid interface, which dictates the concentrations at the liquid-solid interface (c_ℓ^*, c_s^*).

7) A linearised, binary Fe-C phase diagram is used with a constant solute redistribution coefficient *k* and a constant liquidus slope *m*.

8) Resistance to interdendritic flow in the mushy zone is calculated using a permeability law based on the Blake-Kozeny approach [22].

9) The growth of the columnar primary tips stops when the volume fraction of the equiaxed phase reaches 0.49 (hard blocking criterion) in front of the primary columnar dendrite tips [23].

10) The packing limit for the equiaxed phase is set as $f_e + f_c \geq 0.637$ [18-19, 24], and the equiaxed crystals are trapped by the columnar dendrite trunk when the local volume fraction of the columnar phase reaches a critical value of 0.2 [25].

11) Solidification shrinkage is not accounted for, and thermosolutal convection is modelled using the Boussinesq approach.

Conservation equations, sources and exchange terms, and auxiliary equations are summarised in Table 1. The symbols used in the table are described in the nomenclature.

The model described here is developed within the framework of the CFD software package, ANSYS-Fluent version 14.5, which provides a platform for solving the conservation equations and provides flexibility in defining exchange and source terms within the conservation equations, including modification of the transport quantities. For each time step, up to 60 iterations may be necessary to decrease the normalized residuals of continuity, momentum conservation, volume fraction, species transport and user-defined scalar conservation equations to a value below the convergence criterion of 10^{-4} and the enthalpy conservation equations below that of 10^{-7}. Due to the complexity of the multiphase coupling, the time step should be kept small (10^{-2}~10^{-3}) to ensure the above convergence criteria are fulfilled. The optimal time step must be determined by trial simulations. All calculations are run in parallel on 8 CPUs (Intel Nehalem Cluster 2.93 GHz).

3 Configuration of the ingot

A large number of industry steel ingots have been poured and analysed for macrosegregation during the last century [2-3]. They were sectioned longitudinally along the axes, and subject to two different analyses: sulphur print and chemical analysis of drilling samples. The sulphur print, presenting the degree of heterogeneity of the sulphur element, was taken as indicative of general heterogeneity of other elements like carbon and phosphorus. Chemical analysis of drilling samples (average diameter of 10 mm drilled from the ingot section) gave a quantitative macrosegregation map for each alloy element. Here a representative 2.45-ton, large-end-up ingot (Fe-0.45 wt.%C) is studied here. The ingot had a square, cross-sectional area and was cast in a chilled mould; a 2D-axis symmetrical simulation was performed to approximate the solidification behaviour in the square cross-section of the ingot. The configuration of this ingot, along with the necessary boundary and initial conditions, is described in Figure 1. Table 2 lists the thermodynamic and physical properties of the ingot. Because the experiment was performed many decades ago and because of the lack of a precise process description, assumptions must be made for certain process parameters and boundary conditions. Here, the heat transfer coefficient is based on the final solidification time, which refers to the classical theory and experimental values [2].

Table 1. Conservation equations, sources and exchange terms, and auxiliary equations.

I. Conservation equations

Mass:

$$\frac{\partial}{\partial t}\left(f_\ell \rho_\ell\right)+\nabla\cdot\left(f_\ell \rho_\ell \vec{u}_\ell\right)=M_{\mathrm{e}\ell}+M_{\mathrm{c}\ell} \tag{1}$$

$$\frac{\partial}{\partial t}\left(f_{\mathrm{e}} \rho_{\mathrm{e}}\right)+\nabla\cdot\left(f_{\mathrm{e}} \rho_{\mathrm{e}} \vec{u}_{\mathrm{e}}\right)=M_{\ell\mathrm{e}} \tag{2}$$

$$\frac{\partial}{\partial t}\left(f_{\mathrm{c}} \rho_{\mathrm{c}}\right)=M_{\ell\mathrm{c}} \tag{3}$$

Momentum:

$$\frac{\partial}{\partial t}\left(f_\ell \rho_\ell \vec{u}_\ell\right)+\nabla\cdot\left(f_\ell \rho_\ell \vec{u}_\ell\otimes\vec{u}_\ell\right)=-f_\ell\nabla p+\nabla\cdot\bar{\bar{\tau}}_\ell+f_\ell\rho_\ell\vec{g}_\ell^{\,'}-\vec{U}_{\ell\mathrm{e}}-\vec{U}_{\ell\mathrm{c}} \tag{4}$$

with $\vec{g}_\ell^{\,'}=\dfrac{\rho_\ell^{\mathrm{b}}(T,c)-\rho_\ell}{\rho_\ell}\vec{g}$,

$\rho_\ell^{\mathrm{b}}(T,c)=\rho_\ell\cdot\left[1+\beta_{\mathrm{T}}\cdot(T^{\mathrm{ref}}-T_\ell)+\beta_{\mathrm{c}}\cdot(c^{\mathrm{ref}}-c_\ell)\right]$

and $\vec{U}_{\ell\mathrm{e}}=-\vec{U}_{\mathrm{e}\ell}=\vec{U}_{\ell\mathrm{e}}^{\mathrm{p}}+\vec{U}_{\ell\mathrm{e}}^{\mathrm{d}}$ and $\vec{U}_{\ell\mathrm{c}}=\vec{U}_{\ell\mathrm{c}}^{\mathrm{p}}+\vec{U}_{\ell\mathrm{c}}^{\mathrm{d}}$

$$\frac{\partial}{\partial t}\left(f_{\mathrm{e}} \rho_{\mathrm{e}} \vec{u}_{\mathrm{e}}\right)+\nabla\cdot\left(f_{\mathrm{e}} \rho_{\mathrm{e}} \vec{u}_{\mathrm{e}}\otimes\vec{u}_{\mathrm{e}}\right)=-f_{\mathrm{e}}\nabla p+\nabla\cdot\bar{\bar{\tau}}_{\mathrm{e}}+f_{\mathrm{e}}\rho_{\mathrm{e}}\vec{g}_{\mathrm{e}}^{\,'}+\vec{U}_{\ell\mathrm{e}}+\vec{U}_{\mathrm{ce}} \tag{5}$$

with $\vec{g}_{\mathrm{e}}^{\,'}=\frac{\Delta\rho}{\rho_{\mathrm{e}}}\vec{g}$ and $\vec{U}_{\mathrm{ce}}=\vec{U}_{\mathrm{ce}}^{\mathrm{p}}+\vec{U}_{\mathrm{ce}}^{\mathrm{d}}$

Species:

$$\frac{\partial}{\partial t}\left(f_\ell \rho_\ell c_\ell\right)+\nabla\cdot\left(f_\ell \rho_\ell \vec{u}_\ell c_\ell\right)=\nabla\cdot\left(f_\ell \rho_\ell D_\ell \nabla c_\ell\right)-C_{\ell\mathrm{c}}-C_{\ell\mathrm{e}} \tag{6}$$

$$\frac{\partial}{\partial t}\left(f_{\mathrm{e}} \rho_{\mathrm{e}} c_{\mathrm{e}}\right)+\nabla\cdot\left(f_{\mathrm{e}} \rho_{\mathrm{e}} \vec{u}_{\mathrm{e}} c_{\mathrm{e}}\right)=\nabla\cdot\left(f_{\mathrm{e}} \rho_{\mathrm{e}} D_{\mathrm{e}} \nabla c_{\mathrm{e}}\right)+C_{\ell\mathrm{e}} \tag{7}$$

$$\frac{\partial}{\partial t}\left(f_{\mathrm{c}} \rho_{\mathrm{c}} c_{\mathrm{c}}\right)=\nabla\cdot\left(f_{\mathrm{c}} \rho_{\mathrm{c}} D_{\mathrm{c}} \nabla c_{\mathrm{c}}\right)+C_{\ell\mathrm{c}} \tag{8}$$

Enthalpy:

$$\frac{\partial}{\partial t}\left(f_\ell \rho_\ell h_\ell\right)+\nabla\cdot\left(f_\ell \rho_\ell \vec{u}_\ell h_\ell\right)=\nabla\cdot\left(f_\ell k_\ell \nabla\cdot T_\ell\right)+Q_{\mathrm{c}\ell}+Q_{\mathrm{e}\ell} \tag{9}$$

$$\frac{\partial}{\partial t}\left(f_{\mathrm{e}} \rho_{\mathrm{e}} h_{\mathrm{e}}\right)+\nabla\cdot\left(f_{\mathrm{e}} \rho_{\mathrm{e}} \vec{u}_{\mathrm{e}} h_{\mathrm{e}}\right)=\nabla\cdot\left(f_{\mathrm{e}} k_{\mathrm{e}} \nabla\cdot T_{\mathrm{e}}\right)+Q_{\ell\mathrm{e}} \tag{10}$$

$$\frac{\partial}{\partial t}\left(f_{\mathrm{c}} \rho_{\mathrm{c}} h_{\mathrm{c}}\right)=\nabla\cdot\left(f_{\mathrm{c}} k_{\mathrm{c}} \nabla\cdot T_{\mathrm{c}}\right)+Q_{\ell\mathrm{c}} \tag{11}$$

with $Q_{\ell e} = -Q_{e\ell} = Q_{\ell e}^{p} + Q_{\ell e}^{d}$ and $Q_{\ell c} = -Q_{c\ell} = Q_{\ell c}^{p} + Q_{\ell c}^{d}$

where $h_\ell = \int_{T_{ref}}^{T_\ell} c_p^\ell dT + h_\ell^{ref}$, $h_e = h_c = \int_{T_{ref}}^{T_e} c_p^e dT + h_e^{ref}$ and

$L = h_\ell^{ref} - h_e^{ref}$

2. Nucleation and transport of the equiaxed grains

Trans. equation:

$$\frac{\partial}{\partial t} n + \nabla \cdot (\vec{u}_e n) = N_e \tag{12}$$

Nucleation:

$$N_e = \frac{dn}{dt} = \frac{dn}{d(\Delta T)} \cdot \frac{d(\Delta T)}{dt} = \frac{d(\Delta T)}{dt} \cdot \frac{n_{max}}{\sqrt{2\pi} \cdot \Delta T_\sigma} \cdot e^{-\frac{1}{2}\left(\frac{\Delta T - \Delta T_N}{\Delta T_\sigma}\right)^2} \tag{13}$$

where $\Delta T = T_f + m c_\ell - T$ is the constitutional undercooling

3. Mass transfer

Equiaxed

Equi. grain growth velocity:

$$v_{R_e} = \frac{dR_e}{dt} = \frac{D_\ell}{R_e\left(1 - R_e/R_{f,e}\right)} \cdot \frac{c_\ell^* - c_\ell}{c_\ell^* - c_s^*} + \frac{D_s}{\sigma_e} \cdot \frac{(c_s^* - c_s)}{(c_\ell^* - c_s^*)} \cdot \frac{\rho_s}{\rho_\ell} \tag{14}$$

with $\sigma_e = d_e/10$ [14]

Mass transfer:

$$M_{\ell e} = v_{R_e} \cdot \left(n \cdot \pi d_e^2\right) \cdot \rho_e \cdot f_\ell \tag{15}$$

Columnar

Col. trunk growth velocity:

$$v_{R_c} = \frac{dR_c}{dt} = \frac{D_\ell}{R_c} \cdot \frac{\left(c_\ell^* - c_\ell\right)}{\left(c_\ell^* - c_s^*\right)} \cdot \ln^{-1}\left(\frac{R_{f,c}}{R_c}\right) + \frac{D_s}{\sigma_c} \cdot \frac{(c_s^* - c_s)}{(c_\ell^* - c_s^*)} \cdot \frac{\rho_c}{\rho_\ell} \tag{16}$$

with $\sigma_c = d_c/10$ [14]

Mass transfer for the trunks:

$$M_{\ell c} = v_{R_c} \cdot \left(\pi d_c / \lambda_1^2\right) \cdot \rho_c \cdot \Phi_{imp} \tag{17}$$

Mass transfer incl. col. tips:

$$M_{\ell c} = v_{R_c} \cdot n_c \cdot (\pi d_c \cdot l) \cdot \rho_\ell \cdot \Phi_{imp} + v_{tip} \cdot n_c \cdot \left(\pi R_{tip}^2\right) \cdot \rho_\ell \cdot \Phi_{imp} \tag{18}$$

where, v_{tip} and R_{tip} are based on LGK model [26]

Growing surface impingement:

$$\Phi_{imp} = \begin{cases} 1 & d_c \le \lambda_1 \\ 4 f_\ell / (4 - \pi) & d_c > \lambda_1 \end{cases} \tag{19}$$

4. Source and exchange terms

Momentum transfer:

$$\vec{U}_{\ell e}^{p} = \begin{cases} \vec{u}_\ell \cdot M_{\ell e} & \text{solidification} \\ \vec{u}_e \cdot M_{\ell e} & \text{melting} \end{cases} \qquad \vec{U}_{\ell e}^{d} = K_{\ell e} \cdot (\vec{u}_\ell - \vec{u}_e)$$

The drag force coefficient (20)

$K_{\ell e}$ ·refers to [18-19]

$$\vec{U}_{\ell c}^{\,p}=\begin{cases}\vec{u}_{\ell}\cdot M_{\ell c} & \text{solidification}\\ \vec{u}_{c}\cdot M_{\ell c} & \text{melting}\end{cases}$$

$$\vec{U}_{\ell c}^{\,d}=\frac{f_{\ell}^{2}\cdot\mu_{\ell}}{K}\cdot\vec{u}_{\ell}$$

where

$$K=6\times10^{-4}\cdot\lambda_{1}^{2}\cdot\frac{f_{\ell}^{3}}{(1-f_{\ell})^{2}} \qquad (21)$$

Species transfer:

$$C_{\ell e}=\begin{cases}k\cdot c_{\ell}^{*}\cdot M_{\ell e}+ & \text{solidification}\\ S_{A}^{e}\cdot\rho_{e}\cdot\dfrac{D_{s}}{\sigma_{e}}\cdot(c_{s}^{*}-c_{s}) & \\ c_{e}\cdot M_{\ell e} & \text{melting}\end{cases} \qquad (22)$$

$$C_{\ell c}=\begin{cases}k\cdot c_{\ell}^{*}\cdot M_{\ell c}+ & \text{solidification}\\ S_{A}^{c}\cdot\rho_{c}\cdot\dfrac{D_{s}}{\sigma_{c}}\cdot(c_{s}^{*}-c_{s}) & \\ c_{c}\cdot M_{\ell c} & \text{melting}\end{cases} \qquad (23)$$

Enthalpy transfer and latent heat:

$$Q_{\ell e}^{p}=\begin{cases}h_{\ell}\cdot M_{\ell e} & \text{solidification}\\ h_{e}\cdot M_{\ell e} & \text{melting}\end{cases}$$

$$Q_{\ell e}^{d}=H^{*}\cdot(T_{\ell}-T_{e})$$

where $H^{*}=10^{9}$ W·m^{-2}·K^{-1}

$$Q_{\ell c}^{p}=\begin{cases}h_{\ell}\cdot M_{\ell c} & \text{solidification}\\ h_{e}\cdot M_{\ell c} & \text{melting}\end{cases}$$

$$Q_{\ell c}^{d}=H^{*}\cdot(T_{\ell}-T_{c})$$

where $H^{*}=10^{9}$ W·m^{-2}·K^{-1} (24)

5. Auxiliary equation

Mixture concentration:

$$c_{mix}=\frac{c_{\ell}\cdot\rho_{\ell}\cdot f_{\ell}+c_{e}\cdot\rho_{e}\cdot f_{e}+c_{c}\cdot\rho_{c}\cdot f_{c}}{\rho_{\ell}\cdot f_{\ell}+\rho_{e}\cdot f_{e}+\rho_{c}\cdot f_{c}} \qquad (25)$$

Table 2. Thermodynamic & physical properties

Property	Symbols	Units	Quantity
Melting of pure iron	T_f	K	1805.15
Liquidus slope	m	K (wt.%)$^{-1}$	-80.45
Equilibrium partition coefficient	k	-	0.36
Reference density	ρ_ℓ , ρ_e , ρ_c	kg·m^3	6990
Solid-liquid density difference	$\Delta\rho$	kg·m^3	150
Specific heat	c_p^ℓ, c_p^c, c_p^e	J·kg^{-1}·K^{-1}	500
Thermal conductivity	k_ℓ , k_e , k_c	W·m^{-1}·K^{-1}	34.0
Latent heat	L	J·kg^{-1}	2.71×10^5
Viscosity	μ	Kg·m^{-1}·s^{-1}	4.2×10^{-3}
Thermal expansion coefficient	β_T	K^{-1}	1.07×10^{-4}
Solutal expansion coefficient	β_c	wt.%$^{-1}$	1.4×10^{-2}
Dendritic arm spacing	λ_1	m	5×10^{-4}
Diffusion coefficient (liquid)	D_ℓ	m^2·s^{-1}	2.0×10^{-8}
Diffusion coefficient (solid)	D_e , D_c	m^2·s^{-1}	1.0×10^{-9}

4 Simulation result

4.1 Solidification sequence

The solidification sequence is shown in Figure 2 and includes the sedimentation of the equiaxed crystals and both the sedimentation-induced and thermosolutal buoyancy-induced melt convections. The simulated solidification sequence agrees with the theoretical explanation of steel ingot solidification, as summarised by Campbell [27]. Columnar dendrites grow from the mould wall, and the columnar tip front moves inwards; equiaxed grains nucleate near the mould walls. Columnar dendrites are stationary, whereas equiaxed grains sink and settle at the base of the ingot. The accumulation of such grains at the base of the ingot results in a characteristic conic shape. Both the sedimentation of grains and the melt convection influence the global solidification sequence and, thus, the final phase

distribution. More equiaxed grains will be found in the lower region of the ingot, whereas columnar structures will be predominant in the upper region of the ingot.

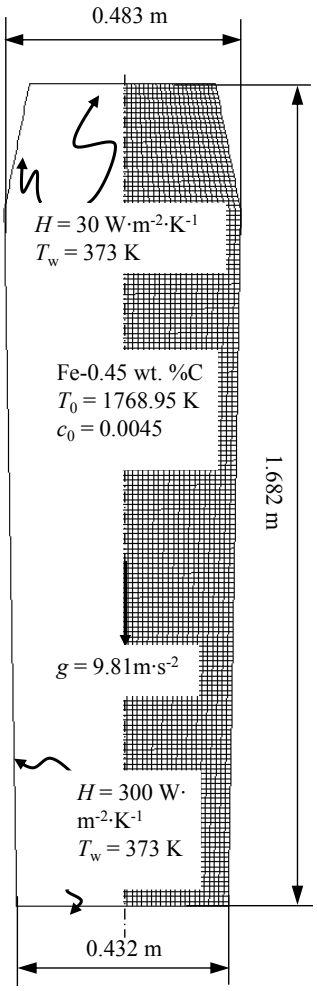

Figure 1: Configuration of the 2.45-ton industry steel ingot.

The flow in the ingot is driven by three forces: the solutal buoyancy force, which leads to upward flow; the thermal buoyancy force, which leads to downward melt flow; and the motion of the sinking equiaxed crystals, which drags the surrounding melt downwards. Initially, the two downward forces are dominant along the side walls of the ingot. The downward flow and the sinking equiaxed crystals change direction at the bottom of the ingot, move inwards, and then rise in the middle region of the ingot. Meanwhile, the cooled melt at the casting top tends to sink directly from the middle part of the ingot. The upward and downward flows interact with each other, and the resulting global flow pattern is highly

unstable and disordered. Large eddies develop dynamically and then are suppressed in the bulk region. Due to the interactions between the sinking equiaxed crystals and the growing columnar tip fronts in the melt, some small convection cells can develop along the columnar tip front. These small convection cells travel with the global flow current, integrate into the global flow current and then may finally disappear in the bulk.

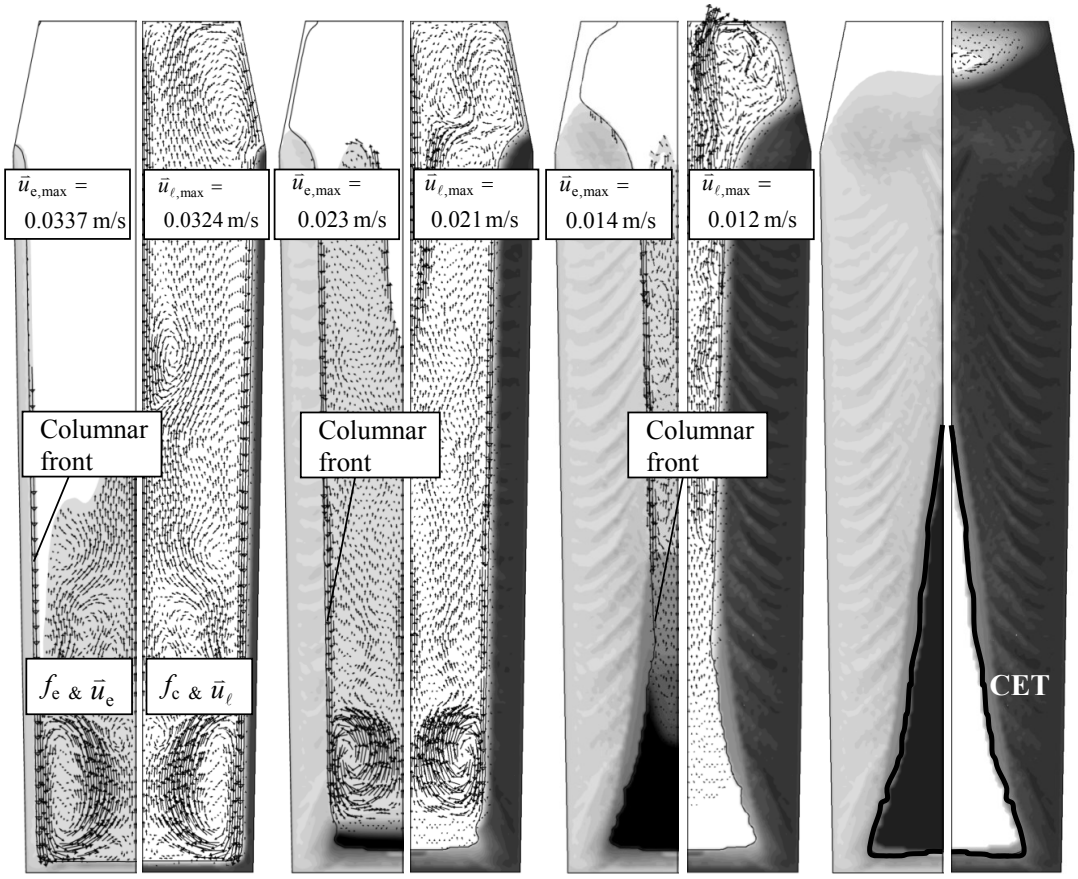

Figure 2: The predicted solidification sequence of the 2.45-ton ingot. The volume fraction of each phase (f_e or f_c) is shown in grey map with 20 grey levels from 0 (white) to 1 (black). The left half of each graphic shows the evolution of the equiaxed volume fraction (f_e) and the equiaxed sedimentation velocity ($\vec{u}_e$), indicated by the black arrows. The right half of each graphic shows the evolution of the columnar volume fraction (f_c) and the melt velocity ($\vec{u}_\ell$), indicated by the black arrows. We did not show velocity vectors for each numerical grid point but rather selected representative vectors. The position of the columnar dendrite tip was marked with a black solid line. The nucleation parameters for this calculation are n_{max} = 2 x 10^9 m^{-3} and ΔT_σ = 2 K, ΔT_N = 5 K; the numerical grid size is 5 mm.

In the middle region of the ingot, columnar tip fronts from both sides meet at the ingot centre during the late stages of solidification. In the lower part of the ingot, however, the large amount of equiaxed grains settle there, and stop the propagation of the columnar tip front. The final position of the columnar tip front, which is blocked by the equiaxed crystals, indicates the columnar-to-equiaxed transition (CET), as shown in Figure 2(d). The CET line separates the areas where only equiaxed grains appear from the areas where both columnar dendrites and equiaxed grains coexist.

Additionally, due to the complexity of the flow pattern and the interaction among the melt, equiaxed and columnar phases, a streak-like distribution pattern between the columnar and equiaxed phases is gradually developed within a specific distance from the side walls. This streak-like phase distribution ultimately affects the final macrosegregation.

Figure 3 shows the comparison of the predicted segregation result with experimental one [3]. The measured carbon segregation map in grey scale is reconstructed from the chemical analysis of 54 drilling samples. The sulphur print gives a qualitative indication of general segregation pattern. In this paper, the macrosegregation was quantified by a segregation index: $(c_{\mathrm{mix}} - c_0)/c_0$. A positive segregation in the top and a conic negative segregation in the bottom were observed. Obviously, the lower conic negative segregation is caused by the equiaxed sedimentation. The settling grains are poor in solute elements, thus their accumulation results in negative segregation. The positive segregation at the top region of the ingot is caused by the flow of the enriched melt in the bulk region. A streak-like segregation pattern in the middle radius region is predicted. One may notice that this streak-like segregation has a similar contour to the classical A-segregation (Figure 3(c)), but the current paper cannot justify if the classical A-segregation is the same as streak-like segregation or originates from this type of streak-like segregation. According to the most widely accepted empirical explanation [16], A-segregation belongs to a type of channel segregation in large steel ingots, which originates and develops in the stationary dendritic mushy zone. Therefore, we referred to the streak-like segregations as quasi A-segregates (or quasi A-segregation). Further discussion about the formation mechanism of the quasi A-segregates is included in section 6.2.

4.2 Experimental verification

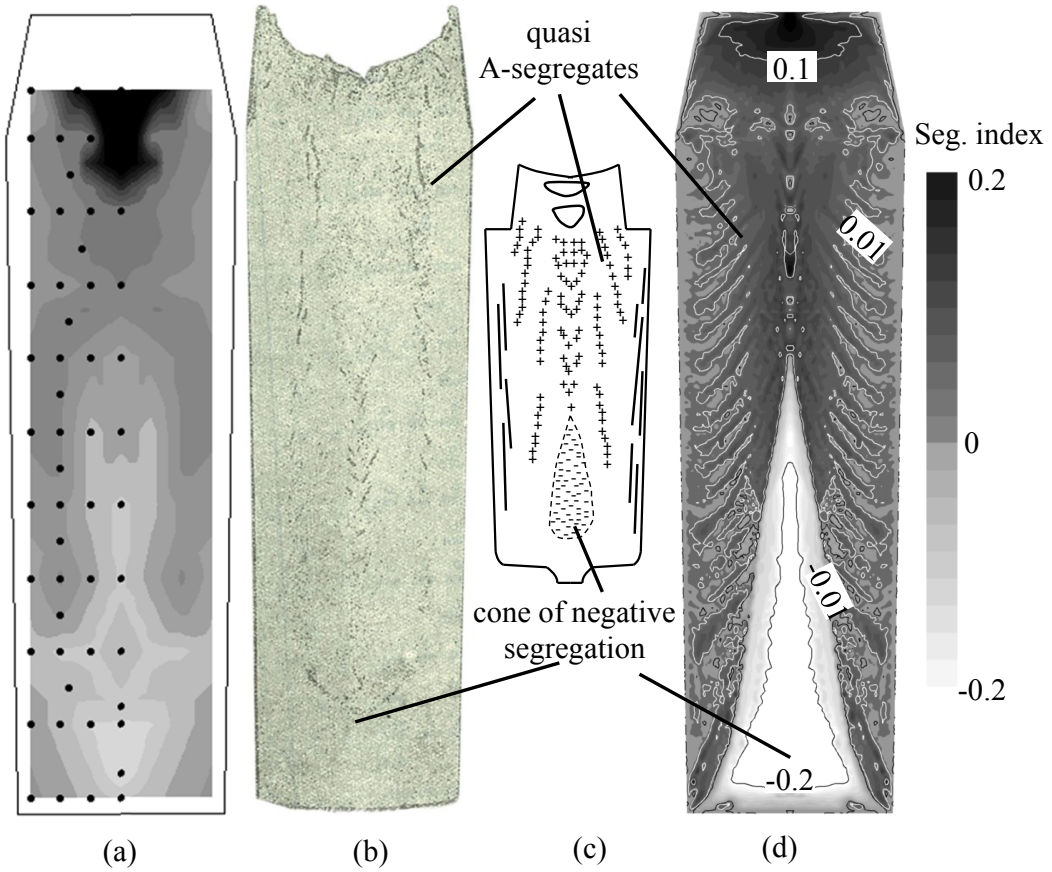

Figure 3: Macrosegregation pattern. (a) Reconstructed segregation map in grey scale out of chemical analysis of 54 drilling samples, (b) sulphur print of the as-cast ingot [3], (c) schematic of the typical macrosegregation pattern in steel ingots [16], and (d) predicted macrosegregation pattern (black for the positive segregation and white for the negative segregation) overlapped with isolines. The segregation is quantified by a segregation index: $(c_{\mathrm{mix}} - c_0)/c_0$.

The predicted macrosegregation pattern was compared with the sulphur print and measured segregation pattern, as shown in Figure 3. Both the conic negative segregation in the lower region of the ingot and the quasi A-segregation bands were predicted. This pattern coincides qualitatively with the experiment result and fit to the typical segregation pattern of steel ingots. The segregation along the ingot centreline is compared with the experiment report [3], as shown in Figure 4. Both the experimental and simulation results show the negative segregation in the lower part and positive segregation in the upper part. However, the negative segregation in the lower part is predicted more severely than the experimental

result. The overestimation of the negative segregation in the lower part by the model results from two aspects. One is the assumption of globular equiaxed morphology, which can cause significant overestimation of the sedimentation-induced negative segregation. The other aspect is the lack of real process conditions and material property, especially in terms of the parameters for the nucleation of equiaxed crystals.

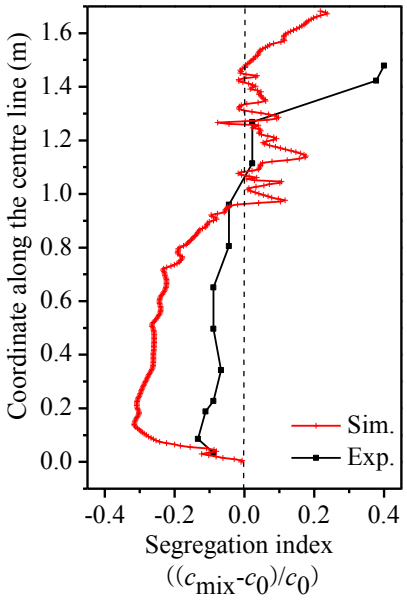

Figure 4: The comparison result of the centre line of the segregation index.

In the upper part of the ingot, the experiment result shows a large positive segregation in the hot top. The modelling result shows also a large positive segregation in the hot top, but a discontinuous distribution between negative and positive segregation can be identified just below the hot top. The predicted position of the hot top is higher than the experimentally indicated position. The reasons for the above discrepancy are from both experimental and modelling aspects. From the modelling aspect, the uncertainty about the thermal boundary conditions and the neglect of the formation of the shrinkage cavity in the top are mainly responsible for the discrepancy between the predicted and experimentally indicated hot top positions. From the experiment aspect, the distance between two sampling points is larger than 10 cm, and it might not provide sufficient measurement resolution. In the practice, people often identified the discontinuous negative-positive segregation below the hot top

[14]. The reason for this type of segregation distribution is due to the formation of mini-ingot in the late stage of solidification. Further discussion of the mini-ingotism is in section 6.1.

One should emphasise that a main motivation of the current study is to verify the capability of the mixed columnar-equiaxed model. This study is not going to adjust the process parameters to cater for the experiment results. Because the experiments were carried out decades ago and many of the process parameters and material properties were not reported, the current simulation results could only qualitatively reproduce the experiment results.

5 Parameters study

5.1 Grid size

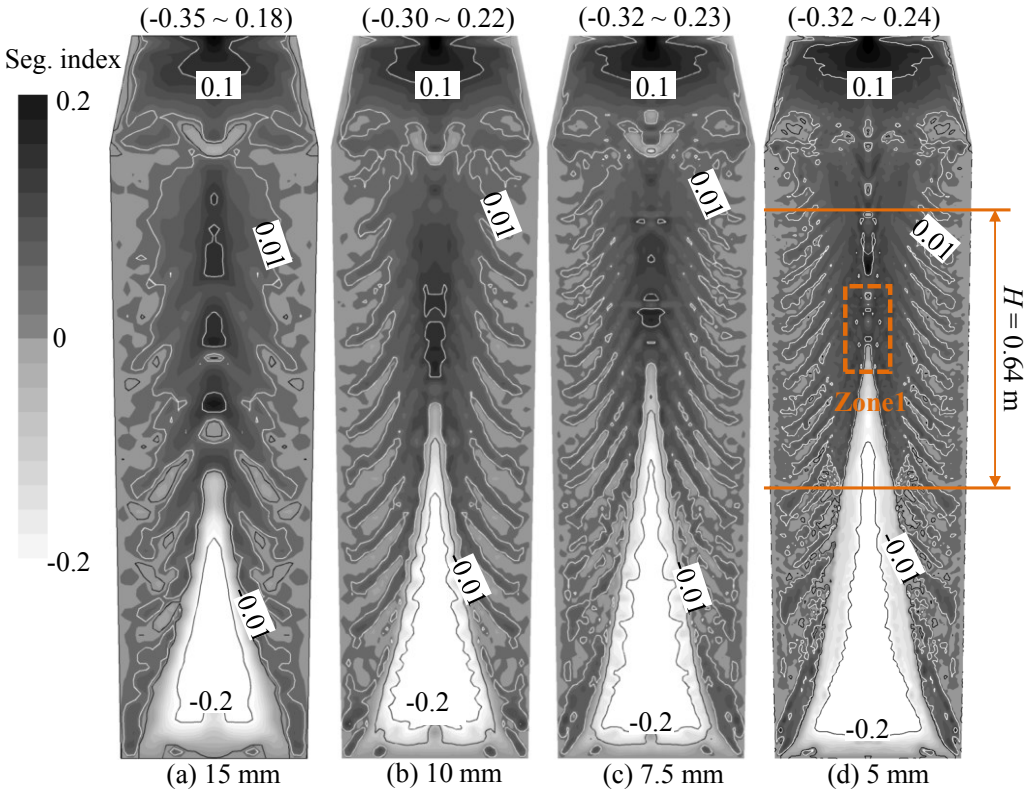

Figure 5: Grid dependency of the macrosegregation map. The segregation index is shown in greyscale from -0.2 (white) to 0.2 (black), overlapped by its isolines. The calculations were made using equiaxed nucleation parameters: n_{max} = 2 x 10^9 m^{-3}, ΔT_σ=2 K, and ΔT_N = 5 K.

Calculations with different grid sizes were performed, and the segregation results are shown in Figures 5 and 6. As the grid size increases from 5 mm to 15 mm, a similar global segregation pattern can be predicted: positive macrosegregation at the hot top, a conic negative segregation in the lower region and some quasi-A segregation bands in the middle radius region between the casting outer surface and the centre line. The positive segregation extreme of approximately 0.22 – 0.24, located in the hot top, and the negative segregation extreme of about -0.30 – 0.32, located in the lower equiaxed sedimentation zone, do not significantly change when the grid size is less than 10 mm. The height of the lower, negative-segregated sedimentation zone increases slightly with the decrease of the grid size, but this change is not significant when the grid size is less than 7.5 mm. We can conclude that for the current 2.45-ton ingot, a grid size of 7.5 – 10 mm is sufficient to attain a global segregation pattern. To reduce the simulation time because the calculation cost (Figure 6(b)) increases exponentially with grid resolution, a relatively coarse grid size (e.g., 10 mm) is recommended to obtain a global macrosegregation pattern.

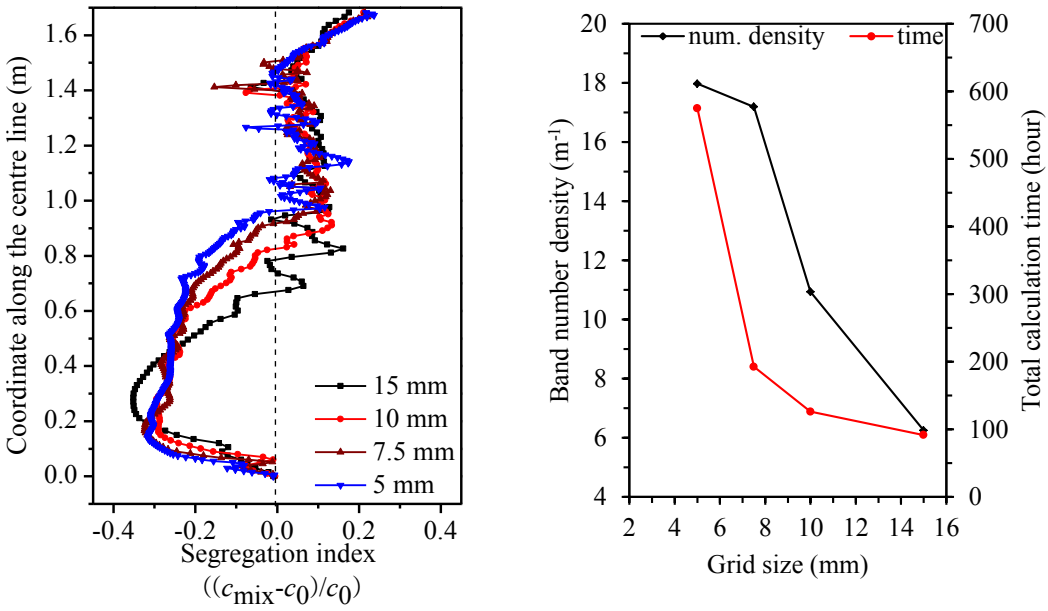

(a) (b)

Figure 6: (a) Grid dependency of the segregation profile along the ingot centre line and (b) grid dependency of the band number density and calculation time. The calculations are run in parallel on a Cluster (Intel Nehalem Cluster 2.93 GHz) with 8 CPU cores.

The quasi A-segregation is more sensitive to grid size. A band number density, N/H (1/m), is defined to investigate the grid dependency of quasi A-segregation. N is the number of quasi-A segregation bands in the range of H, as indicated in Figure 5. The band number density increases with an increase in the grid resolution, as shown in Figure 6(b). The N/H curve is prone to become constant when the grid size is smaller than 5 mm, thereby suggesting that the grid-independent result of the N/H ratio might be achieved. However, the fine details of each quasi A-segregate are still not convergent. An absolute grid-independent result with respect to the fine details of quasi A-segregates has not yet been achieved with a grid size of 5 mm. The calculation time increases exponentially with the increase of the grid resolution.

5.2 The nucleation parameters

A three-parameter law (Eq. (13)) is used to model the nucleation of equiaxed crystals; in this study, only one parameter, n_{max}, is varied from 0 to 5 x 10^9 m^{-3}, while the other two, ΔT_σ = 2 K and ΔT_N = 5 K, are kept constant. The final results are shown in Figures 7-9. The case with n_{max} = 0 corresponds to pure columnar solidification, with no nucleation of equiaxed crystals.

The most significant influence of n_{max} is on the bottom sedimentation-induced negative segregation zone. The height of the conic zone decreases with decreasing n_{max}. For pure columnar solidification, this zone disappears. With respect to the global segregation severity (the extent of variation between the positive segregation extreme and the negative segregation extreme), there is a large difference between mixed columnar-equiaxed solidification and pure columnar solidification. As shown in Figure 7 for pure columnar solidification, the maximum positive segregation is 0.14 and the negative segregation extreme is -0.10. By contrast, for mixed columnar-equiaxed solidification, the maximum positive segregation is approximately 0.21 – 0.22 and the negative segregation extreme is about -0.28 – 0.34. There are two reasons for the differences in segregation behaviour: sedimentation of the equiaxed crystals creates a large amount of negative segregation in the lower segregation zone and this sedimentation induces much stronger melt convection in the bulk region. Thus, sedimentation of crystals is a very important mechanism responsible for global macrosegregation.

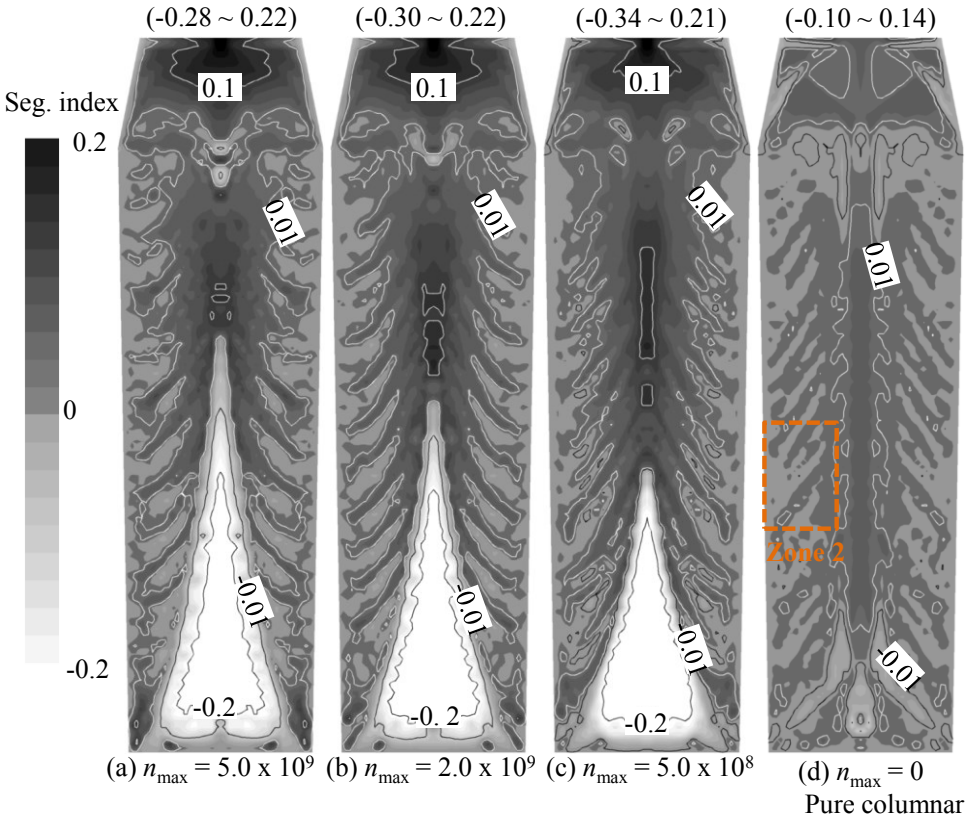

Figure 7: Influence of n_{max} on the macrosegregation map. The segregation index is shown in greyscale from -0.2 (white) to 0.2 (black), overlapped by its isolines. The calculations were made using a grid size of 10 mm; the other nucleation parameters, ΔT_σ = 2 K and ΔT_N = 5 K, were constant.

Upon comparison of the three cases of mixed columnar-equiaxed solidification (Figure 7(a)-(c)), we find that the global segregation patterns are quite similar. The maximum positive segregation in the hot top (0.21 – 0.22) seems to be insensitive to variations in n_{max} from 5 x 10^8 m^{-3} to 5 x 10^9 m^{-3}. The negative segregation extreme in the sedimentation zone becomes slightly more negative with decreasing n_{max} values (Figure 8). The reason is that the average grain size of equiaxed crystals (d_e) is predicted to increase with the decrease of n_{max}. The drag force of the surrounding melt acting on the settling equiaxed crystals decreases with the grain size, i.e. $\bar{U}_{\ell e}^{d} \propto d_e^{-2}$. Therefore, the settling velocity of the equiaxed crystals increases with the decrease of n_{max}, hence negative segregation extreme in the sedimentation zone becomes slightly more negative.

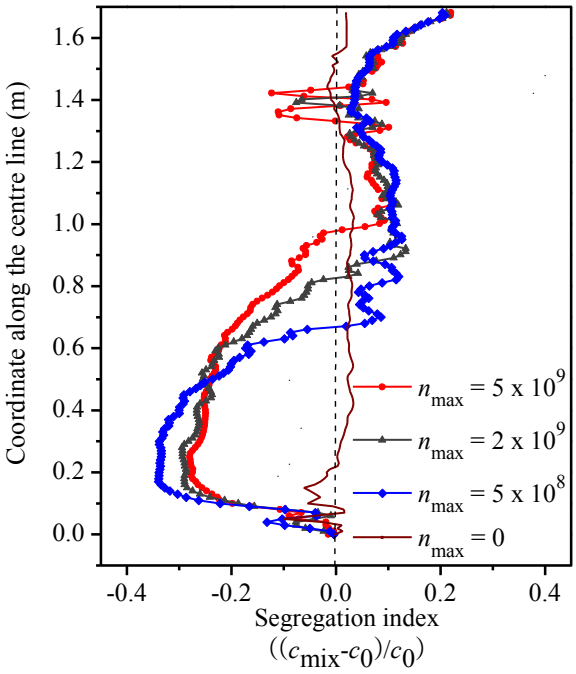

Figure 8: Influence of n_{max} on the centreline segregation profile. Calculations were made using a grid size of 10 mm; the other nucleation parameters, $\Delta T_\sigma = 2$ K and $\Delta T_N = 5$ K, were constant.

In Figure 7, the quasi A-segregation patterns look similar for all cases. The general quasi A-segregation bands (e.g., the band number density) are almost the same. As shown in Figure 9, the band number density is independent of n_{max}. The main difference is the segregation severity across the band space. Here, a new quantity is defined to analyse the segregation severity across the quasi A-segregation band, $(c_{mix}^{max} - c_{mix}^{min})/c_0$, where c_{mix}^{max} is the maximum c_{mix} and c_{mix}^{min} is the minimum c_{mix} across the band space. These two values are actually read from a representative band in the middle of Zone 2 as marked in Figure 7(d). As observed in Figure 9, the segregation severity across the quasi A-segregation band for the cases of mixed columnar-equiaxed solidification is notably larger than for the case of pure columnar solidification. Therefore, the appearance of equiaxed crystals in such a steel ingot strengthens the segregation severity across the quasi A-segregation band.

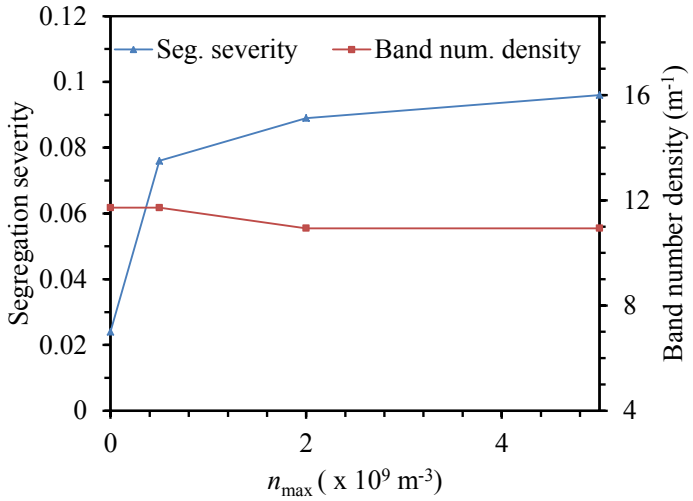

Figure 9: Influence of n_{max} on the segregation severity across the quasi A-segregation band ($(c_{mix}^{max} - c_{mix}^{min})/c_0$) and band number density. Calculations were made with a grid size of 10 mm; the other nucleation parameters, ΔT_σ = 2 K and ΔT_N = 5 K, were constant.

6 Discussion

6.1 Bridging and mini-ingotism

The discontinuous negative-positive segregation below the hot top may result from the formation of a local mini-ingot. Bridging and mini-ingotism are phenomena that were first reported in continuously cast round billets of steel [28]. The ingot used in this study is quite long, and solidification in such a long ingot behaves similarly to that in a continuously cast round billet. At later stages of solidification, because the middle part of the ingot is already blocked by the columnar trunks, the solidification of the remaining melt in the upper part behaves like the solidification of a mini-ingot. This local mini-ingot is observed as a long, narrow, and large-end-up tube. The equiaxed grains sediment from the upper part to the lower part and then accumulate in the lower region of the mini-ingot.

Figure 10 shows the evolution of the equiaxed grain number density and the velocity field of the crystal sedimentation in the lower region of the mini-ingot. There are several locations, some of which are marked with symbols A through C in Figure 10, where the

equiaxed grain number density increases much faster than it does in the neighbouring regions. Correspondingly, the volume fraction of the equiaxed phase in these locations is larger than in the neighbouring regions, as shown in more detail in Figure 11. It is anticipated that the equiaxed crystals accumulate there due to sedimentation and accumulate relatively isolated islands of the equiaxed phase.

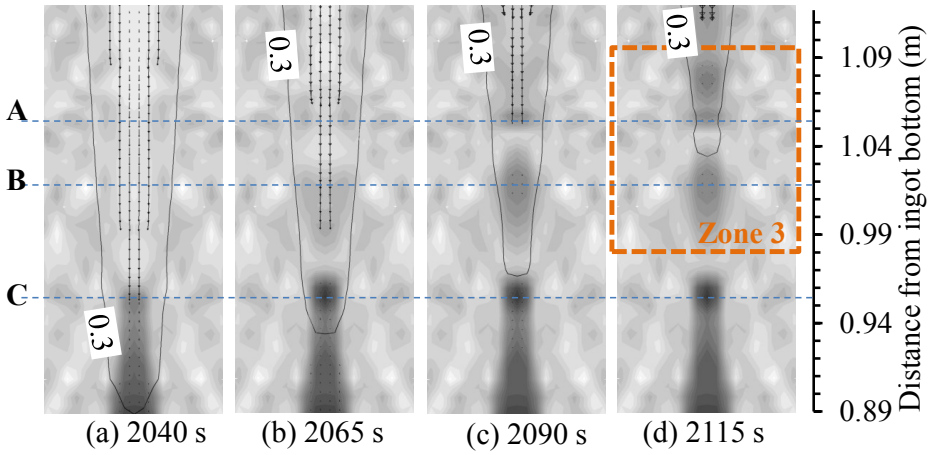

Figure 10: The solidification sequence at the bottom of the mini-ingot, as viewed in Zone 1 (marked in Figure 5(d)). The equiaxed grain number density is shown in greyscale from a minimum value of 10^8 m^{-3} to a maximum value of 8 x 10^8 m^{-3}. The isoline of $f_\ell = 0.3$ is also shown. The vectors indicate the velocity of the settling equiaxed crystals.

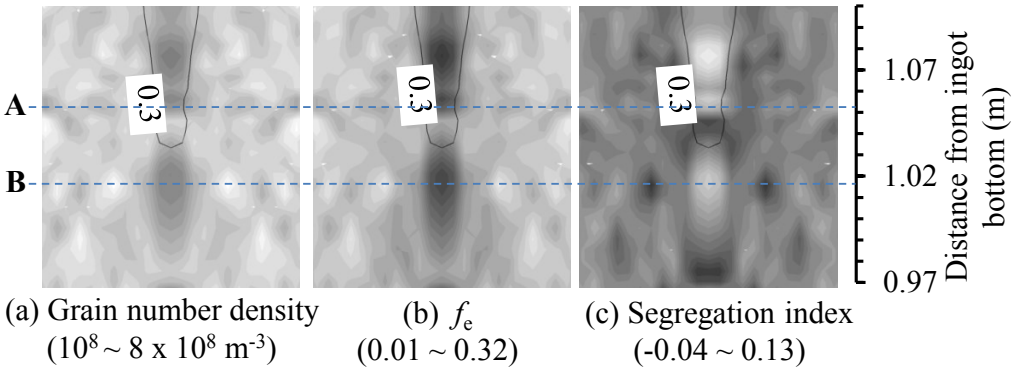

Figure 11: Zoom-in result in Zone 3 (marked in Figure 10(d)) at 2115 s. All quantities are shown in greyscale with maximum and minimum values given. The isoline of $f_\ell = 0.3$ is also overlaid on this Figure.

Figure 12 plots the evolution of the axial component of the equiaxed velocity along the casting centre line. This finding provides more clear evidence about the crystal accumulation. The negative value of the velocity component means that the crystals sink downwards. The variation in the velocity curves along the centre line at different moments is not monotonic. If the magnitude of the velocity component suddenly decreases at a given location, the local accumulation of the crystals occurs. Correlating the velocity curves in Figure 12 with the accumulation locations (A through C) in Figure 10, we find that just above this accumulation site, there is a clear indication of the reduction in velocity.

The accumulation of the equiaxed phase in those islands induces negative segregation, as shown in Figure 11 (c). The mechanism for this negative segregation is the same as the conic negative segregation in the base region of the ingot. The discontinuous distribution between the negative (islands) and positive segregation below the hot top is due to the interaction between the growing columnar tip front and the accumulation of the equiaxed phase. If the columnar tip front blocks the casting centre again inside the mini-ingot, a new mini-ingot would form. This process may repeat several times, depending on the casting geometry and the cooling boundary conditions of the hot top.

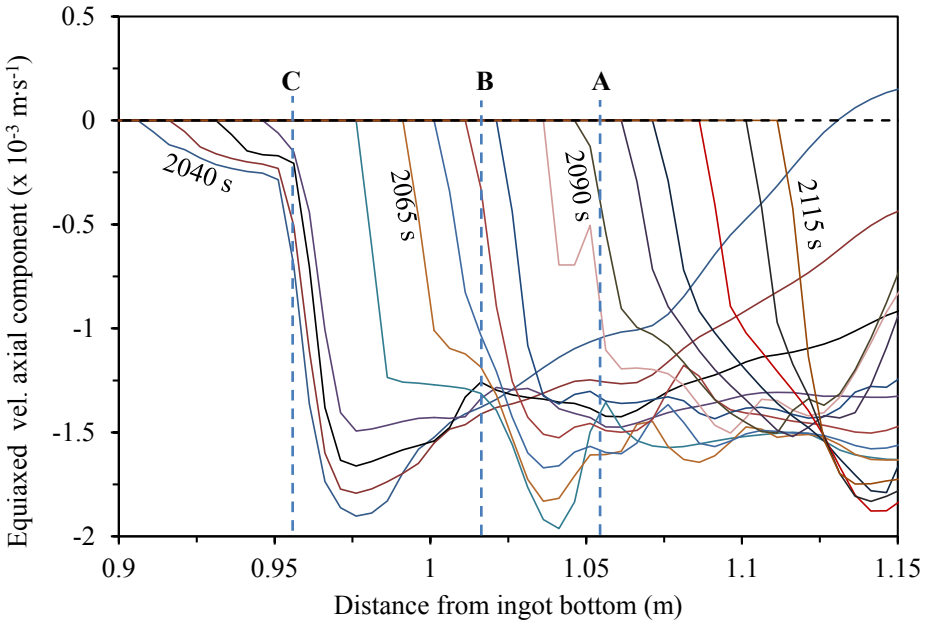

Figure 12: Evolution of the axial component of the equiaxed velocity along the casting centre line. The velocity curves are plotted with equal time interval of 5 s. The corresponding locations (A through C) are also indicated, as marked in Figure 10.

It is interesting to observe that the discontinuous distribution between the negative and positive segregation follows a similar pattern of V-segregates, as seen in Figure 5 and 11. It implies that the formation of mini-ingot and the sedimentation of equiaxed crystals at the bottom of the mini-ingot might contribute to the formation of V-segregates. In addition to its similar appearance to a V-shape, the position where the segregate forms and the thermal conditions under which it forms follow the classical elucidation of V-segregates. However, this hypothesis needs further investigation. As we also learnt [16, 28-29] that some other important factors influencing V-segregates, e.g. the sucking flow due to solidification shrinkage and the deformation of the dendrites in mushy zone along the casting centreline, are not taken into account in the current model.

6.2 Quasi A-segregation

A recent study by the authors [30] in a Sn-Pb laboratory casting has found that channel segrega-tion can originate and develop during pure columnar solidification, in which no equiaxed crystals exist. Channel segregation develops in two steps: (1) the initiation of the channel, caused by flow instability, and (2) the growth of the channel, caused by the flow-solidification interaction. Remelting is not necessary for formation of the channels. Actually, the quasi A-segregates belong to the same channel segregates as those studied in the previous work [30]. The term 'quasi A-segregates' is defined here, distinct from the classical term 'A-segregates,' because it was previously believed that remelting was the key mechanism for formation of A-segregates. However, neither the current work nor the previous work [30] found clear evidence of remelting. Nevertheless, streak-like channel segregates occur.

A parameter study on the nucleation of equiaxed crystals, in Figures 7 and 9, seems to show that the quasi A-segregation pattern is independent of the appearance of equiaxed phases. Both the three-phase mixed columnar-equiaxed solidification model and the two-phase columnar solidification model predict a similar pattern of quasi A-segregates. This result leads to a hypothesis that the appearance of an equiaxed phase is not a necessary condition for formation of quasi A-segregates and that the cause of quasi A-segregates is the same in both solidification cases, i.e., it is initiated by flow instability. However, Figures 7 and 9 show that the segregation severity across each quasi A-segregation band is strengthened by an equiaxed phase. Two possible reasons are discussed as follows.

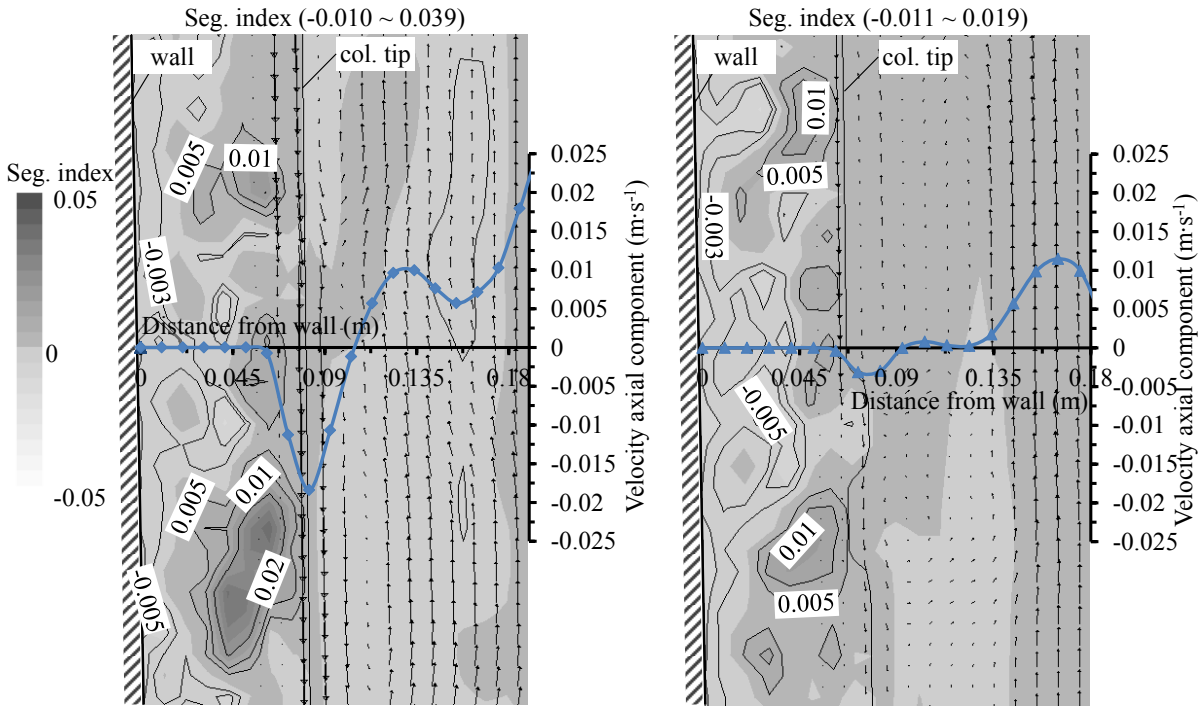

(a) n_{max} = 5 x 10^8 (b) pure columnar

Figure 13: Comparison of the two solidification cases at the initial stage of quasi A-segregate formation: (a) mixed columnar-equiaxed solidification (n_{max} = 5 x 10^8 m^{-3}) and (b) pure columnar solidification. The figures show the zoomed-in results in Zone 2 (marked in Figure 7(d)) at 400 s. The segregation index is shown in greyscale overlapped by its isolines, which denote the initial stage of quasi-A segregation. The melt flow is shown in vectors. Additionally, the axial component of the equiaxed grain sedimentation is plotted along a horizontal line. The position of the columnar tip front is indicated.

Firstly, the appearance of equiaxed phase accelerates the melt flow in the vicinity of the columnar tip front where the quasi A-segregates initiate and develop. Figure 13 compares the melt flow at the initial stage (400 s) of quasi A-segregate formation between the two solidification cases: mixed columnar-equiaxed solidification and pure columnar solidification. Although the quasi A-segregation patterns in both cases are quite similar, they are not quantitatively identical. The magnitude of velocity during mixed columnar-equiaxed solidification is much (approximately 4 times) larger than that during pure columnar solidification. Sedimentation of equiaxed crystals accelerates the flow in the surrounding melt. Ultimately, the accelerated melt flow aggravates the severity of segregates. From Figure 7 it is also noticed that the incline angle of the quasi A-segregates is slightly influenced by the accelerated flow due to equiaxed sedimentation. The

segregation bands in the cases of mixed columnar-equiaxed solidification 'bent' more towards the top of ingot than in the case of pure columnar solidification. This phenomenon was discussed previously by the current authors [30].

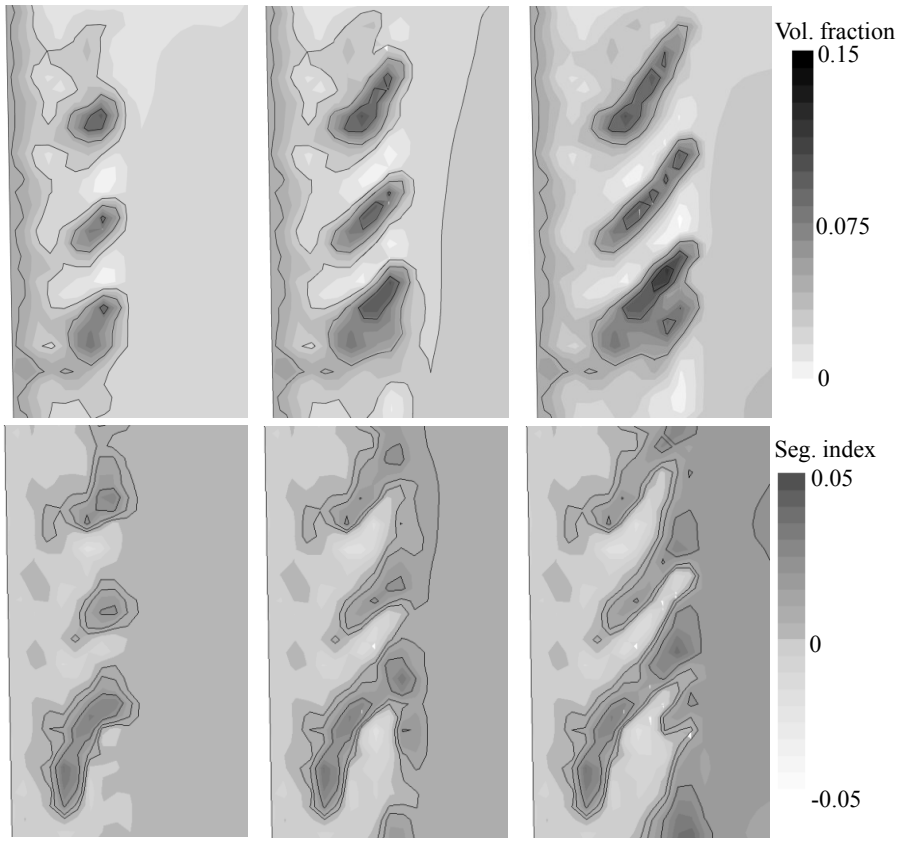

Figure 14: Zoomed-in results (Zone 2 is as marked in Figure 7(d)) of the volume fraction of the equiaxed phase and the segregation index for the case of mixed columnar-equiaxed solidification. The evolution sequences are shown at 600 s, 800 s and 1000 s. The upper row shows the equiaxed volume fraction in greyscale overlapped with isolines at 0.03, 0.05 and 0.08. The bottom row shows the segregation index in greyscale overlapped with isolines at 0.005, 0.01 and 0.02.

Secondly, a streak-like distribution between columnar and equiaxed phases is caused by the initial unstable flow in the vicinity of columnar tip front by the interaction between the sinking equiaxed crystals and the growing columnar tip front and by the entrapment of the equiaxed crystals by the columnar trunks. This streak-like phase distribution coincides with the pattern of quasi A-segregates, as shown in Figure 14. The accumulation of equiaxed phase results in negative segregation. The equiaxed-accumulated region approximately

coincides with the region of negative segregation, and the equiaxed-lean (more columnar phase) region has a positive segregation. This coincidence further confirms that the periodical accumulation of equiaxed phase along the columnar tip front strengthens the quasi A-segregates.

6.3 Prediction of CET

Correct description of columnar-to-equiaxed transition (CET) belongs to an important part of calculation of macrosegregation. The features of the current model to track the columnar primary tip front and to predict CET considering both soft blocking and hard blocking mechanisms were evaluated previously by the current authors [19, 24, 31]. Although we are not able to quantitatively evaluate the CET based on the current ingot due to lack of the primary experimental data, the comparison of the predicted CET and global macrosegregation pattern with the sulphur print and measured segregation distribution (Figure 3) gives additional confidence in the predictive capability of the model with respect to the CET.

Figure 15 records the positions where the mechanism of soft blocking operates in the ingot. It is interesting to find that the final CET line is mostly caused by the mechanism of hard blocking, except for a few elements in the bottom corners of the conic equiaxed zone where columnar tips are finally 'frozen' by the mechanism of soft blocking. In the most cases, the growth of the columnar tips is only stopped temporarily by the mechanism of soft blocking (disappearance of constitutional undercooling). At the right moment the volume fraction of equiaxed phase in the front of columnar tips is smaller than 0.49 (hard blocking criterion). At the next moment if the constitutional undercooling develops again, the columnar tips can continue to grow. This mechanism of temporal soft blocking operates very frequently, in the middle and upper part of the ingot. An additional point should be kept in mind is that the growth of equiaxed grains will stop as well, when the growth of columnar tips is soft-blocked. In other words, if one wants to 'frozen' the soft-blocking position of the columnar tips permanently, the local volume fraction of equiaxed phase should be allowed to increase to over 0.49, and this increase can only happen through transport of equiaxed phase from neighbourhood to the columnar tip front. This soft-blocking induced CET is only observed in the bottom corners of the conic equiaxed zone. To conclude the above discussion, both soft blocking and hard blocking are important, although the final CET line is mainly caused by the mechanism of hard blocking.

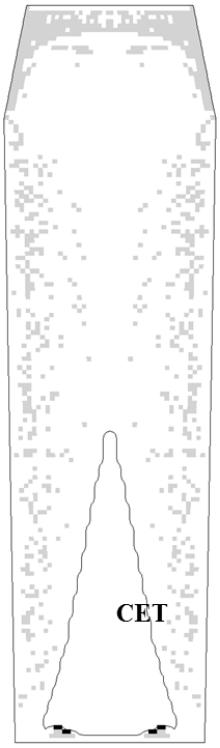

Figure 15: Analysis of the columnar tip blocking mechanism. The marked grey points are positions where the growth velocity of the columnar tip front is temporarily stopped (reduced to smaller than 10^{-5} m/s) by the mechanism of soft blocking. The black points are positions where the CET is finally caused by the mechanism of soft blocking.

6.4 Uncertainties of the results

One novel feature of the chosen model is to incorporate three phases (liquid, equiaxed and columnar), but the calculation becomes exhausting. In order to consider the applicability of the model for large steel ingot, a compromise must be made between the model completeness and the computational cost. Concerns about uncertainties of the modelling results due to model simplifications and some recommendations for further model development are addressed as follows.

As we stated that the ignorance of dendritic morphology of equiaxed crystals leads to an overestimation of the intensity of bottom negative segregation. In practice, it was observed that grain morphology in fairy large steel ingots experiences a transition from globular (mostly in the bottom region) to dendritic (in the upper part of ingot) structure [14, 32-33]. A study by Zaloznik and Combeau has shown that in the lower bottom globular region, the sedimentation is dominant for the negative segregation. In the quite dendritic equiaxed

zone, the dendrites can pack very early, and the contribution of the settling effect on the macrosegregation can be ignorable and the main mechanism for the formation of the macrosegregation is the thermosolutal convection in the interdendritic region. Therefore, a further step incorporating dendritic morphology is desired. The authors have recently developed a 5-phase model [24, 31] considering full dendritic morphology in both equiaxed and columnar phases. Due to the extremely high calculation cost, the model is currently applicable to a size of laboratory ingot [34]. Therefore, an intermediate solution might be applied. For example, the growth of the equiaxed dendritic envelope is treated according to KGT model [35], while the phase change is based on a Stefan problem assuming a spherical geometry of the solid phase inside the grain envelope [14, 33].

In section 4.2 we pointed out that the position and intensity of the positive segregation in the hot top region is not correct due to the ignorance of the solidification shrinkage. Some other consequences caused by this ignorance should also be addressed. One is the sinking top surface might adapt the thermal and flow boundary conditions there. Another important effect is on the interdendritic flow. Due to the solidification shrinkage, feeding flow might influence the shape and intensity of the quasi-A-segregation pattern as well. A new modelling step incorporating 4 phases (air, liquid, equiaxed and columnar) is currently undertaken, but more efforts are demanded.

Current paper used the locally linearized Fe-C binary phase diagram, but technical alloys are mostly multicomponent. Influence of other alloy elements on the segregation of carbon should be considered in two aspects. One is that the included alloy elements may alter the solidification path through thermodynamics and solidification kinetics [36-37]. Another aspect is that they may alter the density of the melt and influence the flow through hydrodynamics [16, 38]. A model incorporating multicomponent thermodynamics, diffusion-governed solidification kinetics and flow is still under development [13, 39].

Appropriate estimation of the diffusion length is also an important issue for determining the diffusion-governed solidification path. In the current model, simple crystal morphology is assumed: sphere for globular equiaxed grain, and cylinder for columnar (cellular) trunks. The diffusion length in liquid phase is estimated by solving a diffusion field around a growing crystal (spherical or cylindrical) analytically [40]. The crystal is assumed to grow in a confined volume with a radius of $R_{\mathrm{f,e}}$ (or $R_{\mathrm{f,c}}$), which is determined according to the equiaxed grain number density (or the columnar primary dendrite arm spacing), hence the

impingement of the solute distribution field at the end of solidification is treated. As shown in Eq. (14)-(15), the liquid diffusion lengths are estimated $R_e\left(1-R_e/R_{f,e}\right)$ and $R_c \ln\left(R_{f,c}/R_c\right)$ for equiaxed and columnar crystals, correspondingly. For dendritic solidification alternative methods should be used to calculate the diffusion length [41-44]. Flow and melt convection would modify the diffusion length as well [45-46].

7 Conclusion

A three-phase mixed columnar-equiaxed solidification model was applied to study the formation of macrosegregation in a 2.45-ton industry steel ingot. The predicted macrostructure and macro-segregation results agree qualitatively with the experimental data.

- Equiaxed sedimentation is a very important mechanism responsible for the formation of global segregation in such ingots. The calculation for solidification of both columnar and equiaxed phases possesses a segregation (index) range between -0.3 and 0.22; whereas the calculation for pure columnar solidification possesses a segregation range between -0.1 to 0.14. For the case of mixed columnar-equiaxed solidification, varying the equiaxed nucleation parameters changes the area of the lower conic negative segregation zone correspondingly, but the lower and upper limits of the global segregation index are only slightly influenced.

- Quasi A-segregates in the middle radius region between the casting outer surface and the centre line were predicted. Flow instability causes the formation of quasi A-segregates, but both the appearance of equiaxed crystals and their interaction with the growing columnar dendrites strengthen the segregates significantly. The equiaxed phase is not a necessary condition for the formation of quasi A-segregates because similar segregation bands with less severity are also found during pure columnar solidification.

- The discontinuous negative-positive segregation under the hot top was predicted. This type of segregation is caused by the formation of a mini-ingot and by the subsequent sedimentation of equiaxed crystals within the mini-ingot.

- The calculated quantitative result of segregation is sensitive to the numerical grid resolution. A very fine grid is required to predict the details of quasi A-segregates. A grid-independent result regarding the fine details of quasi A-segregates in such ingots is not attainable based on current calculations. However, the general segregation pattern, e.g., the positive segregation extreme, negative segregation extreme, and their locations, can be obtained using a relatively coarse grid (10 mm).

The quantitative discrepancy between the calculations and the experimental results is still significant. The main reasons for this discrepancy from a modelling point of view are as follows: (1) over-simplification of the dendritic morphology of the crystals; (2) ignoring the solidification shrinkage; (3) simplification of the phase diagram; etc.. To improve the accuracy of the calculations, further improvements in these areas are needed, in addition to reliable process conditions and improved material properties.

Nomenclature

c_0	wt.%	initial concentration
$c_\ell, c_\mathrm{e}, c_\mathrm{c}$	wt.%	species concentration
c^ref	wt.%	reference concentration
c_ℓ^*, c_s^*	wt.%	equilibrium concentration at interface
$C_{\ell\mathrm{e}}$	$\mathrm{kg\cdot m^{-3}\cdot s^{-1}}$	species exchange between liquid and equiaxed
$C_{\ell\mathrm{c}}$	$\mathrm{kg\cdot m^{-3}\cdot s^{-1}}$	species exchange between liquid and columnar
c_mix	1	mix concentration
$c_{\mathrm{p}(\ell)}$, $c_{\mathrm{p(s)}}$	$\mathrm{J\cdot kg^{-1}\cdot K^{-1}}$	specific heat
$D_\ell, D_\mathrm{e}, D_\mathrm{c}$	$\mathrm{m^2\cdot s^{-1}}$	diffusion coefficient
d_e	m	equiaxed grain diameter
d_c	m	columnar trunk diameter
$f_\ell, f_\mathrm{e}, f_\mathrm{c}$	1	volume fraction of different phases
$f_\mathrm{c}^\mathrm{free}$	1	critical f_c for free moving equiaxed phase
f_e^c	1	equiaxed grain packing limit
$\vec{g}$	$\mathrm{m\cdot s^{-2}}$	gravity
$\vec{g}_\mathrm{e}', \vec{g}_\ell'$	$\mathrm{m\cdot s^{-2}}$	reduced gravity

H	$W \cdot m^{-2} \cdot K^{-1}$	heat transfer coefficient
H^*	$W \cdot m^{-3} \cdot K^{-1}$	volume heat transfer coeff. between phases
h_ℓ, h_e, h_c	$J \cdot kg^{-1}$	enthalpy
$h_\ell^{ref}, h_e^{ref}, h_c^{ref}$	$J \cdot kg^{-1}$	reference enthalpy
K	m^2	permeability of liquid in porous medium
$K_{\ell e} (= -K_{e\ell})$	$kg \cdot m^{-3} \cdot s^{-1}$	the drag force coefficient
k	1	solute partitioning coefficient at the ℓ/s interface
k_ℓ, k_e, k_c	$W \cdot m^{-1} \cdot K^{-1}$	thermal conductivity
l	m	actual columnar length in tip cell
$M_{\ell e} (= -M_{e\ell})$	$kg \cdot m^{-3} \cdot s^{-1}$	liquid-equiaxed net mass transfer rate
$M_{\ell c} (= -M_{c\ell})$	$kg \cdot m^{-3} \cdot s^{-1}$	liquid-columnar net mass transfer rate
m	K	slope of liquidus in phase diagram
N_e	$m^{-3} \cdot s^{-1}$	equiaxed grain production rate by nucleation
n	m^{-3}	equiaxed grain number density
n_c	m^{-3}	columnar trunk number density
n_{max}	m^{-3}	maximum equiaxed grain volume density, or maximum available nucleation sites in simultaneous nucleation law
p	$N \cdot m^{-2}$	pressure
$Q_{\ell e} (= -Q_{e\ell})$	$J \cdot m^{-3} \cdot s^{-1}$	total energy exchange between liquid and equiaxed phases
$Q_{\ell e}^d (= -Q_{e\ell}^d)$	$J \cdot m^{-3} \cdot s^{-1}$	energy transfer between liquid and equiaxed phases
$Q_{\ell e}^p (= -Q_{e\ell}^p)$	$J \cdot m^{-3} \cdot s^{-1}$	energy exchange due to phase change between liquid and equiaxed phases
$Q_{\ell c} (= -Q_{c\ell})$	$J \cdot m^{-3} \cdot s^{-1}$	total energy exchange between liquid and columnar phases
$Q_{\ell c}^d (= -Q_{c\ell}^d)$	$J \cdot m^{-3} \cdot s^{-1}$	energy transfer between liquid and columnar phases
$Q_{\ell c}^p (= -Q_{c\ell}^p)$	$J \cdot m^{-3} \cdot s^{-1}$	energy exchange due to phase change between liquid and columnar phases
$Q_{ec} (= -Q_{ce})$	$J \cdot m^{-3} \cdot s^{-1}$	total energy exchange between equiaxed and columnar phases
$Q_{ec}^d (= -Q_{ce}^d)$	$J \cdot m^{-3} \cdot s^{-1}$	energy transfer between equiaxed and columnar phases
$Q_{ec}^p (= -Q_{ce}^p)$	$J \cdot m^{-3} \cdot s^{-1}$	energy exchange due to phase change between equiaxed and columnar phases
R	m	radius component of the coordinate
$R(R_e, R_c)$	m	grain radius (equiaxed, columnar)

$R_{\mathrm{f,\,e}}$	m	maximum radius of equiaxed grain
$R_{\mathrm{f,\,c}}$	m	maximum radius of columnar trunk
S_{A}	$\mathrm{m^{-1}}$	surface area of columnar per volume
T_0	K	initial temperature
$T, T_\ell, T_{\mathrm{e}}, T_{\mathrm{c}}$	K	temperature
T_{f}	K	melting point of pure metal (Fe)
T_{ref}	K	reference temperature for enthalpy definition
ΔT	K	constitutional undercooling
ΔT_{N}	K	undercooling for maximum grain production rate
ΔT_{tip}	K	undercooling at the columnar dendrite tip
ΔT_σ	K	Gaussian distribution width of nucleation law
t	s	time
Δt	s	time step
$\vec{U}_{\ell\mathrm{e}}(=-\vec{U}_{\mathrm{e}\ell})$	$\mathrm{kg\cdot m^{-2}\cdot s^{-2}}$	total liquid-equiaxed momentum exchange rate
$\vec{U}^{\mathrm{d}}_{\ell\mathrm{e}}(=-\vec{U}^{\mathrm{d}}_{\mathrm{e}\ell})$	$\mathrm{kg\cdot m^{-2}\cdot s^{-2}}$	liquid-equiaxed momentum change due to drag force
$\vec{U}^{\mathrm{p}}_{\ell\mathrm{e}}(=-\vec{U}^{\mathrm{p}}_{\mathrm{e}\ell})$	$\mathrm{kg\cdot m^{-2}\cdot s^{-2}}$	liquid-equiaxed momentum exchange due to phase change
$\vec{U}_{\ell\mathrm{c}}(=-\vec{U}_{\mathrm{c}\ell})$	$\mathrm{kgm^{-2}s^{-2}}$	total liquid-columnar momentum exchange rate
$\vec{U}^{\mathrm{d}}_{\ell\mathrm{c}}(=-\vec{U}^{\mathrm{d}}_{\mathrm{c}\ell})$	$\mathrm{kg\cdot m^{-2}\cdot s^{-2}}$	liquid-columnar momentum change due to drag force
$\vec{U}^{\mathrm{p}}_{\ell\mathrm{c}}(=-\vec{U}^{\mathrm{p}}_{\mathrm{c}\ell})$	$\mathrm{kg\cdot m^{-2}\cdot s^{-2}}$	liquid-columnar momentum exchange due to phase change
$\vec{u}_\ell, \vec{u}_{\mathrm{e}}, \vec{u}_{\mathrm{c}}$	$\mathrm{m\cdot s^{-1}}$	velocity vector
v_{R}	$\mathrm{m\cdot s^{-1}}$	grain growth speed in radius direction
v_{tip}	$\mathrm{m\cdot s^{-1}}$	grain growth speed in tip direction
$\sigma_{\mathrm{e}}, \sigma_{\mathrm{c}}$	m	back diffusion length
β_{T}	$\mathrm{K^{-1}}$	thermal expansion coefficient
β_{c}	1	solutal expansion coefficient
λ_1	m	columnar grain space
ρ_ℓ , $\rho_{\mathrm{e}}, \rho_{\mathrm{c}}$	$\mathrm{kg\cdot m^{-3}}$	density
ρ^{b}_ℓ	$\mathrm{kg\cdot m^{-3}}$	density for buoyancy force
$\mu_\ell, \mu_{\mathrm{e}}$	$\mathrm{kg\cdot m^{-1}\cdot s^{-1}}$	viscosity
$\bar{\bar{\tau}}_l, \bar{\bar{\tau}}_e$	$\mathrm{kg\cdot m^{-1}\cdot s^{-1}}$	stress-strain tensors

Subscripts ℓ, e, c mark liquid, equiaxed and columnar phases.

Acknowledgments

The authors are grateful for financial support from the Austrian Federal Ministry of Economy, Family and Youth and from the National Foundation for Research, Technology and Development. Jun Li would like to thank the China Scholarship Council for their generous support.

References

[1] M. Wu, L. Könözsy, A. Ludwig, W. Schützenhöfer, R. Tanzer, Columnar to Equiaxed Transition During Ingot Casting Using Ternary Alloy Composition, Steel Res. Int. 79 (2008) 56-63.

[2] E. Marburg, Accelerated solidification in ingots: its influence on ingot soundness, Journal of Metals 5 (1953) 157-172.

[3] Report on the heterogeneity of steel ingots, J. Iron Steel Inst. 113 (1926) 39-176.

[4] K. Suzuki, T. Miyamoto, Study on the formation of A-segregation in steel ingot, Trans. ISIJ 18 (1978) 80-89.

[5] M.C. Flemings, Solidification processing, Metall. Trans. 5 (1974) 2121-2134.

[6] M. C. Flemings, Principles of control of soundness and homogeneity of large ingots, Scand. J. Met. 5 (1976) 1-15.

[7] R. Mehrabian, M. C. Flemings, Macrosegregation in ternary alloys, Metall. Trans. 1 (1970) 455-464.

[8] T. Fujii, D. R. Poirier, M. C. Flemings, Macrosegregation in a multicomponent low alloy steel, Metall. Trans. B 10B (1979) 331-339.

[9] M. Wu, A. Ludwig, A. Bührig-Polaczek, M. Fehlbier, P. R. Sahm, Influence of convection and grain movement on globular equiaxed solidification, Int. J. Heat Mass Transfer 46 (15) (2003) 2819-2832

[10] P. Rouxa, B. Goyeau, D. Gobin, F. Fichot, M. Quintard, Chemical non-equilibrium modeling of columnar solidification, Int. J. Heat Mass Transfer 49 (23-24) (2006) 4496-4510.

[11] M. C. Schneider, C. Beckermann, Formation of Macrosegregation by multicomponent thermosolutal convection during the solidification of steel, Metall. Mater. Trans. A. 26A (1995) 2373-2387.

[12] J. P. Gu, C. Beckermann, Simulation of convection and macrosegregation in a large steel ingot, Metall. Mater. Trans. A. 30A (1999) 1357-1366.

[13] A. Ludwig, M. Gruber-Pretzler, F. Mayer, A. Ishmurizin, M. Wu, A way of coupling ternary phase diagram information with multiphase solidification simulations, Mater. Sci. Eng. A 413-414 (2005) 485-489.

[14] H. Combeau, M. Založnik, S. Hans, P. E. Richy, Predication of macrosegregation in steel ingot: influence of the motion and the morphology of equiaxed grain, Metall. Mater. Trans. B 40B (2009) 289-304.

[15] M. Založnik, H. Combeau, Thermosolutal flow in steel ingots and the formation of mesosegregates, Int. J. Therm. Sci. 49 (2010) 1500-1509.

[16] J. J. Moore, N. A. Shah, Mechanisms of formation of A- and V-segregation in cast steel, Inter. Metals Reviews 28 (1983) 338-356.

[17] K. Suzuki, T. Miyamoto, Influence of alloying elements on the formation of "A" segregates in steel ingot, Trans. Iron Steel Inst. Jpn 20 (1980) 375-383.

[18] M. Wu, A. Ludwig, A three-phase model for mixed columnar equiaxed solidification, Metall. Mater. Trans. A 37A (2006) 1613-1631.

[19] M. Wu, A. Ludwig, Using a three-phase deterministic model for the columnar-to-equiaxed transition, Metall. Mater. Trans. A 38A (2007) 1465-1475.

[20] J. Li, M. Wu, J. Hao, A. Ludwig, Simulation of channel segregation using a two-phase columnar solidification model – Part I: Model description and verification, Comp. Mater. Sci. 55 (2012) 407-418.

[21] A. Ludwig, M. Wu, Modelling of globular equiaxed solidification with two-phase approach, Metall. Mater. Trans. A 33 (2002) 3673-3683.

[22] R.B. Bird, W.E. Steward, E.N. Lightfoot, Transport Phenomena, John Wiley & Sons, New York, 1960.

[23] J. D. Hunt, Steady State Columnar and Equiaxed Growth of Dendrites and Eutectic, Mater. Sci. Eng. 65 (1984) 75-83.

[24] M. Wu, A. Fjeld, A. Ludwig, Modeling mixed columnar-equiaxed solidification with melt convection and grain sedimentation – Part I: Model description, Comp. Mater. Sci. 55 (2010) 32-42.

[25] A. Ludwig, M. Wu, Modelling the columnar-to-equiaxed transition with a 3-phase Eulerian approach, Mater. Sci. Eng. A 413-414 (2005) 109-114.

[26] J. Lipton, M.E. Glicksman, W. Kurz, Dendritic growth into under-cooled alloy metals, Mater. Science Eng. 65 (1984) 57-63.

[27] J. Campbell, Castings, Butterworth Heinemann Ltd, Oxford, 1991.

[28] J. J. Moore, Review of axial segregation in continuously cast steel, Continuous casting, Iron & Steel Soc. 3 (1984) 11-20.

[29] K. Suzuki, T. Miyamoto, On the formation mechanism of the V segregation in steel ingot, Trans. ISIJ 14(1974) 296-305

[30] J. Li, M. Wu, J. Hao, A. Kharicha, A. Ludwig, Simulation of channel segregation using a two-phase columnar solidification model – Part II: Mechanism and parameter study, Comp. Mater. Sci. 55 (2012) 419-429.

[31] M. Wu, A. Ludwig, A. Fjeld, Modeling mixed columnar-equiaxed solidification with melt convection and grain sedimentation – Part II: Illustrative modelling results and parameter studies, Comp. Mater. Sci. 55 (2010) 43-58.

[32] G. Lesoult, Macrosegregation in steel strands and ingots: Characterisation, formation and consequences, Mater. Sci. Eng. A 413-414 (2005) 19-29.

[33] M. Založnik, H. Combeau, The influence of the morphology evolution of free-floating equiaxed grains on the macrosegregation in a 3.3-ton steel ingot, in: S. L. Cockcroft and D. M. Maijer (Eds.), Proceedings of MCWASP XII, TMS (The Minerals, Metals and Materials Society), 2009, pp. 165-172.

[34] M. Ahmadein, M. Wu, J.H. Li, P. Schumacher, A. Ludwig A., Prediction of the as-cast structure of Al-4.0 wt.% Cu ingots, Metall. Mater. Trans. A (2013) in press, DOI: 10.1007/s11661-012-1606-6.

[35] W. Kurz, B. Giovanola, R. Trivedi, Theory of microstructural development during rapid solidification, Acta Mater. 34(1986) 823-830.

[36] D. Larouche, Computation of solidification paths in multiphase alloys with back-diffusion, Computer Coupling of Phase Diagrams and Thermochemistry 31 (2007) 490-504.

[37] B. Sundman, B. Jansson, J.O. Andersson J-O, The Thermo-Calc databank system, CALPHAD 9 (1985) 153-190.

[38] W.Q. Jie, Y.H. Zhou, Formation of hot-top segregation in steel ingot and effect of steel components, Metall. Trans. 20B (1989) 723-731.

[39]A. Ishmurzin, M. Gruber-Pretzler, F. Mayer, M. Wu, A. Ludwig, Multiphase/multicomponent modeling of solidification processes: coupling solidification kinetics with thermodynamics, Int. J. Mater. Res. 99 (2008) 618-625.

[40] W. Kurz, D.J. Fisher, Fundamentals of Solidification, Trans. Tech. Publication, Switzerland, 1998, pp. 280-288

[41] Ø. Nielsen, B. Appolaire, H. Combeau, A. Mo, Measurements and modeling of the microstructural morphology during equiaxed solidification of Al-Cu alloys, Metall. Mater. Trans A 32A (2001) 2049-2060.

[42] B. Appolaire, Prise en compte du movement des cristaux equiaxes dans la modelisation de la solidification des lingots d'acier coules en fonderie, Ph.D. Thesis, Institut National Polytechnique de Lorraine, France, 1999.

[43] M. Rappaz, W.J. Boettinger, On dendritic solidification of multicomponent alloys with unequal liquid diffusion coefficients, Acta Mater. 47 (1999) 3205-3219.

[44] M.A. Martorano, C. Beckermann, Ch.-A. Gandin, A solutal interaction mechanism for the columnar-to-equiaxed transition in alloy solidification, Metall. Mater. Trans. 34A (2003) 1657-1674.

[45] A. Badillo, D. Ceynar, C. Beckermann, Growth of equiaxed dendritic crystals settling in an undercooled melt, part 1: tip kinetics, J. Crystal Growth 309 (2007) 197-215.

[46] A. Badillo, D. Ceynar, C. Beckermann, Growth of equiaxed dendritic crystals settling in an undercooled melt, part 2: internal solid fraction, J. Crystal Growth 309 (2007) 216-224.

Publication V

Modelling macrosegregation in a 2.45 ton steel ingot

Jun Li, Menghuai Wu, Andreas Ludwig, Abdellah Kharicha

In: The 13th MCWASP (Modeling of Casting, Welding and Advanced Solidification Processes), Schladming, Austria, June 17-22 2012

IOP Conference Series: Materials Science and Engineering

Volume 33 012091 doi:10.1088/1757-899X/33/1/012091

Modelling macrosegregation in a 2.45 ton steel ingot

J Li[1,2], M Wu[1,2], A Ludwig[2], Abdellah Kharicha[2]

1) Christian Doppler Lab for Adv. Process Simulation of Solidification and Melting,

2) Chair of Simulation and Modelling of Metall. Processes, Univ. Leoben, Austria

E-mail: Jun.Li@unileoben.ac.at

Abstract

A three phase model for the mixed columnar-equiaxed solidification was proposed by the current authors [Wu and Ludwig 2006 *Metall. Mater. Trans*. 37A 1613-31]. The main features of the mixed columnar-equiaxed solidification are considered: the growth of the columnar dendrite trunks from the ingot surface, the nucleation and growth of the equiaxed crystals, the sedimentation of the equiaxed crystals, the thermal and solutal buoyancy flow and its interactions with the growing crystals, the solute partitioning at the solid-liquid interface during solidification, the solute transport due to melt convection and equiaxed sedimentation, the mechanical interaction/impingement between columnar and equiaxed crystals and the columnar-to-equiaxed transition (CET). However, due to the model complexity and the limited computational capability the model has not yet applied to the large steel ingots of engineering scale. This paper is going to simulate a 2.45 ton big-end-up industry steel ingot, for which some experimental results were reported [Marburg 1926 *Iron Steel Inst*. 113 39-176]. Here a simplified binary phase diagram for the steel (Fe-0.45 wt. %C) is considered. Comparison of the modelling results such as as-cast columnar and equiaxed zones, macrosegregation with the experimental results is made. Details about the formation sequence of the distinguished crystal zones and segregation patterns are analyzed.

1 Introduction

Macrosegregation is a very common and serious defect in large steel ingots. The typical segregation pattern in a steel ingot consists of a positive segregation in the top part, a cone-shape negative segregation in the bottom part, inverse segregation near the surface, V segregates along the centerline, and A-segregates in the columnar zone [3-4]. This inhomogeneity occurs due to a relative motion between the liquid and solid phase during solidification. It is understood that this relative motion can arise as a result of thermosolutal convection, shrinkage-induced feeding flow, flotation and sedimentation of free moving grain, mechanical or electromagnetic stirring, flow induced by pore or gas bubble formation, deformation of the solid skeleton, and capillary force induced flow [5].

Since the first modeling attempt of Flemings and co-workers [6-7] many macrosegregation models were presented [8-11]. Gu and Beckermann [11] for the first time have applied a fully coupled, multicomponent solidification model with melt convection to a large industry-scale ingot ($1.016 \times 2.08 \times 2.819$ m^3), their simulation result showed a qualitative agreement with the positive segregation in the top region of the ingot. However, since the neglect of sedimentation of free equiaxed crystals they could not predict negative segregation at the bottom. Combeau and co-workers [12-13] presented a two phase (solid and liquid) model to study the influences of motion and morphology of equiaxed grain on a 3.3 ton big steel ingot. Some progress was made regarding to prediction of the bottom negative segregation zone, and the results have a good agreement with the experiment. Additionally, some streak-like segregates (A-segregates) were predicted.

The current authors [1, 14] for the first time developed a mixed columnar-equiaxed model which accounts directly for the nucleation and growth of the equiaxed globular grains, the growth of columnar dendrite trunks, and the effect of equiaxed grain sedimentation and melt convection. Their previous studies have successfully predicted both the cone negative segregation in the bottom region of ingot, and the columnar-to-equiaxed-transition (CET). However, due to the model complexity and the limited computational capability the previous studies were just based on the laboratorial scale of steel ingot. In this article, the mixed columnar-equiaxed is employed to study the macrosegregation in the industry-scale steel ingot on the base of the classic experiment [2].

2 Cast ingot: experiment and model description

Many industry-scale steel ingots were poured and analysed for the segregation in the last century [2, 15]. As an example the sulphur print of a 2.45 ton big-end-up ingot (Fe-0.45 wt.%C) is shown in Figure 1(a). The mixture concentration (nominal) distribution ((c_{mix}-c_0)/c_0) is shown in Figure 1(b). As reference, this ingot is numerically studied. Configuration of this reference ingot, together with necessary boundary and initial conditions, is described in Figure 1 (c). Since the experiment was done many decades ago, due to the lack of precise process description, some process parameters and boundary conditions have to be derived on the base of assumptions. 2D axis symmetrical simulations are performed. Two cases are considered: Case I – using the mixed columnar-equiaxed three phase model; Case II – using the same model with the ignorance of the occurrence of equiaxed crystal. Table 1 lists some thermo-dynamic and physical properties.

Details of the numerical model are described elsewhere [1, 5, 14]. A brief outline of the model and simulation settings are given below:

1) A simple boundary condition is applied. Here, the value of heat transfer coefficient is taken based on the final solidification time which refers to the classical theory and experiment ones. [15].

2) Three phases are defined: the primary liquid phase (ℓ), the equiaxed phase (e), and the columnar phase (c). The corresponding phase fraction is f_ℓ, f_e, and f_c with $f_\ell + f_e + f_c = 1$. Both the liquid and equiaxed phases are moving phases, for which the corresponding Navier-Stokes equations are solved. The columnar phase is assumed to stick to the wall, and solidifies from the wall towards the bulk melt. Thus, no momentum equation for the columnar phase is considered.

3) Columnar dendrites are approximated by growing cylinders starting from the mold wall towards the casting centre. The advance of the columnar tip front was tracked during the solidification.

4) Equiaxed grains are approximated as spheres. However, for the calculation of drag force the morphology of the equiaxed grains was modified as octahedral.

Table1. Thermo-dynamic & physical properties [12]

Property	Units	Quantity
Melting of pure iron	K	1805.15
Liquidus slope	K (wt.%)$^{-1}$	-80.45
Equilibrium partition coefficient	-	0.36
Reference density	kg·m^{3}	6990
Specific heat	J kg^{-1} K^{-1}	500
Thermal conductivity	W m^{-1} K^{-1}	34.0
Latent heat	J kg^{-1}	2.71×10^{5}
Viscosity	Kg m^{-1} s^{-1}	4.2×10^{-3}
Thermal expansion coefficient	K^{-1}	1.07×10^{-4}
Solutal expansion coefficient	wt.%$^{-1}$	1.4×10^{-2}
Second dendritic arm spacing	m	5×10^{-4}
Diffusion coefficient (liquid)	m^{2} s^{-1}	2.0×10^{-8}
Diffusion coefficient (solid)	m^{2} s^{-1}	1.0×10^{-9}

5) A three-parameter heterogeneous nucleation law is used for the nucleation of equiaxed grains. No fragmentation and grain attachment are currently considered. Growth of the columnar trunk and equiaxed grain is governed by diffusion.

6) The permeability in the columnar mush zone is modelled according to Blake-Kozeny, while the drag law between the melt and equiaxed phase is modelled according to Wang's approach [16].

7) Growth of columnar primary tips is stopped when the volume fraction of equiaxed phase in front of them reaches 0.49 (hard blocking criterion) [17].

8) Packing limit for the equiaxed phase is set as $f_e + f_c \geq 0.637$ [18], and the equiaxed crystals are trapped when the trapping limit of $f_c \geq 0.2$ is reached [19].

3 Simulation results and discussions

3.1 Case I: mixed columnar-equiaxed solidification

In this case full three phases are considered. The nucleation parameters for the equiaxed grains are assumed: $n_{max} = 5\times10^9$ m^{-3}, $\Delta T_\sigma = 2$ K, $\Delta T_N = 5$ K. The simulated dynamic evolution of equiaxed grain volume fraction, columnar volume fraction, equiaxed grain sedimentation velocity and melt velocity at 100 s, 500 s, 1500 s, and 4000 s are shown in Figures 2(a) through (d), respectively. The final macrosegregation pattern is shown in Figure 1(d).

In the early stage of solidification, the equiaxed grains nucleate and grow gradually near the mould walls and bulk melt. Since the density of equiaxed grains are bigger than the melt, the equiaxed grains sink from the upper region to the bottom region, as shown in Figure 2(a). However, one may notice that in the centre part of the ingot there are some differences. In some regions the equiaxed sedimentation velocity is upward. Because the equiaxed volume fraction in these regions is very small (i.e. the momentum is small), the equiaxed grain sedimentation velocity is easily influenced and finally dominated by the upward liquid melt flow.

The direction of the liquid melt velocity near the columnar front is contributed by three factors: the solutal buoyancy force which will lead to the upward melt flow; the thermal buoyancy force which will lead to the downward melt flow; and the equiaxed sedimentation velocity which will drag the surrounding melt flow downwards. It is clearly seen from the liquid melt flow field, which shows the downward melt flow there, that in this ingot the two downward factors are the decisive. The melt velocity direction near the columnar front is downward, however, due to the big scale of the ingot the melt velocity direction in the centre region is obscure and disorder.

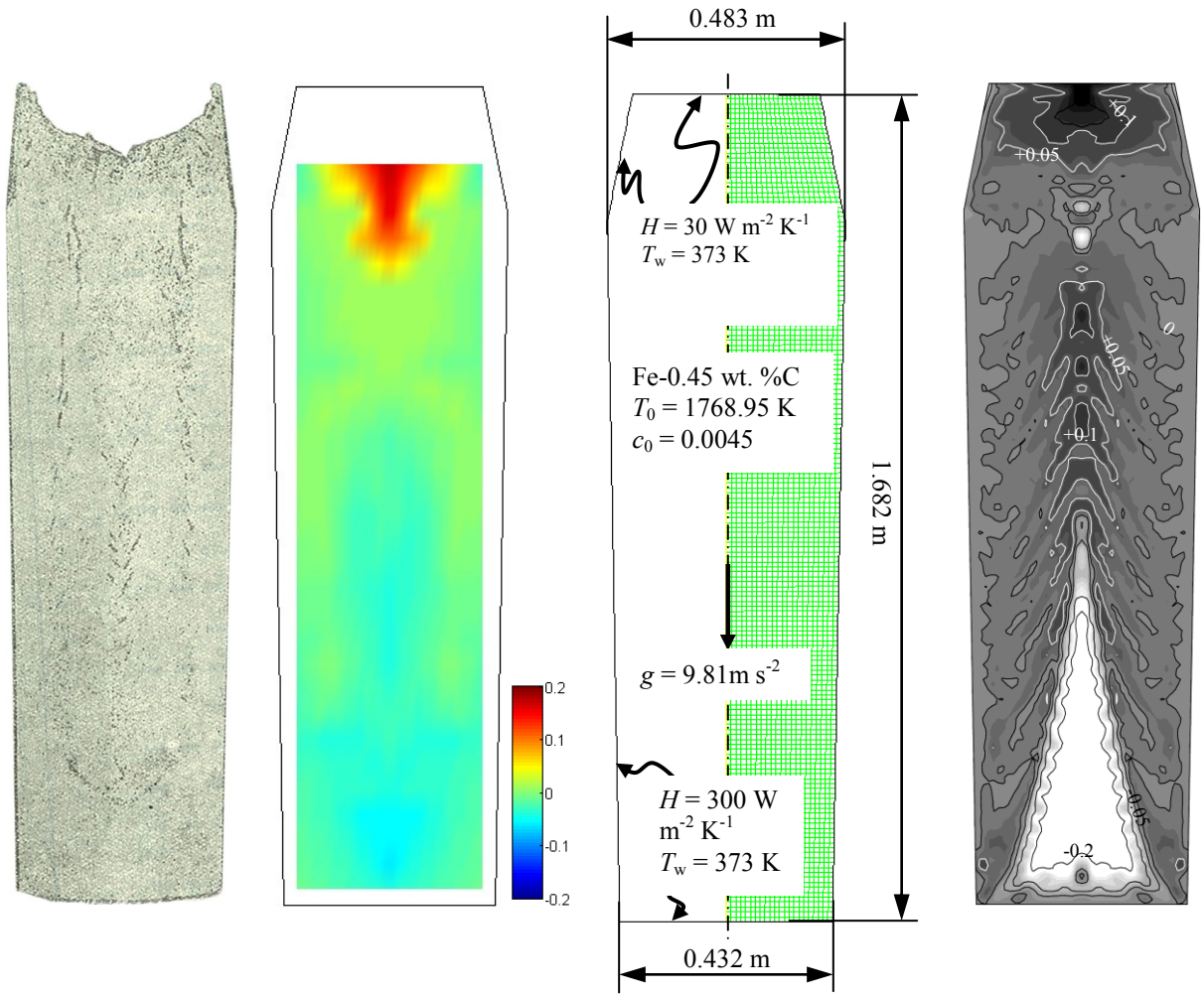

(a) sulphur print (b) measured segregation (c) simulation configuration (d) simulated segregation

Figure 1:Configuration of a 2.45-ton industry-scale steel ingot. (a)-(b) experiment [2], (c) simulation configuration and (d) simulated macrosegregation in grey scale (black for the positive segregation and light for the negative segregation) overlapped with isolines. The macrosegregation, both experimental (b) and simulated (d), is shown for the nominal mixture concentration $((c_{mix}-c_0)/c_0)$.

As the sinking of the equiaxed grains leads to an accumulation of equiaxed grains in the bottom region of the ingot, the equiaxed grain density in the bottom region is bigger than the other regions which will increase the equiaxed solidification rate in this bottom region. As shown in Figure 2, the increasing of equiaxed volume fraction in the bottom region is faster than that in the other regions. This kind of sinking and accumulation of equiaxed grain will form a characteristic cone-shape distribution of equiaxed fraction in the bottom region.

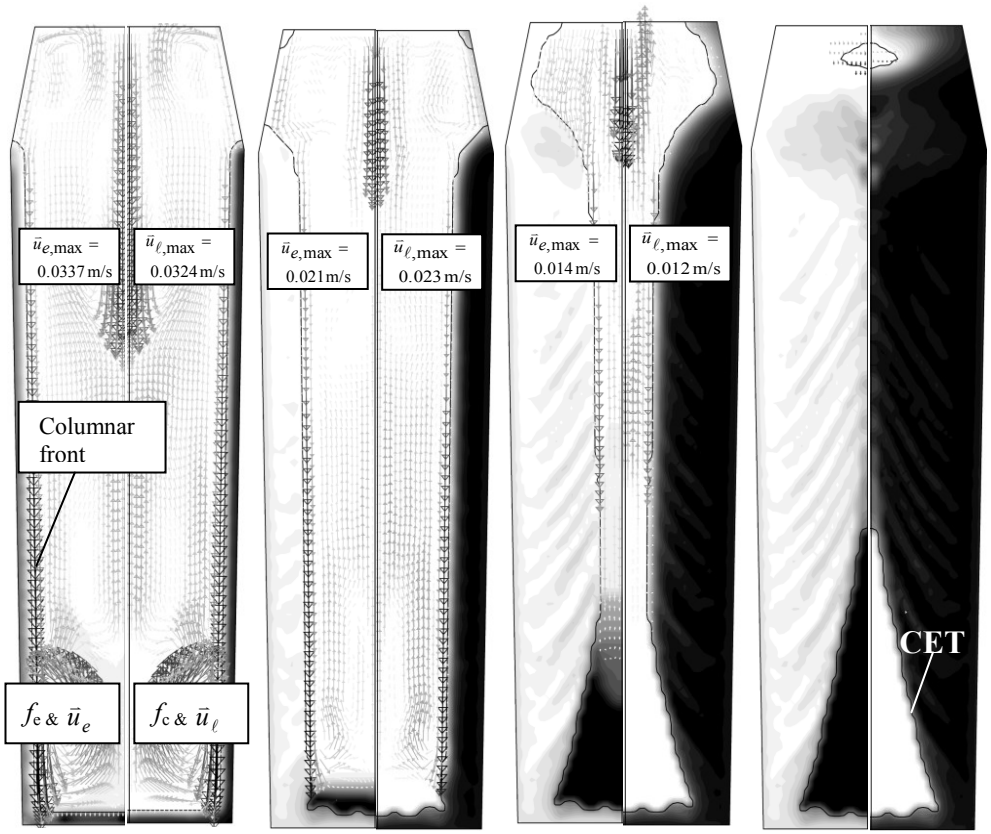

(a) 100 s (b) 500 s (c) 1500 s (d) 4000 s

Figure 2: Solidification sequence of flow fields. The volume fraction of each phase (f_e or f_c) is shown in gray scale from 0 (bright) to 1 (dark). The left half of each figure shows the evolution of equiaxed volume fraction (f_e) together with the equiaxed sedimentation velocity ($\vec{u}_e$) in black arrows. The right half of each figure shows the evolution of columnar volume fraction (f_c) together with the melt velocity ($\vec{u}_\ell$) in black arrows. The columnar dendrite tip position also marked with a black solid line.

As the columnar tip front is explicitly tracked, the simulation shows that the columnar tip fronts from both sides tend to meet in the ingot centre. However, in the lower part of the ingot the large amount of equiaxed grains stop the propagation of the columnar tip front. The final position of columnar tip indicates the columnar-to-equiaxed transition (CET) position. The CET separates the areas where only equiaxed grains appear from the areas where both columnar dendrites and equiaxed grains coexist. The CET line is predicted in this study, as seen in Figure 2(d). In addition, due to the disorder of both the sedimentation velocity and the melt convection, the sawtooth-like distribution of both the equiaxed phase and columnar phase volume fraction was found in the ingot. These sawtooth like profiles of

both equiaxed phase and columnar phase volume fraction will definitely effect the final macrosegregation distribution.

Figure 1(d), presents the predicted final macrosegregation distribution. The cone-shaped negative segregation in the bottom region and a positive segregation zone in the upper region are obviously shown. The main mechanism for this cone-shaped negative segregation zone is grain sedimentation [5]. The settling grains were poor in solute and thus their pile-up results in a negative segregation at the bottom of the ingot. A further contributing factor to the strength of this negative segregation comes from the flow divergence of the residual liquid through this zone at a late solidification stage. The positive segregation in the upper region of the ingot is caused by the flow of the enriched melt in the bulk region. The solidification pattern agrees with the classical explanation of steel ingot solidification, summarized by Campbell [20].

One interesting result is detected that some streak-like patches of positive segregation were predicted near the mould wall and even in the centre region. These streak-like patches are somehow looks like the so called A-segregation [21]. Here we call these streak-like segregation as quasi-A-segregation. Most people consider that the main formation mechanism for A-segregation is: the flow disturbance in the mushy zone which will result in the flow channel and subsequently A segregation. The current authors [22-23] have studied the mechanism of channel segregation in a Sn-Pb benchmark. They denoted that the formation of channel segregation should be considered in two steps: (1) the initiation of channel, which is determined by the Rayleigh number; (2) the growth of channel which is the result of flow-solidification interactions. However, the formation mechanism of quasi-A-segregation in the current ingot must be different. In the early Sn-Pb benchmark the only driving force for the melt flow is thermal-solutal buoyancy force, whereas, in the current case the sedimentation of equiaxed grains and their inteactions with the columnar tip front and melt flow seem to play dominant role. The details about the mechanism for this kind of A-segregation are still to be investigated.

3.2 Case II: two-phase columnar solidification

Here, Case II used the same model and the same parameter as Case I. The only difference in this case is that we did not take into account the nucleation and growth of equiaxed grains.

The solidification sequences and evolution of macrosegregation in two-phase columnar model are shown in Figure 3(a)-(c). The columnar tip front and volume fraction of columnar phase move from the mould walls towards the bulk melt region. For the solute-enriched interdendritic melt near the solidification front, the solutal buoyancy leads to an upward flow. However, the thermal buoyancy leads to a downward flow. In this simulation case (Fe-0.45 wt. %C) the solutal buoyancy dominates over the thermal buoyancy, therefore the upward flow in the solidification front is the primary phenomena leading to the flow, as seen in Figure 3(a). The melt convection in the solidification front is upward, and this upward flow will drive the centre bulk melt to downward. Since the melt domain is large, the melt convection in the inside of bulk melt is disorder.

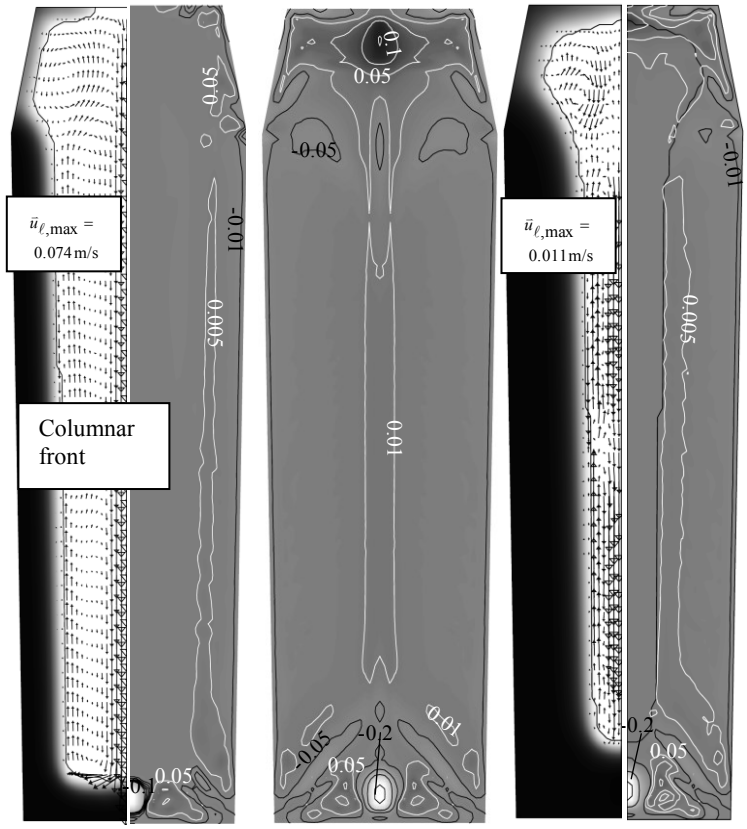

(a) 500 s (b) 1200 s (c) 3000 s

Figure 3: Solidification sequence and evolution of macrosegregation in the case of two-phase columnar solidification. In the left half of each figure the columnar volume fraction (f_c) is shown in gray scale together with the melt velocity ($\bar{u}_\ell$) in black arrows. In the right half of each figure the distribution of macrosegregation (((c_{mix}-c_o)/c_o) is shown in gray scale overlaid with macrosegregation iso-lines in solid lines. The columnar tip position was also indicated with a black solid line. Figure (c) shows the final macrosegregation distribution.

As seen from the final macrosegregation pattern in Figure 3(c), in the near wall region, where the solidification start from, a small degree of negative macrosegregation (-0.005) is predicted, while in the centre region, where the solidification is later on, a small degree of positive macrosegregation (0.01) is predicted. It is noted that a small region negative macrosegregation (relative macrosegregation value equal to -0.2) is found in the bottom region. In the upper region a positive macrosegregation is predicted with a relative macrosegregation value of 0.12. The reason for the negative segregation in the bottom middle region and the positive segregation in the upper middle region can be explained [5]: In the bottom middle region, since the solute enriched melt are replaced by the solute poor melt, the negative segregation tend to formation. The reason for the positive segregation in the upper middle region is that the solute poor melt is replaced by the solute enriched interdendritic melt from the solidification front.

4 Verification and discussions

The centre line segregation distributions are compared between the experiment results and the simulation results, as shown in Figure 4. The experiment shows the negative segregation in the lower part region and positive segregation in the upper region. The mixed columnar-equiaxed three phases model also shows the negative segregation in the lower part region and positive segregation in the upper region. However, the negative segregation in the lower part region is predicted more seriously than the experiment result, and in the middle of upper part region where the mixed three phase model predicted the negative segregation while the experiment shows the positive segregation. The two-phase columnar model predicts a negative segregation region in the bottom region of ingot and a small degree negative segregation in the middle of upper middle region. However, this model predicts a small degree positive segregation in the upper part region where both the experiment and the mixed three phase shown the negative segregation.

The possible explanation for the overestimate of the negative segregation in the lower part region by the mixed columnar-equiaxed model could be in two aspects. On one hand, the assumption of totally spherical equiaxed grain will underestimate the average concentration for each equiaxed grain which subsequently will overestimate the serious of negative segregation in the bottom equiaxed zone. On the other hand, the overestimation of equiaxed

nucleation in the whole ingot which increase the equiaxed solidification will also result in the overestimation of the negative segregation.

As been observed from the lower part region of the ingot, the mixed three phase model (with the sedimentation of the equiaxed grain) overestimates the ne gative segregation. However, the two-phase columnar model underestimates the negative segregation. Therefore, one possible conjecture is as follows: in this experiment there should contain a certain number of equiaxed grains in the lower part region; this mixed three phase model has overestimated the nucleation of equiaxed grain.

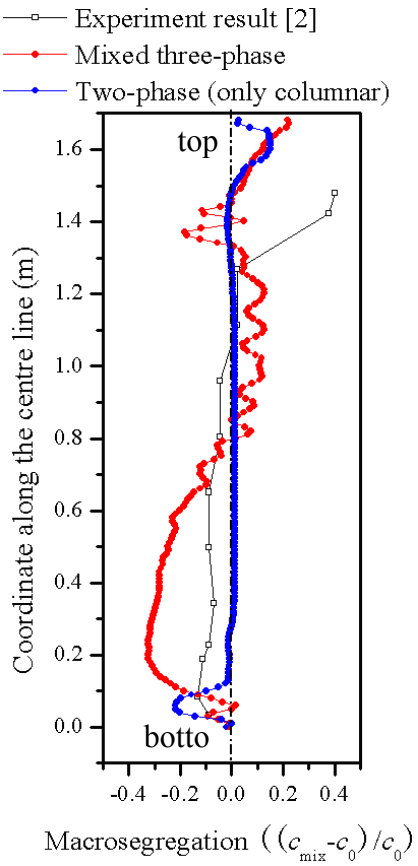

Figure 4: Comparison of macrosegregation (((c_{mix}-c_o)/c_o) distribution along the centre of cast.

In the middle of the upper part, although the experiment shows the positive segregation, both of the simulation models predict the negative segregation. The reason for this deviation may also be in two aspects. Firstly, for the simulation case, during the final stage of solidification in the middle region of the ingot, the columnar tips will grow to the centre which will lead to the bridging and mini-ingotism in the upper part [24]. As the same

mechanism as it forms in the whole steel ingot, eventually, the negative segregation will form in the middle of upper part. The second aspect is due to the ignorance of solidification shrinkage. In addition, as seen from the experiment curve, the distance between two points is in the order at least of 10 cm. It is known that in the region below the hot-topping and in the hot top part strong variations can occur. It means that the measured points did not provide sufficient resolution. People often found the negative segregation in the middle of upper part regions as well [12].

One should emphasize that the main purpose of this study is to show and verify that this mixed columnar-equiaxed model can be applied in the industry scale steel ingot, and can predict some reasonable macrosegregation patterns. We are not going to adjust some of the calculation parameters to cater for the experiment results. Since the experiments were done in many decades ago and many of the process parameters and material properties are unknown, the simulation results could only reproduce the experiment results in a qualitative manner.

5 Summary

A mixed columnar-equiaxed solidification model was applied to study the formation of macrosegregation in a 2.45 ton industry-scale steel ingot. It is verified that the experimentally reported segregation phenomena can be numerically simulated. The cone-shape negative segregation in the bottom region and a positive segregation in the upper region of the ingot were predicted. The CET line, separating the purely equiaxed zone from the coexisting columnar-equiaxed zone, was predicted. The quasi-A-segregates near the mold wall were also found. The global macrosegregation distribution agreed qualitatively with the experimental result. However, the quantitative error of the numerical simulation is still quite large due to the lack of reliable process parameters and nucleation (equiaxed) parameters. The above-mentioned simulation was based on the assumed nucleation parameters ($n_{\max}$ = 5×10^9 m^{-3}, ΔT_σ = 2 K, ΔT_N = 5 K) for the equiaxed grains. One more simulation was performed with ignorance of the occurrence of equiaxed crystal. It is interesting to found that the latter case has a better quantitative agreement with the experimental result along the casting centerline than the former case with full three phases. It implies that the assumed nucleation parameters for equiaxed crystal in the former case

have overestimated the amount of equiaxed grains, or the current 2.45 ton ingot might solidify mostly with columnar morphology. This hypothesis needs further verification.

Acknowledgments

The authors acknowledge the financial support by the Austrian Federal Ministry of Economy, Family and Youth and the National Foundation for Research, Technology and Development. Jun Li would like to thank the support from the China Scholarship Council.

References

[1] Wu M and Ludwig A 2006 Metall. Mater. Trans. 37A 1613-31

[2] Marburg E 1926 J. Iron steel Inst. 113 39-176

[3] Hultgren A 1973 Scand. J. Met. 2 217-27

[4] Flemings M C 1976 Scand. J. Met. 5 1-15

[5] Wu M, Könözsy L, Ludwig A, Schützenhöfer W and Tanzer R 2008 Steel Res. Int. 79 56-63

[6] Mehrabian R and Flemings M C 1970 Metall. Trans. 1 455-64

[7] Fujii T, Poirier D R and Flemings M C 1979 Metall. Trans. B 10B 331-39

[8] Vannier H, Combeau H, Chevrier J C and Lesoult G 1991 in Modeling of casting, welding and advanced solidification process V, TMS (Warrendale, PA) 189-95

[9] Ohnaka I 1986 in state of the art of computer simulation of casting and solidification processm editor Fredriksson H, Les éditons de physique, Les Ulis, France 211-23

[10] Schneider M C and Beckermann C 1995 Metall. Mater. Trans. A. 26A 2373-87

[11] Gu J P and Beckermann C 1999 Metall. Mater. Trans. A. 30A 1357-66

[12] Combeau H, Založnik M, Hans S and Richy P E 2009 Metall. Meter. Trans. B 40B 289-304

[13] Založnik M and Combeau H 2010 Int. J. Therm. Sci. 49 1500-09

[14] Wu M and Ludwig A 2007 Metall. Meter. Trans. A 38A 1465-75

[15] Marburg E 1953 Trans. AIME 5 157-72

[16] Wang C and Beckermann C 1995 Metall. Meter. Trans. B 26B 111-9

[17] Hunt J D 1984 Mater. Sci. Eng. 65 75-83

[18] Wu M and Ludwig A 2009 Acta Mater. 57 5621-31

[19] Ludwig A and Wu A 2005 Mater. Sci. Eng. A 413-414 109-14

[20] Campbell J 1991 Castings, Butterworth Heinemann Ltd, Oxford

[21] Moore J J and Shah N A 1983 Inter. Metals Reviews 28 338-56

[22] Li J, Wu M, Hao J and Ludwig A 2012 Comp. Mater. Sci. 55 407-18

[23] Li J, Wu M, Hao J, Kharicha A and Ludwig A 2012 Comp. Mater. Sci. 55 419-29

[24] Moore J J Iron & Steel Soc. 1984 3 11-20

Publication VI

Multiphase modeling of the macrosegregation in ingot castings

Menghuai Wu, Jun Li, Abdellah Kharicha, and Andreas Ludwig

ICRF-2012 (1st Int. Conf. on Ingot Casting, Rolling and Forging), Aachen, Germany 3-7 June (2012) CD-ROM proc., 1-10.

Multiphase modelling of the macrosegregation in ingot castings

M. Wu[1,2*], J. Li[1,2], A. Kharicha[2], A. Ludwig[2]

[1] Christian Doppler Laboratory for Advanced Process Simulation of Solidification and Melting,

[2] Chair of Simulation and Modelling of Metallurgical Processes, Univ. of Leoben, Austria

[*] Corresponding author, Franz-Josef-Str. 18, A-8700 Leoben, Austria,

Email: menghuai.wu@unileoben.ac.at

Abstract

A brief overview of the state-of-the-art modelling approaches for the macrosegregation in ingot castings is presented, with the emphasis on the recent activities of the multiphase model development being taken up by the current authors at the University of Leoben. A three-phase model for the mixed columnar-equiaxed solidification was recently proposed by the current authors. The progressive growth of the columnar dendrite trunks from the ingot surface into the centre, the nucleation and growth of the equiaxed crystals including the motion of the equiaxed crystals, the thermal and solutal buoyancy flow and its interactions with the growing crystals (equiaxed and columnar), the solute partitioning at the solid-liquid interface during solidification and the solute transport due to melt convection and equiaxed sedimentation, the columnar-to-equiaxed transition (CET) were considered. As modelling result the mixed columnar-equiaxed macrostructure and different macrosegregation patterns can be predicted. Application of the aforementioned model is

mainly limited by two factors: one is the extreme computational expense; one is the lack of the reliable parameters being required by the model. In order to perform a calculation of industry ingot (up to hundreds tons) on the base of the current computer resources, compromise is often made between the model capability and the computational feasibility, i.e. some necessary model simplifications have to be made. In this article the on-going works to scale-up the current models for the industry applications are reported.

Keywords: steel, ingot casting, macrosegregation, multiphase simulation.

1 Introduction

Most valuable experimental researches on the macro-segregation in large steel ingots were done in ca. one century ago [1-2]. A series of steel ingots, scaled from a few hundred kilograms up to 172 tons, were poured and cut for segregation analysis. Primary knowledge was obtained, and typical segregation map in the large steel ingots was drawn [3-5], as shown in Figure 1. To date most segregation phenomena can be physically explained. Multiphase flow such as thermo-solutal convection, happening in the interdendritic and bulk regions, and crystal sedimentation during solidification is the key mechanism for the formation of segregation. The thermodynamics, solidification kinetics and thermal mechanics are also coupled with the flow phenomena, and contribute to the final segregation results.

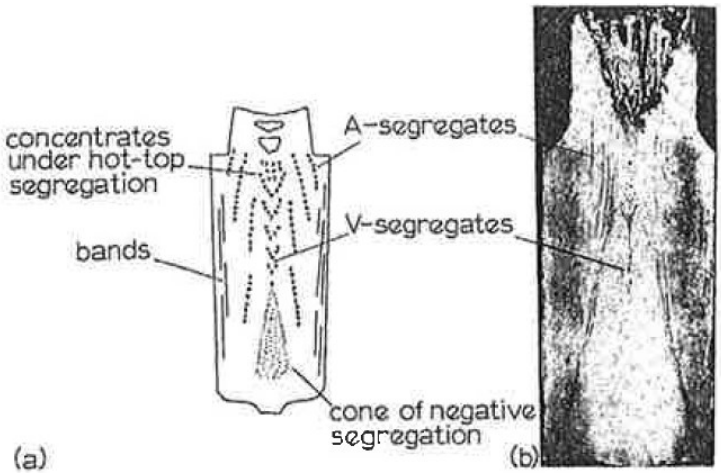

Figure 1: Typical segregation map in steel ingots (the figure is reproduced from [3]). (a) Schematic representation with '+' for positive and '-' for negative segregation; (b) sulphur print of a 10-ton ingot.

Today such experimental trials due to extremely high cost were only carried out occasionally with caution [6-9]. Instead mathematical (both analytical and numerical) modelling approach becomes a most efficient tool for this purpose. Some progresses were reviewed by other authors [9-12]. Understanding to the segregation mechanism was significantly improved by the mathematical models. Unfortunately, the picture of Figure 1 is still not quantitatively reproducible with sufficient details by numerical models of today. The great challenge arises from the multiphase nature of the solidification phenomenon. The solution of the segregation problem demands a precise description of the multiphase flow, which occurs and interacts with the solidifying microstructure (dendritic morphology) at different length scales. From the flow dynamic point of view, at least three (hydrodynamic) phases are involved in a typical ingot casting during solidification: two moving phases (liquid and equiaxed crystals) and one stationary phase (columnar dendrite trunks). In other words, a model being able to reproduce the patterns of Figure 1 needs at least to consider these three phases. However, the limitation of early computational hardware resource has prevented people from considering so many phases. Compromise has to be made between the model capability and the computational feasibility. For example, Gu and Beckermann used a mixture liquid-columnar solidification model [13] and Combeau et al. used a two-phase equiaxed solidification model [8] to simulate the segregation in steel ingots, and some successes were achieved.

This article is not going to give a comprehensive review of the topic of macrosegregation models, but focuses on the relevant activities being taken up by the current authors at the University of Leoben. On the base of previous work of Beckermann's [11, 14-17], a series of multiphase solidification and macrosegregation models were proposed. These include a two-phase globular equiaxed solidification model [18-19], a two-phase monotectic solidification model [20-21], a three-phase mixed columnar-equiaxed solidification model [22-23], an equiaxed solidification model with dendritic morphology [24-25] and a five-phase mixed columnar-equiaxed solidification model with dendritic morphology [26-27]. As the computational expense increases correspondingly with the increasing number of phases, the modelling activities are divided in two directions. One is to further develop comprehensive models by including as many as necessary phases and physics to solve as much as possible segregation features on one hand. Application of this kind of models may still rely on future enhancement of the hardware resource. On the other hand we can base on the available hardware resource by using possibly-simple model to solve the principal

segregation phenomena of the industry ingots. This article is going to report some modelling examples by using a three-phase mixed columnar-equiaxed model [22-23]. The applicability of this model to the industry ingots is investigated, and some merits and limitations are discussed.

2 Characterization of the model

To characterize the three-phase mixed columnar-equiaxed solidification model, a benchmark (ϕ 66 mm x 170 mm) of a steel ingot was simulated. Macrosegregation formation due to the combined thermosolutal convection, grain sedimentation, and sedimentation induced convection was modelled. Details about the settings for this benchmark refer to previous publications [22-23, 28]. Model assumptions are summarized as follows:

1) Solidification starts with an initial concentration Fe-0.34 wt.%C and an initial temperature of 1785 K, mould filling is ignored;

2) Three phases considered are: the melt, globular equiaxed crystals and columnar dendrite trunks;

3) Morphologies are approximated by step-wise growing cylinders for columnar dendrite trunks and spheres for globular equiaxed crystals;

4) Columnar trunks grow from side and bottom walls, and the columnar tip front is explicitly tracked;

5) A three-parameter heterogeneous nucleation law is used for the nucleation of the equiaxed crystals [29]. No fragmentation and grain attachment are considered;

6) Shrinkage flow is ignored. The buoyancy force for the thermosolutal convection and crystal sedimentation is accounted for by a Boussinesq approximation;

7) The equiaxed crystals ahead of the columnar tip front can move freely, but they can be captured by the columnar trunks as the local columnar volume fraction is beyond 0.2;

8) Hunt's blocking mechanism [30] is applied for predicting CET (columnar-to-equiaxed transition);

9) Constant heat transfer coefficients and constant ambient temperatures are assumed [22].

The solidification sequence including sedimentation of the equiaxed crystals, the sedimentation-induced and thermosolutal buoyancy-induced melt convection are shown in Figure 2(a). The simulated solidification sequence agrees with the explanation of steel ingot solidification, as summarized by Campbell [31]. The columnar dendrites grow from the mould wall and the columnar tip front moves inwards. The equiaxed grains nucleate near the mould walls and in the bulk melt. The columnar dendrites are stationary, whereas the equiaxed grains sink and settle in the base region of the ingot. The accumulation of such grains at the base of the ingot has a characteristic cone-shape. The sedimentation of grains and the melt convection influence the macroscopic solidification sequence and thus, the final phase distribution. More equiaxed grains will be found at the bottom and in the base region, while columnar structure will be predominant in the upper part of the ingot.

As the columnar tip front is explicitly tracked, the simulation shows that the columnar tip fronts from both sides tend to meet in the casting centre. However, in the lower part of the casting the accumulation of equiaxed grains stops the propagation of the columnar tip front. Its final position indicates the CET position. The CET separates the areas where only equiaxed grains appear from the areas where both columnar dendrites and equiaxed grains coexist.

The final macrosegregation distribution is predicted, as shown in Figure 2(b). From the simulation results it appears obvious that the main mechanism for the cone-shaped negative segregation in the base region is the grain sedimentation. The settling grains are poor in solute elements, thus their pile-up results in negative segregation in the bottom of the ingot. A further contributing factor to the strength of negative segregation arises from the flow divergence of the residual liquid through this zone at a late solidification stage. The positive segregation at the top region of the ingot is caused by the flow of the enriched melt in the bulk region. This kind of positive segregation coincides with classical experimental results [31]. It should be noted that channel segregations, which are frequently found in large steel ingots, are not predicted in such a benchmark ingot with reduced dimension.

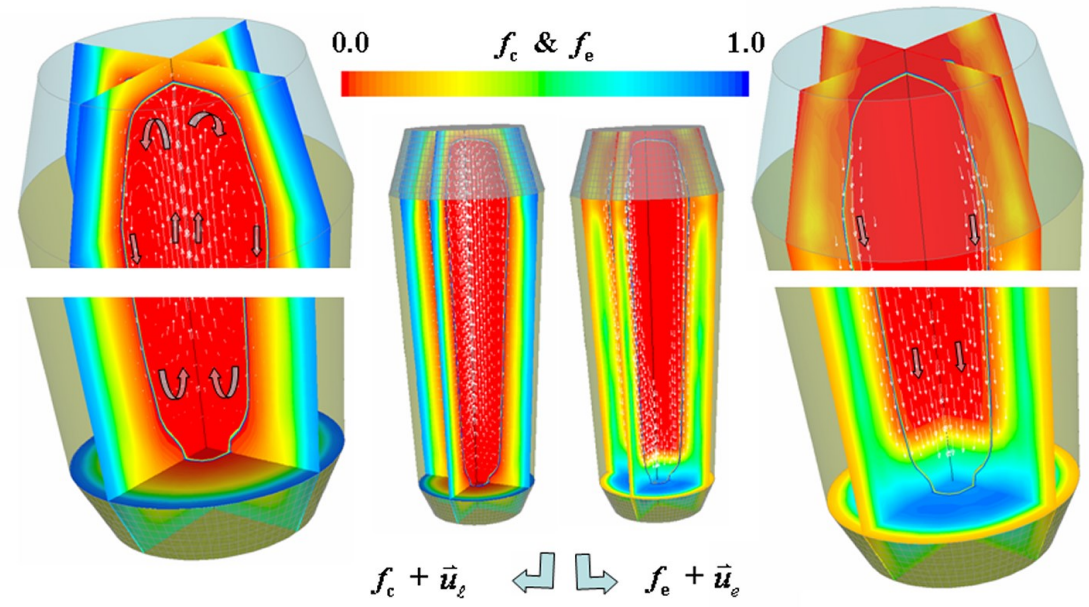

(a)

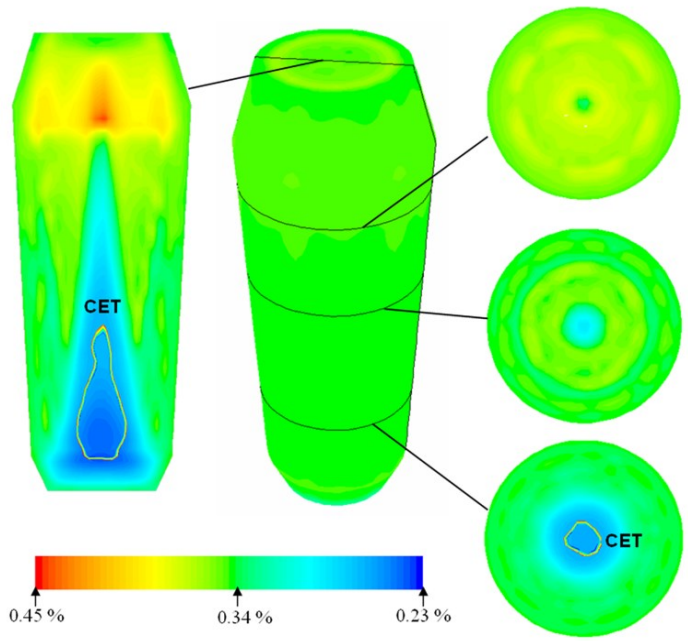

(b)

Figure 2: (a) Simulated solidification sequence (at 20 s) of the benchmark steel ingot. Volume fraction of the columnar and equiaxed phases, f_c and f_e, are shown in colour in two vertical and one horizontal sections, the velocity fields $\vec{u}_\ell$ and $\vec{u}_e$ are shown as vectors. The columnar tip front position is also marked. (b) Predicted mix concentration c_{mix} in the steel ingot, scaled from 0.23 wt.% C to 0.45 wt.% C. The area of 100% equiaxed macrostructure is enveloped by the CET line. Here an arbitrary set of nucleation parameters ($n_{max} = 5\times10^9$ m^{-3}, $\Delta T_\sigma = 2$ K, $\Delta T_N = 5$ K) is used to characterize the formation and sedimentation of equiaxed crystals and their impact on the macrosegregation.

3 2.45 ton ingot

The experimentally measured macrosegregation of a 2.45 ton big-end-up ingot (Fe-0.45 wt.%C) was reported [1]. The ingot had a section of square and was cast in a chilled mould. As reference, the segregation pattern in this ingot is numerically simulated and compared with the experiment, as shown in Figure 3. Due to lack of precise process description, some process parameters and boundary conditions have to be derived on the base of assumptions. The sulphur print of this ingot is shown in Figure 3(a). The measured mixture concentration $((c_{mix}-c_0)/c_0)$ map is shown in Figure 3(b). Configuration of this ingot, together with necessary boundary and initial conditions used for the calculation, is described in Figure 3 (c). More details about the simulation configurations are presented elsewhere [32], and the same three-phase model (Section 2.0) is used. 2D axis symmetrical simulations are performed to approximate the solidification behaviour in the square section ingot. The predicted solidification sequence is shown in Figure 4 and the segregation map is shown in Figure 3(d).

The global solidification sequence in this 2.45 ton ingot (Figure 4) is actually similar to what characterized by the previous small benchmark ingot (Figure 2). The sinking of the equiaxed crystals in front of the columnar dendrite tips leads to an accumulation of equiaxed phase in the bottom region of the ingot. The accumulation of the equiaxed phase in the bottom region will block the growth of the columnar dendrite tips, i.e. CET occurs there, hence finally to cause a characteristic cone-shape distribution of equiaxed zone being enveloped in the CET line. Relatively strong negative segregation is predicted in the low-bottom equiaxed zone. With the sedimentation of large amount of equiaxed crystals downwards, the relatively-positive segregated melt is pushed upwards in the casting centre, hence to cause a positive segregation in the upper region. Despite the above similarity between the 2.45 ton ingot and the small benchmark ingot (Figure 2), significant differences are identified, which are described below.

Firstly, the flow is much more instable (Figure 4). The melt flow in the bulk region ahead of the columnar dendrite tip front is driven by three mechanisms: the solutal buoyancy which drives upwards; the thermal buoyancy which drives downwards; and the equiaxed sedimentation which drags the surrounding melt downwards. Generally the two downward driving forces are decisive, which cause the melt flows downwards along the columnar dendrite tip front. This downward flow along the columnar tips will push the melt to rise in

the ingot centre. This rising melt will interact with the falling equiaxed crystals and with the downward flow near the columnar tip front, to form many local convection cells. The pattern of melt convection and crystal sedimentation becomes chaotic. These local convection cells are developed or suppressed dynamically, and the flow direction in the cells changes with time as well. The flow instability and the flow chaotic behaviour are dependent on the ingot size (ingot height). Therefore, to explain the influence of the ingot size on the macrosegregation demands the knowledge about the influence of the ingot size on the flow pattern.

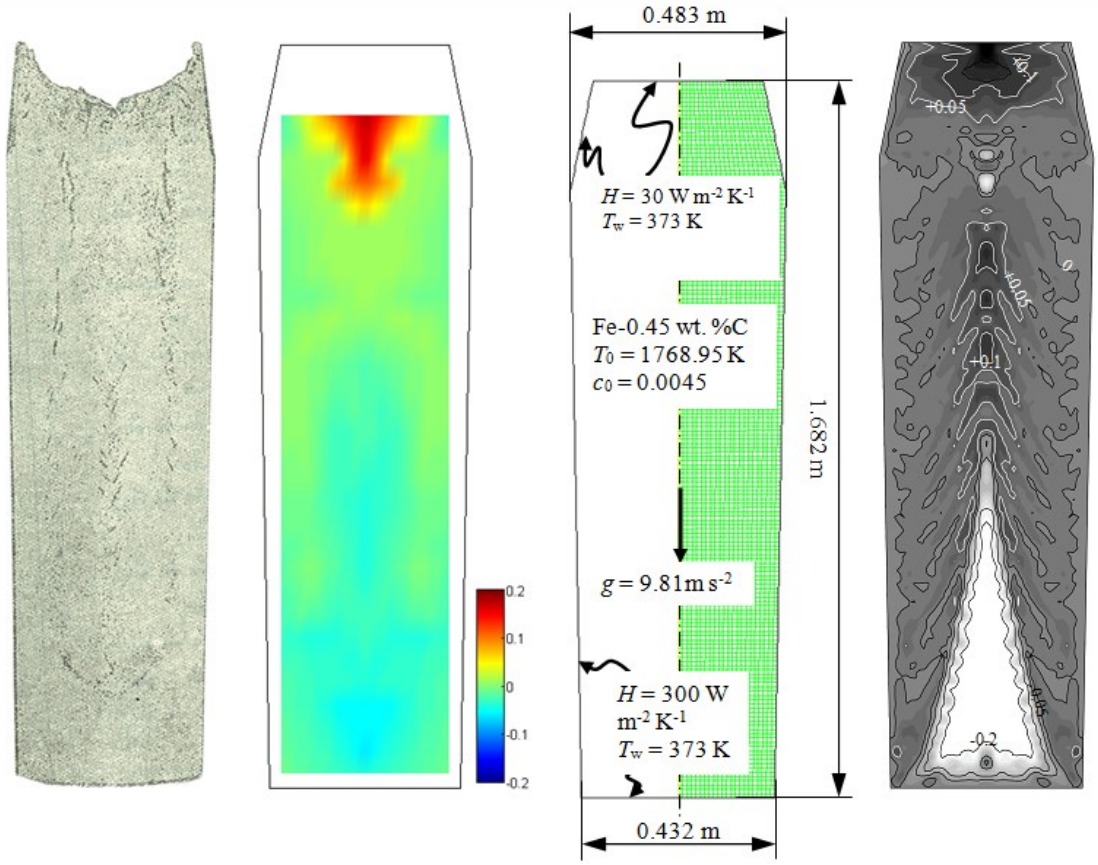

(a) surphur print (b) measured seg. (c) B.C. configuration (d) simulated seg.

Figure 3: Configuration of a 2.45-ton industry-scale steel ingot. (a)-(b) experiment [1], (c) simulation configuration and (d) simulated macrosegregation in grey scale (black for the positive segregation and light for the negative segregation) overlapped with isolines. The macrosegregation, both experimental (b) and simulated (d), is shown for the nominal mixture concentration ($(c_{mix}\text{-}c_o)/c_o$). Nucleation parameters: $n_{max} = 5\times10^9$ m^{-3}, $\Delta T_\sigma = 2$ K, $\Delta T_N = 5$ K.

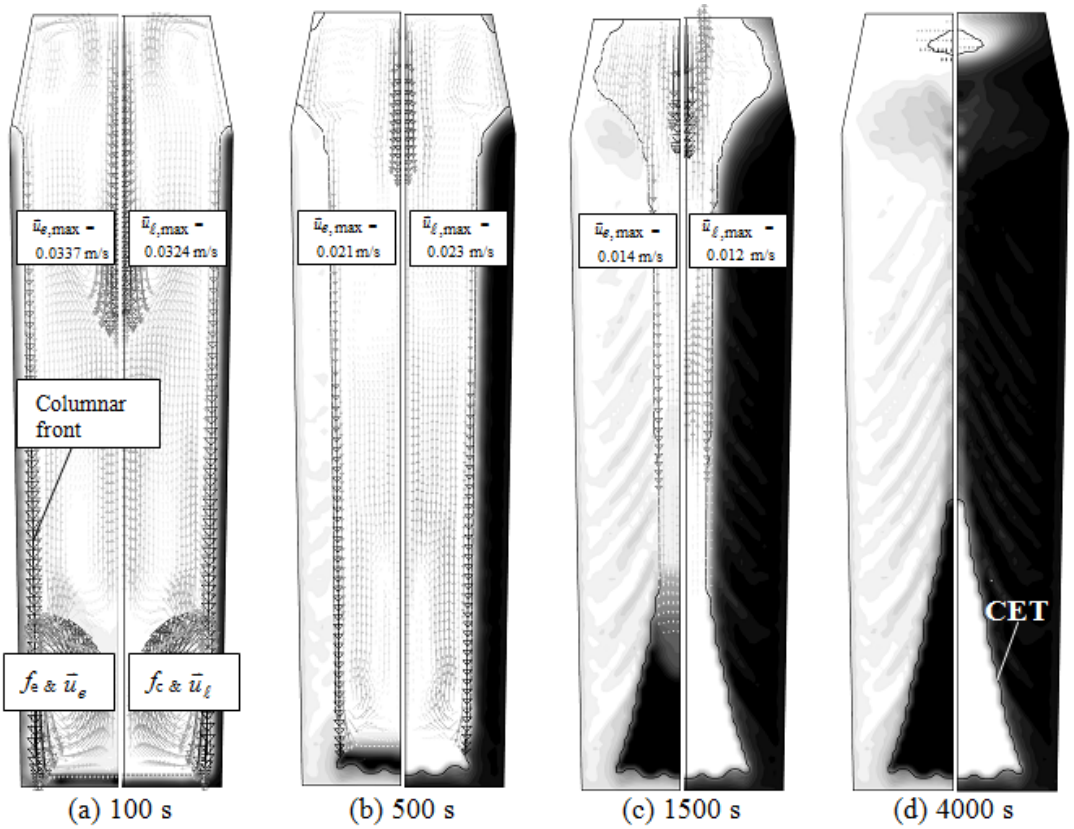

Figure 4: Solidification sequence of the 2.45 ton ingot. The volume fraction of each phase (f_e or f_c) is shown in gray scale from 0 (bright) to 1 (dark). The left half of each figure shows the evolution of equiaxed volume fraction (f_e) together with the equiaxed sedimentation velocity ($\bar{u}_e$) in black arrows. The right half of each figure shows the evolution of columnar volume fraction (f_c) together with the melt velocity ($\bar{u}_\ell$) in black arrows. The columnar dendrite tip position also marked with a black solid line.

Secondly, a streak-like segregation pattern (Figure 3(d)) in the mixed columnar-equiaxed region is predicted, which does not occur in the small ingot (Figure 2(b)). Concrete explanation to this segregation pattern demands more detailed analysis of the flow and sedimentation and their interaction with the solidification, nevertheless a tentative hypothesis is proposed as follows. As the equiaxed crystal can be captured (crystal entrapment) by the growing columnar trunks, the entrapment of the equiaxed crystals will lead to a heterogeneous, i.e. streak-like, phase distribution between the columnar and equiaxed immediately behind the columnar tip front, as seen in Figure 4(b)-(d). The resistance to the interdendritic flow by the columnar trunks and the entrapped equiaxed crystals are different, therefore the flow direction of the melt in this region is slightly diverted by the heterogeneous phase distribution. This diverted-flow can only be visible in

the carefully zoomed view. As the macrosegregation is extremely sensitive to the interdendritic flow, it is not surprising that the induced macrosegregation (Figure 3(d)) takes the similar streak-like pattern of the phase distribution (Figure 4(d)).

One may notice that this streak-like segregation has a similar contour as the classical A-segregation, but it is still not clear if the classical A-segregation is the same one as steak-like segregation or originates from such streak-like segregation. According to the mostly-accepted empirical explanation, A-segregation belongs to a kind of channel segregation in large steel ingots, which originates and develops in the stationary dendritic mushy zone. A recent study of the authors [33-34] in a Sn-Pb laboratory casting has found that the channel segregation can originate and develop in a pure columnar solidification, where no equiaxed crystal exists. Therefore, we name the streak-like segregation here as a quasi-A-segregation. To form this quasi-A-segregation, the sedimentation of equiaxed crystals and its interaction with the columnar tip front and melt flow seem to play important role. Details about the formation mechanism for this kind of quasi-A-segregation are still to be verified.

Thirdly, the simulation of the 2.45 ton ingot shows an isolated hot spot in the upper part (Figure 4(d)), which takes much long time to solidify. As the middle part of the ingot is already blocked by the columnar trunks, the solidification of the hot spot behaves like a mini-ingot. Sedimentation of the equiaxed crystals in the mini-ingot will cause a small region of negative segregation, as shown in Figure 3(d). This kind phenomenon happens very often in long (small section) ingot casting or in the continuously-cast round billet casting, and it is called as ‘bridging and mini-ingotism’ [35]. The experimental result of Figure 3(b) seems to show that no such ‘bridging and mini-ingotism’ occurs, as no such negative segregation zone is identified. It implies that the heat transfer boundary conditions applied in the current simulation might not be coincident with the reality.

The segregation along the ingot centreline is analysed, and compared with the experiment, as shown in Figure 5. The experiment shows the negative segregation in the lower part and positive segregation in the upper part. The model also shows the same tendency. They agree with each other qualitatively. However, the negative segregation in the lower part is predicted more severe than the experimental result. The overestimation of the negative segregation in the lower part by the model may come from two aspects. One is the assumption of globular equiaxed morphology, which can cause significant overestimation of the sedimentation-induced negative segregation according to Combeau et al. [8]. The other aspect is the error assumption of the equiaxed nucleation parameters.

In order to demonstrate the role of the equiaxed phase in the formation of segregation, an additional calculation is performed by ignoring the occurrence of the equiaxed phase. This case seems to show better agreement with the experiment, especially in the middle and lower part (Figure 5). The experimental result falls actually in a range between the two calculations. Based on the above two simulations, one may anticipate that in the reality a certain amount of equiaxed crystals would appear during the solidification of such a 2.45 ton ingot, but the amount of equiaxed crystals is overestimated by the current nucleation parameters.

The quantitative disagreement between the experiment and the calculations in top part of the ingot is mainly due to the formation of the cavity, which is not considered by the current model.

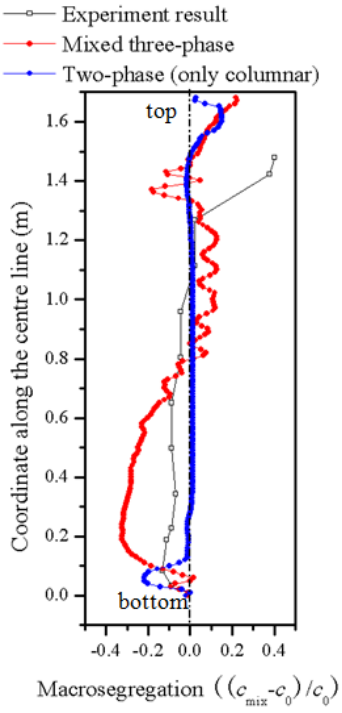

Figure 5: Comparison of the numerically predicted macrosegregation $((c_{mix}-c_o)/c_o)$ along the ingot centreline with the experiment [1]. Two simulations are performed: one is to consider the mixed columnar-equiaxed solidification ($n_{max} = 5\times10^9\ m^{-3}$, $\Delta T_\sigma = 2\,K$, $\Delta T_N = 5\,K$); one is to ignore the appearance of equiaxed crystal.

One should emphasize that the motivation of the current study is to validate the mixed columnar-equiaxed model, hence to explore the limitations of the model. We are not going

to adjust the process parameters without evidence to cater for the experiment results. Since the experiments were made decades ago and many of the process parameters and material properties were not reported, the current simulation results can only reproduce the experiment results qualitatively.

4 3.3 ton ingot

A forging ingot, 3.3 ton, was reported by Combeau and co-authors [8]. As a further step to validate the current three-phase solidification model, this ingot is also simulated. The shape of the ingot was actually octagonal, and an industry multicomponent alloy was poured, but here only a 2D axis symmetrical calculation for a simplified binary alloy (Fe-0.36 wt.%C) is performed. Process parameters and materials' data as reported in literature [8] are referred, but some unknown parameters have to be assumed for this preliminary calculation. Mould filling is ignored, and the nucleation parameters are assumed as: $n_{\max} = 2\times10^{9}\ \mathrm{m}^{-3}$, $\Delta T_{\sigma} = 2\,\mathrm{K}$, $\Delta T_{\mathrm{N}} = 5\,\mathrm{K}$. As no sufficient information for the exothermal powder being added on the hot top is provided, it is here treated as a refractory material. Different from the aforementioned calculations for the small benchmark and 2.45-ton ingots, here the mould system is included in the calculation.

The predicted macrostructure and macrosegregation are compared with the experimentally reported results, as shown in Figure 6 and Figure 7. Qualitatively, satisfactory agreement between them regarding to both macrostructure and macrosegregation is achieved. For example, the bottom equiaxed zone, accompanying relatively strong negative segregation (cone-shape), is predicted. This cone-shape negative segregation is mainly due to the equiaxed crystal sedimentation. Above the tail of the cone-shape negative segregation zone, there is a positive segregation zone (experimentally-shown only one point). Mechanism to form such positive segregation zone is due to the transport of the solute-enriched melt in the bulk. In the upper region of the ingot, just below the hot top, when the columnar dendrite tips, growing from side walls, meet together in the casting centre, some solute-enriched melt is 'frozen' there, to form this positive segregation. The late solidification of the hot top behaves as a mini-ingot. Sedimentation of the equiaxed crystals continues in the mini-ingot, but the crystals can only settle in the bottom of the mini-ingot, causing a small negative segregation zone in the bottom of the mini-ingot. Finally, a large positive segregation occurs in the hot top. Notice that the numerically predicted position of this positive

segregation zone is much higher (Figure 7) and the predicted segregation is less severe than the experimental one.

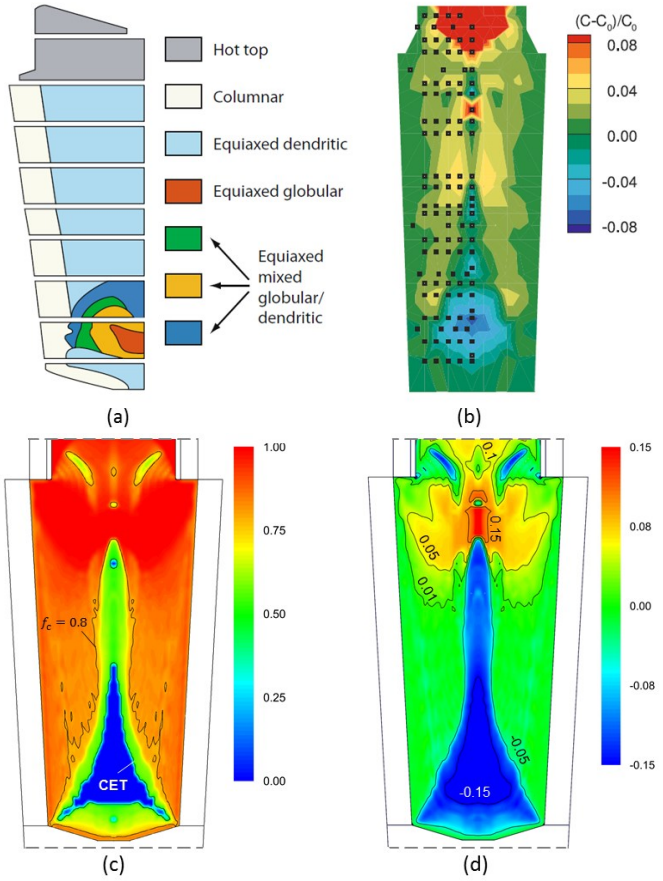

Figure 6: Modelling results of a 3.3-ton steel ingot: (a) experimentally measured macrostructure; (b) experimentally measured macrosegregation; (c) simulated macrostructure (volume fraction of columnar phase) and CET line; (d) simulated macrosegregation (colour scale overlapped with isolines). The macrosegregation, both experimental (b) and simulated (d), is shown for the nominal mixture concentration ($(c_{mix}\text{-}c_o)/c_o$). Nucleation parameters for the calculation are $n_{max} = 2\times10^9$ m^{-3}, $\Delta T_\sigma = 2$ K, $\Delta T_N = 5$ K. The experimental results and casting configuration are reproduced from the literature [8].

Despite of the above agreement, the quantitative difference between numerically predicted and experimentally reported results is still significant. A cone-shape equiaxed zone with a long tail extending beyond the middle height of the ingot is predicted (Figure 6c), while the experimentally found equiaxed zone does not show a cone-shape, instead, the equiaxed zone is more accumulated in the bottom region (Figure 6a). Although the cone-shape equiaxed zone was found typical in many ingots [1-3, 31], but it was not reported

experimentally in this ingot. One interesting phenomenon is that the numerically predicted bottom equiaxed zone (Figure 6c) has the same cone-shape as the negative segregation zone (Figure 6d), while the experimentally reported equiaxed zone (Figure 6a) does not show the same shape as the bottom negative segregation zone (Figure 6b). Explanation to this phenomenon demands further study. Another difference between the simulation and the experiment is the overestimation of the sedimentation induced negative segregation. The main reasons were discussed above: one is the ignorance of the crystal dendritic morphology, and one is the assumption of the crystal nucleation parameters. The error prediction of the position and severity of the positive segregation in the hot top is mainly due to the ignorance of the cavity formation and the unknown condition of the exothermal powder at the top.

For the calculation of this 3.3-ton ingot, 8627 volume elements are divided, and parallel calculation was performed on 8 cores (Intel Nehalem Cluster 2.93 GHz), and the simulation time was about 2 weeks.

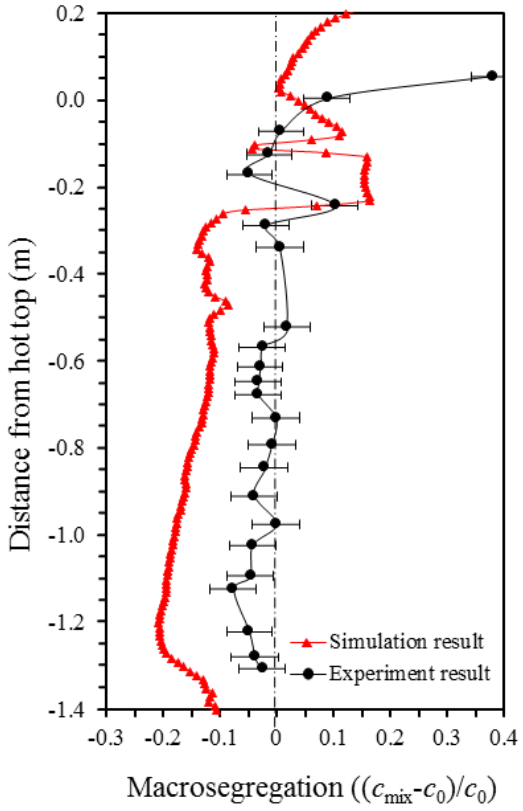

Figure 7: Comparison of the numerically predicted macrosegregation ($(c_{mix}-c_o)/c_o$) along the ingot centreline with the experiment [8].

5 Discussions

This article reported the on-going activities of the authors' group to scale-up a mixed columnar-equiaxed solidification model for the industry applications. Three examples were analysed to evaluate the potentials and limitations of the model.

5.1 Model potentials

Firstly, the simulated solidification sequence, the sedimentation of the equiaxed grains, the growth of the columnar tip front and the formation of the final macroscopic phase distribution fit with the widely accepted explanations of experimental findings, as summarized by Campbell [31]: "The fragments (equiaxed grains) fall at a rate somewhere between that of a stone and snow. They are likely to grow as they fall if they travel through the undercooled liquid just ahead of the growing columnar front, possibly by rolling or tumbling down this front. The heap of such grains at the base of the ingot has a characteristic cone shape." This kind of multiphase flow dynamics and interactions among the melt, equiaxed crystals and growing columnar trunks are the key phenomena for modelling the segregation pattern of Figure 1. They are considered by the current model.

Secondly, it is also verified by the above modelling examples that the most typical segregates, the concentrated positive segregation under hot-top and the cone of negative segregation at the base of the ingot, can be simulated by the model. A widely accepted explanation to the formation of the cone-shaped negative segregation is verified, again in Campbell's words: "The heap of equiaxed grains at the base of the ingot has a characteristic cone shape. Because it is composed of dendritic fragments, its average composition is that of rather pure iron, having less solute than the average for the ingot." A further contributing factor to the purity of the equiaxed cone region probably arises from the divergence of the flow of residual liquid through this zone at a late stage in solidification. The simulated negative segregation formation process by equiaxed crystal sedimentation (Figure 2 and 4) seems to have reproduced the experimental phenomenon. Mechanisms for positive segregations under the hot-top in steel ingots are diverse. It is generally agreed that they are caused by the melt convection in the bulk region or through the partially solidified and/or remelted mushy zone. For example, the upper positive segregation is explained by the melt convection in the bulk region, because the light solute-rich melt rises. Actually, according to the recent modelling results, with the sedimentation of large amount of equiaxed crystals

downwards, the relatively-positive segregated melt is pushed upwards, instead of 'rise' by itself, in the casting centre, hence to cause a positive segregation zone in the upper region.

Thirdly, it has demonstrated the possibility to calculate the distribution of columnar and equiaxed structure. The upper region of the ingot mainly consists of columnar dendrites, whereas a larger amount of equiaxed grains are predicted in the bottom region. Within the CET enclosed region, only the equiaxed phase exists, while outside of the CET region both columnar and equiaxed phases coexist. The macrostructure strongly depends on some modelling and process parameters, i.e. the equiaxed nucleation parameters ΔT_N , $n_{\max}$, ΔT_σ , the primary columnar space λ_1 , and boundary conditions.

Finally, the capability of the current model for the interdendritic-flow-induced channel segregation was also verified [33-34], but not precisely shown in the above examples. The modelling result for the channel segregation is extremely sensitive to the grid resolution. Grid size less than 0.1 mm is often required, and this is unrealistic for the large industry ingots on the base of the current computer resources. One interest finding by the current three-phase solidification model, worth mentioning here, is the streak-like (quasi-A) segregation pattern, which occurs due to the columnar-equiaxed interaction at the columnar tip front. The streak-like segregation pattern has some similarity to the classical A-segregation, but it is not clear if the classical A-segregation is the same one as or originates from the streak-like segregation. It is still to be verified.

5.2 Limitation of the model

Importance of the process conditions, e.g. the pouring temperature, pouring method, mould materials and interfacial heat transfer between the ingot and the mould, etc., is obvious for the quantitative accuracy of the simulated solidification process, hence of the macrosegregation. It is not discussed here. Following discussions focus on the aspect of numerical model.

Firstly, the influence of the nucleation event on the macrosegregation was addressed in the example of 2.45-ton ingot. The origin of the equiaxed grains may be due to different mechanisms, e.g. heterogeneous nucleation, and/or fragmentation and detachment of dendrites by re-melting, and/or nucleation formed during pouring by contact with the initial chilling of the mould. The recent model condenses all these phenomena into a single effective nucleation description. Here, a three-parameter heterogeneous nucleation law [29]

is applied for the origin of equiaxed crystals. The reliable nucleation parameters can be only possibly obtained experimentally.

Secondly, no shrinkage cavity and porosity is considered. This ignorance will influence the accuracy of the calculation, especially in the hot-top region. As shrinkage contributes or influences the interdendritic flow, it will influence the final distribution of the channel segregation as well. However, the global segregation pattern, e.g. the concentrated positive segregation in the upper region and the cone of negative segregation at the base of the ingot, will not be significantly influenced by the shrinkage.

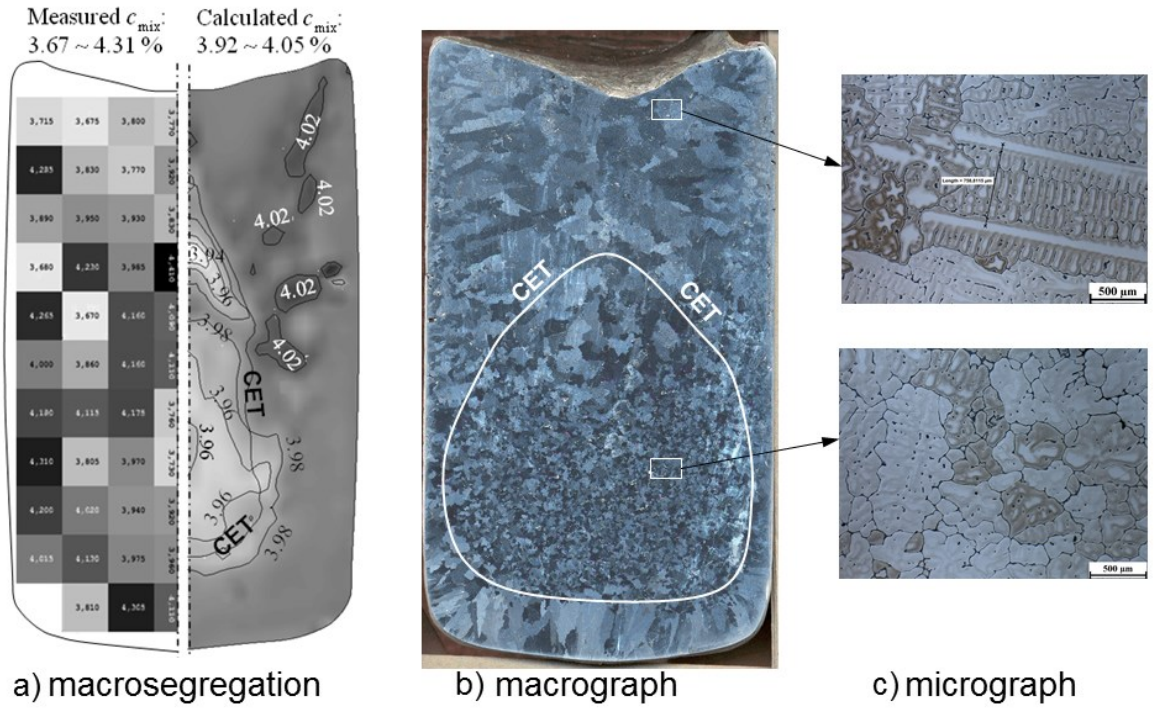

Figure 8: An example of the modelling result of an Al-4wt.%Cu ingot with a five-phase mixed columnar-equiaxed solidification model with dendritic morphology. (a) Comparison of the measured (spark analysis) macrosegregation (left half) with the calculated one (right half). The casting is poured at 800 °C. c_{mix} is shown in gray scale (dark for the highest and light for the lowest value). CET positions are plotted. This numerical simulation result shows satisfactory agreement to the as-cast macrostructure (b) macrograph, (c) micrograph.

Thirdly, no thermal mechanics is considered. The thermal mechanical shrinkage of the solidified outer shell of the ingot will influence the internal flow, but this may not be so

significant. What is most important is the deformation of the growing crystals, due to the thermal shrinkage or the solid phase transition, which would have great impact on the flow near end of solidification at the centreline. The 'V' segregation is mostly related to such deformation. This 'V' segregation is not modelled by the current model.

Finally, the current three-phase model does not include dendritic morphology. This ignorance has overestimated the cone of the negative segregation at the base, as what we see in Figure 5 and 7. In order to consider the dendritic morphology, more phases, i.e. the interdendritic melt, must be separately considered. In the authors' group, a five-phase model was developed to consider the mixed columnar-equiaxed solidification with dendritic morphology [26-27]. The calculation expense is so heavy to prevent from applying it in the industry ingots. However, the validity of this model for such purpose has been verified, but in a laboratory Al-4.0 wt.%Cu ingot casting, as shown in Figure 8. A cylindrical casting (ϕ 75 mm x 133 mm) was poured, analysed for both macrostructure and macrosegregation. The experimental results were used to validate the numerical simulations. Satisfied agreement between them was obtained, as reported elsewhere [36-37].

5.3 Outlook

The future modelling activities for the macrosegregation in large steel ingots will keep in two directions. One is to further enhance the model capability by including more physics such as solidification shrinkage, thermal mechanics, dendrite fragmentation as new crystal origin, etc. Another direction is to further validate and improve the existing multiphase model, and to apply it for the purposes of solving engineering problem and enhancing fundamental understanding of different segregation phenomena.

1. Thanks to the work of the Iron Steel Institute [1], many steel ingots scaled from 600 kg to 172 tons were poured and sectioned for segregation analysis. This work provides most valuable information for the validation of the numerical models.

2. The existing model can be applied for the process parameter study. Despite of the difficulty to quantitatively reproduce the segregation pattern of the reality, the influence of the process parameters, such as casting geometry, mould materials, pouring temperature, or other engineering measures, on the segregation can be well

described by the model. By performing such parameter study, metallurgists would achieve idea for the process optimization.

3. Any segregation mechanism, as proposed from the experimental observation, can (should) be verified quantitatively by the mathematical (numerical or analytical) model. The three-phase model can help to explain many well-known segregation phenomena in details. It may also help to explore the new segregation phenomena, which are caused by the multiphase flow. For example, the question of streak-like segregation, here we name it as a quasi-A-segregation, is first raised by the authors on the base of current modelling result. The equiaxed-columnar interaction at the columnar dendrite tip front and its influence on the melt flow seems to induce such kind of streak-like macrosegregation.

Acknowledgement

The authors acknowledge the financial support by the Austrian Federal Ministry of Economy, Family and Youth and the National Foundation for Research, Technology and Development.

References

[1] J. Iron Steel Institute, 103(1926), p. 39-176.

[2] Marburg E.: J. Met., 5(1953), p.157-172.

[3] Moore J.J., Shah N.A.: Int. Metals Rev., 28(1983), p. 338-356.

[4] Blank J.R., Pickering F.B.: The solidification of metals, London: The Iron & Steel inst., 1968, p. 370.

[5] Yamada H., Sakurai T., Takemonchi T., Suzuki K.:Proc. Annual Meeting of AIME, Dallas, 1982, A82-39, p.1-6.

[6] Klug J.S., Ernst C., Hartmann L.: Proc. SteelSIM, Düsseldorf, 27 June – 1 July 2011.

[7] Broytman O.A., Yu D., Monastyrsky A., Ivanov I.: Proc. SteelSIM, Düsseldorf, 27 June – 1 July 2011.

[8] Combeau H., Zaloznik M., Hans S., Richy P.E.: Metall. Mater. Trans., 40B(2009), p.289-304.

[9] Lesoult G.: Mater. Sci. Eng. A, 413-414 (2005), p. 19-29.

[10] Flemings M.C.: ISIJ Int., 40(2000), p. 833-841.

[11] Beckermann C.: Int. Mater. Rev.: 47(2002), p. 243.

[12] Ohnaka I.: ASM Handbook, 15 – Casting, ASM Int., USA, p.136.

[13] Gu J.P., Beckermann C.: Metall. Mater. Trans., 30A(1999), p. 1357.

[14] Ni J., Beckermann C.: Metall Mater Trans 22B(1991), p.49.

[15] Wang C.Y., Beckermann C.: Metall Trans 24A(1993), p. 2787.

[16] Beckermann C., Viskanta R.: Appl Mech Rev 46(1993), p.1.

[17] Wang C.Y., Beckermann C.: Metall Mater Trans 27A(1996), p.2754.

[18] Wu M., Ludwig A., Bührig-Polaczek A., Sahm P.: Int. J. Heat Mass Transfer, 46(2003), p. 2819.

[19] Ludwig A., Wu M.: Metall. Mater. Trans., 33A(2003), p.3673.

[20] Wu M.; Ludwig A., Ratke L.: Metall. Mater. Trans., 34A(2003), p.3009.

[21] Wu M.; Ludwig A., Ratke L.: Modell. Simu. Mat. Sci. Eng., 11(2003), p.755.

[22] Wu M.; Ludwig A.: Metall. Mater. Trans., 37A(2006), p.1613.

[23] Wu M.; Ludwig A.: Metall. Mater. Trans., 38A(2007), p. 1465.

[24] Wu M., Ludwig A.: Acta Mater., 57(2009), p. 5621.

[25] Wu M., Ludwig A.: Acta Mater., 57(2009), p. 5632.

[26] Wu M., Fjeld A., Ludwig A.: Comp. Mater. Sci.: 50(2010), p. 32.

[27] Wu M., Fjeld A., Ludwig A.: Comp. Mater. Sci.: 50(2010), p. 43.

[28] Wu M., Könözsy L., Ludwig A., Schützenhöfer W, Tanzer R.: Steel Res. Int., 79(2008), p.637.

[29] Rappaz M.: Int. Mater. Rev., 34(1989), p.93.

[30] Hunt J.D.: Mater. Sci. Eng., 65(1984), p. 75.

[31] Campbell J.: Castings, Butterworth Heinemann Ltd, Oxford, 1991.

[32] Li J., Wu M., Ludwig A.: Int. Conf. on MCWASP XIII, June 17-22, 2012, Austria.

[33] Li J., Wu M., Hao J., Ludwig A.: Comp. Mater. Sci., 55(2012), p.407.

[34] Li J., Wu M., Hao J., Kharicha A., Ludwig A.: Comp. Mater. Sci., 55(2012), p.419.

[35] Moore J.J.: Iron & Steel Soc., 3(1984), p.11-20.

[36] Wu M., Nunner G., Ludwig A., Li J.H., Schumacher P.: IOP Conf. Series: Mater. Sci. Eng., 27(2011), doi: 1088/1757-899X/27/1/012018.

[37] Wu M., Ahmadein M., Ludwig A., Kharicha A., Li J.H., Schumacher P.: Int. Conf. on MCWASP XIII, June 17-22, 2012, Austria.